
Kinematics of Coronal Mass Ejections in the Inner Corona and its Coupling with the Heliosphere

A Thesis
Submitted for the Degree of
Doctor of Philosophy

in

The Department of Physics,
Pondicherry University,
Puducherry - 605 014, India



by

Satabdwa Majumdar
Indian Institute of Astrophysics,
Bangalore - 560 034, India



July 2022

Kinematics of Coronal Mass Ejections in the Inner Corona and its Coupling with the Heliosphere

Satabdwa Majumdar

Indian Institute of Astrophysics



Indian Institute of Astrophysics

Bangalore - 560 034, India

Title of the thesis : **Kinematics of Coronal Mass Ejections in the Inner Corona and its Coupling with the Heliosphere**

Name of the author : **Satabdwa Majumdar**

Address : Indian Institute of Astrophysics
II Block, Koramangala
Bangalore - 560 034, India

Email : satabdwa.m@iiap.res.in

Name of the supervisor : **Prof. Dipankar Banerjee**

Address : Indian Institute of Astrophysics
II Block, Koramangala
Bangalore - 560 034, India

Email : dipu@iiap.res.in

Declaration of Authorship

I hereby declare that the matter contained in this thesis is the result of the investigations carried out by me at the Indian Institute of Astrophysics, Bangalore, under the supervision of **Prof. Dipankar Banerjee**. This work has not been submitted for the award of any other degree, diploma, associateship, fellowship, etc. of any other university or institute.

Satabdwa Majumdar

PhD Scholar, IIA,

Bangalore-560034, India

Date : 25th July, 2022

Certificate

This is to certify that the thesis entitled “**Kinematics of Coronal Mass Ejections in the inner corona and its coupling with the Heliosphere**” submitted to the Pondicherry University by Mr. Satabdwa Majumdar for the award of the degree of Doctor of Philosophy, is based on the results of the investigations carried out by him under my supervision and guidance, at the Indian Institute of Astrophysics. This thesis has not been submitted for the award of any other degree, diploma, associateship, fellowship, etc. of any other university or institute.

Dipankar Banerjee

Thesis Supervisor,

Indian Institute of Astrophysics,

Bangalore-560034, India

Date : 25th July, 2022

List of Publications

1. Connecting 3D evolution of Coronal Mass Ejections to their source regions; **Satabdwa Majumdar**, Vaibhav Pant, Ritesh Patel, & Dipankar Banerjee; *The Astrophysical Journal* (2020) 899:6 (15pp)
2. Imaging and Spectral Observations of a Type-II Radio Burst Revealing the Section of the CME-Driven Shock that Accelerates Electrons; **Satabdwa Majumdar**, Srikar Paavan Tadepalli, Samriddhi Sankar Maity, Ketaki Deshpande, Anshu Kumari, Ritesh Patel & Nat Gopalswamy; *Solar Physics* (2021) 296:62
3. Investigating width distribution of slow and fast CMEs in solar cycles 23 and 24; Vaibhav Pant, **Satabdwa Majumdar**, Ritesh Patel, Ankur Chauhan, Dipankar Banerjee & Nat Gopalswamy; *Frontiers in Astronomy and Space Sciences* (2021) 8:634358
4. An Insight into the Coupling of CME Kinematics in Inner and Outer Corona and the Imprint of Source Regions; **Satabdwa Majumdar**, Ritesh Patel, Vaibhav Pant, & Dipankar Banerjee; *The Astrophysical Journal* (2021) 919:115 (8pp)
5. * A Simple Radial Gradient Filter for Batch-Processing of Coronagraph Images; Ritesh Patel, **Satabdwa Majumdar**, Vaibhav Pant & Dipankar Banerjee; *Solar Physics* (2022) 297:27
6. On the Variation of Volumetric Evolution of CMEs from Inner to Outer Corona; **Satabdwa Majumdar**, Ritesh Patel & Vaibhav Pant; *The Astrophysical Journal* (2022) 929:11 (12pp)
7. * A CME Source Region Catalogue and their Associated Properties; **Satabdwa Majumdar**, Ritesh Patel, Arushi Rawat, Abhas Pradhan, Kavya Bindu, Vaibhav Pant, & Dipankar Banerjee; *The Astrophysical Journal* (Under preparation).

*Not included in this thesis

Presentations

1. Presented a poster titled “Connecting CMEs to their source regions, and understanding their 3D evolution: A preparatory study for the ADITYA L1 mission” 37th Meeting of the Astronomical Society of India, February 2019, Christ University, Bangalore, India
2. Presented a talk titled “3D evolution of slow and fast CMEs in solar cycle 23 and 24” in Young Astronomers Meet, 23-27 September, 2019, Kodaikanal Solar Observatory, IIA, Kodaikanal, India.
3. Presented a poster titled “3D Kinematics of slow and fast Coronal Mass Ejections in solar cycle 23 and 24 and the effect of their source regions: A preparatory study for the ADITYA L1 mission” in IRIS-10, 4-8 November, 2019, Christ University, Bangalore, India.
4. Presented a poster titled “Connecting 3D Kinematics of slow and fast CMEs to their source regions: A preparatory study for the ADITYA L1 mission” in 38th Meeting of the Astronomical Society of India, 13-17 February, 2020, IISER Tirupati, Tirupati, India.
5. Presented a poster titled “Insights from connecting 3D evolution of CMEs to their source regions” in IIA-50 Conference on Advances in Observations and Modelling of Solar Magnetism and Variability, 1-4 March, 2021, IIA, Bangalore, India.
6. Presented an invited talk under the theme “Properties of Solar Sources of CMEs” in the ADITYA Science Meet – 3, 19-20 April, 2021, ISRO, India, Online.
7. Presented a talk titled “Insights on 3D evolution of CMEs in the inner corona” in PUNCH 2 Science Meet, 9-11 August, 2021, Online.
8. Presented a poster titled “Insights on 3D kinematics of Coronal Mass Ejections in the inner corona” in 16th European Solar Physics Meeting, 6-10 September, 2021, Online.

9. Presented a talk titled “Coupling of CME kinematics from Inner to Outer Corona, and influence of their Source Regions” 21st National Space Science Symposium, January 31 – February 4 2022., Online.
10. Presented a talk titled ”A study of Volumetric Evolution of CMEs & constraints on our present understandings” on the 40th meeting of the Astronomical Society of India, 25-29 March 2022, Indian Institute of Technology Roorkee.

Acknowledgements

“I don’t want to be an engineer or a doctor”, said I, when I was in class 11. My mother replied, “What do you like studying the most?”, I said ‘Physics!’, “Then do a BSc. MSc. and a PhD. in physics” said my mother. I asked, “But why should I do a PhD. maa ?”, she replied, “Well if you do it, then you will become a scientist !!”. My father added, “ Be whatever you want, we are with you, and I am sure you will be very good in whatever you do !”. My little brother smiled to re-assure me. I was awestruck by the first ever alignment of the word ‘scientist’ with me, and the amount of faith these three people had on me. Tonight, while writing the acknowledgement of my thesis, it gives me goosebumps to realise that I am living my dream, all four of us are living this one little dream, and I am loving it!!

At the very onset, I want to acknowledge my PhD. supervisor, Prof. Dipankar Banerjee, or as we all lovingly call him, Dipu da!! He has wonderfully guided me throughout my PhD. journey. The things that I have learned from him is not just limited to my work. From him, I have developed my scientific temperament, realised the fruits of having patience, belief in hard work, leadership qualities and many more. I enjoy the occasional discussions with him on music, football, theatre etc. It’s been just amazing throughout.

Then comes the person on whom, with absolute pleasure I put the blame of bringing me into solar astrophysics. I am talking of Dr. Vaibhav Pant, or as I call him, Vaibhav da!! Starting from that 2.5 hr discussion with him, in Bhaskara lobby in my first year, till today, I have thoroughly enjoyed exchanging my scientific thoughts with him. He has inspired me, supported me and helped me grow as an independent researcher. I extend my heartfelt gratitude to him.

I also want to thank Prof. Nat Gopalswamy (GSFC/NASA), for his wonderful guidance during my work with him in the COSPAR workshop in 2020. It was very

exciting to work with him. I also acknowledge Dr. Elke D'Huys, Dr. Marilena Mierla and also Ketaki of the Royal Observatory of Belgium, for all the wonderful discussions and all the help that I have received from them during my Guest Investigator visit.

These years of PhD. became even simpler and wonderful, having Bibhuti around, not just as a group mate, but as a very close friend. I will always look back and cherish the varied discussions that we have had, rarely related to our work, and the beautiful insights that I have imbibed from him makes me treasure this friendship even more.

Also, throughout my PhD. I have received so so much help from my group mate, my colleague, and my friend Ritesh. He has been a constant source of help and support for me. Working with him is simply fun and exciting. So cheers to that, and to many more in the years to come !!

I would also like to extend my gratitude to our research group (or Dipu's gang as we are called), my seniors Sudip da, Shubhamoy da, Chandru da, Nancy di, Rakesh da and my juniors, Arpit, Samriddhi, Nitin, Aditya, Jyoti, Dibya, Upasna for their valuable inputs during our group discussions.

I will never be able to thank enough my close friends, Partha, Sharmila and Bibhuti for being by my side, all the time. I had never thought that even during my PhD. I will get friends like you guys, to whom I can turn to, anywhere, anytime, without any hesitation. Thanking you will be such an understatement of this friendship.

I would like to take this opportunity to thank my batchmates, Sharmila, Suman, Manika, Vikrant, Ankit, Sahel for everytime they helped me or did something for me.

I absolutely cherish my friendship with Athira, and the frequent candies that she keeps in my office desk, will always remain close to my heart. It was pleasure to share my office space with Anirban, and I will miss those engrossing (and at times complete non-sense) conversations which helped us stay in rhythm and in our senses in the middle of our work pressure. Spending time with him was always relaxing and fun. I cherish my friendship with Bharat, and would always look back to the fun-filled moments.

I would also like to thank Soumya, Sonith, Deepthi, Fazlu, Jyoti for being such good friends. I also share a strong bond with my juniors, especially Shubham, Judhajeet, Neeraj, and two sisters that I have got in Saili and Payal. They have been such wonderful juniors, and I thank them for that.

I had Anirban da as my roommate for most part of my PhD. journey, and he has been so much more than just a roommate. He has been my friend, my elder brother at times. The amount of love, care and support that I received from him will always remain special to me. I also want to thank my present roommate Nitish. He has been a wonderful roommate, more like a younger brother to me, and I thank him for being such an adjusting and understanding junior and roommate.

I would also extend my heartfelt thanks to Swastik, for being such a lovely friend, and helping me out everytime I needed a help from him.

I want to thank my seniors Chayan da, Dipa di, Avrajit da, Rakesh da, Anirban da, Samrat da, Sneha di, Megha di, Aritra da, Tridib da, Sandeep da, Pavna di, Bhoomika Di, Rubi Di, Debjit da, Ramya di, Manoj, Priya di, Purna, Panini, Avinash, Raghu. They made me feel so comfortable when I came to bhaskara, and I thank all of them from my heart.

I especially treasure the times I have spent with Avrajit da, Chayan da and Dipanwita di, and I will always remember the amount of love I have received from them.

I have also had the privilege of having such wonderful juniors; Judhajeet, Payel, Saili, Neeraj, Sioree, Pallavi, Rishabh, Ravi, Anohita, Aratrika, Dhanush, Amrutha, Akhil, Parvathy, Sayuf, Shubhangi, Sushant, Rupesh, Khushbu, Chandan, Pravash, Shivani, Renu, Radhika, Raveena. I am sure I have missed some names, but I thank them all for being there along my journey.

I would like to acknowledge the contribution of my dadu (maternal grandpa) in shaping me as a person, and for inspiring and loving me throughout. Also, I must acknowledge my thaam (paternal grandma) who used to always support, love and propel me. I thank all my relatives who have showered their good wishes on me all throughout my life.

My sincere gratitude also goes to my school physics teacher (Sinha sir), for his love, support and appreciations that I have received over the years. My school friends have also been a huge source of love and support, and I am so glad to have friends like them.

I must thank the friends that I have made in ARIES, during my 3 month stay there, the way they welcomed me and made me feel one amongst them was indeed wonderful. In particular, I will never forget the amount of affection that was showered upon me by Anjasha di, making me feel so special that my existence as a guest visitor vanished to make space for all the shower of loving sentiments.

Also, a lot of credit goes to my friends that I have had during my BSc. at St. Xavier's college Kolkata and during my MSc. at IIT Madras. My love for physics got shaped so beautifully through them. The way they approach the subject

(Shaswata, Minhajur, Indranil, Aditya, Debmallya, Provakar, Souvik, Sumit, San-
ket, to name a few) have fascinated me, clinically, and I feel glad to have a share
of their sentiments. Also, a big shout-out to Debmalya, Provakar and Madhumita,
with whom I have shared my BSc. and MSc. days, and they have become more
of family now than just friends.

Thanks a lot to all the administrative staff, library and computer support team,
for their help during my stay at IIA. I would like to convey my sincere gratitude
to Sankara Sir for his help in completing all the administrative processes. I sin-
cerely applaud the COE, HOD Physics Department and administration staff of
Pondicherry University; without their constant support, it was not possible for
me to concentrate on my work without worrying about the different non-academic
processes which were involved along with.

To be true to myself, I would never be able to thank you all enough, and hence I
wouldn't go for that. I would rather wish all of you my best wishes for the years
to come, and if I can be of any help anytime, never hesitate to ask for it. Keep
smiling.

—Satabdwa

Data usage

I have used several space and ground-based data facilities throughout my different projects included in this thesis. Here, I take the opportunity to extend my heartfelt gratitude to all the respective instrument team members for providing the data in public domain, which has provided me with the opportunity to work on the projects of my interest.

The SECCHI data used here were produced by an international consortium of the Naval Research Laboratory (USA), Lockheed Martin Solar and Astrophysics Lab (USA), NASA Goddard Space Flight Center (USA), Rutherford Appleton Laboratory (UK), University of Birmingham (UK), Max-Planck-Institut for Solar System Research (Germany), Centre Spatiale de Liège (Belgium), Institut d'Optique Théorique et Appliquée (France), Institut d'Astrophysique Spatiale (France).

The CDAW CME catalog is generated and maintained at the CDAW Data Center by NASA and The Catholic University of America in cooperation with the Naval Research Laboratory.

I acknowledge SDO team for making AIA data available.

The SOHO/LASCO data used here are produced by a consortium of the Naval Research Laboratory (USA), Max-Planck-Institut fuer Aeronomie (Germany), Laboratoire d'Astronomie (France), and the University of Birmingham (UK). SOHO is a project of international cooperation between ESA and NASA.

Courtesy of the Mauna Loa Solar Observatory, operated by the High Altitude Observatory, as part of the National Center for Atmospheric Research (NCAR).

NCAR is supported by the National Science Foundation.

I thank the Gauribidanur Radio Observatory for providing the radio spectral and imaging data, during the COSPAR capacity building workshop held at Kodaikanal, January 2020.

SWAP is a project of the Centre Spatial de Liege and the Royal Observatory of Belgium funded by the Belgian Federal Science Policy Office (BELSPO)

*“Parents are like a bow,
And children like arrows.
The more the bow bends and stretches,
farther the arrow flies.
I fly, not because I am special,
but because they stretched for me..”*

~ Khalil Gibran

To Maa & Baba

Abstract

Ever since the dawn of astronomy, we and the Sun have not been celestial strangers anymore, and it was soon realised that there is a close Sun-Earth connection that was awaiting our acknowledgement. With that came several dedicated space and ground based solar missions, and it was understood that Coronal Mass Ejections (CMEs) lies at the heart of this Sun-Earth connection. After several decades of observing and studying CMEs, our understanding of their behaviour have touched great heights. But, inspite of the strident progress in this area, there are some challenges that have left certain grey patches in our understanding of CMEs. Although we do have a good understanding of the propagation of the CME in the outer corona and the heliosphere, we are yet to have a clear understanding of the early evolutionary phase of the CMEs in the inner corona region ($< 3R_{\odot}$). This has been mainly due to limited observational data in the inner corona, and projection effects occurring due to measurements made on the plane of the sky. This thesis particularly aims at improving our understanding on the above two aspects, and dedicates the results obtained to several existing and upcoming solar missions that will be observing the inner corona.

As an attempt to remove projection effects and to understand the kinematics of CMEs in the inner corona, the Graduated Cylindrical Shell (GCS) model is applied on the stereoscopic observations of 59 CMEs from COR-1 and COR-2 on-board the twin spacecraft Solar Terrestrial Relations Observatory (STEREO-A/B). This enabled a two vantage point tracking of CMEs through a combined field of view of $1.5 - 14 R_{\odot}$. We combined the 3D width evolution and acceleration profiles to report for the first time an observational evidence in support of the conjecture that CME acceleration and width expansion are just different manifestations of the same Lorentz force, and based on this we report that statistically, the Lorentz force impact on the kinematics remains dominant in a height range of $2.5 - 3 R_{\odot}$. We also show that combining latitude and

position angle distributions to understand CME deflections, might be misleading. With a statistical study on the distribution of projected widths of CMEs, we report for the first time that slow ($< 300 \text{ km s}^{-1}$) and fast ($> 500 \text{ km s}^{-1}$) CMEs arising from different source regions (i.e. active regions (ARs) and prominence eruptions (PEs)) follow different power laws in their width distributions, thus indicating different physical mechanisms of width expansion. We also study the coupling of the 3D kinematics in the inner corona, to the kinematics in the outer corona, and we find that the kinematics in the inner corona largely controls the later kinematics, and that this coupling of kinematics is different for CMEs arising from ARs and PEs. We report on several statistical correlations between different kinematic parameters in the inner and outer corona, and we present empirical relations that can be used in extrapolating outer coronal parameters from inner coronal parameters. But, owing to the limited field of view of COR-1, the full main acceleration phase of the CME could not be captured, because a part of that crucial phase was already over by the time the CME came in the COR-1 field of view. Further, due to 2 vantage point tracking, there are degeneracy in certain parameters for some CME orientations.

Motivated by the above results and the shortcomings that came along, we extended the application of the GCS model to the inner coronal observations from the ground-based coronagraph K-Cor of the Mauna Loa Solar Observatory (MLSO) along with the pair of observations from STEREO as earlier. This Extended - GCS (EGCS) model enabled for the first time 3D tracking of CMEs, uniquely in white light observations from heights as low as $1.1 R_{\odot}$. Apart from being able to capture the early acceleration phase of the CMEs in white light observations, we also studied the evolution of the true volume of the CME with height. For the first time, we report a power law dependence of the CME volume with distance from the Sun. We further find the volume of ellipsoidal leading front and the conical legs follow different power laws, thus indicating differential volume expansion through a CME. The study also reveals two distinct power laws for the total volume evolution of CMEs in the inner and outer corona, thus suggesting different expansion mechanisms at these different heights. Also, this differential volume

expansion of CMEs further motivated me in studying the velocity dispersion inside CMEs in the inner corona, as that will have profound significance on the validity of the assumption of self-similar expansion of CME evolution.

A multi-wavelength study is also presented here on a CME that occurred on January 26 2014. In this work, the significance of combining radio observations with white-light and extreme ultraviolet observations is presented in better understanding the shock driving phenomenon of CMEs that are responsible for producing type-II radio bursts. It was with the help of the radio spectral and imaging observations, that it became possible to pin point that it was the flank of the CME than the nose, that hosted the type-II burst location, and that too, the Southern flank.

Encapsulating in a nutshell, this thesis will largely aid in filling in some of the crucial gaps and connect the missing links (as mentioned earlier) towards a holistic understanding of CME kinematics in inner corona, and the way the kinematics gets coupled at the higher heights. The different chapters besides highlighting the sole potential of white-light observations in arriving at the above scientific goals, will also provide rich inputs in observational plannings of the existing and upcoming solar missions that will observe the inner corona. It will also provide crucial constraints to the models that tries to emulate the ejection and propagation of CMEs at the lower and higher heights.

Contents

Abstract	i
List of Figures	ix
List of Tables	xv
Abbreviations	xvii
1 Introduction	1
1.1 The solar interior	2
1.2 The solar atmosphere	4
1.3 The solar wind and heliosphere	6
1.4 Coronal Mass Ejections	7
1.4.1 Brief historical background	8
1.4.2 Observation of CMEs	9
1.4.3 Properties of CMEs	11
1.4.4 Kinematics of CMEs	11
1.4.5 Source regions of CMEs	13
1.4.6 CMEs and type-II radio bursts	14
1.5 Motivation	14
1.6 Outline of the thesis	18
2 Data	21
2.1 Solar Dynamics Observatory	22
2.1.1 AIA	24
2.2 Solar and Heliospheric Observatory	24
2.2.1 EIT	26
2.2.2 LASCO	27
2.3 Solar Terrestrial Relations Observatory	28
2.3.1 SECCHI	30
2.3.2 SWAVES	33
2.4 K-Coronagraph	33

2.5	Project for Onboard Autonomy-2	34
2.5.1	SWAP	35
2.6	Co-ordinated Data Analysis Workshops catalogue	36
3	Study of 3D evolution of CMEs	39
3.1	Introduction	39
3.2	Data and Method	44
3.2.1	Data Source and Data Preparation	44
3.2.2	Event selection and Source Region identification	45
3.2.3	3D Reconstruction and Estimation of Geometrical Parameters	47
3.2.4	Methods of the estimation of 3D kinematical properties	49
3.3	Results	51
3.3.1	Connecting Width to the 3D Kinematics	53
3.3.2	Affinity for the equator - 3D Deflection of CMEs	58
3.3.3	Comparison of average projected and true Speeds	61
3.3.4	Distribution of Peak Speeds and Accelerations	63
3.3.5	Acceleration duration and acceleration magnitude	66
3.4	Summary and Conclusions	68
4	Coupling of CME kinematics from inner to outer corona	75
4.1	Introduction	75
4.2	Data and Method	80
4.2.1	Data Source and Data Preparation	80
4.2.2	Event Selection for the study of width distribution	80
4.2.3	Segregation of CMEs into slow and fast	81
4.2.4	Parameter description for the study of coupling of 3D kinematics	82
4.3	Results	84
4.3.1	Width distribution of slow and fast CMEs	84
4.3.2	The coupling of 3D kinematics	90
4.4	Summary and Conclusions	99
5	Insights of Volumetric evolution of CMEs	103
5.1	Introduction	103
5.2	Data and Method	106
5.2.1	Data Source and Data Preparation	106
5.2.2	Event Selection	107
5.2.3	The GCS fitting to STEREO and K-Cor data	108
5.3	Results	111
5.3.1	Improvement in the understanding of early CME kinematics	111
5.3.2	Insights on width expansion of CMEs	113
5.3.3	Evolution of modelled CME volume	116
5.4	Discussions and Conclusions	126

6	Understanding the Type-II burst association with CME shock	131
6.1	Introduction	131
6.2	Data Selection	134
6.3	Event description and timeline	134
6.4	Data Analysis and Results	138
	6.4.1 CME Kinematics from white-light data	138
	6.4.2 Connecting Radio and White-Light Data	139
6.5	Summary and Conclusions	145
7	Study of velocity dispersion inside CMEs in inner corona	153
7.1	Introduction	153
7.2	Data sources	155
7.3	Working method	156
7.4	Results	157
7.5	Conclusion	159
8	Conclusion	161
8.1	Chapter 3	162
8.2	Chapter 4	163
8.3	Chapter 5	164
8.4	Chapter 6	165
8.5	Chapter 7	166
8.6	Novelty of the thesis	167
8.7	Future Work	168

Bibliography	171
---------------------	------------

List of Figures

1.1	A sectional view of the internal structure of the Sun, and the various atmospheric layers some of the associated features. <i>Credit: astronomyopenstar</i>	3
1.2	A plot depicting how the temperature and density change with height in the solar atmosphere. <i>Image Courtesy: Lang (1995)</i>	5
1.3	(a): A CME as observed in the LASCO-C2 coronagraph on-board SOHO. <i>Image credit: NASA</i> (b): A three-part CME with the leading edge, the dark cavity and the inner core, as seen in LASCO-C2 image. <i>Image credit: Colaninno (2012)</i>	7
1.4	A historical representation of the spacecrafts that are relevant to the study of CMEs. <i>Image credit: Howard (2011)</i>	8
1.5	Images of the same CME obtained from three different viewing locations within an hour: a) from STEREO/COR2-B at 11:39 UT, b) from LASCO/C2 at 10:55 UT, and c) from STEREO/COR2-A at 11:08 UT. At this time (April 2010) the STEREO spacecraft were approximately 70° in longitude from the Sun-Earth line and $\sim 140^\circ$ from each other. <i>Image taken from Webb and Howard (2012a)</i>	9
1.6	A CME observed in LASCO-C2, with the measured quantities of position angle, width depicted. <i>Image credits : Pierantoni et al. (2014)</i>	10
1.7	(a): An illustration of the three different phases of CME kinematics and its relation with temporal evolution of GOES soft X-ray flux (<i>Image credits: Zhang and Dere (2006)</i>). (b): A plot of the velocity profile for the CME on June 11, 1998, showing the 3 phase kinematics (<i>Image credits: Zhang et al. (2001a)</i>).	12
2.1	A view of the SDO spacecraft with the instruments on-board. <i>Image credits : (Pesnell, Thompson, and Chamberlin 2012)</i>	23
2.2	A view of the four telescopes on-board the SDO. <i>Image credits : (Lemen et al. 2011)</i>	24
2.3	(a): The SOHO spacecraft in launch configuration. (b): A schematic view of the SOHO spacecraft. <i>Image credits Domingo, Fleck, and Poland (1995)</i>	25

2.4	A schematic view of the Extreme Ultraviolet Imaging Telescope, with the major instrument subsystems indicated along with. <i>Image credits Delaboudinière et al. (1995)</i>	27
2.5	A front view of the LASCO instruments with the three coronagraphs. <i>Image credits Brueckner et al. (1995a)</i>	28
2.6	An artistic conception of the STEREO spacecraft. <i>Image credits STEREO team</i>	30
2.7	A view of the EUVI telescope, before being integrated into the SECCHI package.. <i>Image credits : Howard et al. (2008a)</i>	31
2.8	A layout of the COR-1 telescope. <i>Image credits : Howard et al. (2008a)</i>	32
2.9	A layout of the COR-2 telescope. <i>Image credits : Howard et al. (2008a)</i>	32
2.10	(a): The K-Cor coronagraph at the Mauna Loa Solar Observatory, Hawaii. (b): A schematic layout of the K-Cor telescope. <i>Image credits: MLSO</i>	34
2.11	(a): The PROBA-2 spacecraft. (b): A schematic view of the SWAP instrument. <i>Image credits : PROBA-2 Team.</i>	36
2.12	A layout of the COR-2 telescope. <i>Image credits : CDAW Team</i>	37
3.1	The CME on 2012 – 11 – 09 observed by COR-1 A and COR-1 B at 01:00:00 UT, with the GCS model generated flux-rope structure (green wireframe) overlaid on them. Note that the CME has a face on view in (a) and an edge on view in (b)	49
3.2	3D kinematic profiles of slow CMEs in (a) and (b), and fast CMEs in (c) and (d). In every panel, the top figure shows the height-time plot derived from COR-1 and COR-2 data using the GCS model. The solid red line represents the smooth-spline fit to the height-time data. The second and third plots show the CME speed and acceleration derived by the numerical differentiation of (a) and (b), respectively. The uncertainty in the fitted model is shown in the grey shaded region. An inset with a zoom into the residual acceleration phase is provided for each event in the bottom corner of the acceleration plots. The axis scale in x coincides with the x axis at the bottom.	54
3.3	(a): Variation of the half-angle of CMEs with height. Only those events are showed which showed expansion by greater than 10 degrees. Different colors correspond to different events. (b): Distribution of the height of the saturation of the width and the height where impulsive acceleration vanishes.	57

3.4	(a) Top panel: The latitudinal distribution of the locations of source regions of CMEs. Bottom panel: Distribution of the PA equivalent latitude of the CME leading front. (b) Top panel: Distribution of the initial GCS latitude. Bottom panel: Distribution of the final GCS latitude. (c) Plot of final versus initial GCS latitude, with the solid line being the boundary where both the values are equal. The dashed line represents the zero latitude (i.e. equator) (d) Change of latitude of the CME with height estimated from the GCS model. only those cases where the deflection was at least more than 10 degrees are shown. The different data points denote different events - 2011-01-24 (circle), 2011-06-20 (triangle), 2012-02-24 (square), 2012-03-12 (cross) and 2012-10-12 (rhombus).	59
3.5	A comparison between the average projected 2-D speeds as recorded in the CDAW catalogue and the average 3D speeds as calculated using the GCS model. The dashed line is the boundary where both the 2-D and 3D speeds are equal.	62
3.6	(a) Distribution of peak speeds of all the CMEs. The dashed line denotes the mean value. (b) shows the contribution of peak speeds of CMEs originating from APs, ARs and PEs to (a).	64
3.7	Panel (a) shows the distribution of peak accelerations of all the CMEs. The dashed line denotes the mean value. Panel (b) shows the contribution of peak accelerations of CMEs originating from APs, ARs and PEs to panel (a).	64
3.8	(a) Distribution of acceleration duration of all the CMEs. The dashed line denotes the mean value. (b) Acceleration magnitude versus duration of all the CMEs. Different colors indicate CMEs originating from different source regions.	66
4.1	Width distribution of all CMEs (excluding "very poor" events) during solar cycle 23 and 24 using the CDAW catalogue. The black line corresponds to a power law fit to the width distribution where α is the power law index.	85
4.2	Width distribution of CMEs (excluding the intermediate and "very poor" events) during solar cycle 23 and 24 using the CDAW catalogue. The black line corresponds to a power law fit to the width distribution where α is the power law index.	87
4.3	(Left)Width distribution of slow CMEs from different source regions, with their widths taken from the CDAW catalogue. (Right) power-law fitting of the width distribution. The black line is the power-law fit to the data.	87
4.4	(Left)Width distribution of fast CMEs from different source regions, with their widths taken from the CDAW catalogue. (Right) power-law fitting of the width distribution. The black line is the power-law fit to the data.	88

4.5	Plot of (a) a_{\max} versus V_{\max} and (b): V_{\max} versus a_{\max} of all the CMEs. The dashed curves denote the fitted power-law relation. The data points and fitted curves are color coded according to the source regions.	91
4.6	Plot of (a) V_{lin} and V_{mi} and (b) V_{\max} versus V_{m} . The dashed curves denote the fitted power-law relation. The data points are color coded according to the source regions.	93
4.7	Plot of (a) a_{const} versus V_{mi} . The dashed curves denote the fitted power-law relation. The data points are color coded according to the source regions.	96
4.8	(a): Distribution of V_{mi} and V_{m} (b): V_{mi} versus V_{m} . (c) Distribution of a_{mi} and a_{m} . (d) Distribution of h_{amax} and h_{vmax} . The data points are color coded according to the source regions.	97
5.1	The fitting of the GCS flux-rope to K-Cor and the pair of COR-1 images for the 5 CMEs studied in this work.	110
5.2	The complete 3D kinematic profiles of two out of five impulsive CMEs are shown as representative examples. The height-time data is fitted with a cubic smooth spline (shown in solid red line). The speed and acceleration plots are obtained by taking first and second order numerical derivatives of the height-time plot. The grey shaded region corresponds to the uncertainty in the fitted model parameters. The impulsive phase is highlighted in the second and third panels in yellow. An inset with a zoom into the residual acceleration phase is provided in the bottom right hand corner of the acceleration plots. Please note that the time axis of the zoomed insets is overlapped with the common time axis shown at the bottom. In the bottom, the evolution of the half-angle (α) parameter is plotted.	111
5.3	The evolution of the modelled (a) face-on and (b) edge-on width of CMEs in the inner corona. Different regions of the plot are highlighted according to the data used.	114
5.4	A schematic for the estimation of CME volume from the GCS reconstructed 3D flux-rope structure. The entire CME volume can be sub divided into three parts, A: the ellipsoidal front, B: the asymmetric middle disc and C: the conical legs. The figure is adapted from Holzkecht et al. (2018).	116
5.5	The evolution of the modelled CME volume and its different parts. The color coded plots denote evolution of different volume elements (the ellipsoidal front, the middle asymmetric disc and the conical legs) in the inner and outer corona.	123
5.6	The evolution of the total modelled CME volume in the inner and outer corona. The data points and curve in black mark the volume in IC($< 4R_{\odot}$), while the ones in red are for those in the outer corona ($> 4R_{\odot}$).	125

- 6.1 *Left:* The source region of the CME as observed in SDO/AIA 193 Å shown in the enclosed rectangle at the western limb. The image is made at 08:28:07 UT. The ‘white’ circle represents the photospheric Sun. *Right:* The GOES soft X-ray light curve of the associated C1.5 class flare on 26 January 2014. Note that the flare is occulted, so the actual soft X-ray intensity is expected to be higher than the one showed in the figure here. 136
- 6.2 The CME on January 26, 2014 observed with (a) STEREO/COR-2A; (b) SOHO/LASCO-C3; and (c) STEREO/COR-2B. The diffused shock structure beyond the bright flux-rope can be seen in STEREO A and STEREO B views as marked with ‘white’ color arrow. The location of STEREO A and STEREO B were W151 and E156, respectively. 136
- 6.3 The figure shows the composite dynamic spectra of the metric type II burst recorded with the GLOSS (ground-based) and the DH continuation of the same as observed by STEREO B/WAVES. The start frequency of the Type II bursts is ~ 90 MHz as seen in Learmonth spectrograph. The type II burst shows fundamental harmonic structures in metric-DH wavelengths. The two bands are shown with ‘red’ lines. 138
- 6.4 The height–time profile of CME shock and flux-rope as observed in (a) STEREO/COR-2A (measured at PA $\approx 242^\circ$); (b) STEREO/COR-2B (measured at PA $\approx 234^\circ$). In panel a and b, the red and blue points correspond to the shock front the flux-rope of the CME, respectively. The speed measured at the leading edge of the CME with the SOHO/LASCO data from CDAW catalogue (c). The CME leading edge speed variation with position angles is shown in panel d and the corresponding position angles are marked in Figure 6.2a . 148
- 6.5 (a) The CME as observed in COR-2A; (b) COR-2B at 09:24 UT with the GCS model fit in green; (c) The variation of CME leading front speed with time in the LASCO C2 and C3 FOV and from the GCS model fit to the CME in the COR-1 and COR-2 A/B FOV. The CME is clearly decelerating in the coronagraphs FOV. 149
- 6.6 (a) The composite of the WL CME as seen in the SOHO/LASCO-C2 FOV with the 80 MHz contours obtained with GRAPH radio observations and the SDO/AIA-193 Å. The red circle marks the solar disk. The radio contours are shown at 50, 72, 75, 87, and 99% of the peak radio flux at 80 MHz. The contour intervals are at $\approx 6.6 \times 10^3$ Jy. The de-projected height of the radio contours are at $\approx 1.1R_\odot$ and the position angle is $\approx 157^\circ$. An inset with a zoom into the AIA image shows the spatial location of the associated flare (top right). The location of 80 MHz centroid is marked with blue color in the inset image; The North and South flank speeds of the CME from height–time measurements in (b) COR-2A FOV; and (c) in LASCO C2 and C3 FOV. 150

-
- 6.7 CME interacting with the streamer at the southern flank as depicted in the LASCO-C2 image at 08:48 UT. The LASCO image is superposed on with SDO/AIA 193 Å image. 151
- 7.1 A three part structure CME as observed on 2015-07-02 at 17:44:12 (left) and 17:55:35 (right) UT by SWAP and K-COR. In the left panel it is seen that the filament is still in the SWAP field of view whereas, the leading front has travelled into K-COR. In the right panel, the leading front, flux-rope and filament can be identified with their separation increased than the first image. 155
- 7.2 A height time profile of the CME flux-rope and core in K-Cor and SWAP respectively, along different position angles is shown. 157
- 7.3 Evolution of the CME aspect ratio for the CME on 2012-03-12, as observed in the COR-1A and COR-1B field of view. The different color coded data points denoted different position angles of tracking. 158

List of Tables

3.1	The GCS model parameters of all the CMEs are tabulated below. h is the height of the leading front, θ , and ϕ are the latitude and longitude of the foot-points of the CME, the tilt-angle (γ) is the angle between the axis of symmetry of the CME and the local parallel of latitude, aspect-ratio (k) is the ratio of the radius of cross-section of the leading front and the radial distance of the leading front from the center of the Sun and α is the half-angle between the legs of the best fit GCS model. The Time is the time of observation, V_{CDAW} is the average linear speed taken from the CDAW catalogue, and V_{GCS} is the average 3-D speed calculated from the GCS model. . . .	53
4.1	Summary of the fitted parameters with the Correlation Coefficients (CCs), Critical Correlation Coefficients (CCCs), p-values and the fitted relations. Note that apart from the overall empirical relation, the same is also shown separately only for the source regions for which the CC is distinctly different and higher than the CC of others. In (a) and (b) the CC for AR is much higher than others. In (c) and (d), the individual CCs are similar, while in (e) the CC for AR and AP are similar to the overall CC, and the CC for PE is much poor.	83
4.2	A summary of the fitted power-laws using GF and MLE for CMEs originating from different source regions.	86
5.1	The GCS model parameters fitted to the CMEs are tabulated. The Time is the time of observation, ϕ , and θ are the longitude and latitude of the CME, the tilt-angle (γ) is the angle between the axis of symmetry of the CME and the solar equator, h is the height of the leading front, aspect-ratio (k) is the ratio of the minor to the major CME radius and α is the half-angle between the legs of the CME.	109
5.2	The empirical relations for the volume evolution of CMEs with the corresponding R^2 values and P - values for the different sections of the CME.	121
5.3	The empirical relations for the volume evolution of CMEs in the IC and outer corona with the corresponding R^2 values and P - values.	124

6.1 Timeline of the January 26 2014 CME and the associated phenomena. 137

Abbreviations

NASA	National A eronautics and S pace A dministration
SOHO	S olar and H eliospheric O bservatory
EIT	Extreme ultraviolet I maging T elescope
LASCO	Large A ngle and S pectrometric C oronagraph
STEREO	Solar T errestrial R elations O bservatory
SECCHI	Sun E arth C onnection C oronal and H eliospheric I nvestigation
MLSO	Mauna L oa S olar O bservatory
GCS	Graduated C ylindrical S hell
FOV	F ield O f V iew
CME	C oronal M ass E jection
ESA	E uropean S pace A gency
ASPIICS	Association de S atellites P our l' I magerie et l' I nterferométrie de la C ouronne S olaire
SWAP	Sun W atcher using A ctive pixel system detector and I mage P rocessing
PROBA	P roject for O n- B oard A utonomy
SDO	Solar D ynamics O bservatory
AIA	A tmospheric I maging A ssembly

Chapter 1

Introduction

The Sun, which is a star of spectral type G2V, belonging to the main sequence branch, age around 4.6 billion years is in the Milky Way galaxy, located at its Orion arm. It has an effective surface temperature of ~ 5780 Kelvin, $\sim 1.99 \times 10^{30}$ kg of mass, and ~ 696000 km radius. The Sun rotates around its own axis, but unlike a rigid body, the rotation of the Sun is non-uniform across its different latitudes. It takes around 25 days to complete one rotation at the equator, while it takes around 35 days to complete a rotation at the poles. The Sun comprises of ~ 74.9 % Hydrogen, ~ 23.8 % Helium and ~ 1.3 % heavy metals ([Ross and Aller 1976](#); [Lodders 2003](#)). With the strident progress in the field of astronomy, it is now understood that the Sun is the nearest star from the Earth, with a Sun-Earth distance of $\sim 1.49 \times 10^{11}$ m. This has allowed us to understand the Sun, and the different phenomena occurring there, in great details, by observing the Sun in various bands of the electromagnetic spectrum.

With the advancement in technology, with more ground and space based observations of the Sun, we now try to understand the dynamic and active nature of our

nearest star. Besides, it is also now understood that the Sun is the driving factor behind space and terrestrial weather, and thus the study of Sun so as to understand better, the solar-terrestrial relation has now become of utmost importance.

1.1 The solar interior

The understanding of the internal structure of the Sun that we have reached, has happened over time, and the three building blocks that have made significant contributions to our understanding of the solar interior are the standard solar model (Bahcall et al. 1982), helioseismology (Leibacher et al. 1985) and observations of solar neutrinos (Bahcall 2001). Since the interior of the Sun cannot be directly observed, its structure is obtained by modelling and then comparing the modelled structure with observed properties, by recursively tuning the model parameters until the model matches the observed properties. The standard solar model, thus is essentially, several differential equations, which are further constrained by boundary conditions (the mass, luminosity and radius of the Sun), where the boundary conditions are in turn, derived from the principles of fundamental physics. Helioseismology, on the other hand, helps us probe the solar interior structure, by studying and understanding the propagation of waves, especially sound waves in the Sun.

The solar interior comprises of three main parts, the core, the radiative zone and the convective zone (see Figure 1.1). At the very central region of the Sun, lies the core. At the core, which extends out up-to a height of $0.25 R_{\odot}$ from the Sun center, has a temperature of $\sim 1.5 \times 10^7$ Kelvin, and density of $\sim 1.5 \times 10^5 \text{ kg m}^{-3}$ (Lang 1995). It is the core of the Sun, where energy is generated through the process of thermonuclear fusion which also results in the formation of heavier elements and also releases energy through the formation of gamma ray photons.

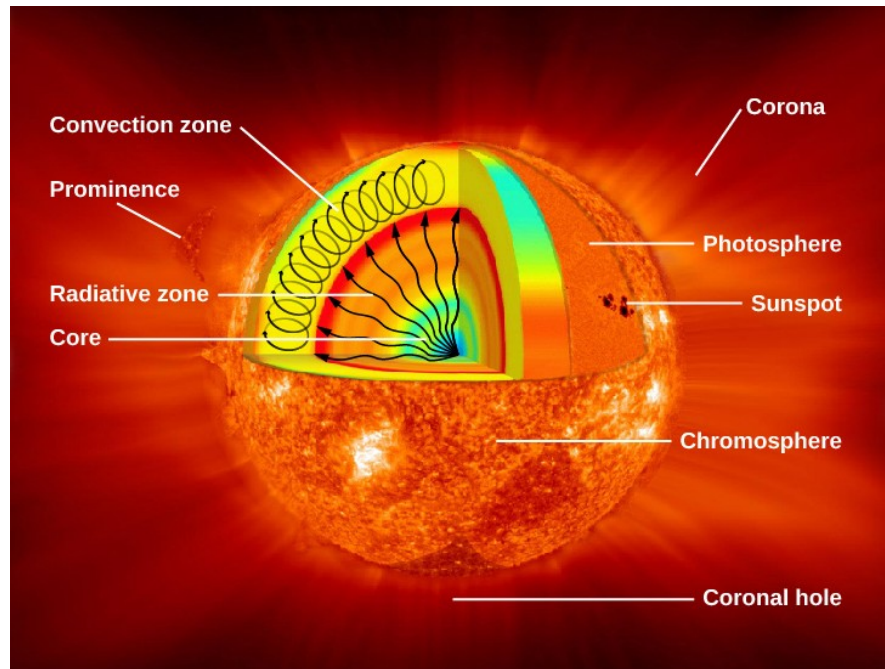


FIGURE 1.1: A sectional view of the internal structure of the Sun, and the various atmospheric layers some of the associated features. *Credit: astronomy-openstax*

After the core, the radiative zone starts and it extends from $0.25 R_{\odot}$ to $0.7 R_{\odot}$. In the radiative zone, the temperature drops from $\sim 7 \times 10^6$ Kelvin at the base, to 2×10^6 Kelvin at the top. The gamma ray photons from the core, gets repeatedly absorbed and re-emitted by the nuclei in the radiative zone. Owing to a high density here ($\sim 2 \times 10^4 \text{ kg m}^{-3}$), the mean free path of these photons become small ($\sim 2 \times 10^{-2}$), and thus it takes around tens to some hundreds and thousands of years for the photons to travel through the radiative zone (Mitalas and Sills 1992).

From $0.7 R_{\odot}$ to $1 R_{\odot}$ lies the convective zone and as the name suggests, energy transport in this region, occurs through the process of convection. In this region, the temperature gradient set up by radiative transport is larger than the adiabatic gradient which results in the convection pattern (Foukal 2004) (see Figure 1.1). The temperature in this region, starts to decrease very rapidly with height, thereby reaching ~ 5700 Kelvin at the outer boundary. It has been proposed that around

$0.7 R_{\odot}$ (in a layer of thickness $\sim 0.04 R_{\odot}$), the solar magnetic field is generated through a dynamo mechanism, where the sound speed and density profiles show a sudden 'bump', called the tachocline (Spiegel and Zahn 1992).

1.2 The solar atmosphere

Based on the temperature, density and composition, the solar atmosphere is divided into four parts, namely the photosphere, the chromosphere, the transition region and the corona (see Figure 1.1). Photosphere is nothing but the visible surface of the Sun that we observe everyday. It is a layer of depth ~ 500 km, and the optical depth here becomes 1 at a wavelength of 500 \AA . The solar photosphere has a temperature of ~ 5700 Kelvin, and it features sunspots (areas of high and concentrated magnetic field, which can be identified on the Sun's surface as dark spots (Figure 1.1)). The extension of photosphere is till a height where the temperature reaches to an minimum ~ 4300 K (see Figure 1.2).

Above the photosphere, lies the solar chromosphere, which starts beyond the temperature minimum layer, up to a height at which the temperature touches ~ 20000 K. The name chromosphere is derived from the Greek word *chroma*, which means color, since it was observed as a red feature in total solar eclipse observations. The chromosphere extends for a height range of ~ 3000 to 5000 km. The chromosphere is known to exhibit several dynamical features like spicules, prominences/filaments etc.

Beyond the chromosphere, a thin layer of ~ 100 km thickness lies, which is termed as the transition region. This region marks a rapid rise of temperature to 10^6 K and a rapid fall of the electron density from 10^{11} cm^{-3} to 10^9 cm^{-3} (see Figure 1.2). Beyond the transition region, lies the outermost layer, the corona. The name

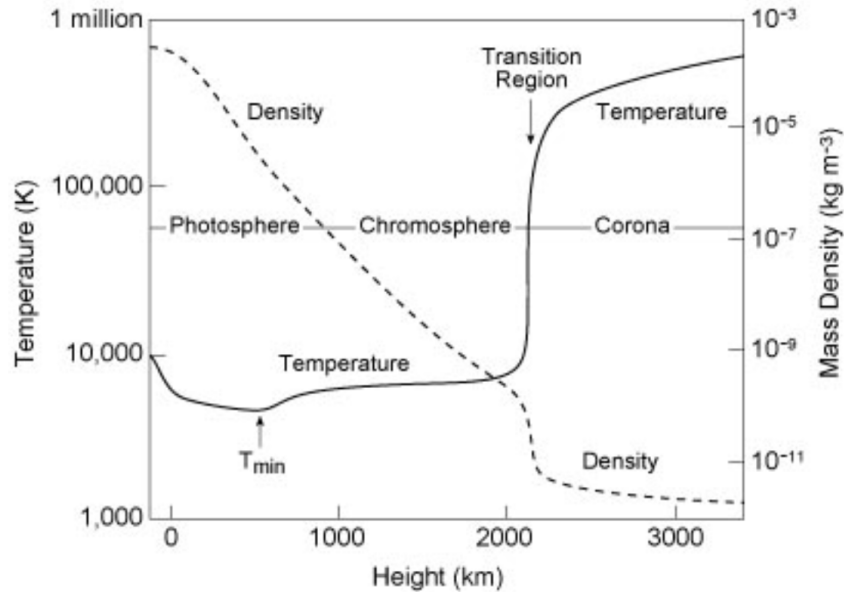


FIGURE 1.2: A plot depicting how the temperature and density change with height in the solar atmosphere. *Image Courtesy: Lang (1995)*

derives itself from a crown like appearance around the solar limb, as observed in total solar eclipse observations. The corona is at a temperature of $\sim 10^6$ K and is a lot fainter than the disk of the Sun, hence it can only be observed, if the solar disk is blocked out, as it happens during the occurrence of a total solar eclipse. With the advent of coronagraph, artificial eclipses are created, so as to observe and monitor the corona every minute. The corona is also known to host several features in the likes of coronal loops, streamers, coronal holes, active regions etc.

Figure 1.2 shows how the temperature varies with height in the different layers of the solar atmosphere, as reported by Vernazza, Avrett, and Loeser (1981). It is worth noting that the curve is based on a one-dimensional model which is averaged over quiet Sun, and hence the actual variations might be different across different structures and different regions of the Sun. It can be seen that the temperature initially, gradually decreases and reaches a minimum at the base of the chromosphere, after which, it again starts increasing slowly until we see a rapid increase in the transition region, which is seen to continue further into the corona. This rise in temperature of the corona is known as the "coronal heating problem"

(Grotrian 1939), and this is something still not well understood. The corona extends millions of kilometers into the outer space and exist beyond 1 AU. The solar corona is comprised of three components, namely the K-corona, the F-corona and the E-corona. This categorisation is based on the nature of radiation emitted by them. From the K-corona, the emitted scattered light shows the continuum spectra of the photosphere with no Fraunhofer lines and the emission is found to be strongly polarised. The F-corona again shows the continuum spectra, but with the Fraunhofer lines superimposed on it, while the E-corona comprises of the spectral line emission from the several atoms and ions present there.

1.3 The solar wind and heliosphere

The outermost atmosphere of the Sun (i.e. the corona) is so immensely hot, that even gravity cannot prevent it from continuously evaporating. This leads to a constant out-stream of plasma, called the solar wind, that arises from the Sun's atmosphere, and fills the ambient space (Biermann 1951; Parker 1958). The escaping particles, comprising the solar wind, carries energies of ~ 1 keV, and this solar wind is observed in two states, the fast solar wind and the slow solar wind. The later has a speed of ~ 400 kms⁻¹ with a proton density of around ~ 10 cm⁻³, while the former has a speed of ~ 800 kms⁻¹ with a proton density of ~ 3 cm⁻³ (Schwenn and Marsch 1990). In the Skylab era, Krieger, Timothy, and Roelof (1973) discovered coronal holes (which are usually found where the magnetic field lines are prevalently open) as the source of fast solar wind.

As the solar wind runs into the interstellar medium (ISM), it slows down from supersonic to sub-sonic speed, at a certain location from the Sun, which is called the termination shock. In 2004, the Voyager 1 spacecraft and in 2007, the Voyager 2 spacecraft passed through the termination shock at a distance of ~ 94 AU and

84 AU respectively, from the Sun (Richardson et al. 2008). After the termination shock, lies the heliosheath, where the ISM and the solar wind are in pressure balance. The outer boundary of this heliosheath is termed as heliopause, which is also known as the edge of heliosphere. The solar wind does not expand infinitely into space, but it stops at the heliopause. In 2012, Voyager 1 crossed the heliopause at a distance of 121 AU from the Sun. This region around the Sun, which is dominated mostly by the solar wind, is termed as the heliosphere.

1.4 Coronal Mass Ejections

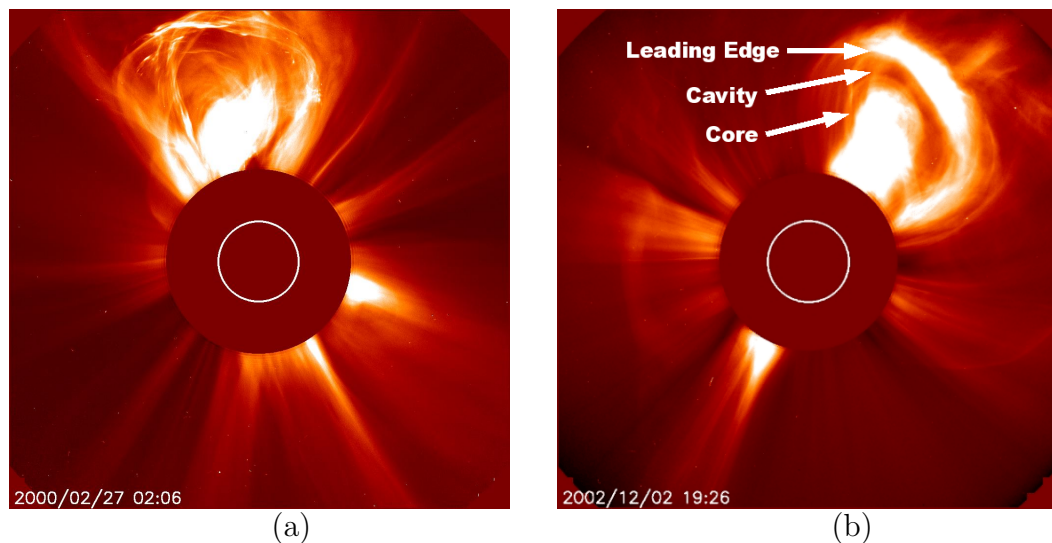


FIGURE 1.3: (a): A CME as observed in the LASCO-C2 coronagraph on-board SOHO. *Image credit: NASA* (b): A three-part CME with the leading edge, the dark cavity and the inner core, as seen in LASCO-C2 image. *Image credit: Colaninno (2012)*

Since I aim to study and understand the kinematics of Coronal Mass Ejections (CMEs), as is evident from the title of my thesis, let me introduce CMEs at this point and then let's see how our understanding of such phenomena took birth and evolved with time. The most general way of defining CMEs is that they are regarded as an observed change in structure of the corona (see Figure 1.3), that occurs on a timescale of minutes to even hours, and involving new, discrete, bright,

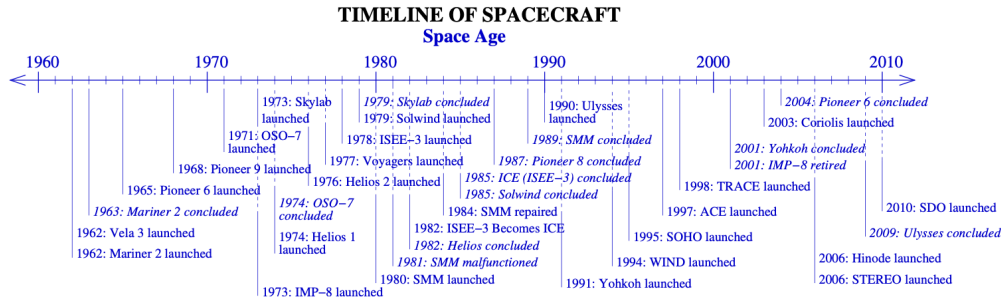


FIGURE 1.4: A historical representation of the spacecrafts that are relevant to the study of CMEs. *Image credit: Howard (2011)*

white-light (WL) feature, propagating outwards, in the FOV of the coronagraph (Hundhausen et al. 1984a). However, it is now well established that CMEs are violent explosions of magnetic field and plasma, that are expelled from the Sun's corona, into the heliosphere.

1.4.1 Brief historical background

The act of observing the Sun's corona took birth through solar eclipse photography much earlier. However, the CME was probably observed distinctly for the first time during a solar eclipse of 1860 as was shown from a drawing recorded by G. Temple. It was soon realised that the faint solar corona could be observed only in a total solar eclipse, and hence the frequency with which the corona could be observed and hence studied was limited by the frequency of occurrences of the eclipses. Such a big hurdle towards un-interrupting coronal observations was removed with the discovery of a coronagraph. A coronagraph is an instrument which occults the solar disk and hence the bright photosphere, thus creating an artificial eclipse which makes the fainter corona visible. Then, with the advent of space era, a CME was imaged on December 14, 1971 by a coronagraph onboard the seventh Orbiting Solar Observatory (OSO-7) satellite (Tousey 1973).

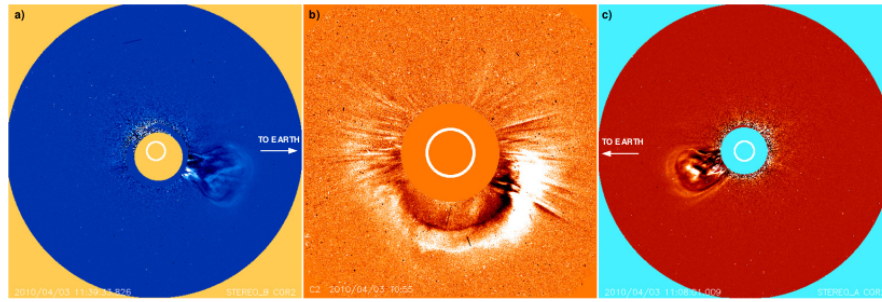


FIGURE 1.5: Images of the same CME obtained from three different viewing locations within an hour: a) from STEREO/COR2-B at 11:39 UT, b) from LASCO/C2 at 10:55 UT, and c) from STEREO/COR2-A at 11:08 UT. At this time (April 2010) the STEREO spacecraft were approximately 70° in longitude from the Sun-Earth line and $\sim 140^\circ$ from each other. *Image taken from Webb and Howard (2012a)*

Since then, thousands of CMEs have been observed by several space based coronagraphs, through the likes of Apollo Telescope Mount on-board Skylab (Gosling et al. 1975), Solwind coronagraph on board P78-1 satellite (Sheeley et al. 1980), Coronagraph/Polarimeter on board Solar Maximum Mission (SMM) (MacQueen et al. 1980a), LASCO on board SOHO (Brueckner et al. 1995a) and the coronagraphs (CORs) on STEREO (Howard et al. 2008a).

1.4.2 Observation of CMEs

CMEs are usually observed in traditional WL images, by the process of Thomson scattering of the light (from the photosphere) off the free electrons of the coronal and heliospheric plasma. WL observations provides an additional advantage over radio, infrared or extreme ultraviolet observations from the fact that Thomson scattering depends only on the density structure, and is independent of the wavelength and temperature, however, it must be noted that the intensity of Thomson scattered light depends on the relative angle of observation, which must be taken care of, in the calculated brightness of CMEs (Billings 1966; Vourlidis and Howard 2006). CMEs are fainter than the background solar corona, but they are relatively

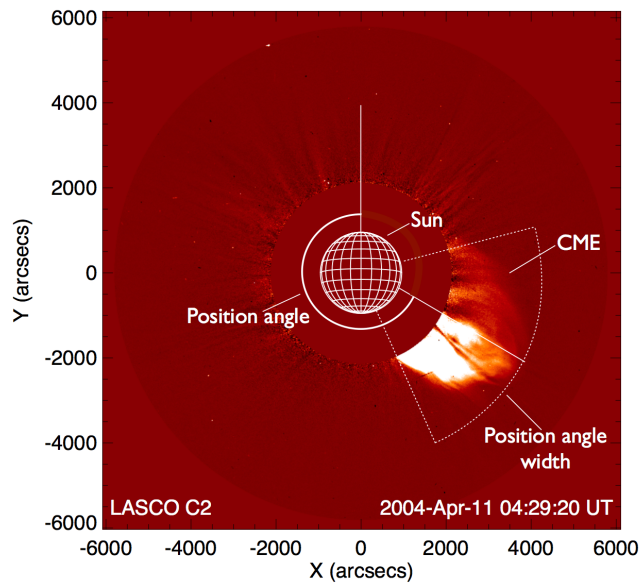


FIGURE 1.6: A CME observed in LASCO-C2, with the measured quantities of position angle, width depicted. *Image credits : Pierantoni et al. (2014)*

more transient, thus a suitable background subtraction is required to identify them in the images. In this regard, it is worth noting that a coronagraph records a two-dimensional (2D) image of a three-dimensional (3D) structure, projected onto the sky plane. As a result of this, the observed morphology of CMEs in coronagraphic images, largely depends on the location of the observing instrument and the direction of launch of the CME (Figure 1.5). For the CMEs, which are launched towards or away from the Earth, when observed from the near Earth coronagraphs, they appear as a halo, surrounding the occulting disk (Howard et al. 1982). Such a CME is termed as a 'halo' CME. A typical CME is often known to show a three-part structure in coronagraphic observations, comprising of a bright leading front, followed by a darker cavity and then a bright inner core (Figure 1.3(b)).

1.4.3 Properties of CMEs

The basic properties by which CMEs are characterised are their speeds, accelerations, angular widths, masses and energies. It has been reported in earlier works that CMEs tend to show a wide range in their speeds, from a few tens to a few thousands of kms^{-1} , and an even wider range of accelerations, from a few tens to even 10^4 ms^{-2} (Wood et al. 1999; St. Cyr et al. 2000; Zhang et al. 2001a; Bein et al. 2011a). CME widths can vary from a few tens of degrees to 360 degrees. CMEs having 360° width are termed as "full halo" CME, and with widths lying between 120° but less than 360° are termed as "partial halo" CMEs (Yashiro et al. 2004a). The estimated mass of CMEs are known to range from 10^{10} to 10^{13} kg, and energies from 10^{20} to 10^{26} J, while the average mass and energy of CME tends to be $\sim 1.4 \times 10^{12}$ kg and 2.6×10^{23} J respectively (Vourlidas et al. 2010). The occurrence rate of CMEs vary with the solar cycle, with around 4 to 5 CMEs per day in the solar maximum to around 1 CME per day during the solar minimum (Yashiro et al. 2004a; Webb and Howard 2012a).

1.4.4 Kinematics of CMEs

The kinematics of CMEs is governed by the interplay of three forces, namely the Lorentz force, the gravitational force and the viscous drag force (Wood et al. 1999; Zhang et al. 2001b; Vršnak et al. 2007a; Webb and Howard 2012a). As a result of the outcome of the interplay of these three forces, CMEs tend to follow a three phase kinematic profile (see Figure 1.7). The first, initial phase is a slow rise phase, which is followed by a second phase of impulsive acceleration, where the CME speed increases rapidly, in a short interval of time, and then comes the third phase, called the propagation phase, where the CME tend to experience very little or no acceleration (Zhang et al. 2001a; Zhang and Dere 2006). In this regard, the

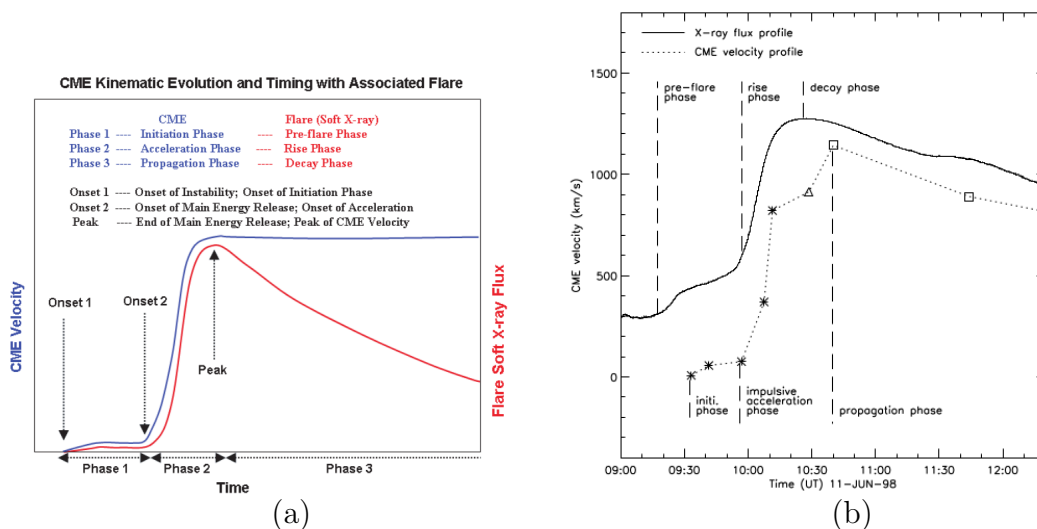


FIGURE 1.7: (a): An illustration of the three different phases of CME kinematics and its relation with temporal evolution of GOES soft X-ray flux (*Image credits: Zhang and Dere (2006)*). (b): A plot of the velocity profile for the CME on June 11, 1998, showing the 3 phase kinematics (*Image credits: Zhang et al. (2001a)*).

first two phases are usually over in the low coronal heights ($< 3R_{\odot}$) (Temmer et al. 2008; Bein et al. 2011b; Patel et al. 2021a), and hence to have a good understanding of CME kinematics, it is essential to capture their kinematics in the inner corona (IC) region ($< 3R_{\odot}$) as reported by Temmer et al. (2008); MacQueen and Fisher (1983). At later stages of their evolution, CMEs experience drag due to solar wind resulting in the deceleration (Gopalswamy et al. 2000a; Moon et al. 2002; Webb and Howard 2012a). Prior to the launch of the STEREO mission, several studies on CME kinematics were reported (Dere et al. 1997; St. Cyr et al. 1999a; Zhang et al. 2001a; Vršnak et al. 2004; Gopalswamy 2006b), but as mentioned earlier, tracking a CME from single view point observations introduces discrepancies due to projection effects into the measurements (Balmaceda et al. 2018a). It was after the launch of the twin STEREO spacecraft, that, multiple vantage point observations became available, and using different 3D reconstruction techniques, the 3D kinematics of CMEs were studied (Mierla et al. 2008a; Thernisien, Vourlidas, and Howard 2009a; Mierla et al. 2010; Moran, Davila, and Thompson 2010).

CMEs, apart from propagating radially, they also expand laterally, which is seen as an initial increase in their angular width (Kay, Opher, and Evans 2015; Cremades, Iglesias, and Merenda 2020a). It is now understood that the CME width provides a lot of crucial information on their kinematic properties and hence should be an integral part of their study (Moore, Sterling, and Suess 2007; Lugaz et al. 2017). During the early evolution phase, CMEs often show non-radial deflections in their trajectories (Gopalswamy et al. 2009a; Gui et al. 2011; Lugaz et al. 2012; Wang, Hoeksema, and Liu 2019). It has been observed that CMEs can get deflected from their initial path when they get ejected near a coronal hole (Gopalswamy et al. 2009a; Kahler, Akiyama, and Gopalswamy 2012). Such deflections, can happen both latitudinally and/or longitudinally (see; Kay, Opher, and Evans 2015), and should be taken into consideration for height time measurements, especially from single vantage point observations.

1.4.5 Source regions of CMEs

CMEs are associated with several on-disk features, which are considered to be their source regions, from which they erupt. Such features can be coronal streamers and blowouts (Illing and Hundhausen 1986), active regions and prominence eruptions (Subramanian and Dere 2001; Moon et al. 2002), coronal dimming, arcade formation (Kahler 1977; Tripathi, Bothmer, and Cremades 2004), sigmoids (Canfield, Hudson, and McKenzie 1999) etc. Locating the source regions of the CMEs on the disk of the Sun, is particularly important for getting a primary sense of direction, along which the CME is propagating, especially to ensure whether a halo CME is travelling towards or away from Earth, based on whether the source region is located on the frontal side of the solar disk facing the Earth, or towards the back side (Cane, Richardson, and St. Cyr 2000).

1.4.6 CMEs and type-II radio bursts

Fast CMEs, with speeds higher than the ambient Alfvén speed, are capable of driving shocks in the low corona and interplanetary (IP) medium (Hundhausen 1987). These shocks associated with CMEs, are often observed in WL images, and in such cases, the shock signatures can be tracked directly from the WL CME images (Sheeley, Hakala, and Wang 2000; Vourlidas et al. 2008). In such cases, often, a type-II radio burst is found to be accompanying the CME. These type-II bursts are now understood to be produced by electrons accelerated at the shock front (Uchida 1962), and they are identified as slanted, slowly drifting features in a frequency-time dynamic spectrum, with the slope related to the density scale height of the medium and the speed of the shock (Gopalswamy 2006b). These type-II bursts, accompanying the CMEs, provide remote diagnostic tools for studying CMEs, and they provide the earliest signature of shock formation (Gopalswamy et al. 2012; Carley, Vilmer, and Vourlidas 2020), which is usually within a height of a small fraction of the solar radius from the solar surface (Cane and Stone 1984; Cho et al. 2013).

1.5 Motivation

After outlining a brief overview of CMEs and the different associated phenomena that are studied for a holistic understanding of CMEs, let me discuss the where we are lacking in our understanding of CME kinematics, what are challenges involved in reducing the gray patches in our understanding, and hence, how my thesis aims at contributing to this domain of research by providing new inputs to our present understandings.

On the very outset, it is important to point out that studying CMEs are of interest, not just from scientific point of view, but from a technological and economical point of view as well. This is due to the fact that CMEs, apart from being such dynamic events with such wide range of kinematic properties, they happen to be the major space weather drivers. They are capable of producing transient interplanetary disturbances, shock waves and the ones travelling towards Earth can have a severe impact by creating geomagnetic storms that can pose a threat to our several technological advancements and life as a whole (see; [Gosling 1993a](#); [Schwenn et al. 2005](#)). Thus it is imperative, to have a very good understanding of their kinematics, for better preparedness for such drastic events.

As pointed out earlier, the kinematics of the CMEs tend to have three phases, out of which, the first two phases gets over by the time CME goes beyond the inner corona (IC; $< 3 R_{\odot}$). Furthermore, it has been pointed out that it is the Lorentz force that is primarily responsible for accelerating and expanding a CME ([Subramanian et al. 2014](#)), and hence, if the early kinematics occurring during the first two phases gets captured, then that will reveal crucial information on the role of Lorentz force behind propelling a CME. Now, despite several attempts at understanding the kinematics of CMEs, we are yet to reach a clear understanding of their kinematics in the inner corona (IC) region, and hence an understanding of the impulsive acceleration phase. Having said that, it is worth pointing out that there have been several studies that have probed the early kinematics of CMEs, right from their initiations (to name a few; [Dere et al. 1997](#); [St. Cyr et al. 1999a](#); [Zhang et al. 2001a](#); [Gallagher, Lawrence, and Dennis 2003](#); [Temmer et al. 2008](#); [Bein et al. 2011a](#); [Cheng et al. 2020a](#), and many more). In most of these works, the method either relied on measurements made on the plane of the sky, thus introducing discrepancies due to projection effects (e.g. [Zhang and Dere 2006](#); [Balmaceda et al. 2018a](#)), or involve combining WL observations with extreme ultraviolet (EUV) observations, for tracking a CME (e.g. [Vršnak et al. 2007b](#); [Bein et al. 2011a](#)), where whether the same features are observed in emission lines

and in WL are still debatable (see [Song et al. 2019](#)). Thus the need is to stitch together these missing links and probe the 3D kinematics of CMEs, in the inner and outer corona, and that too, uniquely in WL observations, so as to preserve the uniqueness of the tracked physical feature in successive frames. Also, since the width of a CME holds important clues to its kinematic behaviour, a unification of the process of width evolution with the process of impulsive acceleration will provide a more unified insight on the role of Lorentz force in the kinematics of CMEs. Another key challenging aspect is the loss of STEREO-B spacecraft in 2014, after which we did not have stereoscopic observations of the IC in WL. Although, the coronagraphic observations from STEREO-A can be combined with LASCO observations, but unfortunately, due to the limited FOV of LASCO, the impulsive phase of the CME gets already over by the time the CME enters the FOV of LASCO.

Another important aspect in the understanding of CME kinematics is the change of kinematics as the CME propagates from the inner to the outer corona. In the initial stage, the CME experiences rapid acceleration, which is usually over in the IC ([Temmer et al. 2008](#); [Bein et al. 2011a](#)), while the later stage marks the experience of drag force owing to the interaction of the ambient solar wind ([Gopalswamy et al. 2000b](#)). Thus, it seems working with kinematic parameters averaged over the entire trajectory, might be misleading, and hence it is important to appreciate the change in the kinematics. Further, it has been reported that CMEs originating from active regions and prominence eruptions tend to be impulsive or gradual CMEs ([MacQueen and Fisher 1983](#); [Sheeley et al. 1999](#)), but it is yet to be understood the implications of this classifications on the subtle kinematic properties of CMEs.

As discussed earlier, CMEs tend to exhibit a three part structure in WL coronagraph images. Although we do have an understanding of the overall kinematic evolution of the CME, the individual kinematics of the three parts comprising the three-part structure is still poorly understood. It has been reported that there

seems to be a velocity dispersion in the radial propagation of a CME, with the leading edge moving with the highest speed, while the inner core moves slowest (Webb and Jackson 1981). This phenomenon of velocity dispersion will have important impact on the validity of self-similar expansion of CMEs, which is an important assumption used in several CME models.

Thus, motivated by the above interesting attributes of CMEs and the limitations in our understandings associated with it, I attempted to study the 3D kinematics of CMEs in both inner and outer corona, by applying the GCS model (Thernisien, Vourlidas, and Howard 2009a) to the pair of observations from COR-1 and COR-2 on-board the twin spacecraft STEREO-A/B. This enabled me in capturing the early 3D kinematics of CME uniquely in WL observations. As an attempt to unify the width and acceleration profiles, I have reported for the first time a statistical height of influence of Lorentz force on the CME kinematics. I also attempt to understand the coupling of the kinematics of CMEs in the IC to that occurring in the outer corona. Owing to the association of impulsive and gradual CMEs with active regions and prominence eruptions, I also looked at the imprint these source regions can have on the above kinematic coupling, and the insights that can be extracted on the manifestation of impulsiveness or gradualness. Also, since the GCS model has provision for incorporating a third vantage point observation for 3D reconstruction, I report in my thesis, a first time application of the GCS model to the ground-based WL observations from K-Cor of the Mauna Loa Solar Observatory. This extension of the model helped in capturing the CME kinematics in 3D and that too, uniquely in WL uniquely, from as low as $1.05 R_{\odot}$. From this, I report for the first time a power-law variation of true CME volume with height in inner and outer corona. I also aim at combining extreme ultraviolet and WL observations to study the fascinating phenomenon of velocity dispersion in the IC. I believe these results will provide crucial inputs to the planning of observational campaigns of existing and upcoming solar missions that will be observing the

IC, like ADITYA-L1 (Seetha and Megala 2017a; Prasad et al. 2017a), PROBA-3 (Renotte et al. 2014a) and the recently launched Solar Orbiter (Müller et al. 2013a) and to models that study CME ejection and propagation.

1.6 Outline of the thesis

This thesis provides a compilation of works done to have a better understanding of CME kinematics in the IC, and also to understand, how the kinematics in the IC gets coupled with the kinematics in the outer corona, the heliosphere. The thesis is structured into the following chapters:

In chapter 2, a brief overview of the different data sources that have been used from different space and ground-based instruments, for the various projects done in this thesis is presented.

Chapter 3 presents a study of 3D kinematics of 59 CME events. It aims at connecting the two major missing links in our understanding of CME kinematics, that are lack of a good understanding of kinematics in IC and discrepancies due to projection. The (GCS) model (Thernisien, Vourlidas, and Howard 2009b) is implemented to the pair of simultaneous observations from COR-1 and COR-2 on-board STEREO-A and STEREO-B to capture the 3D evolution of CMEs in inner and outer corona. The CMEs are further associated to the source regions they arise from, and this allowed me to connect the true kinematics of the CMEs to their source regions, thereby, studying the imprint of the source regions on the kinematics of CMEs, if any. This chapter unifies the acceleration and width expansion of CMEs as a veritable manifestation of the same Lorentz force, and uses this to report for the first time, a statistical height range till which the imprint of Lorentz force remains dominant on the kinematics of CMEs.

In chapter 4, the work in the previous chapter is extended further. I present in this chapter different results based on statistical 3D kinematic properties, that indicate that the source regions of CMEs have a strong impression on their kinematic properties. I also show here that the kinematics happening in the IC is strongly coupled with the kinematics happening in the outer corona, thereby, showing that even the coupling of the kinematics is different for CMEs coming from different classes of source regions. The results also display the importance of capturing the kinematics in the IC, which can be used in different ways to arrive at the kinematic properties in the outer corona.

In chapter 5, I present the first ever implementation of the GCS model to the ground based coronagraphic observations from K-Cor/MLSO along with the pair of coronagraphic observations from STEREO. This extended GCS model would enable stereoscopy in the IC with WL observations, even after the loss of STEREO-B in 2014. This chapter shows that with this extension in the model, the complete early kinematics of CMEs can now be captured uniquely in WL coronagraphic observations, without the need of combining EUV data. For the first time, a power law variation of the true CME volume with height is reported here. The results in this chapter show that there is a differential volume expansion inside a CME, and that the rate of expansion of total volume is different in the inner and outer corona, thus hinting at different expansion mechanisms at these different height regimes.

Chapter 6 studies a CME that occurred on 26 January 2014 that was associated with a Type-II burst by using several space and ground based observations. It shows the necessity of the use of radio imaging and spectral observations, along with WL coronagraphic observations, for pin pointing the section of the CME associated shock surface that accelerates the electrons which are responsible for the Type-II burst.

Chapter 7 tries to probe the individual kinematics of the three part structure of CMEs as observed in EUV and WL (in a well overlapping FOV) observations, separately and compare their kinematic profiles, so as to understand better, the phenomenon of velocity dispersion inside CMEs in IC. This will provide crucial inputs and constraints on the validity of self-similar expansion of CMEs in IC. This work is under progress, and some preliminary results are showed here.

Finally, in chapter 8, a summary of the different studies done in this thesis is presented, with the main conclusions that are drawn from each project. It also discusses the future prospects of the projects that are done, and the novelty that my thesis brings into this research domain.

Chapter 2

Data

Pioneering enquiry into the nature of the Sun, with a scientific thirst can be dated back to around 1610 in Western Europe through the first telescopic observations of sunspots by J. Fabricius, Galileo Galilei, C. Scheiner and others ([Foukal 2004](#)). Since then, the Sun has been challenging our intellect and demanding our attention as it rises and sets every day. Besides being the only star which can be observed in detail, the Sun also became the touch-stone for stellar models. Now, although the systematic study of the Sun started earlier, the realization of the significance of such studies dawned upon us, only when we realized the significance of the interaction of the Sun with the terrestrial environment. It was soon realized that, apart from being a nearest cosmic laboratory for astronomers from a scientific point of view, the practical benefits of understanding our host star was not less important. Thus to connect all these inquisitiveness, the need of the hour was data.

In order to understand how the Sun operates, we must examine the radiation. The human eyes are sensitive to only the visible region of the electromagnetic spectrum,

and it is imperative that there is much more to the Sun than what meets our eyes. In other words, in addition to the visible light, there is invisible radiation from the Sun as well, and for capturing that, artificial eyes are required. Radio waves are the only kind of invisible radiation in this context, that is not absorbed in the atmosphere of the Earth, and hence ground-based radio observations of the Sun opened the first new window to watch the Sun. The atmosphere of the Earth absorbs effectively most of the Sun's radiation in the shorter wavelengths, from ultraviolet to X-rays and gamma rays, and thus, to capture these wavelengths, space based observations were commenced. Since then, there has been several dedicated solar ground and space based missions to study the Sun in detail.

Since this thesis primarily aims at understanding the kinematics of CMEs in the inner corona (IC), and how the kinematics in the IC gets coupled with the kinematics at the higher heights in the outer corona, I have used those data sources that have helped me in reaching these aims. Further, the thesis also aims at understanding the effect of different CME source regions on the kinematic properties of CMEs, I have also used data sources that have helped me in identifying and associating CMEs to their source regions on the solar disk.

2.1 Solar Dynamics Observatory

The SDO ([Pesnell, Thompson, and Chamberlin 2012](#)) is a mission of NASA. It is a mission under NASA's Living With a Star (LWS) program. SDO was launched on 11 February 2010, with a main aim of understanding the varied eruptions from the Sun that might affect life on Earth, and the technologies that have been developed. The SDO observes the Sun near-simultaneously in white light (WL) and in different ultraviolet (UV) and extreme-ultraviolet (EUV) emission lines. Apart from these, it also has an instrument that measures the line of sight (LOS)

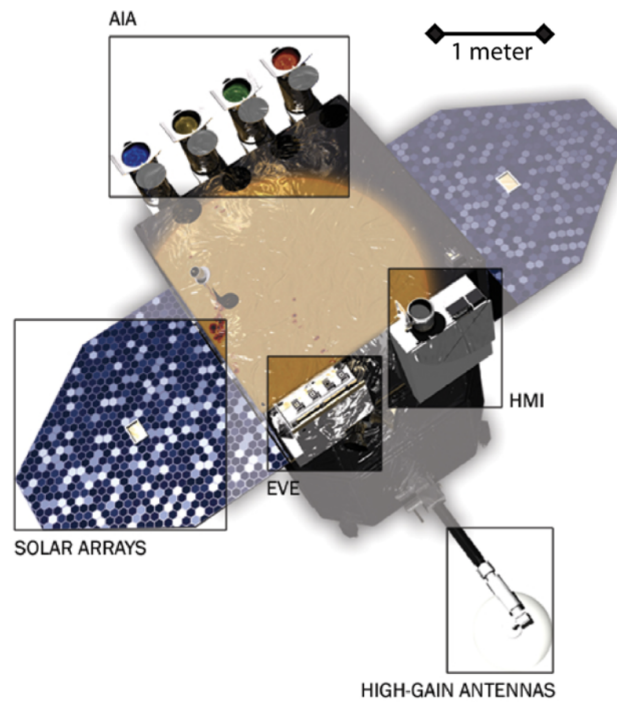


FIGURE 2.1: A view of the SDO spacecraft with the instruments on-board.
Image credits : (Pesnell, Thompson, and Chamberlin 2012)

vector magnetic field at the surface of the Sun. The mission spacecraft comprises of three main instruments :

- The Atmospheric Imaging Assembly (AIA; Lemen et al. 2011)
- Extreme Ultraviolet Variability Experiment (EVE; Woods et al. 2012)
- Helioseismic and Magnetic Imager (HMI; Scherrer et al. 2012)

For my thesis work, I have mainly used the data from AIA.



FIGURE 2.2: A view of the four telescopes on-board the SDO. *Image credits :* (Lemen et al. 2011)

2.1.1 AIA

The AIA is comprised of four sets of telescopes that observe the atmosphere and surface of the Sun by providing continuous full-disk observations in seven extreme ultraviolet (EUV) and three ultraviolet-visible channels with the help of an array of four telescopes (see Figure 2.2). These passbands span approximately 20,000 K to 20 million K for a temperature range. With an image cadence of 12 seconds, in 4K X 4K images at a resolution of 0.6 arcsec/pixel, an unprecedented coverage of the different fascinating phenomena happening at the atmosphere of the Sun, is covered. Thus the AIA telescopes provide a global coverage of the solar atmosphere with a fascinating cadence that enables the study and understanding of both gradual and impulsive processes, in a wide range of temperatures.

2.2 Solar and Heliospheric Observatory

The SOHO (Domingo, Fleck, and Poland 1995) is a space mission which is a part of the Solar-terrestrial Space Program (STSP) which was developed as a

collaborative effort between the ESA and the NASA. These missions primarily aim to study the interior of the Sun with the help of helioseismology, to study the heating mechanisms of the corona, and to understand the behaviour of the solar wind and its acceleration process. The mission was launched on December 2, 1995 (Figure 2.3(a)), and was placed at the first Sun-earth Lagrangian point (L1), which will facilitate an uninterrupted view of the Sun.

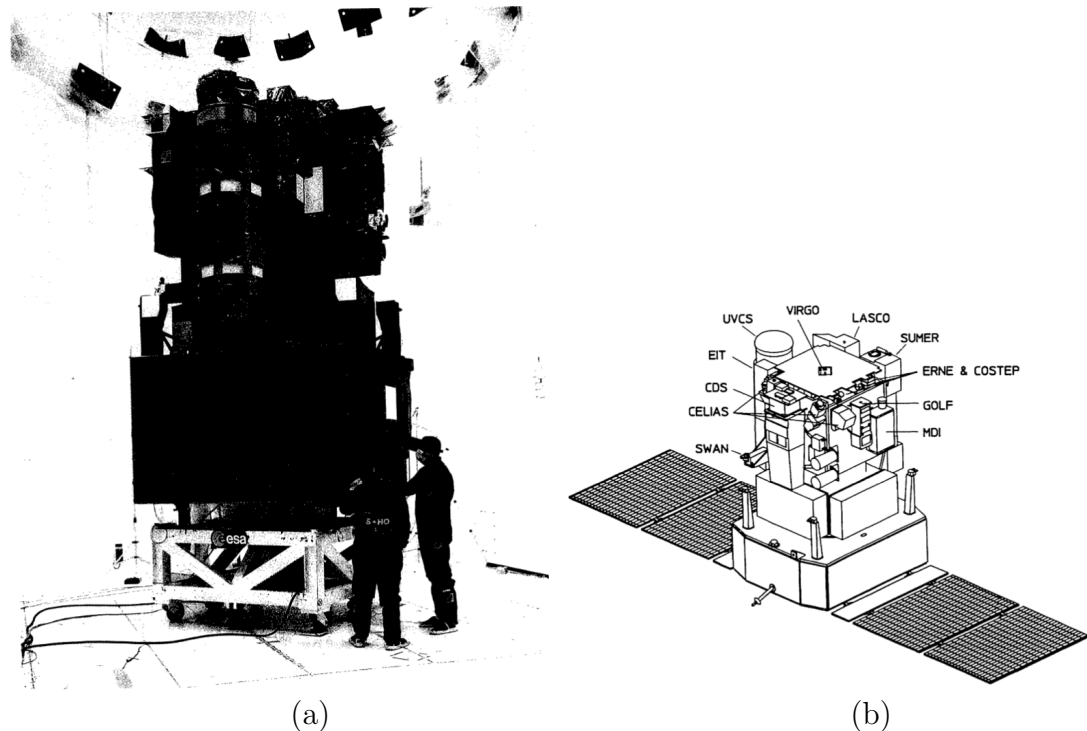


FIGURE 2.3: (a): The SOHO spacecraft in launch configuration. (b): A schematic view of the SOHO spacecraft. *Image credits Domingo, Fleck, and Poland (1995)*

The spacecraft consists of 12 sets of complimentary instruments (see Figure 2.3(b)), which are as follows:

- Coronal Diagnostic Spectrometer (CDS; [Patchett et al. 1988](#))
- Charge, Element and Isotope Analysis System (CELIAS; [Hovestadt et al. 1995](#))

- Comprehensive Suprathermal and Energetic Particle Analyser (COSTEP; [Müller-Mellin et al. 1995](#))
- Extreme-ultraviolet Imaging Telescope (EIT; [Delaboudinière et al. 1995](#))
- Energetic and Relativistic Nuclei and Electron experiment (ERNE; [Torsti et al. 1995](#))
- Global Oscillations at Low Frequency experiment (GOLF; [Gabriel and GOLF Team 1991](#))
- Michelson Doppler Imager (MDI; [Scherrer et al. 1995](#))
- Large Angle and Spectrometric Coronagraph experiment (LASCO; [Brueckner et al. 1995a](#))
- Solar Ultraviolet Measurements of Emitted Radiation (SUVI; [Wilhelm et al. 1995](#))
- Study of Solar Wind Anisotropies (SWAN; [Bertaux et al. 1988](#))
- Ultraviolet Coronagraph Spectrometer (UVCS; [Noci et al. 1995](#))
- Variability of solar Irradiance and Gravity Oscillations (VIRGO; [Fröhlich et al. 1995](#))

Out of the above 12 instruments, I have mainly used the data from EIT and LASCO for the work in this thesis.

2.2.1 EIT

The EIT provides full-disk observations of the solar corona and the transition region, with a FOV up to $1.5 R_{\odot}$ above the solar limb (see [Figure 2.4](#)). With

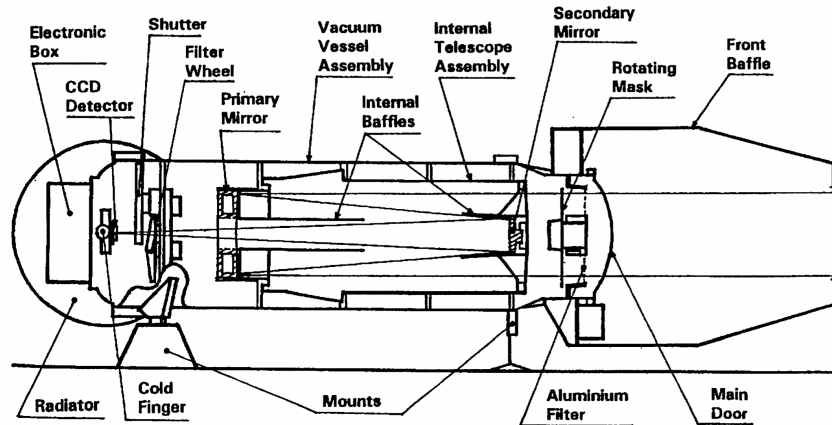


FIGURE 2.4: A schematic view of the Extreme Ultraviolet Imaging Telescope, with the major instrument subsystems indicated along with. *Image credits Delaboudinière et al. (1995)*

spectral bands that covers a temperature range of 80,000 Kelvin to 2 million Kelvin, the EIT aims at studying the dynamics and evolution of different coronal structures at different temporal and spatial scales which will largely help in the understanding of different mechanisms that might be responsible for heating the solar corona. These EIT images thus plays a crucial role in providing the inter-connection between structures that are observed on the disk of the Sun to those structures seen above the solar limb, for example by a coronagraph like LASCO.

2.2.2 LASCO

The LASCO is comprised of a set of three coronagraph (C1, C2 and C3) telescopes on-board the SOHO satellite (see Figure 2.5). These three coronagraphs have a well overlapping combined FOV from $1.1 R_{\odot}$ to $30 R_{\odot}$. This fascinating FOV largely facilitates in tracking outward moving coronal structures above the solar limb for a very extended height range as stated above. The C1 coronagraph is an internally occulted coronagraph, whereas, the other two coronagraphs (C2, C3) are externally occulted. Unfortunately, in 1998, there was a loss of contact with SOHO for several weeks, and although, as a miracle, a contact was re-established

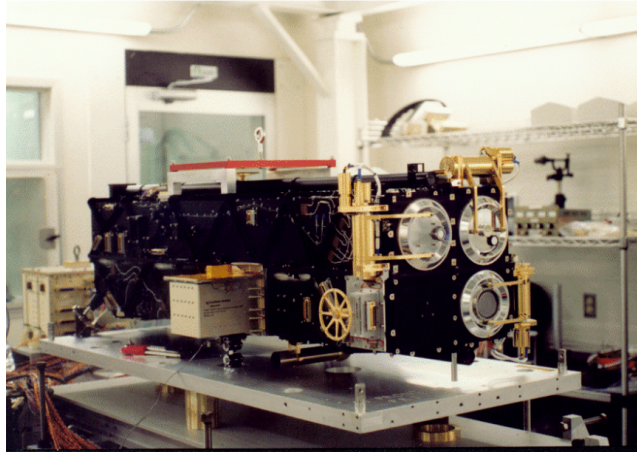


FIGURE 2.5: A front view of the LASCO instruments with the three coronagraphs. *Image credits Brueckner et al. (1995a)*

with SOHO, the C1 coronagraph was lost. Despite such an event, the other two coronagraphs, C1 and C2 are still working and is sending us images of the solar corona for a combined height range of $2.2 - 30 R_{\odot}$. The two existing coronagraphs, C2 and C3 observes the solar corona in WL with a cadence of 12 minutes and 30 minutes respectively, and with a band pass of 540-640 nm, with a resolution of $11.4 \text{ arcsec pixel}^{-1}$ and $56 \text{ arcsec pixel}^{-1}$ respectively.

2.3 Solar Terrestrial Relations Observatory

Owing to the fact that the solar corona is optically thin at most wavelengths, the major drawbacks faced by the previous single spacecraft observations were from line of sight integration effects, which leads to a lot of ambiguity and confusion in the analysis of the observed images. Tracking the solar eruptions in images taken from a single view point introduces projection effects in the measured quantities. To remove such shortcomings on our way to a clear understanding of the different processes happening at the sun and its atmosphere, the concept of a twin spacecraft mission was conceived. As a result, two similar spacecrafts STEREO-A (Ahead)

and STEREO-B (Behind) were launched on October 25, 2006 as the third mission of NASA's Solar Terrestrial Probes Program (STP) ([Kaiser et al. 2008a](#)). As the name of the two spacecrafts go, STEREO-A is slightly ahead and STEREO-B is slightly behind the orbit of Earth, which lies at a distance of 1 astronomical unit (AU) from the Sun. These two identical spacecrafts thus drift away from each other in their own elliptical orbits around the Sun, at a rate of ~ 22.5 degrees every year. As a result of this, not only does the twin spacecrafts provides the unique opportunity for stereoscopy, but it also changes the vantage points of observations with time. Taking advantage of this stereoscopic observation of the Sun and the Heliosphere, the major aim of the STEREO mission lies in understanding the 3 dimensional structure and magnetic topology of CMEs, to understand what initiates a CME, and how it propagates from the corona, out into the Heliosphere. Both the spacecrafts (STEREO-A and STEREO-B) of this twin STEREO mission consists of the following instruments:

- Sun Earth Connection Coronal and Heliospheric Investigation (SECCHI; [Howard et al. 2008a](#))
- STEREO/WAVES (SWAVES; [Bougeret et al. 2008](#))
- In-situ Measurements of Particles and CME Transients (IMPACT; [Luhmann et al. 2008](#))
- Plasma and Suprathermal Ion Composition (PLASTIC; [Galvin et al. 2008](#))

Out of the above four instrument packages, I have used the data from the following:

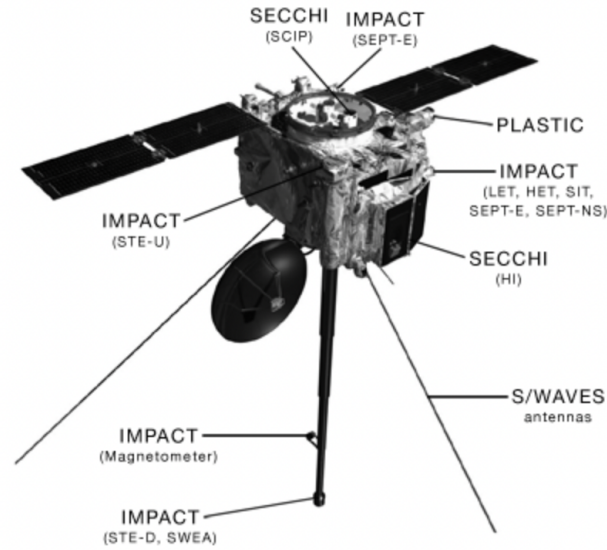


FIGURE 2.6: An artistic conception of the STEREO spacecraft. *Image credits STEREO team*

2.3.1 SECCHI

The instrument acronym comes from the name of Angelo Secchi (1818 - 1878) who was an Italian astrophysicist, being the the pioneer in applying the technology of photography to record eclipses. The SECCHI instrument package comprises of five telescopes. These telescopes are, an extreme ultraviolet imager (EUVI), an inner coronagraph (COR-1), an outer coronagraph (COR-2) and two heliospheric imagers (HI-1 and HI-2). The coronagraphs and the heliospheric imagers have a well overlapping FOV which helps in tracking CMEs from the IC to the heliosphere. In my thesis work, I have used the data from the following telescopes of SECCHI:

2.3.1.1 EUVI

The EUVI, developed at Lockheed Martin Solar and Astrophysical Laboratory (LMSAL), uses four different EUV emission lines (304 Å, 195 Å, 171 Å and 284 Å) and images the chromosphere and the lower corona (see Figure 2.7). It images

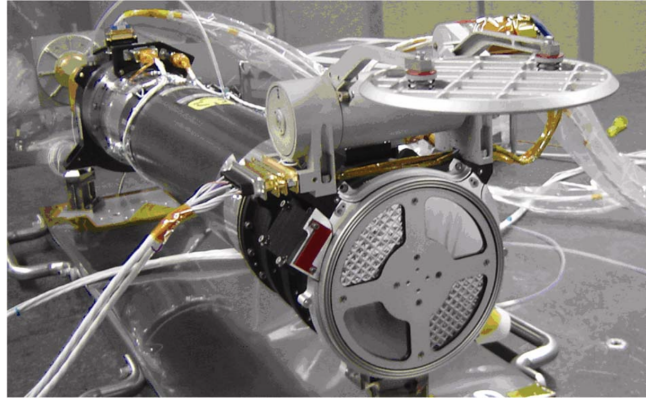


FIGURE 2.7: A view of the EUVI telescope, before being integrated into the SECCHI package.. *Image credits : Howard et al. (2008a)*

the full disk of the Sun up to a FOV of $1.7 R_{\odot}$. It has a spatial resolution of $1.6 \text{ arcsec pixel}^{-1}$ with a cadence of 8 minutes.

2.3.1.2 COR-1 and COR-2

The COR-1 coronagraph is a classic Lyot internally occulted refractive coronagraph with a FOV from 1.3 to 4 solar radii (see Figure 2.8). In this telescope, a linear polarizer is incorporated to reduce the scattered light component, thereby to extract out the polarized brightness signal from the solar corona. The polarized brightness signal is extracted by taking polarized brightness images of the solar corona with polarization angles of 0° , 120° and 240° in WL. It observes the corona through a pass-band of 633-658 nm with a resolution of $3.75 \text{ arcsec pixel}^{-1}$. The COR-2 is on the other hand, an externally occulted coronagraph (see Figure 2.9) with an overlapping FOV of 2 to 16 solar radii. It observes the solar corona at a pass-band of 650-750 nm, and has a resolution of $15 \text{ arcsec pixel}^{-1}$. The image cadence varies from 5 minutes to 30 minutes, depending on the mode of observation.

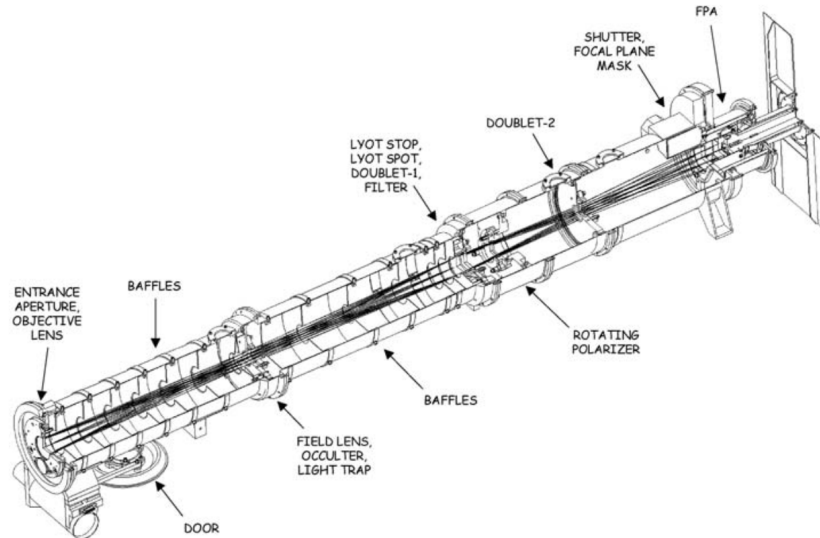


FIGURE 2.8: A layout of the COR-1 telescope. *Image credits : Howard et al. (2008a)*

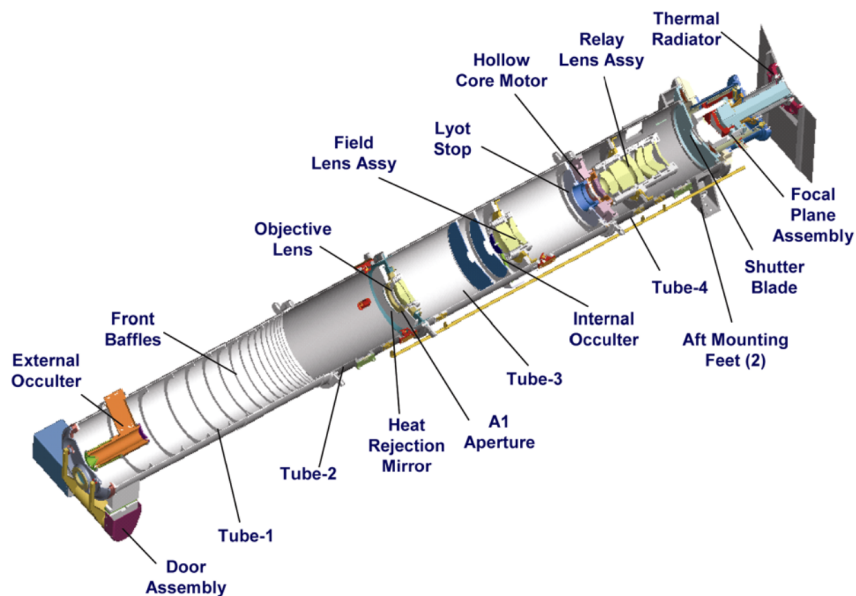


FIGURE 2.9: A layout of the COR-2 telescope. *Image credits : Howard et al. (2008a)*

2.3.2 SWAVES

The SWAVES includes a suite of experiments that provides measurements of the three different components of the fluctuating electric field from a few fraction of a Hertz up to a 16 MHz, along with a single frequency channel placed near 30 MHz. The SWAVES is capable of performing 3D localization and hence, tracking of radio emissions which are connected with shock waves and energetic electrons that are in turn associated with CMEs, thereby bridging the gap in our understanding between the close inter relation between CMEs and the type II bursts.

2.4 K-Coronagraph

The COronal Solar Magnetism Observatory (COSMO) K-coronagraph (K-Cor) is one of the three instruments included in the COSMO facility suite. It is a WL ground based coronagraph located at the MLSO (see Figure 2.10(a)) in Hawaii ([de Wijn et al. 2012](#)). It is an internally occulted refractive coronagraph that observes the solar corona in a pass band of 720-750 nm by taking polarized brightness images in a FOV of 1.05 to 3 solar radii (see Figure 2.10(b)). It has a pixel resolution of 5.5 arcsec pixel⁻¹ and a very high cadence of 15 seconds, but the cadence can change based on campaigned observations. The K-Cor replaced the earlier working MK4 K-Coronameter, and has been taking images of the lower corona since September, 2013. With the help of such a fascinating FOV, K-Cor provides the capability of capturing the early evolution of CMEs through the absolute lower heights in the inner corona, where our understanding of the kinematics of CMEs is still not very clear.

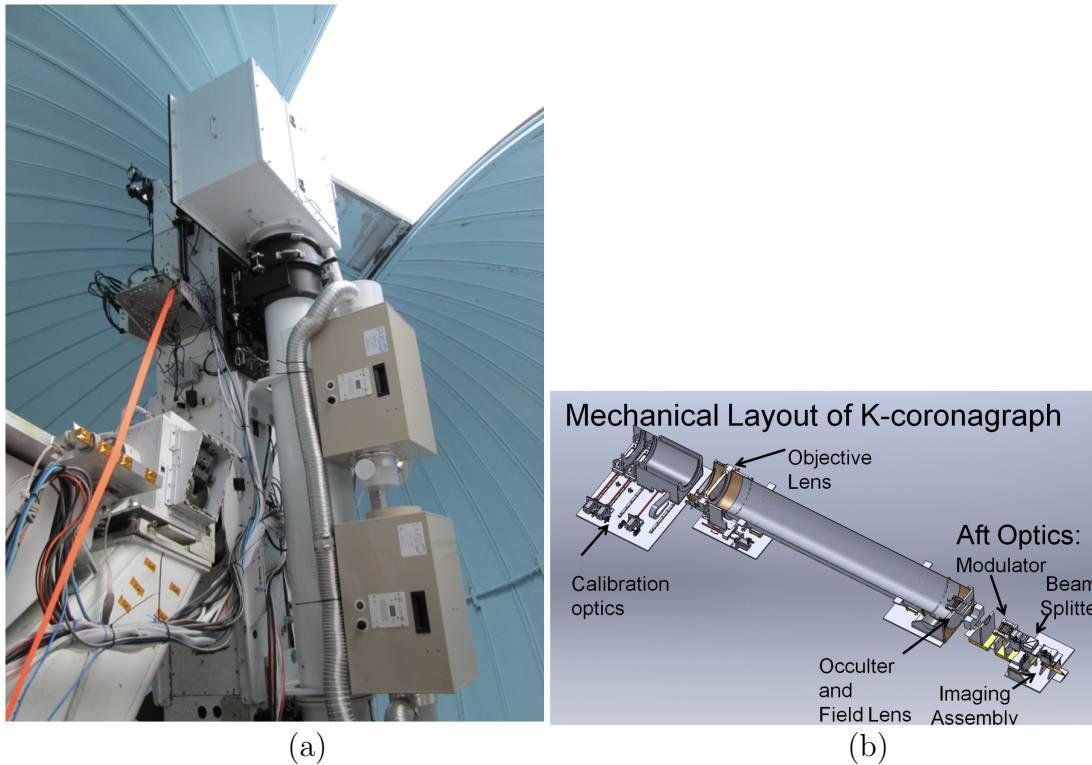


FIGURE 2.10: (a): The K-Cor coronagraph at the Mauna Loa Solar Observatory, Hawaii. (b): A schematic layout of the K-Cor telescope. *Image credits: MLSO*

2.5 Project for Onboard Autonomy-2

The Project for OnBoard Autonomy or PROBA satellite (Figure 2.11(a)) is among the smallest of satellites flown by ESA, and PROBA-2 is the second of the series (Santandrea et al. 2013). It is a part of ESA's in-orbit technology demonstration program and was launched on November 2, 2009. Placed in a sun-synchronous orbit, PROBA-2 has 4 scientific instruments, two remote sensing and two in situ instruments, which will complement each other in space weather forecasting. The four instruments on-board PROBA-2 are the following:

- Large Yield Radiometer, formerly LYman alpha Radiometer (Dominique et al. 2013)

- Sun Watcher using Active Pixel System detector and Image Processing (Seaton et al. 2013; Halain et al. 2013)
- Thermal Plasma Measurement Unit (Podolska, Hruska, and Truhlik 2016)
- Dual Segmented Langmuir Probe

Among the above four instruments, I have used the data from SWAP for my thesis work.

2.5.1 SWAP

SWAP is an outcome of the collaboration of Centre Spatial de Liège (CSL) and the Royal Observatory of Belgium (ROB). It images the solar corona at 17.4 nm, which corresponds to a temperature of around 1 million kelvin, with a cadence of 1 to 2 minutes. With a pixel resolution of 3.2 arcsec pixel⁻¹, it has a wide FOV upto 1.7 R_☉ (Figure 2.11(b)). Apart from this, it is also worth noting that SWAP has an additional off-pointing mode of observation, where a large part of the sun's corona above the limb, can be observed by pointing the telescope away from the Sun. With the aid of the wide FOV, and the cadence, SWAP provides the opportunity to follow the temporal evolution of several features (filaments, CMEs, coronal foles), which are capable of triggering potential space weather events.

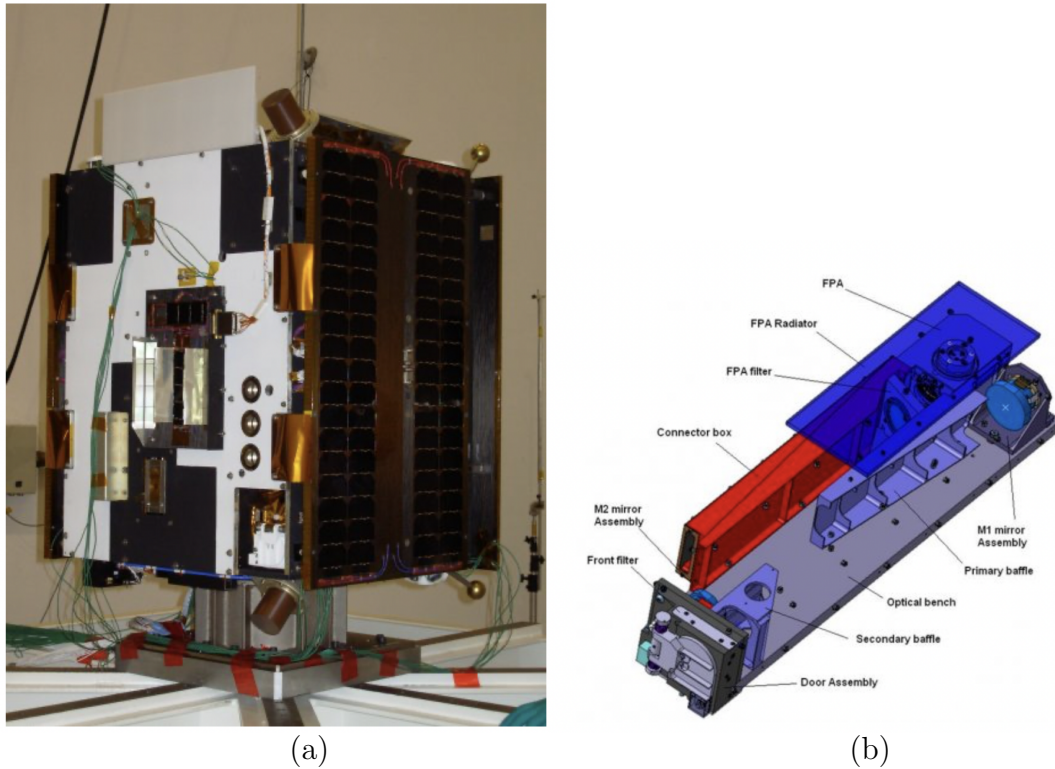


FIGURE 2.11: (a): The PROBA-2 spacecraft. (b): A schematic view of the SWAP instrument. *Image credits : PROBA-2 Team.*

2.6 Co-ordinated Data Analysis Workshops catalogue

The Co-ordinated Data Analysis Workshops or the CDAW catalogue is a CME catalogue, which contains all CMEs identified manually in SOHO/LASCO images, from 1996, since the launch of SOHO [Yashiro et al. \(2004a\)](#). Although LASCO has 3 telescopes, C1, C2 and C3, only C2 and C3 is used for the measurements in this catalogue in order to keep uniformity, since the C1 telescope got disabled in 1998. Several essential information on the CMEs are provided in the catalogue (see [Figure 2.12](#)). It provides the date and the time when the CME first appears in the LASCO FOV, the Central Position Angle (CPA) which is the angular position of the central point on the CME leading edge, measured counter-clockwise from the solar North. For multiple CMEs occurring almost at the same time, the CPA

First C2 Appearance Date Time [UT]	Central PA [deg]	Angular Width [deg]	Linear Speed [km/s]	2nd-order Speed at final height [km/s]	2nd-order Speed at 20 Rs [km/s]	Accel [m/s ²]	Mass [gram]	Kinetic Energy [erg]	MPA [deg]	Movies, plots, & links	Remarks
2012/01/01 01:25:49	40	23	801	701	606	-18.7 ^{*1}	4.3e+14	1.4e+30	43	C2 C3 195 PHTX DST Java Movie	
2012/01/01 04:12:07	266	33	247	265	372	3.6 ^{*1}	1.2e+13	3.5e+27	268	C2 C3 195 PHTX DST Java Movie	Poor Event
2012/01/01 06:24:05	47	13	96	106	303	3.5 ^{*1}	----	----	50	C2 C3 195 PHTX DST Java Movie	Very Poor Event; Only C2

FIGURE 2.12: A layout of the COR-2 telescope. *Image credits : CDAW Team*

helps in distinguishing them from each other. The catalogue provides the angular width of the CME. Each CME in the catalogue is provided with three speeds, 1) a linear speed, found by a straight line fitted to the height-time data, 2) a quadratic speed, found from a quadratic polynomial fitted to the same data, and quoting the speed calculated at the last measured height, and thirdly 3) a speed obtained from 2) where the speed is calculated at a height of 20 R_{\odot} . A CME is also provided with an acceleration, a mass and a kinetic energy. There is also a remarks column, where a CME is categorised as "poor" or "very-poor" based on its intensity in the LASCO images. However, it is worth noting that all the measurements of this catalogue are made in the plane of the sky and hence the measured numbers suffer from projection effects.

Chapter 3

Study of 3D evolution of CMEs in inner and outer corona

3.1 Introduction

CMEs are large structures of plasma with embedded magnetic fields that are ejected from the atmosphere of the Sun into the heliosphere ([Webb and Howard 2012a](#)). They appear as discrete, bright, white light (WL) feature propagating outwards in the FOV of the coronagraph ([Hundhausen et al. 1984b](#)). CMEs apart from being such dynamics events, they are also the major drivers of space weather as they are capable of producing events like transient interplanetary disturbances, shock waves ([Gosling 1993b](#)). Thus, it is important to understand their kinematics. CMEs have been studied for several decades, with their observations dating back to the 1970s ([Hansen et al. 1971](#)). [Dere et al. \(1997\)](#) made first observation of the CME from its initiation to propagation in the outer corona while combining data

from *Extreme ultra-violet Imaging telescope* (EIT) (Delaboudinière et al. 1995) and *Large Angle Spectroscopic COronagraph* (LASCO) (Brueckner et al. 1995b) on board SOHO. St. Cyr et al. (1999a) investigated the kinematics of 246 CMEs observed between 1980 and 1989 combining the overlapping observations from the inner ($< 2R_{\odot}$) to outer ($> 2R_{\odot}$) corona using MK-3 K-coronameter (FOV: $1.12 - 2.44 R_{\odot}$) at Mauna Loa Solar Observatory (MLSO) and Solar Maximum Mission (SMM) ($1.5 - 6 R_{\odot}$; MacQueen et al. 1980b). It was proposed that a driving force is responsible for the continuous acceleration and expansion of CMEs up to the FOV of the SMM. Later, it was reported that CMEs pose three-phase kinematic profile with an initial slow gradual rise phase, an impulsive acceleration phase below $2 R_{\odot}$, and the final phase with constant or decreasing speed (Zhang et al. 2001b; Zhang et al. 2004; Bein et al. 2011b). Beyond this, a CME propagates in the interplanetary medium with almost constant speed or show very minimum acceleration or even retardation as it interacts with the solar wind (Gopalswamy et al. 2000a). Thus, an anti-correlation between the average speed and acceleration, interpreted as an effect of aerodynamic drag, was found in height between $2-30 R_{\odot}$ for over 5000 CMEs (Vršnak et al. 2004). Furthermore, it was found that during the CME propagation, greater acceleration magnitudes (A) have small duration (T) and vice versa following $A \sim T^{-1}$ (Zhang and Dere 2006).

The study of the observable properties of CMEs using a large sample from SOHO provided an understanding on the nature of CMEs and variation of their properties with the solar cycle (St. Cyr et al. 2000; Yashiro et al. 2004a; Gopalswamy 2006b; Vršnak et al. 2007a; Gopalswamy et al. 2009d).

CMEs are observed to be associated with flares and eruptive prominences (Webb and Howard 2012a). The kinematics of CMEs associated with these two classes are investigated in previous reports (Sheeley et al. 1999; Moon et al. 2002; Chen, Chen, and Fang 2006; Bein et al. 2012). Vršnak, Sudar, and Ruždjak (2005) studied a sample of 545 CMEs and reported a contrasting result demonstrating

that both the CME classes have similar kinematics characteristics. It has been observed that the CME kinematics is governed by the interplay of three forces, namely the Lorentz force, the gravitational force and the viscous drag force which is manifested in a wide range in their kinematics with their speeds varying from a few tens to thousands km s^{-1} and their acceleration ranging from a few tens to even a few 10^4 m s^{-2} (Wood et al. 1999; Zhang et al. 2001b; Webb and Howard 2012a; Vršnak et al. 2007a). Also, CMEs attain enormous acceleration in the inner corona (IC) where a strong magnetic field generates large Lorentz force (Vršnak et al. 2007a; Bein et al. 2011b). Recently, Cheng et al. (2020b) studied the slow rise and main acceleration phase of 12 CMEs using the data from AIA on-board SDO (Lemen et al. 2011) and EUVI on-board STEREO and suggested that the main phase of acceleration is very much different from the initial phase of slow rise, and the possibility that these two phases being governed by different mechanisms altogether. Hence to understand this initial impulsive acceleration and the forces involved in propelling the CME, it is crucial to understand the kinematics of CMEs in the IC ($< 2 R_{\odot}$).

Apart from radial propagation, CMEs also exhibit lateral expansion leading to a increase in the width from the inner to outer corona (Kay, Opher, and Evans (2015), and references therein). In earlier studies of CMEs the variation of radial and expansion speeds was found and shown that it was dependent on the width of the CMEs (MacQueen and Fisher 1983; Gopalswamy et al. 2009c).

The lateral expansion of CMEs is due to the injected energy from the magnetic field contained in the source region. The Lorentz force from this injected magnetic energy gives the necessary thrust that translates the CME and leads to its expansion (Subramanian et al. 2014; Suryanarayana 2019a).

Recently Cremades, Iglesias, and Merenda (2020a) studied 12 CMEs using the data from the SDO/AIA, SOHO/LASCO, STEREO/SECCHI coronagraphs and

inferred from 3D reconstruction that the initial true expansion of CMEs below $3 R_{\odot}$ is asymmetric and non-self-similar.

It should be noted that in the studies based on LASCO-C1, EUVI or AIA to probe inner corona, the images observed in emission lines were used to track CMEs. It is still debatable if the same features are observed in emission lines and WL. Moreover, a major limitation that all these studies face is that the properties of CMEs, width, speed, acceleration, propagation direction, are measured using observations from single view-point. As a result these values obtained by taking measurements in the sky plane suffer from projection effects (Cremades and Bothmer 2004; Burkepile et al. 2004; Temmer 2016; Balmaceda et al. 2018b). To overcome such limitation, Sarkar et al. (2019) (and references therein) exploited the coronal cavity observed in EUV and WL images and found that the spatial relationship is preserved while tracking the feature in 3D in these pass-bands. Further to minimise the projection effects, Mierla et al. (2008b) derived the 3D-kinematics of CMEs using STEREO/COR-1, COR-2 images from two vantage points by a triangulation method and compared it with other methods (Mierla et al. 2009, 2010, 2011). Using polarimetric capability of COR-1 A and B coronagraphs, Moran, Davila, and Thompson (2010) determined the 3D orientation of a CME. Another method based on forward modelling to fit the CME flux rope on multi vantage point images was developed assuming the self-similar expansion of CMEs (Thernisien, Howard, and Vourlidas 2006a; Thernisien, Vourlidas, and Howard 2009c; Thernisien 2011a). An automated method based on triangulation to identify and track 3D structure of CMEs is recently developed by Hutton and Morgan (2017a).

One of the first 3D kinematical study of CMEs combining the data from STEREO/EUVI and coronagraphs was done by Joshi and Srivastava (2011a). Bosman et al. (2012) derived and catalogued 3D properties of 51 CMEs from January 2007 to December 2010 using the data from STEREO/COR-2. Sachdeva et al. (2015)

used a sample of 8 CMEs observed by SOHO/LASCO C2, STEREO/COR2 and STEREO/HI to study their propagation in 3D and the impact of aerodynamic drag, and further extended their study in [Sachdeva et al. \(2017\)](#) to 38 events to understand the relative importance of Lorentz force and drag force, but their height measurements left out the information in the inner corona. The multi-viewpoint analysis of a CME observed on March 28, 2013 yielded a linear increase in angular width of CME up to $5 R_{\odot}$ ([Cabello et al. 2016a](#)).

A sample of 460 CMEs observed by twin STEREO spacecrafts was used to compare the single-viewpoint and 3D kinematics (via triangulation) of CMEs in COR-2 FOV ([Balmaceda et al. 2018b](#)). It is worth noting that although these studies provide 3D kinematic information, most of the analysis ([Cremades, Iglesias, and Merenda \(2020a\)](#) and [Cabello et al. \(2016a\)](#) being exceptions in this context) are carried out starting from the COR-2 FOV, and hence the essential information in the IC is left out. Thus the major gap in our understanding of CME kinematics is to understand their 3D evolution in the inner corona.

During the early evolution phase, CMEs often show non-radial deflections in their trajectories ([Gopalswamy et al. 2009a](#); [Gui et al. 2011](#); [Lugaz et al. 2012](#); [Wang, Hoeksema, and Liu 2019](#)). It has been observed that CMEs can get deflected from their initial path when they get ejected near a coronal hole ([Gopalswamy et al. 2009a](#); [Kahler, Akiyama, and Gopalswamy 2012](#)).

[Kay, Opher, and Evans \(2013\)](#) developed a tool, ForeCAT (Forecasting a CME's Altered Trajectory) for studying CME deflections due to the magnetic forces. [Kay, Opher, and Evans \(2015\)](#) (and references therein), reported on observed latitudinal and longitudinal deflections suffered by CMEs as they propagated outwards. A study of these deflections is important for a better understanding of their trajectories and also for better space weather forecasting ([Kay, Opher, and Evans 2015](#)).

As it has been established that the Lorentz force is responsible for propelling and expanding the CME (Subramanian et al. 2014), a connection between the evolution of the width of CMEs with their kinematic profiles will shed light on the imprint of Lorentz force on the evolution of CMEs. In this work, to improve our understanding of the kinematics of CMEs, we perform a statistical study of 3D evolution of 59 CMEs in the inner and outer corona occurring between May 2007 to April 2014 and connect them to their source region. To keep uniqueness in the physical feature we track the CME only in WL coronagraph data. Since the use of triangulation method involves a smaller feature (point) reconstructed in 3D, we used the GCS model developed by Thernisien, Howard, and Vourlidas (2006a); Thernisien, Vourlidas, and Howard (2009c) which fits a flux rope to entire CME structure using a pair of observed images by the coronagraphs COR-1 and COR-2 on-board STEREO spacecrafts from two different points. In this work we track the 3D structure of CMEs and try to understand their true evolution during the propagation. The paper is organised as follow: in Section 3.2 we outline the data sources that have been used followed by the working method. The results of our analysis are presented in Section 3.3 followed by summary and conclusions in Section 3.4.

3.2 Data and Method

3.2.1 Data Source and Data Preparation

We have used the Coordinated Data Analysis Workshop (CDAW) catalogue, which records the properties of CMEs detected manually in the SOHO/LASCO images (Gopalswamy et al. 2009d) to select events. The data from different passbands of AIA on-board SDO (Lemen et al. 2011) and EIT (Delaboudinière et al. 1995) on-board SOHO were used to identify the source regions of CMEs that were coming

from the frontal side of the Sun. For events happening at the back side of the Sun, data from EUVI on-board SECCHI package (Howard et al. 2002) of the twin spacecraft STEREO-A and STEREO-B was used. Since we aim to understand the 3D evolution of CMEs in the inner corona, high cadence data from multiple vantage points are needed. The COR-1 coronagraph on-board STEREO-A and STEREO-B offers high cadence (5 minutes) observation of the IC from two vantage points, which can be used to reconstruct the 3D structure of the CME. In this regard, the data from COR-1 with FOV $1.5 - 4 R_{\odot}$ and COR-2 having FOV from $2.5 - 15 R_{\odot}$ of the SECCHI package on-board STEREO-A and STEREO-B was combined to study the kinematics of CMEs close to their initiation in the IC and their further evolution. Level 0.5 data of EUVI, COR-1 and COR-2 was reduced to level 1 using *secchi_prep.pro* in IDL. Next, base difference images were created by subtracting a pre-event image from successive images of the event, thus ensuring that we are tracking the same feature in all images.

3.2.2 Event selection and Source Region identification

We select CMEs from the CDAW catalogue, occurring during the period from May 2007 to April 2014 which includes the period of minimum sunspots in solar cycle 23 to the period of maximum sunspots of cycle 24, and which are bright in STEREO data, so that GCS model can be fitted with reasonable accuracy. We selected CMEs which showed a distinct leading edge that can be clearly tracked in successive images of COR-1 and COR-2. We did not select CMEs which were marked as "very poor" in the CDAW catalogue because such CMEs have a very faint leading edge which is not clearly seen in the successive frames of COR-1 and COR-2 images, thus tracking them can be ambiguous. In this regard, we note that there are also other automated CME catalogues like SEEDs (Olmedo et al. 2008), CACTUS (Robbrecht and Berghmans 2004; Pant et al. 2016), ARTEMIS (Boursier et al. 2009), CORIMP (Morgan, Byrne, and Habbal 2012; Byrne et al.

2012), and others. JHUAPL (Vourlidas et al. 2017) identifies the events visually, the measurements are however estimated by a semi-automatic algorithm. But Since, we choose bright events in our analysis so that GCS model can be fitted with reasonable accuracy, these events are likely to be captured by both manual and automated catalogs. It seems it does not matter which catalog we use to identify the CMEs. Having said that, we understand that the estimates of the kinematic properties (such as velocity, width, and accelerations) might be different in different catalogs due to different measurement techniques used. But, our conclusions are not based on any catalogued parameters, and is completely based on the computed GCS parameters. Thus, the choice of catalogue will not affect our results. Only in Section 3.3.3 we show a comparison of projected and true speeds to show the importance of true speeds over projected speeds. For this we use CDAW speed because CDAW tracks the leading edge manually, and our work also involves manual fitting of the GCS model. Thus we believe that using automated catalogs instead of manual catalog will not significantly alter the results of this study. Motivated by the facts that CMEs show a wide range in their speeds (Webb and Howard 2012a) and that the solar wind (and its average speed) naturally divides CMEs into slow and fast ones (Gopalswamy et al. 2000a), we segregate the selected CMEs into slow ($< 400 \text{ km s}^{-1}$) and fast ($> 400 \text{ km s}^{-1}$) based on the average speed of the solar wind, which is around 400 km s^{-1} (Schwenn 2006). After putting these constraints on our event selection, we then back project the CMEs on to the solar disk and with the help of the data from SOHO/EIT (195 Å, 304 Å), SDO/AIA (171 Å, 193 Å, 304 Å), STEREO-A/EUVI-A (195 Å, 304 Å) and STEREO-B/EUVI-B (195 Å, 304 Å), we identify their source regions. For associating a CME to its source region we follow a similar procedure as mentioned in Gilbert et al. (2000). We spatially associate a source region to a CME by requiring that the latitude of the source region to be around $\pm 30^\circ$ to that of the central position angle (PA) of the CME converted to equivalent apparent latitude (lat_{PA}) by the following relation:

$$lat_{PA} = 90 - PA \quad [0 \leq PA \leq 180] \quad lat_{PA} = PA - 270 \quad [180 < PA \leq 360]. \quad (3.1)$$

We temporally associate them by requiring that the source region erupts or shows radially outward movement in the above latitude window within at least 30 minutes before the time at which the CME leading edge appears for the first time in the LASCO C2 FOV. We classify the identified source regions into three broad categories. Active Regions (ARs), which are areas of strong magnetic field showing bright emissions in EUV and X-rays, Prominence Eruptions (PEs), which are the quiescent prominences seen as dense hanging feature in the solar atmosphere and Active Prominences (APs) which are PEs with their one or more foot-points connected to ARs (also refer [Subramanian and Dere \(2001\)](#)). After associating the CMEs to their source regions, we segregated the CMEs into 6 separate classes, fast CMEs from ARs, PEs, and APs and similarly for slow CMEs.

3.2.3 3D Reconstruction and Estimation of Geometrical Parameters

To study the 3D kinematics of these CMEs, we use the GCS model developed by [Thernisien, Vourlidas, and Howard \(2009c\)](#). This model assumes that CMEs have a flux-rope structure. It provides 6 parameters: height of the leading front (h), tilt-angle (γ), half-angle (α), aspect-ratio (k), latitude (θ) and longitude (ϕ), to fit the model to an event and reproduce the large scale flux-rope structure of the CME. We use this model by fitting a geometrical wireframe structure of the model simultaneously to a synchronized pair of SECCHI (EUVI, COR-1 and COR-2) images. This geometrical structure resembles a hollow croissant with conical legs, and with a front section which is in the approximate shape of a

torus. This cross-section ($a(r)$) increases with height (r) subject to the condition that the ratio of the former to the later ($k = a(r)/r$) is constant with time, where the k is the aspect-ratio parameter. The fitting is done interactively, until a good visual match is obtained between the wireframe projection of the model and both the data views from COR-1 (A and B) or COR-2 (A and B). We begin with a pair of image where the CME leading front is well developed. We set the half-angle to zero initially and adjust the latitude and longitude to set the location of the foot-point of the model. Then the height is adjusted until the wireframe covers the leading outer front of the CME. Next, we adjust the aspect-ratio so as to consider the spatial extent of the CME. Finally, we change and adjust the half-angle and tilt angle until the best visual match is obtained. Figure 3.1 shows an example of fitting the synthetic wireframe structure (in green) using GCS model to a pair of COR-1 images for the CME observed on 2012-11-09 at 01:00:00 UT. To quantify how well we have fitted the model in reproducing the overall structure, the uncertainty in fitting is found by outlining a hand drawn contour on the stereoscopic pair of images (an automatic optimizer is further used to refine this fit) and then a comparison is done between the hand drawn contour and the binary contour of the projected wireframe structure of the model (for details refer [Thernisien, Vourlidas, and Howard \(2009c\)](#)). This whole process is repeated iteratively for a time sequence of images in the COR-1 and COR-2 FOV and the evolution of each of the parameters is recorded. In this context, [Thernisien, Vourlidas, and Howard \(2009c\)](#) reported that for some cases, it is tricky to determine the complete flux-rope orientation from observation from two vantage points (in particular for periods in which STEREO-A and STEREO-B are in/close to opposition.), use of a third vantage point will help in a better 3D reconstruction (also refer [Balmaceda et al. \(2018c\)](#)). In this regard, use of LASCO images can help in better constraining the parameters. But, since we want to study the CME evolution in the inner corona, and LASCO C2 FOV starts from $2 R_{\odot}$, we will be able to use LASCO only beyond $2 R_{\odot}$, and below this height we have to use COR-1 only. Thus, to keep consistency throughout our analysis, we

didn't use LASCO data in this work.

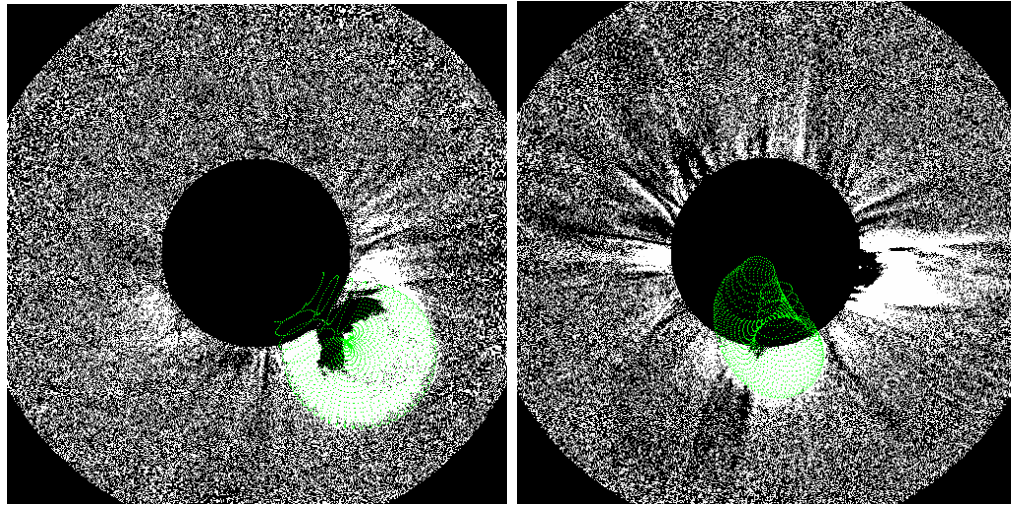


FIGURE 3.1: The CME on 2012 – 11 – 09 observed by COR-1 A and COR-1 B at 01:00:00 UT, with the GCS model generated flux-rope structure (green wireframe) overlaid on them. Note that the CME has a face on view in (a) and an edge on view in (b)

3.2.4 Methods of the estimation of 3D kinematical properties

After fitting the GCS model to a time sequence of images of COR-1 and COR-2, the fitted parameters are recorded. The height time data is fitted with a cubic smooth spline (red curve in top panel of Figure 2). A R-based procedure “smooth.spline.R” (R Core Team 2018) is used to perform cubic smooth spline fitting. In this method, the number of nodes are supplied by the user, and the fitting function then decides on the position of the nodes, thus dividing the entire height time data into those many segments. We choose on average, six to ten nodes to characterise the spline, depending on the number of data points present in each event, thus if the number of data points were less, then the number of nodes was reduced to 6 or 7, such that the different phases of evolution can be captured. The speed and acceleration are calculated by the first and second order numerical differentiation of the height time data. The speed and acceleration profile (red curve in second and third panel)

is similarly obtained by differentiating numerically the fitted height time smooth spline function. We also plot an inset with a zoom into the residual acceleration phase in the bottom corner of the panel displaying acceleration.

The grey band around the red curve in the top panel denotes the uncertainty in the fitted parameter which is estimated by computing the uncertainty in the fitting of the GCS model to the pair of observed images. The uncertainty in fitting is found by outlining a hand drawn contour on the stereoscopic pair of images (an automatic optimizer is further used to refine this fit) and then a comparison is done between the hand drawn contour and the binary contour of the projected wireframe structure of the fitted model (for details refer [Thernisien, Vourlidas, and Howard \(2009c\)](#)). This procedure is repeated several times on several images and the average uncertainty was found to be 20%. Thus the grey band denotes the 20% uncertainty region.

In section 3.3.5, we study the acceleration magnitude and acceleration duration of the CMEs. The acceleration phase is determined from the velocity profiles. We identify the starting time of acceleration (when the velocity starts changing) and the ending time of acceleration (when the velocity reaches the highest value and then becomes constant or decelerates from thereupon), from which we estimate the acceleration duration. The acceleration magnitude is then calculated (as reported by [Zhang and Dere \(2006\)](#)) as the increase in velocity divided by the duration of acceleration. The uncertainty in the duration of the acceleration is due to the cadences of COR-1 and COR-2. The uncertainties in height measurements (as mentioned earlier) and the time interval (from cadence of COR 1 and COR 2) are used to compute the uncertainty in acceleration magnitude. Since the uncertainty of velocity change, and acceleration duration is inherited into the uncertainty of acceleration magnitude, the uncertainty is higher for impulsive events, and smaller for gradual events (also reported by [Zhang and Dere \(2006\)](#)). Apart from the image cadence, uncertainty in the acceleration phase can come from the inconsistencies that may arise from the CME leading edge measurements in different wavelengths

(EUV and WL), and from the change in intensity that often occurs over the FOV of a single instrument (Temmer et al. 2010). As we have mentioned earlier, we have not used EUV data with WL data, to remove such inconsistencies in the measurement of the leading edge in different wavelengths. We cannot rule out the acceleration below COR-1 FOV, and in such cases, the measurement of the duration of the acceleration phase would be an under estimate. However, including EUV data will be tricky since we do not know if the structures seen in EUV map to the same features that are observed in WL. Thus we confined the analysis to WL only.

3.3 Results

The details of the GCS fitting is presented in Table 3.1 with all fitting parameters at the time when the CME leading front is well developed in the COR-1 FOV. The third column specifies the identified source region of the CMEs. In case of events where both the view points gave an edge-on view of the CME, in those cases, we have an ice cream cone shape, which is reproduced by the model by setting α to zero, and in such cases we put a ‘-’ in the column for γ in Table 3.1. Different physical parameters of the model provide physical insights on their evolution. A change in the GCS latitude, or longitude is generally interpreted as true deflection, a change in γ is generally interpreted as rotation as the CME propagates into the heliosphere, and a change in the half-angle can be interpreted as true 3D expansion of the CME (Thernisien, Vourlidas, and Howard 2009c; Bosman et al. 2012)

Once we record parameters of CME for a time series during the CME evolution through COR-1 and COR-2 FOV, we explore the physics conveyed by these parameters and their impacts on the evolution of CMEs through the inner and outer corona.

Date	Time	Source	h	ϕ	θ	γ	k	α	V_{CDAW}	V_{GCS}
-	(UT)	-	(h_{\odot})	(Deg.)	(Deg.)	(Deg.)	-	(Deg.)	(Kms^{-1})	(Kms^{-1})
2007-05-09	02:00:00	AR	3.36	69	3.9	-	0.33	0	264	277
2008-03-25	19:20:00	AR	3.36	188	-15	69	0.17	12	1103	1074
2008-03-26	10:52:22	AR	3.71	1	-5	2	0.21	4	163	241
2008-04-05	16:15:00	PE	3.35	258	0	-65	0.13	14	962	994
2008-04-09	10:45:00	AP	3.22	193	-21	2	0.12	8	650	543
2008-10-17	05:25:00	PE	3.21	276	-22	-31	0.26	18	143	244
2010-02-13	00:30:00	AR	2.98	199	44	8	0.21	9	1005	325
2011-01-24	01:45:00	PE	3.39	0	-24	-36	0.22	11	258	301
2011-04-02	11:50:00	AP	3.29	119	-43	61	0.19	30	238	300
2011-05-12	13:40:00	AP	3.37	0	18	40	0.13	11	274	390
2011-05-17	05:20:00	PE	3.36	239	13	90	0.13	12	220	231
2011-05-30	10:40:00	PE	3.25	273	61	90	0.19	27	299	254
2011-06-01	18:05:00	AR	3.29	38	-5	-43	0.38	5	198	378
2011-06-11	13:10:00	PE	3.31	252	30	-58	0.15	18	269	258
2011-06-20	17:55:00	PE	3.21	28	16	7	0.28	19	329	470
2011-07-09	00:40:00	AP	3.29	278	-17	57	0.17	21	209	692
2011-09-20	13:15:00	AP	3.22	234	24	68	0.17	31	337	427
2011-12-26	11:50:00	AR	3.24	186	24	62	0.20	25	448	782
2012-01-02	01:47:30	AP	3.34	265	-19	90	0.28	39	531	540
2012-01-06	21:30:00	AR	3.33	279	51	24	0.24	20	443	407
2012-01-08	02:30:00	AR	3.27	240	-31	-45	0.35	37	557	530
2012-01-15	03:10:00	AR	3.20	224	39	-52	0.26	36	407	526
2012-01-18	12:10:00	AR	3.21	226	-30	-21	0.28	22	267	367
2012-01-19	10:25:00	AR	3.21	278	46	51	0.13	22	270	363
2012-02-24	03:20:00	PE	3.11	107	25	-64	0.20	38	800	473
2012-03-12	01:30:00	PE	3.15	181	-53	-3	0.09	29	638	357
2012-03-15	00:20:00	AR	3.15	335	12	-38	0.19	30	750	354
2012-03-16	20:55:00	PE	3.20	263	43	-	0.20	0	862	515
2012-03-20	23:20:20	AR	3.00	36	53	22	0.18	6	253	324
2012-03-30	15:00:00	PE	3.08	318	29	-71	0.27	30	584	506
2012-04-08	01:40:00	PE	3.25	13	-27	-17	0.40	7	624	565
2012-04-19	15:30:00	AP	3.29	104	-30	90	0.16	11	540	495
2012-04-28	12:30:00	PE	3.14	26	-38	3	0.37	17	260	213
2012-04-30	07:50:00	AR	3.21	51	-28	-27	0.18	32	992	935
2012-05-03	14:45:00	AR	3.16	200	14	-75	0.58	6	584	554
2012-05-24	22:30:00	AP	3.21	358	-5	45	0.14	15	563	405
2012-06-03	18:25:00	AP	3.42	197	26	-73	0.25	24	605	710
2012-06-15	14:45:00	AP	3.07	275	-9	57	0.22	59	262	502
2012-06-26	10:10:00	AR	3.43	103	-22	-10	0.24	14	283	367
2012-06-27	11:30:00	PE	3.29	32	53	-3	0.33	9	511	441
2012-06-29	01:55:00	PE	3.15	231	-12	77	0.11	18	207	437
2012-07-05	13:45:00	AR	3.28	229	-42	10	0.25	27	741	623
2012-07-06	06:10:00	AR	3.07	287	-11	73	0.23	29	258	570
2012-07-08	16:40:00	AP	3.57	225	-38	-53	0.24	7	1572	1492
2012-07-17	14:20:00	AR	3.16	69	-32	-21	0.21	20	958	504
2012-07-26	23:20:00	PE	3.15	161	58	-18	0.53	34	542	421
2012-08-02	13:15:00	PE	3.01	274	-26	45	0.41	25	563	551
2012-08-04	12:50:00	AR	3.12	93	-20	50	0.20	38	187	318
2012-10-12	01:50:00	AP	3.14	166	56	-58	0.30	10	275	228
2012-10-22	02:00:00	AP	3.17	341	-17	90	0.12	14	304	300
2012-11-09	01:00:00	PE	3.13	182	-38	-49	0.27	17	771	664
2012-12-10	15:55:00	AP	3.07	114	-13	65	0.22	32	305	424
2012-12-14	02:15:00	PE	3.14	232	-17	56	0.18	30	304	440
2013-04-05	22:10:24	AP	3.22	234	-5	90	0.19	14	207	306
2014-01-02	07:30:00	PE	3.00	235	-48	79	0.17	23	168	230
2014-01-04	23:02:30	AP	3.13	237	1	89	0.23	34	567	559
2014-01-07	03:45:00	AP	2.99	259	-31	-90	0.40	61	688	619
2014-02-11	19:30:00	AP	3.00	105	-19	-32	0.32	26	613	658
2014-04-07	21:45:00	PE	3.03	107	-28	-75	0.22	18	160	512

TABLE 3.1: The GCS model parameters of all the CMEs are tabulated below. h is the height of the leading front, θ , and ϕ are the latitude and longitude of the foot-points of the CME, the tilt-angle (γ) is the angle between the axis of symmetry of the CME and the local parallel of latitude, aspect-ratio (k) is the ratio of the radius of cross-section of the leading front and the radial distance of the leading front from the center of the Sun and α is the half-angle between the legs of the best fit GCS model. The Time is the time of observation, V_{CDAW} is the average linear speed taken from the CDAW catalogue, and V_{GCS} is the average 3-D speed calculated from the GCS model.

3.3.1 Connecting Width to the 3D Kinematics

Since we aim to understand the 3D evolution of CMEs in the inner and outer corona, in this section we explore the 3D kinematic profiles of them. Of the three forces (Lorentz force, viscous drag force and gravitational force), that govern the dynamics of CMEs, since Lorentz force is the main driving force in the initial eruption process (Kliem et al. 2014; Isenberg and Forbes 2007) that leads to the initial translation and expansion of the CME (Subramanian et al. 2014), we connect here the true width evolution of CMEs to their 3D kinematic profiles. Figure 3.2, shows the kinematic profiles of four different CMEs out of which the top left and right panels are two slow CMEs and the other two are fast ones based on their speeds recorded in CDAW catalogue. Every panel further contain four subplots. From the top, the first panel contains the height-time curve of the CMEs derived using GCS model fitting on COR-1 and COR-2. The height-time data is fitted with a cubic smooth spline which has an additional advantage of choosing the number and position of nodes. This provides the advantage of capturing the different stages of evolution in the kinematic profiles. For the fitting, we choose on average from six to ten knots to characterise the spline. A similar fitting procedure was adopted by Mierla et al. (2013) and Bein et al. (2011b). The uncertainty in fitting due

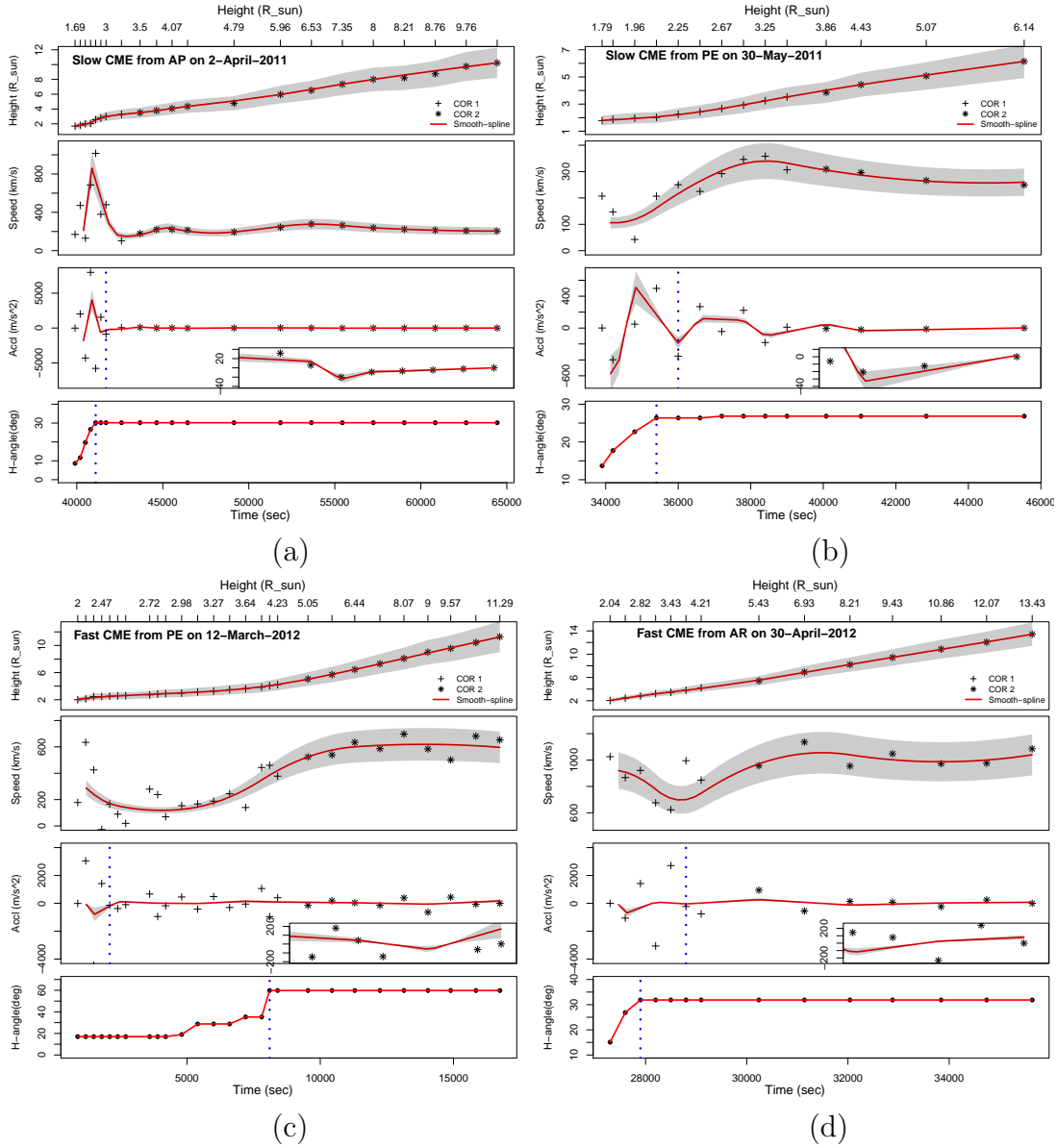


FIGURE 3.2: 3D kinematic profiles of slow CMEs in (a) and (b), and fast CMEs in (c) and (d). In every panel, the top figure shows the height-time plot derived from COR-1 and COR-2 data using the GCS model. The solid red line represents the smooth-spline fit to the height-time data. The second and third plots show the CME speed and acceleration derived by the numerical differentiation of (a) and (b), respectively. The uncertainty in the fitted model is shown in the grey shaded region. An inset with a zoom into the residual acceleration phase is provided for each event in the bottom corner of the acceleration plots. The axis scale in x coincides with the x axis at the bottom.

to the uncertainty in the fitted model parameters (refer Section 3.2) is shown by the light grey shaded region around the fitted spline in red (Figure 3.2). We use

only WL data for the study of kinematics so as to ensure that we are tracking the same physical feature in the FOV of different instruments. The second and third panels from the top show the variation of the speed and acceleration with time derived by numerical differentiation of the height and velocity, respectively. To understand the nature of variation of the width of CMEs, in the bottom subplot, we plot the evolution of the half-angle of the CME, which signifies the width of the CME. We also show the height axis on top for a better understanding. Figure 3.2(top left) shows a slow CME coming from AP on April 2, 2011. The second and third panels show that the CME experienced an initial impulsive acceleration which accelerated the CME to a high speed and then it got decelerated, with the speed eventually slowing down and becoming constant at a smaller speed. Such increase and then decrease in speed of a CME hints towards the drag experienced by the CME owing to the solar wind, which reduces the speed to a lesser value and the CME propagates with that constant speed as reported by [Gopalswamy et al. \(2000a\)](#). The acceleration also shows a similar nature of variation, with a sudden initial impulsive phase and then almost vanishes for the later part of the propagation phase. The expansion of the CME shown in the fourth panel shows that the CME expand during its initial evolution and then propagated with a constant width beyond $2.57 R_{\odot}$. Figure 3.2(b) shows a similar behaviour, but the speed after attaining a higher value, became constant at that value, without showing much signs of further deceleration. A similar behaviour is seen for bottom left and right panels of Figure 3.2. Similar profiles were also reported by [Bein et al. \(2011b\)](#), but in this work we report on true speed and acceleration profiles.

It is understood that the viscous drag force dominates over other forces at the higher heights ([Sachdeva et al. 2015](#)), and the CME is expected to have a constant speed profile with little or no acceleration (also refer [Webb and Howard 2012a](#)). Thus, we plot a blue dotted vertical line on the acceleration plot corresponding to the height where the initial impulsive acceleration vanishes. We also draw a similar

vertical line on the width evolution plot, where the width is becoming constant there upon. A comparison of these two heights (the height at which impulsive acceleration vanishes and the height at which the width becomes constant) will tell us the height till which the Lorentz force leaves its imprint on the kinematic profiles of the evolution of CME from the inner corona, to the heliosphere. For event (a), the acceleration drops down at $3.28 R_{\odot}$, while the width becomes constant at $2.57R_{\odot}$. Similarly, the respective heights for events (b), (c) and (d) are ($2.25 R_{\odot}$, $2.02 R_{\odot}$), ($2.52 R_{\odot}$, $4.06 R_{\odot}$) and ($3.81 R_{\odot}$, $2.82 R_{\odot}$) respectively. We note that the heights of vanishing impulsive acceleration and expansion are similar for events (a), (b) and (d), while there is a reasonable difference in the two heights for event (c), where we find that despite the initial acceleration ceasing at $2.52R_{\odot}$, the CMEs show expansion till $4.06R_{\odot}$. We do not understand the reason yet for the difference in the heights in event (c) and a detailed analysis is needed for a better understanding.

Thus, in the 3D kinematic profiles, we find that CMEs first experience impulsive acceleration, followed by a gradual acceleration and finally a little or no acceleration, confirming early works from a single vantage point (Zhang et al. 2001b; Zhang et al. 2004; Bein et al. 2011b). It is also evident that the average values of different kinematic parameters like speed, width, acceleration fail to provide insights about the complete nature of variation and hence can be misleading. Motivated by the varied width evolution, and the connection between width expansion and vanishing impulsive acceleration, we study the evolution of true width of CMEs and the impact of Lorentz force on the kinematics.

We study the evolution of true widths of CMEs in inner and outer corona and then further connect the true widths of CMEs to their true accelerations to have a better understanding of the impact of Lorentz force on their 3D evolution close to their initiation heights. Using the fitted GCS model parameters, we select the CMEs which showed a change in their half-angle as they propagated outwards.

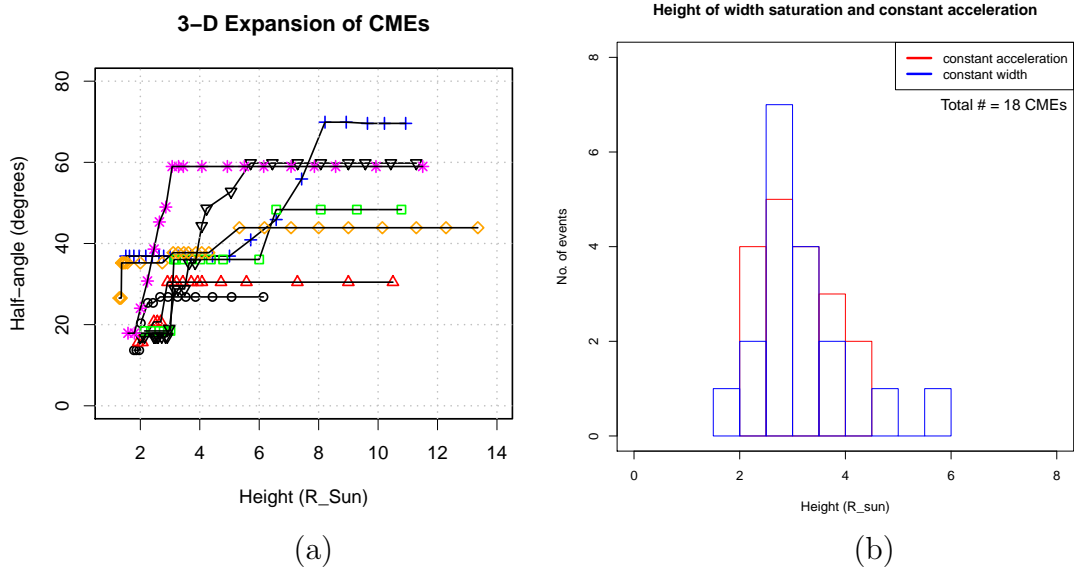


FIGURE 3.3: (a): Variation of the half-angle of CMEs with height. Only those events are showed which showed expansion by greater than 10 degrees. Different colors correspond to different events. (b): Distribution of the height of the saturation of the width and the height where impulsive acceleration vanishes.

In Figure 3.3(a), we plot the change in half-angle of the CMEs which show a change of more than 10 degrees of their initial half-angle (α). A change in α exhibits expansion of CMEs (Thernisien, Vourlidas, and Howard 2009c) and we found that in 27 % (16 out of 59) cases, CMEs showed true expansion (12 % (7 out of 59) of those showed more than 10 degrees of expansion, refer Figure 3.3(a)). We see that some CMEs show initial rapid increase in width and then a subsequent saturation, whereas, some cases show a very gradual increase in the width and then it becoming constant. The expansion of the CMEs in most of the cases is found to saturate before $4 R_{\odot}$, whereas, in a few cases the CMEs keep on expanding till $8 R_{\odot}$. Thus we find a wide range of heights where the width of the CME attains a constant value. Since, the Lorentz force leads to the impulsive acceleration and their expansion in the inner corona, we selected the events which showed impulsive acceleration and 3D expansion in their kinematic profiles (refer Figure 3.2). In Figure 3.3(right), we plot the histogram distribution of the heights where the widths become constant (in blue) and the distribution of heights where the impulsive acceleration of the CME vanishes (in red). We

find that both the distributions have a well overlapping height ranges, while the distribution of heights of constant width has a wider spread than that of the heights of vanishing impulsive acceleration. We find that for most of the CMEs, the width became constant in the height range of $2.5 - 3 R_{\odot}$. This is in agreement with the results of [Cremades, Iglesias, and Merenda \(2020a\)](#) who reported that the width of the CMEs changed considerably below $3 R_{\odot}$. We also note from the right panel that the mode of both the distributions fall in the overlapping height range of $2.5 - 3 R_{\odot}$. This tells us that for most events, the vanishing of initial impulsive acceleration and the constancy of width happens in this height range. Thus, this is the height range till which the impact of Lorentz force remains evident in the kinematic profiles on the initial evolution of CMEs. This is also supported by the results of [Sachdeva et al. \(2017\)](#) who reported that Lorentz forces peaked in the height range of $1.65 - 2.45 R_{\odot}$ in the evolution of CMEs.

3.3.2 Affinity for the equator - 3D Deflection of CMEs

We investigate whether or not CMEs show any signatures of deflection from a radial path of propagation. We first look into the latitude distribution (refer top panel of [Figure 3.4\(a\)](#)) of the source regions of the CMEs. We can see that it shows a bi-modal distribution with the peaks of the distribution lying in the latitude range of $\pm 10^{\circ} - 30^{\circ}$, which led us to believe that most of the source regions were associated with ARs ([Murray et al. 2018](#)), which in our case are either ARs or APs. In the bottom panel of the same figure, we convert the central Position Angle (PA) of the leading front of the CME as given in the CDAW catalogue, to its equivalent latitude and again plot the distribution of the PA equivalent latitude. Unlike the case for the bi-modal distribution of source location latitudes, for the CMEs we find a broad distribution with a distinct peak around the equator. This tells us that a majority of the CMEs while ejecting, got deflected towards the equator. Similar signature was also reported by [Gopalswamy et al. \(2003\)](#) as they found

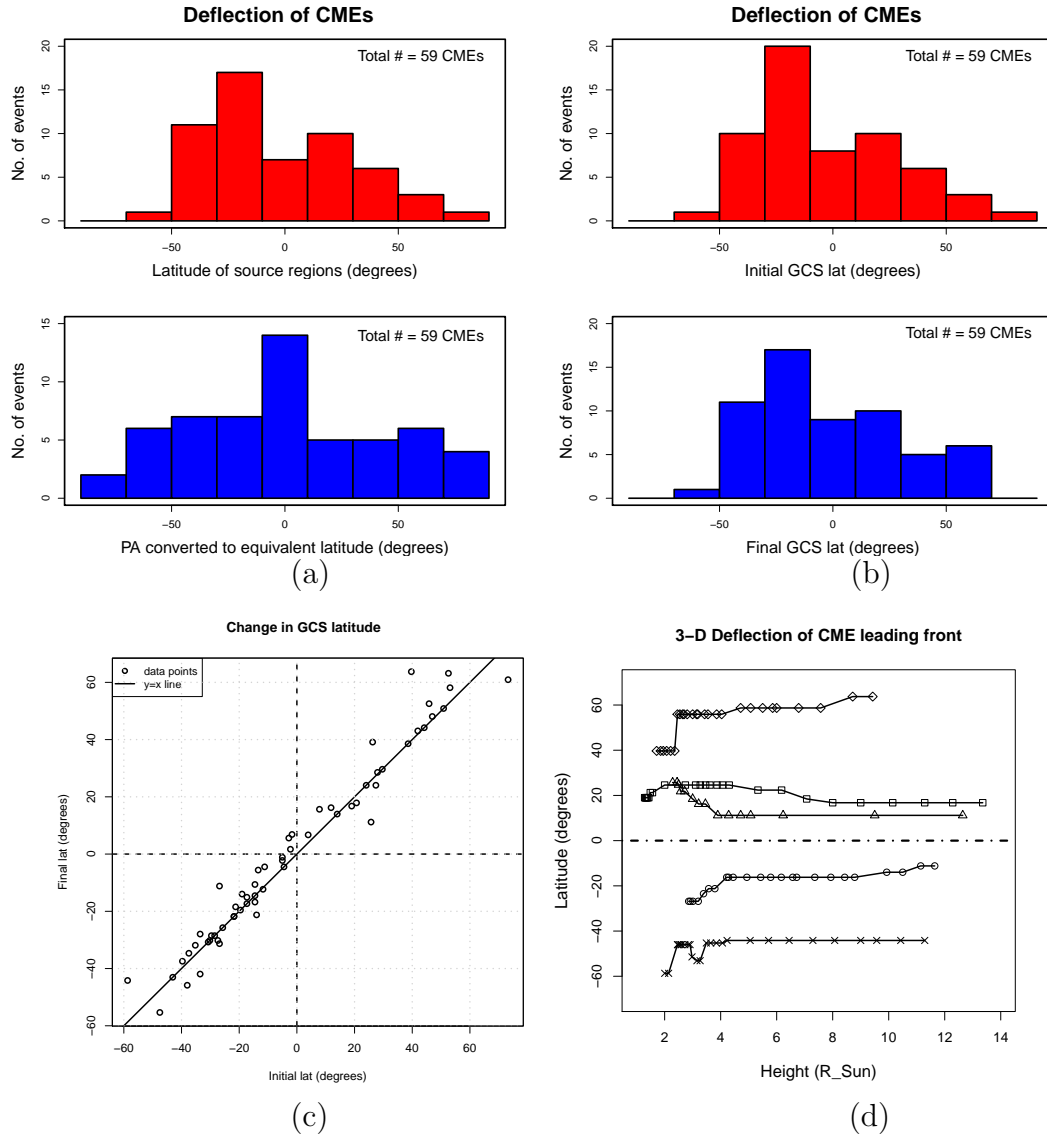


FIGURE 3.4: (a) Top panel: The latitudinal distribution of the locations of source regions of CMEs. Bottom panel: Distribution of the PA equivalent latitude of the CME leading front. (b) Top panel: Distribution of the initial GCS latitude. Bottom panel: Distribution of the final GCS latitude. (c) Plot of final versus initial GCS latitude, with the solid line being the boundary where both the values are equal. The dashed line represents the zero latitude (i.e. equator) (d) Change of latitude of the CME with height estimated from the GCS model. only those cases where the deflection was at least more than 10 degrees are shown. The different data points denote different events - 2011-01-24 (circle), 2011-06-20 (triangle), 2012-02-24 (square), 2012-03-12 (cross) and 2012-10-12 (rhombus).

CMEs originating from prominences got predominantly deflected towards equator from the latitude distribution of prominences and that of the CMEs. However, the

latitude distribution in that study suffers from the projection in the plane of the sky. To check whether the deflections (from Figure 3.4(a)) were actual deflections suffered by the CMEs, we look into the GCS latitude of all the events. We plot in (b) the distribution of initial GCS latitude (top), and final GCS latitude (bottom). In this case we do not find such change in the latitude distribution as we find in (a). We find that the distribution remains bi-modal. To further look into this, we plot the final versus initial GCS latitude. The solid line is the boundary where both the initial and final latitudes are equal, and hence the points lying on this line denotes CMEs which did not get deflected. The dotted line marks the equator. The data points lying to the left of the vertical dotted line denote CMEs with initial latitude in Southern hemisphere. In this region, the points lying above the solid line shows events for which the final latitude is greater than the initial latitude, and thus denote equator-ward deflection, and vice versa in the region that is to the right of the vertical dotted line. As we see from the figure, we do find that most of the CMEs which suffer deflections, get deflected towards the equator. But in most of these cases, the angle of deflections are small, and hence a distribution of GCS latitude does not show a single mode around the equator. From this, we find that the apparent deflection as found from the latitude v/s PA equivalent latitude plot is not a conclusive proof of deflection of CMEs, as the actual deflection suffered (as measured from gcs lat) is much lesser. Due to the uncertainty in the model fitting ($\sim 20\%$), in Figure 3.4(d), we plot the variation of GCS latitude with height for only those cases which showed deflection greater than 10 degrees. In this case too, we find that most of the CMEs get deflected towards the equator irrespective of their location being in the northern or southern hemisphere. In this context, [Gopalswamy et al. \(2009a\)](#), [Kahler, Akiyama, and Gopalswamy \(2012\)](#) reported that CMEs can get deflected from their initial path when they get ejected near a coronal hole. In our sample of events, using the data from AIA and EUVI, we found that for all the events that show large deflections (> 10 degrees) coronal hole was present near their location. We used the JHelioviewer software ([Muller et al. 2009](#); [Müller et al. 2017](#)) and the data from SDO/AIA 193 Å and STEREO/EUVI

195 Å and identified the location of the coronal holes near the source regions of the deflected CMEs. With the coordinates of the coronal holes provided by the Jhelioviewer, we found that on an average the coronal holes are located within 17° of latitude of the eruption. [Kay, Opher, and Evans \(2015\)](#) reported that such interaction of CMEs with the open field lines of coronal holes guides the CMEs towards the heliospheric current sheet. Further, we also found that five events plotted in Figure 3.4(a) have either active or quiet prominences (or filaments) as their source regions. This is also supported by the reports on non-radial ejections of CMEs from prominences with majority of them getting deflected towards the equator by [Gopalswamy et al. \(2003\)](#).

Thus we found true deflection in 31 % (18 out of 59) cases (9 % (5 out of 59) of those showed more than 10 degrees of deflection). We found the average height till which CMEs got deflected around $3.35 R_\odot$. These deflections are also very crucial from the perspective that they provide an indirect evidence of the CMEs exhibiting interactions with ambient coronal structures like coronal holes and can largely affect height-time measurement in 2-D images, giving spurious results. Thus we conclude that from our analysis, we do not find a significant statistical deflection, as expected from earlier works ([Gopalswamy et al. 2003](#)), and thus Figure 3.4 (a) does not provide a conclusive evidence of deflection of CMEs, as the numbers largely suffer from projection effects. Further extending this study on a larger data set with actual 3-D values will help establish our conclusions better.

3.3.3 Comparison of average projected and true Speeds

Since our events are selected from the CDAW catalogue, it is worthwhile to compare results that we have obtained applying GCS model with those already catalogued using 2-D studies. We first find the average 3D speed of all the CMEs as estimated using the GCS model. We find a wide range in the average true speeds

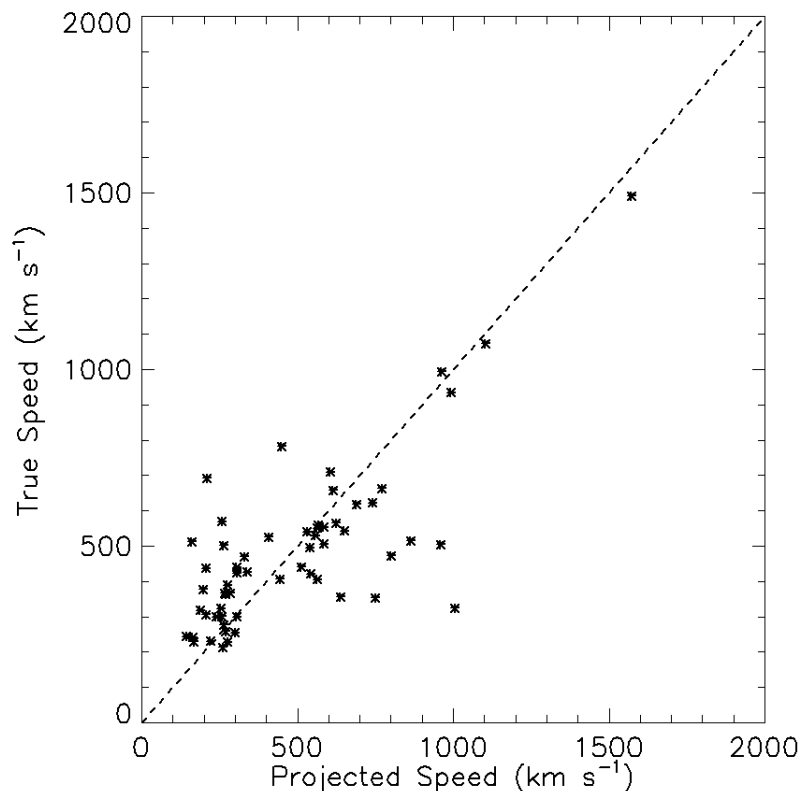


FIGURE 3.5: A comparison between the average projected 2-D speeds as recorded in the CDAW catalogue and the average 3D speeds as calculated using the GCS model. The dashed line is the boundary where both the 2-D and 3D speeds are equal.

from 213 km s^{-1} to 1492 km s^{-1} . The CMEs were segregated into slow and fast based on their average 2-D speed as quoted in the CDAW catalogue. In Figure 3.5 we plot the average true speed versus the average projected speed for slow and fast CMEs. Each data point represent the average speed of one single event. The dashed line is the boundary where both the projected and true speeds are equal. In case of the slow CMEs, we find that, almost all the true speeds are higher than the projected speeds, which is expected. We thus find that a good fraction ($\sim 52\%$) (15 out of 29) of the slow CMEs ($< 400 \text{ km s}^{-1}$ in CDAW catalogue) have higher true speeds. In the case of fast CMEs, we find a good fraction ($\sim 63\%$) (19 out of 30) of the events showing 2-D speeds higher than 3D speeds. This contradicts our intuition. Shen et al. (2013a) reported several reasons for this discrepancy. The GCS model does a 3D fitting of the leading front of the CME, whereas speeds in

the CDAW catalogue is calculated by tracking the part of the leading edge which move with the highest speed (which may be a part of the shock front of the CME). We also note that the projected speeds are greater than the true speeds mostly for the fast CMEs which are capable of driving shocks. We also found that all these fast CMEs with projected speeds higher than true speeds were marked as partial-halo events in the CDAW catalogue. In this context, [Gopalswamy et al. \(2009c\)](#) and [Shen et al. \(2013b\)](#) reported that the speed of lateral expansion might be greater than the radial propagation speed, and in the projected image, especially for halo or partial halo CMEs, it is difficult to distinguish between the two. Thus, for such events which are halo or partial-halo with respect to one viewing point, it is important to study their kinematics by performing a 3D reconstruction with images taken from more than one vantage point and then find their true propagation speed and not their lateral expansion speed. Further, at different latitudes, the solar wind speeds might be different, which can have different imprints on different parts of the CME leading edge, which will also influence the results of CDAW catalogue (as they track one single point on the leading edge). But the GCS model fits the leading front completely and hence this effect will be much lesser.

3.3.4 Distribution of Peak Speeds and Accelerations

In Figure 3.6(a) we plot the distribution of peak 3D speeds (V_{peak}) for all the 59 CMEs studied in this work. We find a wide range for V_{peak} from 396 to 2465 km s⁻¹ with an average of 984 km s⁻¹, and the peak of the distribution being in the range 600 to 800 km s⁻¹. [Bein et al. \(2011b\)](#) reported a range for V_{peak} from 56 to 1279 km s⁻¹ with an average of 526 km s⁻¹ and mode lying in the range 300 to 400 km s⁻¹ for 95 events during 2007 to 2010 which was during the solar minimum of cycle 23. [Vršnak et al. \(2007a\)](#) studied 22 events during 2002 to 2005 which was the maximum and decay phase of cycle 23 and found V_{peak} to range between 365

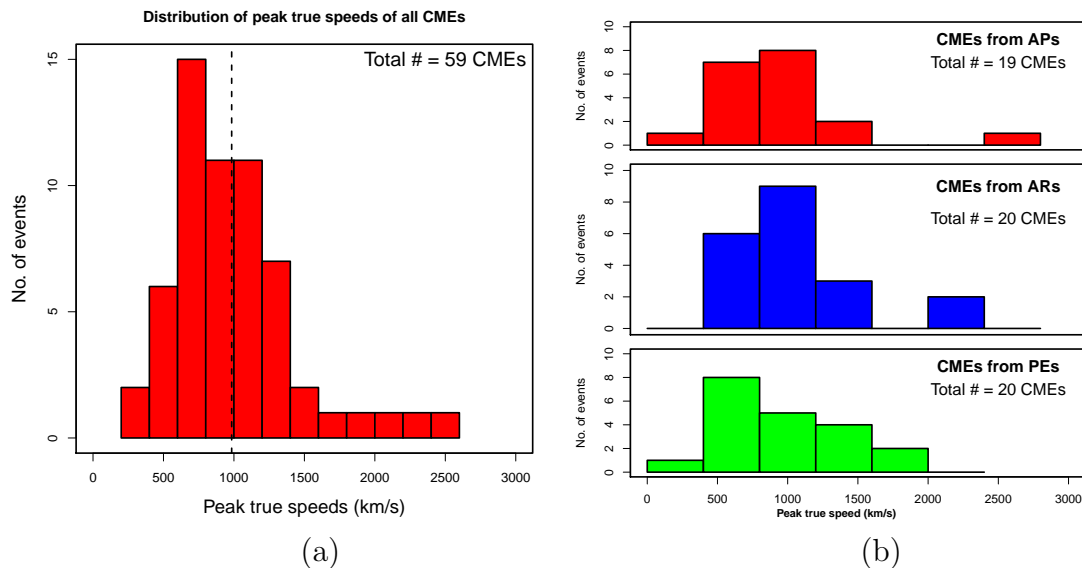


FIGURE 3.6: (a) Distribution of peak speeds of all the CMEs. The dashed line denotes the mean value. (b) shows the contribution of peak speeds of CMEs originating from APs, ARs and PEs to (a).

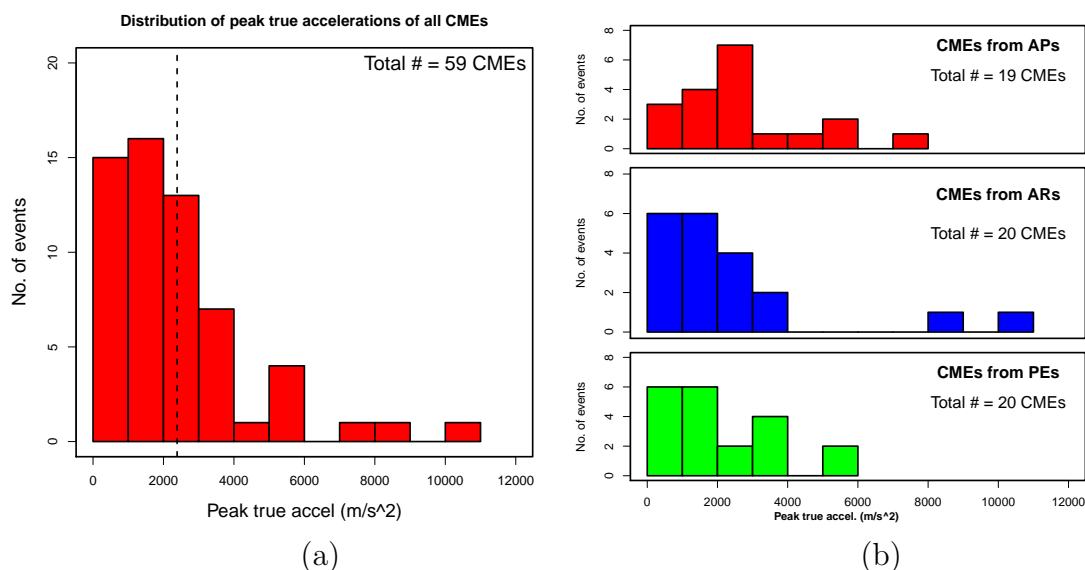


FIGURE 3.7: Panel (a) shows the distribution of peak accelerations of all the CMEs. The dashed line denotes the mean value. Panel (b) shows the contribution of peak accelerations of CMEs originating from APs, ARs and PEs to panel (a).

to 2775 km s^{-1} with an average of 940 km s^{-1} . We find our results are similar to the results of Vršnak et al. (2007a) and our events were selected during 2007 to 2014 which includes cycle 23 minimum, cycle 24 rising phase and maximum with

a majority of the events ($\sim 69\%$) coming from cycle 24 maximum, and further, the speeds in our work are the true peak speeds. [Bein et al. \(2011b\)](#) reported on a long tail of the distribution of V_{peak} towards high velocities. We also find a similar trend in our result (Figure 3.6(a)) and since we have the information of the source region, we wanted to look at the contribution of the CMEs coming from the different source region to this distribution. In panel (b), we plot the peak speed distribution but for the CMEs segregated on the basis of their source regions. We find that the tail of the distribution towards high velocities is contributed by the CMEs coming from ARs and APs. We also note that the mode of the distribution is the same for CMEs coming from ARs and APs (800 to 1200 km s⁻¹), while for CMEs from PEs it is between 400 to 800 km s⁻¹, which further implies that the CMEs from ARs and APs tend to have higher peak speeds than the ones from PEs. In this regard, we also found that most of the CMEs (42 %) (25 out of 59) reached their true peak speeds below 5 R_⊙.

We also plot the distribution of peak true acceleration (a_{peak}) in Figure 3.7(a). We note that while the distribution of V_{peak} increases gradually to a peak and then decreases with a long tail, in case of a_{peak} , the distribution falls off with increasing acceleration, but with a similar tail towards higher values. We further find an even wider range for a_{peak} from 176 to 10922 m s⁻² with an average of 2387 m s⁻² and the mode of the distribution lying in the range 1000 to 2000 m s⁻². This is again higher than the range obtained by [Bein et al. \(2011b\)](#) from 19 to 6781 m s⁻² with an average of 756 m s⁻². whereas [Vršnak et al. \(2007a\)](#) reported a higher range from 40 to 7300 m s⁻². Again to find the contribution of different source regions to the peak acceleration distribution, we again plot the distribution separately for the three different sources in panel (b). We again find that the high acceleration tail is coming from the CMEs which had either ARs or APs as their source regions. Thus, based on the distribution of peak true speeds and accelerations, we find that the CMEs originating from ARs and APs are more energetic than the ones

coming from PEs. This conclusion is based on the speed and acceleration of these CMEs. The injected flux in the flux-rope is responsible for translating the CMEs (Subramanian et al. 2014; Webb and Howard 2012a), and thus, according to our definition of ARs, and APs, CMEs associated with AR and AP might have more flux injection leading to strong accelerations. This could be responsible for large speeds and accelerations. A detailed investigation needs to be done considering the magnetic field of the source region and the injected flux to the CMEs to further quantify this statement.

3.3.5 Acceleration duration and acceleration magnitude

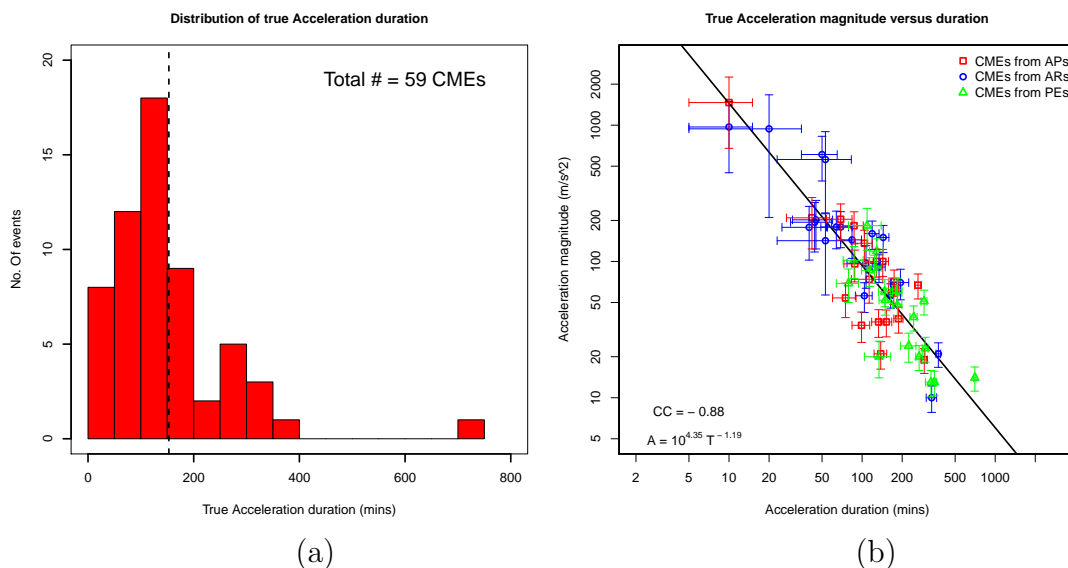


FIGURE 3.8: (a) Distribution of acceleration duration of all the CMEs. The dashed line denotes the mean value. (b) Acceleration magnitude versus duration of all the CMEs. Different colors indicate CMEs originating from different source regions.

Since CME events can range from being extremely impulsive to extremely gradual based on their accelerations, a study of the true acceleration duration and acceleration magnitude is important as they greatly affect the speeds of CMEs (Zhang and Dere 2006). Based on the 3D kinematic profiles (refer Figure 3.2), we were able to track the change in velocity, thereby identifying the onset and ending time,

and hence the acceleration duration. In Figure 3.8(a), we plot the distribution of the acceleration duration in minutes. We find a wide range in the acceleration duration from 10 minutes to 703 minutes with the peak of the distribution in the range of 100-150 minutes and the mean duration being 153 minutes. Such wide range in acceleration duration was also reported by Zhang and Dere (2006), Vršnak et al. (2007a) and Bein et al. (2011b) with a mean duration of 180, 120 and 44.6 minutes respectively. We find our average acceleration duration to be in agreement with the results of Zhang and Dere (2006) and Vršnak et al. (2007a) while Bein et al. (2011b) suggested such a relatively lower value was due to the fact that majority of the events studied were impulsive events. Since the acceleration magnitude is also important for understanding the kinematics, we further found the acceleration magnitudes of all the CMEs. For this we followed a similar procedure as Zhang and Dere (2006), who reported that the acceleration magnitude is the increase in velocity divided by the duration of acceleration. The uncertainty in the duration of acceleration is determined by the observational cadences, and the same for acceleration magnitude is contributed from the uncertainty in the acceleration duration and the velocity change (Zhang and Dere (2006)). In Figure 3.8(b), we plot the acceleration magnitude versus acceleration duration. We find a strong inverse correlation between acceleration magnitude and acceleration duration, that is higher acceleration magnitudes have shorter duration and vice versa. This inverse correlation can be outlined with the following relation:

$$\log(A) = 4.35 - 1.19\log(T), \quad (3.2)$$

where A is the magnitude of acceleration in m s^{-2} and T is the duration of acceleration in minutes. The correlation coefficient is -0.88. Similar inverse correlation was also reported by Zhang and Dere (2006) (power law index -1.09), Vršnak et al. (2007a) (power law index -1.14) and Bein et al. (2011b) (power law index -1.09). We note from our results that the scaling relation remains similar in 3D study.

This thus shows that impulsive events tend to experience stronger acceleration for shorter duration while the gradual events tend to experience weaker acceleration for longer duration. We also note from panel (b) that the CMEs coming from PEs (in green data points) are distributed in the lower region of the scatter plot, indicating that they are gradual events with weaker acceleration magnitude with longer acceleration durations.

3.4 Summary and Conclusions

In this work we study the 3D evolution of Coronal Mass Ejections in the inner and outer corona originating from different source regions, which are Active Regions, Prominence Eruptions and Active Prominences. A total of 59 CMEs were studied, of which 29 CMEs were slow ($< 400 \text{ km s}^{-1}$) CMEs and 30 CMEs were categorised as fast ($> 400 \text{ km s}^{-1}$) CMEs based on their recorded 2-D speeds in the CDAW catalogue. The source regions of all these 59 CMEs were identified. This helped us to connect the true kinematics of CMEs in 3D to the source regions they are coming from. Multi-viewpoint coronal observations from the twin spacecraft STEREO A and STEREO B was used for the 3D reconstruction of the CME morphology by using the GCS model. The data from COR-1 and COR-2 was used in tracking the CME for studying its kinematics. Table 3.1 shows the GCS fitting parameters of events we studied in this work. The table also lists alongside, the identified source region of these CMEs and their average true and projected speeds. For CMEs which were observed edge-on (that gives an ice cream cone shape appearance) from both the view points, we couldn't determine the half-angle uniquely for them and as a consequence, the tilt-angle for such events are kept zero as it has no meaning when the half-angle cannot be determined (for details refer [Thernisien, Vourlidas, and Howard \(2009c\)](#)). This problem might be fixed, if another vantage point of observation can be used to fit the model to the event. For example,

LASCO C2 data can be used to address this issue. We conclude our main results that we have discussed in different sections of this paper as follows.

- We studied the true width evolution of CMEs in the inner and outer corona (refer Figure 3.3(a)), and found that in 28 % cases, CMEs showed true expansion (12 % of those showed more than 10 degrees of expansion). We also found that some of the width profiles showed an initial rapidly increasing phase and then a saturation, while some events showed a gradually rising phase or a late rising phase and then a subsequent saturation. Another important feature is that there was a wide range of heights ($2.5-8 R_{\odot}$) till which CMEs showed an increase in its width. Since, Lorentz force drives the initial rapid acceleration of the CME and is also responsible for the expansion, we plotted the distribution of heights where the width became constant and the heights where the initial impulsive acceleration vanished (Figure 3.3(b)). We found that both the distributions peaked at an overlapping height range of $2.5 - 3 R_{\odot}$. Thus, we believe that the effect of Lorentz force remained dominant in the initial phase of evolution till a height range of $2.5 - 3 R_{\odot}$. In this regard, we note that Patsourakos, Vourlidas, and Kliem (2010) tracked a circular bubble shaped cavity of a CME using the GCS model, but with a further constraint that the legs of the model being co – incident (that is alpha being 0, giving the ice cream cone shape). They studied the timing of bubble expansion and acceleration and its relation to the associated flare, and they do not talk about the height of influence of Lorentz force. In this work, we do not put any such constraints on the model parameters, and we further statistically find the height of influence of Lorentz force on the evolution of CMEs, by connecting width evolution and acceleration profile. To our knowledge this is the first time the observational impact of Lorentz force on CME kinematics is statistically shown by connecting true width evolution to the true acceleration profile using the GCS model.

- We found latitudinal deflection suffered by a subset of the events we have studied (Figures 3.4(a), (b), (c) and (d)). We found true deflection in 31 % (18 out of 59) cases (9 % (5 out of 59) of those showed more than 10 degrees of deflection). A distribution of the latitudinal location of the source regions of these CMEs and of the PA of the CME leading edge converted to equivalent latitude showed that the most of the CMEs propagated non-radially and a majority of them apparently getting deflected towards the equator. But a distribution of the initial and final GCS latitudes did not show such strong signatures of equator-ward deflection. From the plot of final versus initial GCS latitude, we do find most of the CMEs showing deflections towards the equator, but the angle of deflection being small in most cases as mentioned earlier. Thus we conclude that the latitude versus PA equivalent latitude plot does not provide a conclusive evidence of deflection of CMEs, as the numbers largely suffer from projection effects, and a study with the true numbers (the true latitudes found from 3D reconstruction) give a better understanding. A plot of the change in latitude of the CMEs from the GCS model fitting (refer Figure 3.4(b)), further showed that most of the CMEs got deflected towards the equator. The presence of coronal holes results in CMEs getting deflected and in our case too, coronal holes were found near the CMEs which were deflected by more than 10 degrees. [Kay, Opher, and Evans \(2015\)](#) reported that such interaction of CMEs with the open field lines of coronal holes guides the CMEs towards the heliospheric current sheet. Such equator-ward deflection of fast CMEs can be potential indicators of strong Solar Energetic Particle (SEP) events happening at 1 AU ([Kahler, Akiyama, and Gopalswamy 2012](#)), as such CME and coronal hole interactions indicate a possible interaction between the coronal hole magnetic field and the magnetic field of the CME, producing driverless shocks at 1 AU, capable of producing SEP events. Driverless shocks are the shocks at 1 AU which do not accompany any in-situ observation of the associated interplanetary CME drivers (for details, please refer [Gopalswamy et al. \(2010\)](#)). Since

we find only 5 cases which show strong equator-ward deflection, extending this study on a larger data set will help in confirming our conclusions.

- We found the peak 3D speeds of CMEs ranging between 396 to 2465 km s⁻¹ with a mean value of 984 km s⁻¹, mode lying in the range 600 to 800 km s⁻¹ and the peak 3D acceleration having an even wider range from 176 to 10922 m s⁻² with a mean value of 2387 m s⁻² and mode lying in the range 1000 to 2000 m s⁻². We further found that the distribution of V_{peak} and a_{peak} showed a long tail towards high speeds and accelerations and this contribution to high values came from CMEs which had either ARs or APs as their source regions, thus showing that such CMEs are more energetic than the ones originating from PEs. This conclusion is based on the speed and acceleration of these CMEs. A detailed investigation needs to be done considering the magnetic field of the source region and the injected flux to the CMEs to further quantify.
- We studied the distribution of acceleration duration of CMEs and found a wide range from 10 minutes to 703 minutes with the peak of the distribution in the range of 100-150 minutes and the mean duration being 153 minutes. We also plotted the true acceleration magnitude versus acceleration duration and found a strong inverse correlation (correlation coefficient -0.88) between them with a power law index of -1.19, implying that stronger acceleration magnitudes have shorter acceleration duration. Further by comparing our result with previous results by [Zhang and Dere \(2006\)](#), [Bein et al. \(2011b\)](#) and [Vršnak et al. \(2007a\)](#), we found that this scaling relation between acceleration magnitude and acceleration duration remains similar in 3-D. Furthermore, we noted that the CMEs from PEs were mostly gradual events with weaker accelerations and longer acceleration duration. We also note that there would be acceleration below COR-1 FOV, and in such cases, the measurement of the acceleration phase would be an under estimate. But including EUV (to capture the acceleration below COR-1 FOV)

will be tricky since we do not know if the structures seen in EUV map to the same WL features. Thus we confined the analysis to WL only. This can be done in future using data from Solar Orbiter (Müller et al. 2013a), PROBA-3 (Renotte et al. 2014a) and ADITYA L1 (Seetha and Megala 2017a; Prasad et al. 2017a), which will observe the inner corona.

- We compared the average values of true speeds and projected speeds in Figure 3.5. The average true speeds showed a wide range from 213 km s^{-1} to 1492 km s^{-1} . We found that for almost all the slow CMEs, the 3D values are higher than the projected 2-D values. However, for the fast CMEs, a large fraction of the CMEs ($\sim 63\%$, (19 out of 30)) showed projected speeds greater than the actual 3D speeds. Thus we see a striking dissimilarity in the comparison of speeds for slow and fast CMEs. These fast CMEs were marked as partial-halo CMEs in the CDAW catalogue. A 3D reconstruction from multi-view points where the CME was non-halo gives the true picture with their true speeds. We also remind here that the method of tracking the CME height is different in our case and the one used in the LASCO images for the catalogue. One of the principal aim of studying CME kinematics is to calculate their arrival times at Earth, and it is clear from here that for the slow CMEs, the projected speeds will give a wrong estimation of the predicted arrival times. These considerations are important for better arrival time predictions with the true 3D speed for halo CMEs and not with the misleading projected speed which for halo CMEs might be the lateral expansion speed instead of the radial propagation speed.

We believe that this study will help us to understand and connect the true width evolution of CMEs in the inner corona, and the presence of impulsive acceleration in the 3D kinematic profiles will provide important inputs to CME ejection models. Comparison of projected and true speeds showed the importance of studying kinematics in 3D. We also point out that extending this work on a larger data set will help in confirming our conclusions. It is also worth noting that the future

solar missions, like ADITYA-L1 ([Seetha and Megala 2017a](#); [Prasad et al. 2017a](#)), PROBA-3 ([Renotte et al. 2014a](#)) and the recently launched Solar Orbiter ([Müller et al. 2013a](#)) have coronagraphs that will be observing the inner corona. This work will provide essential inputs to plan the observing campaigns of these missions and the data from these missions can be incorporated to extract more information on the kinematics of CMEs close to their initiation heights.

Chapter 4

The coupling of 3D kinematics from inner to outer corona and the imprint of source regions

4.1 Introduction

CMEs are large scale eruption of magnetic field and plasma, from the solar corona into the heliosphere ([Webb and Howard 2012a](#)). Their speed ranges from a few hundreds to some thousands of km s^{-1} , and acceleration ranging from few tens to a few 10^4 m s^{-2} (for a review, see [Webb and Howard 2012a](#)). CMEs are also the major drivers of space weather, as they are capable of producing shock waves, interplanetary disturbances, causing huge technological damages ([Gosling 1993b](#)). Thus, they are of interest from both scientific and technological point of views, and hence a good understanding of their kinematics is essential. It is understood

that the kinematics of CMEs are governed by the interplay of three forces, namely the Lorentz force, the gravitational force and the viscous drag force (Wood et al. 1999; Zhang et al. 2001b; Webb and Howard 2012a; Vršnak et al. 2007a). As a result of these forces, CMEs follow a three phase kinematic profile. According to Zhang and Dere (2006), the first, initial phase is a slow rise phase, followed by an impulsive acceleration phase (observed as rapid increase in their velocity) and then the final phase where the CMEs propagate with little or no acceleration. In this regard, the first two phases are usually over in the low coronal heights ($< 3R_{\odot}$) (Temmer et al. 2008; Bein et al. 2011b; Patel et al. 2021a). At later stages of their evolution, CMEs experience drag due to solar wind resulting in the deceleration (Gopalswamy et al. 2000a; Moon et al. 2002; Webb and Howard 2012a). This average solar wind speed reportedly divides the CMEs into slow and fast (Gopalswamy et al. 2000a). So as kinematics of CMEs change from inner to outer corona, averaging of the different kinematic parameters over their entire trajectory might lead to washing away of a lot of crucial information that might hold clue to the coupling of kinematics of CMEs in the inner corona, to the heliosphere.

CMEs are also known to be associated with different source regions, Active Regions (ARs) and Prominence Eruptions (PEs) (Subramanian and Dere 2001; Moon et al. 2002; Majumdar et al. 2020a). CMEs associated with ARs are known to be mostly impulsive whereas the ones associated with PEs are gradual CMEs (MacQueen and Fisher 1983; Sheeley et al. 1999). Apart from their radial propagation, CMEs are also known to exhibit lateral expansion that leads to an increase in their angular width as they propagate outwards (Kay, Opher, and Evans 2015; Cremades, Iglesias, and Merenda 2020a; Majumdar et al. 2020a). In this regard, Zhao et al. (2017) reported on the importance of the angular width of a CME, in determining whether the corresponding interplanetary CME and the preceding shock will reach Earth. Lugaz et al. (2017) reported on the importance of studying the expansion in slow CMEs on their ability to drive shocks. The width

of the CME also sheds light on the source region of the CME it is coming from. Moore, Sterling, and Suess (2007) showed that the strength of the magnetic field of the source region flare arcade producing a CME can be estimated from the final angular width of the CME and the angular width of the flare arcade. So, it is evident that the width of a CME is an essential ingredient in the understanding of their kinematics, and is also an important parameter for the consideration of their space weather impact. Furthermore, since the width largely influences the kinematics of CMEs, it is still not known whether we observe any differences in the angular width distribution of slow and fast CMEs originating from different source regions. It has also been reported that the width distribution of CMEs follow a power law (Yashiro et al. 2006; Robbrecht, Berghmans, and Van der Linden 2009; D’Huys et al. 2014). A study of the statistical distribution of a physical parameter sheds light on the underlying physics of it, and a presence of power law in the distribution of a quantity indicates the presence of Self-Organized Criticality (Bak, Tang, and Wiesenfeld 1987). The presence of power laws, and hence Self-Organized Criticality (SOC) in nature have become evident in the last few years in many different areas and astrophysical phenomena (Aschwanden et al. 2018, and references therein). The presence of power laws in solar astrophysics, in the global energetics of solar flares, has also been reported by Aschwanden (2016). Thus, a study of the distribution of the angular width of CMEs should provide important clues in understanding the physical mechanisms responsible for expanding the CMEs. Recently, Bidhu, Iren, and Benjamin (2017) studied the distribution of width of CMEs during the solar maximum phase of cycle 23 and 24. Meng et al. (2014) studied the distribution of CME width and its comparison with the phase of sunspot number in solar cycle 23. In spite of these studies, whether the slow and fast CMEs follow different width distributions or whether there is any imprint of the source regions on the width distribution of these fast and slow CMEs, is still not properly understood. Thus it is worth looking at the distribution of width, of fast and slow CMEs and also if there is any imprint of the source region of these two dynamical classes on their width distribution.

A major concern in the study of CME kinematics is regarding the measurements that are carried out in the plane of the sky, thus leading to projection effects in the measured quantities (Balmaceda et al. 2018b). A primary step to minimise such projection effects, is to connect the CMEs to their source regions on the disk of the Sun. An even better way to remove the projection effects is to use 3D reconstruction techniques. In this regard, several works based on the tracking of CMEs in 3D have been reported (Thernisien, Howard, and Vourlidas 2006a; Mierla et al. 2008b; Thernisien, Vourlidas, and Howard 2009c; Moran, Davila, and Thompson 2010; Joshi and Srivastava 2011a; Sarkar et al. 2019). A method based on forward modelling to fit the CME flux rope on multi-vantage-point images was also developed assuming the self-similar expansion of CMEs (Thernisien, Howard, and Vourlidas 2006a; Thernisien, Vourlidas, and Howard 2009c), which was termed as the GCS model. Thus a study based on the fitted parameters of the model will be free from projection effects. Recently, Majumdar et al. (2020a) connected 3D profiles of width evolution and acceleration to report on the observational evidence of the imprint of the height of influence of Lorentz force on the 3D kinematics. One of the most significant relevance of these 3D parameters is in the context of arrival time prediction of CMEs. Several models have been developed that takes the average speed of the CME as input to predict their arrival times (for a review see Zhao and Dryer 2014; Riley et al. 2018).

Since the kinematics of the CMEs change as they propagate outwards, it is important to look at the coupling of the kinematics of the CMEs from the inner corona (IC) to the outer corona. As it is already reported several times in the past that quiescent prominences and active regions tend to classify the ejected CMEs from them into two dynamical classes, with the former tending to be gradual CMEs while the later being impulsive CMEs (Sheeley et al. 1999), it is worth looking at the manifestation of this distinction in the behaviour of different kinematic parameters that reflect the kinematics of a CME. In this work, keeping in mind the above existing shortcomings in our understanding of CME kinematics, we try look

into the correlation between different 3D kinematic parameters of the CMEs as they evolve from the inner to the outer corona. With the additional information of the source region of the CMEs, we also look into the imprint of the source regions (if any) on the behaviour of these different 3D kinematic parameters. We study the same 59 events as studied by [Majumdar et al. \(2020a\)](#) and follow the same analysis. In this context, it should be noted that a shock spheroid model is also available as a part of the GCS model (as reported earlier by [Hess and Zhang \(2014\)](#)) for fitting the shock front ahead of the flux-rope. Since we were not interested in the shock dynamics and our aim was focused on the CME kinematics, we used only the flux-rope GCS model in our work. Alike [Majumdar et al. \(2020a\)](#), two vantage point observations are used for fitting the GCS model. It must be noted that provision for the use of a third vantage point in the form of observations from LASCO ([Brueckner et al. 1995b](#)) on-board the SOHO can be used for better constraining parameters like the tilt-angle (see [Thernisien, Vourlidas, and Howard 2009c](#)). Since the aim of this work was to probe the radial kinematics of CMEs, hence the tilt-angle parameter was not used in our analysis, thus reducing the need for the third vantage point. Also, the FOV of LASCO starts well beyond the starting FOV of COR-1, and since we don't want to include Extreme Ultraviolet observations with white light, in order to keep consistency, we did not include LASCO observations for the GCS fitting. In section [4.2](#) we outline the data source used and the working method, followed by our results in section [4.3](#) and we summarize the main conclusions from our work in section [4.4](#)

4.2 Data and Method

4.2.1 Data Source and Data Preparation

We use the data from CDAW catalogue for the analysis presented on the study of width distribution. The CDAW catalog consists of several properties of CMEs based on manual detection (Yashiro et al. 2004b; Gopalswamy et al. 2009e) in SOHO/LASCO images. The data used for the study of 3D kinematics is primarily taken from COR-1 and COR-2 on-board SECCHI package (Howard et al. 2002) of the twin spacecraft STEREO (Kaiser et al. 2008b). Also data from different passbands of AIA on-board SDO (SDO; Lemen et al. 2011) and EIT (Delaboudinière et al. 1995) on-board SOHO were used to identify the source regions of CMEs that were coming from the frontal side of the Sun. For more details on the data source, please refer Majumdar et al. (2020a).

4.2.2 Event Selection for the study of width distribution

We have selected the CMEs from the CDAW catalogue that have occurred during different phases of solar cycle 23 and 24. For the analysis presented in this work, Firstly, the “very poor” CMEs are removed from our analysis sample, as their detection is largely influenced by the observer’s discretion (as reported by Wang and Colaninno (2014)), and thus might bring an unwanted bias to our sample set. It should be noted that some of the “very poor” CMEs may be the real CMEs but we remove them from the analysis because there are large errors in the measurement of the properties of such CMEs. Also, to remove the narrow CMEs, a threshold of 30° is applied on the cataloged width. Yashiro, Michalek, and Gopalswamy (2008) and Gopalswamy et al. (2010) have reported that there exists a discrepancy in the detection of the number of CMEs with width $< 30^\circ$ when both

CACTus and CDAW catalogs were compared. Also [Yashiro et al. \(2003\)](#) studied the statistical properties of narrow CMEs, and reported that they do not form a subset of normal CMEs and have different acceleration mechanism. In addition to the lower threshold, an upper threshold of 180° is also applied, as such CMEs are prone to suffer from large projection effects, which will in turn, affect the measured widths. However, we must also note that CMEs with width between the above two thresholds are also expected to suffer from projection effects. So, to lower down the discrepancy arising from the projection effects, we also consider limb CMEs (whose source regions were found within 30° of the limb) for our analysis. The method for selecting the limb CMEs is vividly discussed in [Gopalswamy et al. \(2014\)](#).

4.2.3 Segregation of CMEs into slow and fast

After shortlisting the CMEs based on the above criteria of selection, we further classify the CMEs as slow and fast, (with respect to the solar wind speed) depending on their projected speeds as recorded in the catalogue. Taking the average solar wind speed as 400 km s^{-1} (see, [Schwenn 2006](#)), CMEs with projected speeds lesser than 300 km s^{-1} are considered slow, while the ones faster than 500 km s^{-1} are considered fast. The CMEs lying in between the above two cut-offs are termed as “intermediate” CMEs. This is because, due to the uncertainty involved with the projected speeds, such CMEs can neither be strictly considered fast nor slow.

4.2.4 Parameter description for the study of coupling of 3D kinematics

To understand the relationship between the different parameters associated with kinematics of the 59 CMEs studied in [Majumdar et al. \(2020b\)](#), as the CME propagates from the inner corona, to the outer corona, we list out the different parameters used in this work in [Table 4.1](#) and define them as follows.

- a_{\max} (V_{\max}) - peak acceleration (velocity) of the CME in the entire (COR-1 and COR-2) FOV
- $V_{a_{\max}}$ - Velocity of the CME at a_{\max}
- V_{lin} - average velocity of the CME from linear fit to the height-time data for the entire FOV
- V_{mi} (a_{mi}) - mean velocity (acceleration) in the IC($< 3 R_{\odot}$) computed by taking the mean of the velocity (acceleration)-time data points obtained from derivatives of the height-time data
- a_{m} (V_{m}) - Overall mean acceleration (velocity) in the entire FOV by computing the mean of the acceleration (velocity)-time data points calculated from derivatives of the height-time data
- a_{const} - constant acceleration in the entire FOV, found from quadratic fit to the height-time data for the entire FOV.
- $h_{a_{\max}}$ ($h_{V_{\max}}$) - height at which peak acceleration (velocity) was attained

Parameters studied	Correl. Coeff. (CC)	Crit. Correl. Coeff. (CCC)	P-values	Empirical relation
(a) a_{\max} v/s V_{\max}	0.63 (overall)	0.25	7.8×10^{-8}	$a_{\max} = 10^{-0.35} V_{\max}^{1.21}$
	0.45 (AP)	0.46	0.053	–
	0.91 (AR)	0.44	4.3×10^{-8}	$a_{\max} = 10^{-2.71} V_{\max}^{1.98}$
	0.41 (PE)	0.44	0.075	–
(b) V_{\max} v/s a_{\max}	0.57 (overall)	0.25	3.2×10^{-6}	$V_{\max} = 10^{1.30} a_{\max}^{0.43}$
	0.42 (AP)	0.46	0.07	–
	0.77 (AR)	0.44	7.4×10^{-5}	$V_{\max} = 10^{1.31} a_{\max}^{0.44}$
	0.57 (PE)	0.44	0.009	–
(c) V_{lin} v/s V_{mi}	0.68 (overall)	0.25	2.6×10^{-9}	$V_{\text{lin}} = 10^{1.51} V_{\text{mi}}^{0.46}$
	0.78 (AP)	0.46	9.8×10^{-5}	–
	0.63 (AR)	0.44	0.003	–
	0.78 (PE)	0.44	5.8×10^{-5}	–
(d) V_{\max} v/s V_{m}	0.73 (overall)	0.25	4.6×10^{-11}	$V_{\max} = 10^{1.05} V_{\text{m}}^{0.72}$
	0.88 (AP)	0.46	5.1×10^{-7}	–
	0.67 (AR)	0.44	0.001	–
	0.66 (PE)	0.44	0.002	–
(e) a_{const} v/s V_{mi}	-0.67 (overall)	-0.25	8.9×10^{-9}	$a_{\text{const}} = 10^{2.74} V_{\text{mi}}^{-0.52}$
	-0.62 (AP)	-0.46	0.006	–
	-0.61 (AR)	-0.44	0.005	–
	-0.30 (PE)	-0.44	0.202	–

TABLE 4.1: Summary of the fitted parameters with the Correlation Coefficients (CCs), Critical Correlation Coefficients (CCCs), p-values and the fitted relations. Note that apart from the overall empirical relation, the same is also shown separately only for the source regions for which the CC is distinctly different and higher than the CC of others. In (a) and (b) the CC for AR is much higher than others. In (c) and (d), the individual CCs are similar, while in (e) the CC for AR and AP are similar to the overall CC, and the CC for PE is much poor.

4.3 Results

4.3.1 Width distribution of slow and fast CMEs

We first study the distribution of widths of the CMEs selected from the CDAW catalogue. In the CDAW catalog, the CME width is generally taken as the maximum angle a CME subtends at the Sun-center, by the time it reaches the LASCO C3 FOV where it is expected that the width will saturate to a fixed value ([Gopalswamy 2004](#)). To investigate the width distribution of CMEs during solar cycle 23 and 24, we fit a power law to it as follows:

$$N(W) = CW^\alpha, \quad (4.1)$$

where α is the power-law exponent, N being the number of CMEs in our sample with width W , and C being the proportionality constant. In [Figure 4.1](#) we plot the histogram (left panel) of the width distribution and the width distribution in log scale (right panel) with the power law fit for all CMEs excluding the "very poor" events as mentioned in the CDAW catalogue. We find an overall power law index of -1.9. In order to understand the goodness of fit we perform the Kolmogorov Smirnov (KS) test where the KS distance (see [Clauset, Rohilla Shalizi, and Newman 2007](#)) is minimum for the distribution which fits the data best with a corresponding high p-value that gives the probability confidence. Here we find the KS distance and p-value as 0.13 and 0.99. It is worth noting from [Figure 4.1](#), that the width distribution is not fitted well by a single power law. This serves as a motivation for us to investigate power laws segregating fast and slow CMEs. Since we aim to understand the width distribution of slow and fast CMEs, we next remove the intermediate events from our study sample, as such events are neither fast nor slow (refer [section 3.2](#)). We again study the width distribution of all events except the "very poor" and the intermediate events ([Figure 4.2](#)). We

find that after removing the intermediate events, we still get the same power law index of -1.9 with the KS distance and p-value to be the almost same. Thus we ensure that there is no bias introduced in the estimation of the power law index of widths distribution by rejecting the intermediate events from our sample. The usual method of graphical fitting (GF) of the data points with a power-law cannot be always considered as the best method of estimating a power-law, especially when the sample set is not large (D’Huys et al. 2016). Thus, the method of maximum likelihood estimate (MLE) is used to fit a power-law. Using MLE, we get the power law index to be -1.6 which again remains the same for CMEs with or without the intermediate events.

Now that we have ensured that the exclusion of the intermediate events does not affect our study, we try to understand now if the slow and fast CMEs follow different power laws in their width distribution.

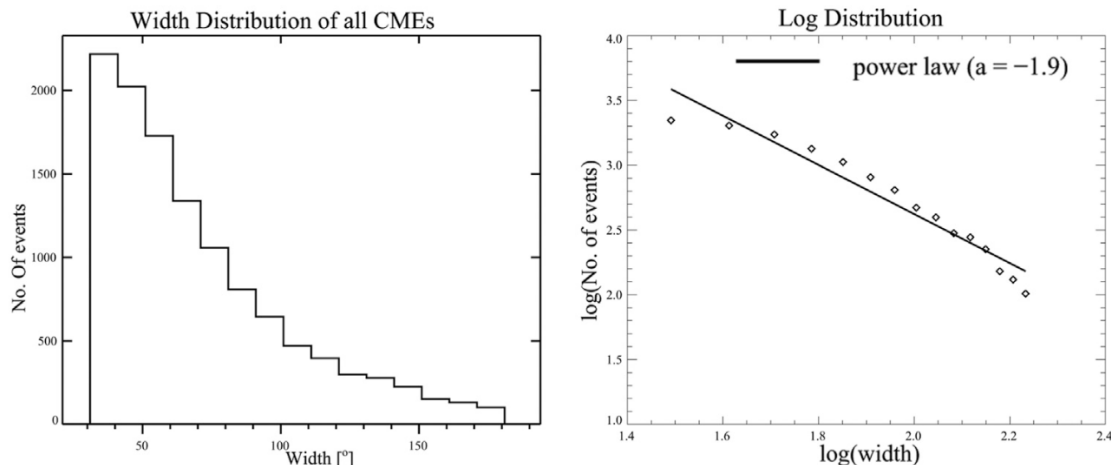


FIGURE 4.1: Width distribution of all CMEs (excluding ”very poor” events) during solar cycle 23 and 24 using the CDAW catalogue. The black line corresponds to a power law fit to the width distribution where α is the power law index.

The entries in Table 4.2 have been computed by taking events from different phases of cycle 23 and 24 as mentioned in Section 2.4. After segregating the source regions, their width distribution is studied separately. Here we use a similar power-law fitting to the width distribution of CMEs coming from the two source regions. We

TABLE 4.2: A summary of the fitted power-laws using GF and MLE for CMEs originating from different source regions.

Source Regions	Total CMEs	Fast CMEs						Slow CMEs									
		Total	W_m	α	W_m	α	MLE	W_d	α_d	Total	W_m	α	W_m	α	MLE	W_d	α_d
ARs	694	291	30	-1.29	30	-1.23	-	-	403	60	-3.20	30	-1.91	60	-3.11		
PEs	281	89	60	-3.43	30	-2.00	60	-3.74	192	60	-3.53	30	-2.08	60	-3.75		

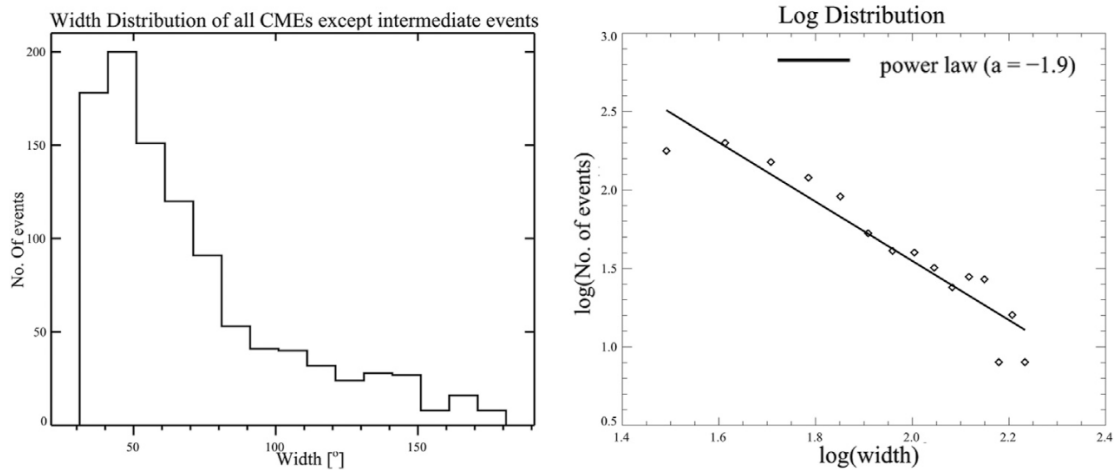


FIGURE 4.2: Width distribution of CMEs (excluding the intermediate and "very poor" events) during solar cycle 23 and 24 using the CDAW catalogue. The black line corresponds to a power law fit to the width distribution where α is the power law index.

do power-law fitting by graphical fitting and also by MLE to estimate power-law indices.

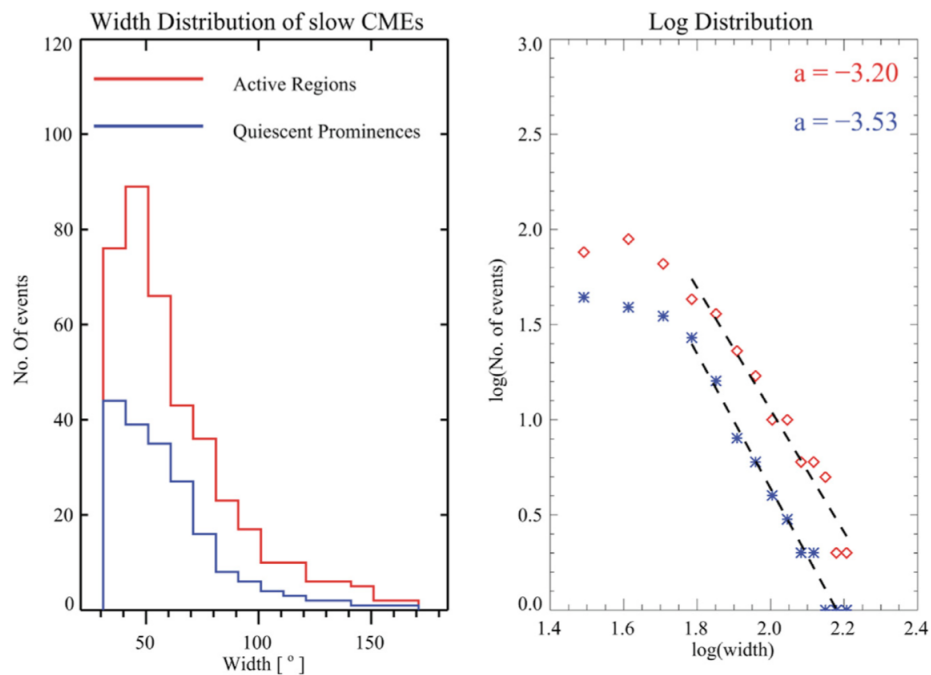


FIGURE 4.3: (Left) Width distribution of slow CMEs from different source regions, with their widths taken from the CDAW catalogue. (Right) power-law fitting of the width distribution. The black line is the power-law fit to the data.

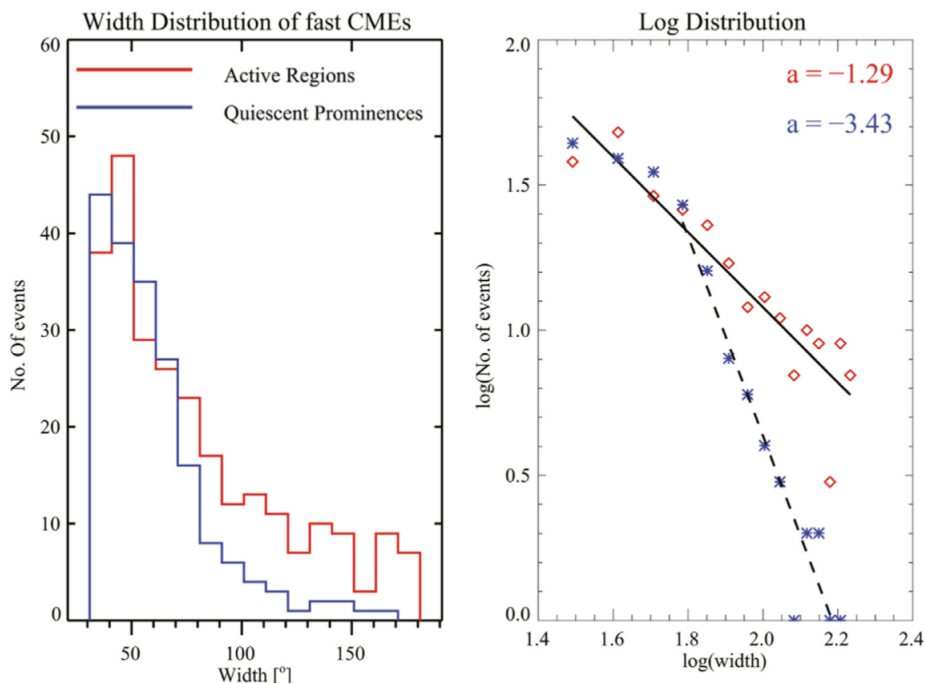


FIGURE 4.4: (Left) Width distribution of fast CMEs from different source regions, with their widths taken from the CDAW catalogue. (Right) power-law fitting of the width distribution. The black line is the power-law fit to the data.

Figures 4.3 and 4.4 show the width distribution of fast and slow CMEs originating from ARs and PEs, and plotted alongside it are the power-law fit (in black). We get α as -1.29 and -3.43 for fast CMEs coming from ARs and PEs with a KS distance of 0.13 (p-value 0.99) and 0.22 (p-value 0.86) respectively. Thus we see different power indices for fast CMEs originating from ARs and PEs. In the case of slow CMEs we get α as -3.20 and -3.53 for CMEs from ARs and PEs with a KS distance of 0.14 (p-value 0.99) and 0.21 (p-value 0.86) respectively. Thus for slow CMEs too the power indices are slightly different for CMEs from ARs and PEs. Again, by using MLE fitting, we get α as -1.23 and -2.00 for fast CMEs coming from ARs and PEs respectively, whereas for slow CMEs we get α as -1.91 and -2.08 for CMEs from ARs and PEs keeping $W_m = 30^\circ$ (refer, table 4.2). The 1-sigma error involved for power-law fitting of width of fast CMEs from ARs and PEs are 0.22 and 0.24 respectively, and that for slow CMEs from ARs and PEs are 0.14 and 0.03 respectively. Table 4.2 clearly depicts that the power-laws followed by slow and fast CMEs coming from ARs and PEs are distinctly different and thus

supports our earlier conjecture.

We note that although the slow CMEs are seen to follow a steeper power-law than the fast ones, the difference in power law indices is more pronounced for the case of CMEs associated with the ARs. Furthermore, CMEs associated with prominence eruptions and slow CMEs have steeper power index than fast CMEs coming from the active regions. The power index of fast CMEs matches with those estimated for flares. Thus it is evident that possibly the mechanism involved in the expansion of the angular width of fast and slow CMEs are different for the CMEs originating from ARs and PEs. We also note that the p-value for the power law fit to the width distribution for CMEs from different sources is lower, and this is due to the lower statistics that we have in each cases.

Thus the fact that slow and fast CMEs from ARs and PEs following different power laws in their width distribution vividly points towards a possibly different mechanism that leads to the width expansion of these CMEs and hence demands a more deeper understanding of the same. It should be noted that a few studies [Zuccarello et al. \(2014\)](#); [Seaton et al. \(2011\)](#); [O’Kane et al. \(2019\)](#) have tried to explore the possible mechanisms of the CMEs but these studies are confined to isolated cases of CMEs. Also, a few statistical studies on large number of CMEs suggested that there may be different classes of CMEs with different driving mechanisms ([St. Cyr et al. 1999b](#); [Subramanian and Dere 2001](#); [Moon et al. 2002](#)).

From Figures [4.3](#) and [4.4](#) we also note that in case of the fast CMEs, effect of change in source region is more pronounced unlike the case for slow events. The limit of the field strength in the source region could be the physical reason for the strength of field in ARs, which in turn determines the available energy to power the eruptions, whereas in case of the CMEs from PEs, the magnetic structure in the periphery of the ejection site controls the chances of ejection and eventually the observed kinematic properties of the ejected material ([Gopalswamy 2017](#)). So,

possibly a different mechanism governs the width expansion of CMEs coming from ARs and PEs, irrespective of them being slow or fast.

4.3.2 The coupling of 3D kinematics

Since we find that the source regions do have a strong imprint on the distribution of CME widths, we now try to study the coupling of 3D kinematics for the CMEs studied in [Majumdar et al. \(2020b\)](#), thereby check if the source regions have an imprint on this kinematic coupling as well. We derived the parameters mentioned in Section 4.2.4 from the velocity and acceleration calculations of the 59 CMEs described in [Majumdar et al. \(2020a\)](#), studied their correlations and established several empirical relations amongst them. In this regard, some of the CMEs studied in [Majumdar et al. \(2020a\)](#) show deceleration very close to the Sun (see Figure 2 of [Majumdar et al. 2020a](#)). It should be noted that we have used coronagraph images with a FOV starting from $1.4 R_{\odot}$ (in the plane of sky) and in some cases the CMEs have already reached $2 R_{\odot}$ (projected height) for the first measurement. According to [Gui et al. \(2011\)](#), the impulsiveness of the CMEs occurs below $1.5 R_{\odot}$. As the above mentioned CMEs are well beyond this height for the initial points of measurement, it is possible to have deceleration at the start of the coronagraph FOV. Further, in this regard, [Sachdeva et al. \(2017\)](#) had reported that for fast CMEs, solar wind drag can act earlier, leading to the deceleration. It should also be noted that the widths mentioned in Table 1 of [Majumdar et al. \(2020a\)](#) is the value of the half-angle parameter measured at a particular instant of time and height (as mentioned in the table), beyond which the parameter experiences further evolution. Further, while comparing the GCS width with the width given in the Coordinated Data Analysis Workshop (CDAW) catalogue ([Gopalswamy et al. 2009d](#)), it must be kept in mind that the complete width of the CME as measured from the GCS model is estimated as $2(\text{half angle} + \sin^{-1}(\text{aspect ratio}))$, while CDAW provides the final projected width, and for halo or partial-halo CMEs, the

projected width becomes an over-estimate. In Table 4.1 of this work, we provide the Pearson's correlation coefficient (CC) and for better appreciation of our results, the Pearson's critical correlation coefficients (CCCs). We also provide the associated p-value which shows the statistical significance of the correlation. The average significance level (α) for the correlations was found to be 0.05 on average, thus correlations with p-values lesser than 0.05 and CCs higher than CCCs implies statistically significant result. In Figure 7.1(a) We plot a_{\max} versus V_{\max} . We find that the two parameters are positively correlated with a CC of 0.63 and can be described by the following relation:

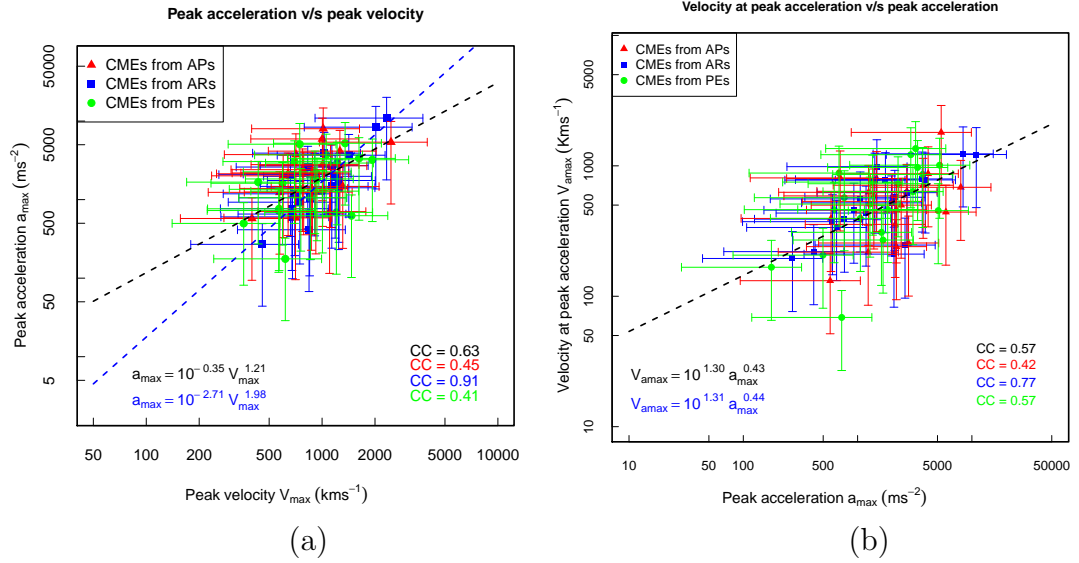


FIGURE 4.5: Plot of (a) a_{\max} versus V_{\max} and (b): V_{amax} versus a_{\max} of all the CMEs. The dashed curves denote the fitted power-law relation. The data points and fitted curves are color coded according to the source regions.

$$a_{\max} = 10^{-0.35} V_{\max}^{1.21}. \quad (4.2)$$

A similar result was also reported by Bein et al. (2011b) but it must be noted that their numbers suffered from projection effects and their numbers were obtained by combining White Light (WL) and Extreme Ultraviolet (EUV) observations which brings in an additional ambiguity of whether the same physical feature is being tracked in EUV and WL (for a discussion, see Song et al. 2019, and references

therein), as the former corresponds to the temperature structure of a CME while the later corresponds to the density structure (Ying et al. 2020). In our work, we do away with both of these limitations, as our measured numbers are in 3D and the measurements are done uniquely in WL. Thus, we find that the power law remains unchanged in 3D. Since we also have the information of the source regions of the CMEs, we further find the correlation between these quantities, separately for CMEs coming from different source regions. From this, we find that a_{\max} and V_{\max} are strongly correlated ($CC = 0.91$) for CMEs coming from ARs, while the ones coming from APs and PEs show weaker correlations of 45% and 41% respectively. This thus indicates at the difference in the CCs for CMEs connected to ARs and CMEs connected to prominences (APs and PEs). We also find that the the two quantities for CMEs from ARs are now related by the relation,

$$a_{\max} = 10^{-2.71} V_{\max}^{1.98}. \quad (4.3)$$

Thus, besides arriving at a similar conclusion in 3D as was reported earlier by Bein et al. (2011b) in 2D, with the aid of the source region information, we now understand that the source regions have a distinct imprint on the correlation between these parameters, and concluding based on just the overall correlation washes away this crucial information. For a better understanding, we also plot in Figure 7.1(b) V_{\max} versus a_{\max} . In this case too we find an overall positive correlation of 0.57. This positive correlation can be described by the relation,

$$V_{\max} = 10^{1.30} a_{\max}^{0.43}. \quad (4.4)$$

A similar behaviour was also reported by Joshi and Srivastava (2011a) based on fewer samples, although no such power law relation (or any CC) was reported by them. Further looking into the CCs for CMEs coming from different sources, we find that the ones coming from ARs show a relatively higher correlation with a CC of 0.77, while it is lesser for those coming from APs and PEs (with CC of 0.42 and 0.57 respectively). Thus once again (in support of our previous result) hinting

towards the fact that possibly the dynamics of the CMEs connected to ARs are different from those which are connected to prominences.

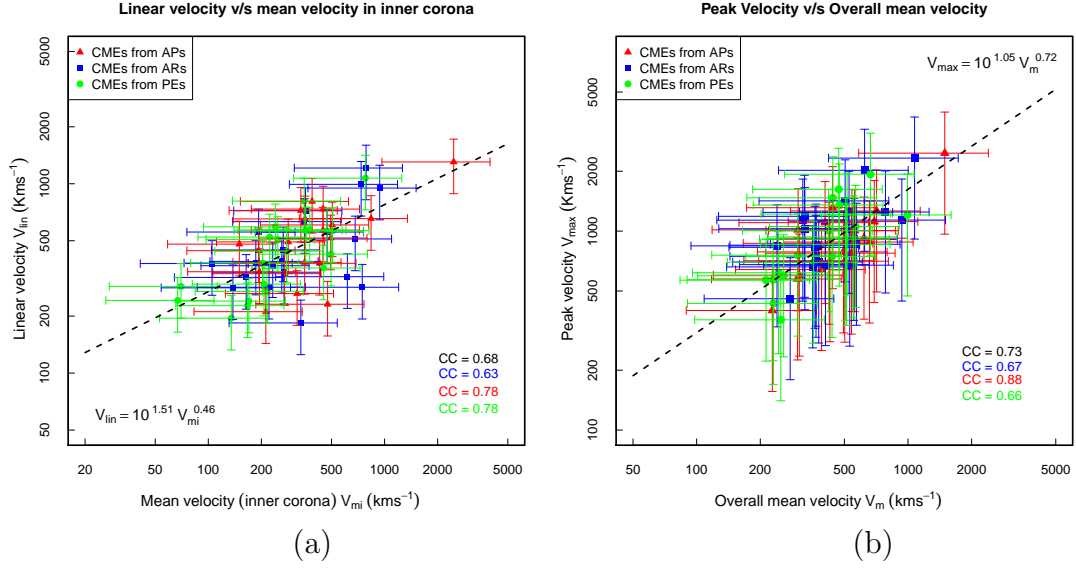


FIGURE 4.6: Plot of (a) V_{lin} and V_{mi} and (b) V_{max} versus V_m . The dashed curves denote the fitted power-law relation. The data points are color coded according to the source regions.

Figure 7.3(a) shows the plot between V_{lin} and V_{mi} . We find a positive correlation between them, with an overall CC of 0.68, and they are related by the relation,

$$V_{lin} = 10^{1.51} V_{mi}^{0.46}. \quad (4.5)$$

The CMEs from ARs have a CC of 0.63, while the CMEs connected to prominence eruptions (that is APs or PEs) have a higher correlation of 0.78. This indirectly indicates that such CMEs connected to erupting prominences, experience a small and gradual acceleration that continues during their propagation in the higher heights, while the ones from ARs are more prone to an initial impulsive acceleration followed by a decelerating or constant velocity profile from thereon. Although this was reported in earlier works (Sheeley et al. 1999; Moon et al. 2002; Webb and Howard 2012a), it is important to note that this result is based on 3D quantities,

and with the relative contribution of different source regions to the overall correlation. Also, from our results we show that similar conclusions (which are well known from previous studies as mentioned above) on the kinematics of gradual and impulsive CMEs can also be obtained from a different perspective by studying the statistical kinematic properties.

Figure 7.3(a) also projects the importance of considering the kinematics in the inner corona, and how the kinematic parameters in the outer corona is influenced by those in the inner corona. Also, several models of CME arrival time predictions, use V_{lin} as input to calculate their arrival times (for a review see [Zhao and Dryer 2014](#); [Riley et al. 2018](#)). An important aspect in this regard is the lead time of forecast, which is the difference in the actual CME arrival time, and the time of submission of the forecast ([Riley et al. 2018](#)). With the help of equation 4.5, the lead time can be minimised, by estimating V_{lin} from V_{mi} , thereby reducing the absolute dependency on outer corona observations for arrival time predictions. Please note that an estimate of the gain in lead time would be possible only with the availability of near-real time data. Apart from that, it will also depend on the telemetry rate of the instruments involved, as that would dictate the accessibility of the near real time data. Having said that, we would also like to emphasize that our result will help in the implementation of inner coronal observations from space missions like ADITYA-L1 ([Seetha and Megala 2017a](#); [Prasad et al. 2017a](#)) and PROBA-3 ([Renotte et al. 2014a](#)) (which do not have outer coronal observations) solely for the purpose of arrival time estimation of CMEs.

In Figure 7.3(b), we plot V_{max} versus V_{m} and find that these two quantities are positively correlated, with an overall CC of 0.73, and they can be related by the relation,

$$V_{\text{max}} = 10^{1.05} V_{\text{m}}^{0.72}. \quad (4.6)$$

This throws light on the kind of acceleration profiles, the CMEs experienced.

The ones experiencing impulsive acceleration also experience a high retardation (see Figure 2 in [Majumdar et al. 2020a](#)) which will largely affect V_m , while the ones experiencing uniform acceleration do not experience such high retardation. Again, looking at the source region contributions, we see that the ones from ARs have a comparatively lower CC of 0.67, and similar value for the ones from PEs, while the CMEs from APs shows a higher CC of 0.88. This thus re-establishes that CMEs connected to ARs are mostly impulsive ones and experience higher deceleration than those connected to APs, which is leading to a lower correlation in the former. A lower correlation in the case of CMEs from PEs again point that they are gradual events where a steady small acceleration prevents the mean velocity to correlate more strongly with the peak velocity (as the later keeps on increasing). It is important to note that this was also pointed out by [Majumdar et al. \(2020a\)](#), and thus we re-affirm those results in a more statistical manner here. The above relation (Equation 6.4) could also be empirically used to estimate one of the quantities when the other is known. For example, if we have IC observations in the future from Aditya-L1/VELC and STEREO/COR-1A, then V_{\max} could be measured in IC from which the mean speed (V_m) could be estimated based on such empirical relation quickly. V_m has further different applications such as in drag based models for CME propagation.

We look into the correlation between a_{const} and V_{mi} in Figure 4.7(a). We find a clear anti-correlation between the two quantities with a CC of -0.67, where the two quantities are related by

$$a_{\text{const}} = 10^{2.74} V_{\text{mi}}^{-0.52}. \quad (4.7)$$

This indicates at the interaction happening between the CME and the solar wind and hence the drag experienced by the former due to the later. It is worthwhile to note that such acceleration velocity anti-correlation has been reported earlier

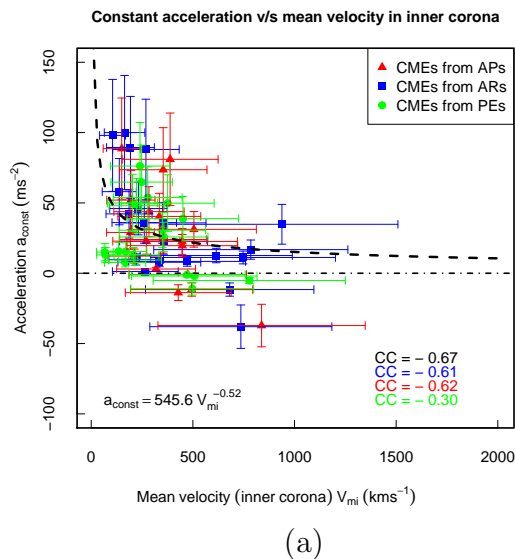


FIGURE 4.7: Plot of (a) a_{const} versus V_{mi} . The dashed curves denote the fitted power-law relation. The data points are color coded according to the source regions.

(see Moon et al. 2002; Vrřnak et al. 2004), but such reports only include results in the outer corona and with projected values of acceleration and velocities (starting with projected height of at least $2 R_{\odot}$). In our work, we report on a similar anti-correlation that exists in the IC as well, and our result is based on 3D acceleration and velocity. This anti-correlation thus shows that the influence of the drag forces comes into play as early as in the inner corona. Further, on looking into the individual source region contributions, we find that the CMEs from ARs have a CC of -0.61, and a similar correlation (-0.62) for CMEs from APs, while this anti-correlation is relatively poor for PEs (-0.30). This distinct difference in the CC for CMEs from PEs and CMEs from active regions (ARs and APs) points to the contrasting acceleration experienced by the CMEs. CMEs with impulsive acceleration are faster, which increases the drag, and hence a higher retardation which is reflected in the higher value of anti-correlation in the case of CMEs connected to ARs. This is not the case for CMEs from PEs which are predominantly gradual events, and hence a weaker anti-correlation reflecting a weaker drag experienced. Thus we again find the importance of the source region information in the study of statistical kinematics of CMEs.

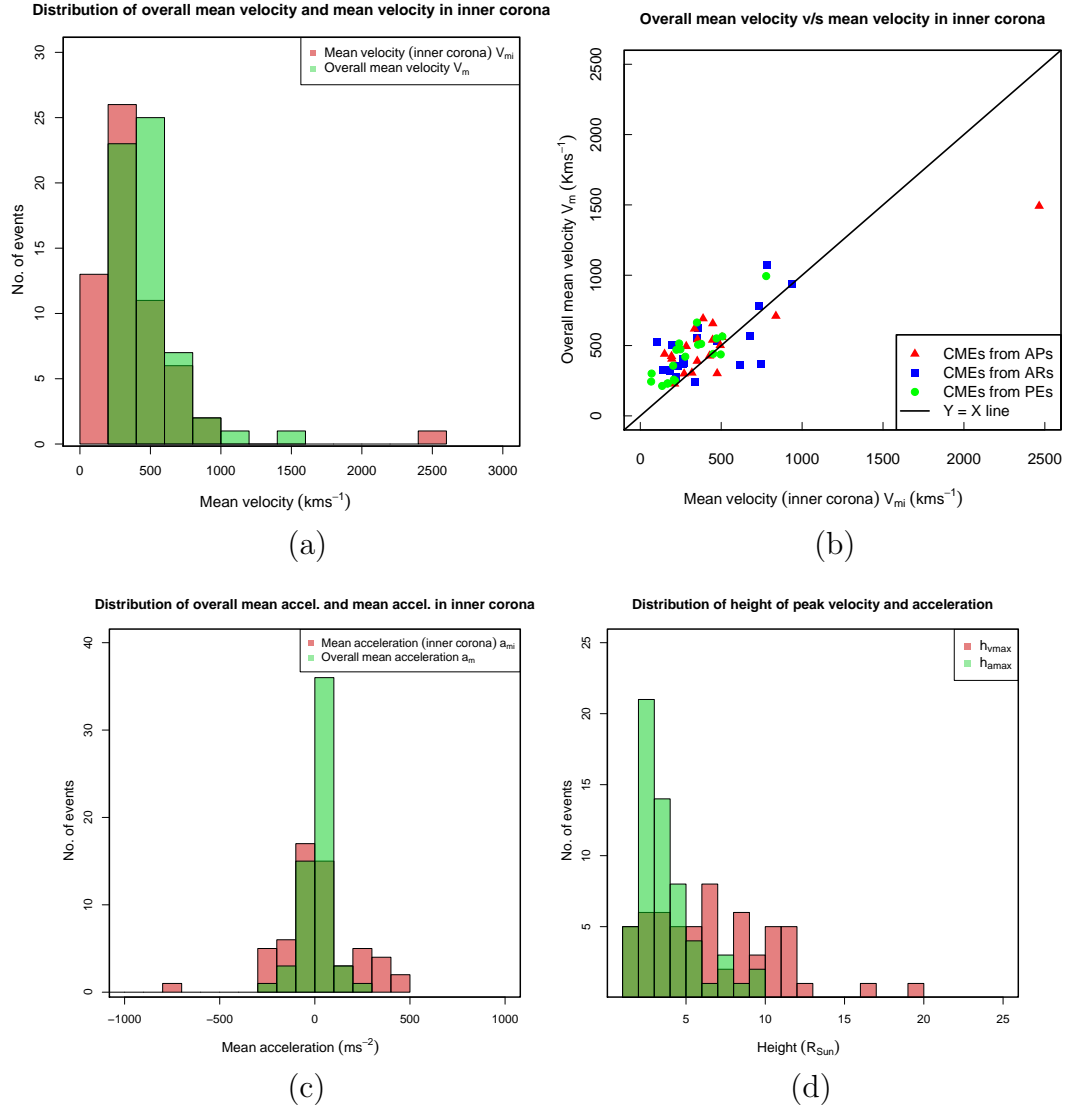


FIGURE 4.8: (a): Distribution of V_{mi} and V_m (b): V_{mi} versus V_m . (c) Distribution of a_{mi} and a_m . (d) Distribution of h_{amax} and h_{vmax} . The data points are color coded according to the source regions.

In Figure 4.8(a) we plot the distribution of V_{mi} and V_m . We find that the distribution of V_m has been shifted towards the right side with respect to the distribution of V_{mi} . Thus, for average quantities, it is important to specify the region where the average has been taken, as we can see that the numbers change from the inner to the outer corona. For a better illustration, in Figure 4.8(b) we plot V_m versus V_{mi} . The solid line represents the boundary where both the quantities are equal. We see that for most of the CMEs, V_m is greater than V_{mi} implying that the

CMEs have gained speed while propagating in the outer corona. We also note that for CMEs which have V_{mi} greater than V_m , most of them are from ARs, thus re-indicating the presence of impulsive accelerations in the lower heights, followed by deceleration later. Also, the CMEs coming from PEs have V_m greater than V_{mi} , thus confirming that they experience gradual acceleration for a longer duration that lead to a steady increase in their velocities as they propagate outwards. So, we note that working with a single average velocity of the CME for its entire trajectory, often masks this important information. Similarly, in Figure 4.8(c) we plot the distribution of a_{mi} and a_m . We find that the distribution of a_{mi} was relatively more spread out around the zero value, thus indicating acceleration and deceleration and hence the wide range of kinematics exhibited by CMEs connected to different source regions, while the distribution of a_m is more narrowed around the zero value with the mode of the distribution lying in the range of 0-100 m s^{-2} . Thus showing that the CMEs experience very little acceleration in their higher heights. For a better understanding, in Figure 4.8(d) we plot the distribution of h_{amax} and h_{vmax} . In support to our former argument on Figure 4.8(c), here too we see that the distribution of h_{amax} is not as spread out as the distribution of h_{vmax} . We also see that the mode of the distribution of h_{amax} lies at 2-3 R_\odot , which is also supported by the results of [Majumdar et al. \(2020a\)](#) on the fact that the impact of Lorentz force on the 3D kinematics of CMEs stays dominant till a height range of 2.5-3 R_\odot . Thus, this result also points to the fact that it is also the Lorentz force that is closely responsible for the CMEs attaining their peak accelerations during their propagation. While looking into the distribution of h_{vmax} , we find that we do not get to see any such clear peak in the distribution, and that it is much more spread out. This is possibly because we have selected events from three different classes, CMEs from ARs which show presence of impulsive acceleration which occur for a short duration and CMEs from PEs which show presence of small gradual accelerations that occur for a longer duration.

4.4 Summary and Conclusions

In this work, we study the width distribution of CMEs that occurred during different phases of solar cycle 23 and 24. The CMEs were then segregated into slow ($\leq 300 \text{ km s}^{-1}$) and fast CMEs ($\geq 500 \text{ km s}^{-1}$) based on the average solar wind speed, and then their width distribution was studied. We further associate the slow and fast CMEs to the source regions they originated from, and classified the identified source regions into two broad categories, ARs and PEs. We investigate if the source regions have any imprint on the width distribution of these slow and fast CMEs. The data from the CDAW catalogue has been used throughout this study. In the following, we conclude our main results from this work. CMEs excluding ‘very poor’ events from the CDAW catalogue tend to follow a power law in their width distribution with a power law index of -1.9 (Figure 4.1). Using MLE, we find the power law index to be -1.6. This power law index remains unchanged on the exclusion of the intermediate events from our sample set (Figure 4.2). Thus the intermediate events do not affect our results and thus we removed them from our sample set, as they cannot be strictly considered either slow or fast. Using GF method, we note that a single power law is unable to explain the observed distribution. We study the width distribution of slow and fast CMEs coming from different source regions (ARs and PEs), and find that the power law indices are different for CMEs coming from ARs and PEs (refer Table 4.2). Furthermore, CMEs coming from PEs tend to follow a steeper power law irrespective of their speeds. Also, we find that slow CMEs tend to follow a steeper power law than fast CMEs, irrespective of the source region they are coming from. This clearly hints towards a possibly different mechanism for width expansion of these CMEs.

We have also studied the behaviour of several 3D kinematic parameters of the 59 CMEs studied by [Majumdar et al. \(2020a\)](#) and we extended their analysis in this work. Several correlations studied between different kinematic parameters showed the importance of considering IC observations in the understanding of

CME kinematics, and how different kinematic parameters in the outer corona are influenced by the parameters in the inner corona. We also found that the overall correlations often washes away crucial information and individual correlations for CMEs from different source regions show the imprint of source regions on the kinematics. In this regard, the change in the power law exponent for the different CCs is not much pronounced which has led to a considerable overlapping of the data points for different source regions. Recently, [Pant et al. \(2021\)](#) reported on the clear influence of the source region on the width distribution of slow and fast CMEs, concluding on the possibility of different physical ejection mechanisms for the CMEs from ARs and PEs. In this work, we thus look into the correlations of several kinematic parameters, and we again find a clear imprint of the source regions (in the form of distinctly different individual CCs) on the overall correlations. Further, we find that while working with average kinematic quantities, it is important to specify the region where the average is taken, as the average values change with the CME propagating from the inner to the outer corona. It should also be noted that even within the inner corona, the average values change, and in this work, we pointed out this, that tagging a single average speed to a CME might not be the best way to comment on its speed and hence we show as an example that the average speed of a CME indeed changes as the CME travels from the inner to the outer corona. It is also worth noting that our results are based on 3D parameters and are hence independent of projection effects. In the following, we conclude our main results,

- A study of a_{\max} and V_{\max} revealed that the two quantities are positively correlated with a CC of 0.63. The CC is significantly higher (0.91) for CMEs from ARs as compared to the ones from APs and PEs. A study of a_{\max} and V_{\max} further showed that despite a moderate overall correlation, the ones coming from ARs show a much higher positive correlation (CC 0.77), indicating that the maximum velocity and accelerations are better correlated for CMEs from ARs.

- We found V_{lin} and v_{mi} to be positively correlated (CC 0.68), and that the former can be estimated from the later through equation 4.5, thus enabling the use of inner coronal observations to CME arrival time predictions with better lead time of forecast. Further a study of V_{max} and v_{m} indicated indirectly at the acceleration experienced by the CMEs from different source regions.
- We also found an anti-correlation between a_{const} and V_{mi} with a CC of -0.67 that shows evidence of the drag experienced by the CME due to interaction with the solar wind. Thus showing that the influence of the drag forces comes into play as early as in the inner corona. While, the CMEs from ARs and APs have similar CCs, for PEs, the correlation is much weaker with a CC of -0.30.
- From Figure 4.8(a) and (b), we found the average velocities change as the CMEs travel from the inner to the outer corona, and that the CMEs from PEs experience weak and gradual accelerations, while the ones from ARs experience impulsive accelerations followed by retardation. This was further supported by Figure 4.8(c) which showed that a_{m} is more confined around the zero value while a_{mi} is relatively more spread about the zero value. Also, we found the distribution of h_{amax} peaks around $2 - 3 R_{\odot}$, which supports the results of [Majumdar et al. \(2020a\)](#) on the fact that the impact of Lorentz force stays dominant in $2.5-3 R_{\odot}$. Thus indicating the role of Lorentz force in propelling the CMEs to their peak accelerations.

A number of upcoming space missions like ADITYA-L1, PROBA-3 and the recently launched Solar Orbiter ([Müller et al. 2013a](#)) will be observing the inner corona, and we believe these results will provide rich inputs to their observation plans. Also, the above correlations correlating the parameters in the IC to the parameters in the outer corona will help in better exploiting the inner coronal observations. Further extending this study over a larger sample size, will help in

better establishing our claims. The results will also provide inputs to models that study CME ejection mechanisms, thus aiding in our present understanding of the same.

Chapter 5

Combined ground and space based stereoscopy : Insights on Volumetric evolution of CMEs

5.1 Introduction

One of the most fascinating and intriguing phenomena occurring in the Sun's corona are the CMEs, which involve large scale release of magnetised plasma outwards into the heliosphere. They are most generally defined as discrete, bright, white-light (WL) features propagating outwards in the FOV of coronagraph ([Hundhausen et al. 1984a](#)). They largely vary in their shapes and appearances, and are known to show a wide range in their kinematic properties (for a review, refer [Webb and Howard 2012b](#)). Apart from that, CMEs are also the major drivers of space weather and the ones travelling towards Earth can have a severe impact on it by

creating geomagnetic storms that can pose a threat to our several technological advancements and life as a whole (Schwenn et al. 2005; Gosling 1993a). This demands better preparation for such a plausible event of chance, and hence as a prerequisite, a very good understanding of their kinematics.

It has been known that CME kinematics is an outcome of the interplay of three forces, namely the Lorentz force, the gravitational force and the viscous drag force, the latter arising due to the interaction with the ambient solar wind (Webb and Howard 2012b). The outcome of this interplay of forces is reflected into a three-phase kinematic profile (Zhang et al. 2001a; Zhang et al. 2004). The initial rise phase is marked by a very weakly accelerated motion (Cheng et al. 2020a), while the later residual phase is seen as propagation with almost constant or decreasing speed (see Gopalswamy et al. 2000b). The main impulsive acceleration phase however, involves a rapid increase in acceleration in a short interval of time, that shoots the CMEs to high velocities (e.g. Bein et al. 2011a; Cheng et al. 2020a; Patel et al. 2021b). Earlier studies have suggested that this main acceleration phase occurs at the lower coronal heights and hence might not be always captured using traditional WL coronagraphic observations (Gallagher, Lawrence, and Dennis 2003; Temmer et al. 2008; Majumdar et al. 2021b). Earlier attempts at measurements of this main acceleration phase have been reported by several studies in the past. In most of these works, the method either relied on measurements on the plane of the sky, thus introducing discrepancies due to projection effects (e.g. St. Cyr et al. 1999b; Zhang and Dere 2006; Balmaceda et al. 2018a), or involve combining WL with Extreme Ultraviolet (EUV) data for tracking a CME (e.g. Vršnak et al. 2007b; Bein et al. 2011a), where whether the same features are observed in emission lines and in WL are still debatable (see Song et al. 2019). Now, although we do have now an understanding of the impact of drag force on the kinematics (Sachdeva et al. 2015, and references therein), the impact of Lorentz force still eludes a clear understanding. Recently Majumdar et al. (2020b) used the GCS

model (developed by [Thernisien, Howard, and Vourlidas 2006b](#); [Thernisien, Vourlidas, and Howard 2009a](#); [Thernisien 2011b](#)) to study the 3D evolution of CMEs in the inner and outer corona, and reported that the true height till which the imprint of Lorentz force remains dominant lies in the range $2.5 - 3 R_{\odot}$, thus further indicating the importance of inner corona (IC) observations.

CMEs, apart from radial propagation, also show lateral expansion of their angular width (see [Kay, Opher, and Evans 2015](#)) until a certain critical height, after which they propagate with almost constant width (e.g. [Moore, Sterling, and Suess 2007](#); [Zhao et al. 2010](#)). The usual method of width estimation involves the projected angular span between the position angles of the two extreme flanks of the CME ([Zhao et al. 2010](#)), but such estimation suffers from a lot of projection effects. In this regard, [Cremades, Iglesias, and Merenda \(2020b\)](#) used the GCS model to study the axial and lateral width expansion of CMEs by combining WL and EUV observations. Also, [Majumdar et al. \(2020b\)](#), using the GCS model, reported on the observational evidence that the angular width expansion and the impulsive accelerations are just manifestations of the same Lorentz force, as conjectured earlier by [Subramanian et al. \(2014\)](#); [Suryanarayana \(2019b\)](#). In this regard, it was further reported that the evolution and width expansion of CMEs is non self-similar in the IC ([Cremades, Iglesias, and Merenda 2020b](#)), while it is self-similar in the outer corona ([Subramanian et al. 2014](#)). It is also worth noting that the distribution of angular widths of slow and fast CMEs from different source regions have been known to follow different power law profiles, thus indicating the possibility of different generation mechanisms (as reported recently by [Pant et al. 2021](#)). Thus, a study of the evolution of CME volume (which is influenced by the width expansion of CMEs) would shed more light on this aspect of CME evolution. In this regard, [Holzknecht et al. \(2018\)](#) used the GCS model to estimate the volume of a CME. Later this treatment was also used by [Temmer et al. \(2021\)](#) to study the density evolution of CMEs with distance from the Sun, but both these works reported on results in the outer corona and the heliosphere, and thus

we do not have a good understanding on how the total volume evolve in the inner corona.

A major challenge in the understanding of early CME kinematics in the IC has been due to limited observational WL data below $3 R_{\odot}$ and projection effects. Several techniques have been developed to address the later issue (see [Mierla et al. 2008a](#); [Thernisien, Vourlidas, and Howard 2009a](#); [Joshi and Srivastava 2011b](#); [Hutton and Morgan 2017b](#)), but the implementation of such techniques to IC has been limited. To address these shortcomings, we extend the implementation of the GCS model to the IC observations from the ground-based coronagraph K-Cor of the MLSO which offers a FOV of $1.05 - 3 R_{\odot}$. This will enable us to capture the initial impulsive phase of the CMEs uniquely in white light observations. Using this extended GCS model, we thus study the early 3D evolution of 5 CMEs by studying their kinematic profiles, widths and volume evolution as they propagate from the IC to the outer corona. We outline the data source and working method in Section 5.2, followed by our results in Section 5.3, and we present our main conclusions and discussions in Section 5.4.

5.2 Data and Method

5.2.1 Data Source and Data Preparation

The data used in this work are taken from coronagraphs COR-1 (FOV of $1.5-4 R_{\odot}$), COR-2 (FOV of $2.5-15 R_{\odot}$) and Extreme UltraViolet Imager (EUVI) of the SECCHI package ([Howard et al. 2002](#)) on-board the twin spacecraft STEREO ([Kaiser et al. 2008a](#)), the K-Cor (DOI: 10.5065/D69G5JV8) ground based coronagraph (FOV of $1.05-3 R_{\odot}$) of the MLSO and the data from LASCO ([Brueckner et al. 1995a](#)) (FOV of $2.2-30 R_{\odot}$). Level 0.5 data of EUVI, COR-1 and COR-2

was reduced to Level 1.0 using the *secchi_prep.pro* routine in IDL. For the K-Cor data, we used the 2 min cadence Level 2.0 data processed through the Normalized Radially Graded Filter (NRGF; Morgan, Habbal, and Woo 2006; Morgan, Byrne, and Habbal 2012), and for LASCO, we used level 1 data (corrected for instrumental effects, solar North and calibrated to physical units of brightness). Finally, base difference images were created for K-Cor, COR-1, COR-2 and LASCO by subtracting a pre-event image from successive images of the event thereafter.

5.2.2 Event Selection

Since this work involves combining data from the COR-1, COR-2 coronagraphs on STEREO, LASCO coronagraphs (FOV of 1.5–4 R_{\odot}) on SOHO and K-Cor of MLSO, only those events could be selected which were simultaneously observed by these instruments. It is worth noting here that K-Cor and LASCO are not simultaneously used by the GCS model, but rather LASCO is replaced by K-Cor for the lower coronal heights. Now, K-Cor being a ground-based coronagraph, only the day time observations are available (approximately 17:30 UT to 02:30 UT), and this largely restricted the event selection. Also, those CMEs were selected which had a distinct leading edge in the FOV of the above coronagraphs, thus assuring unambiguous tracking in the successive frames. Since K-Cor views the solar corona through the Earth's atmosphere, the data is affected by weather conditions. Also, the identified CMEs tend to be fainter in K-Cor as compared to COR-1, thus rendering tracking more challenging. This can be due to the bright sky background leading to a low signal or due to the fact that CMEs tend to gather mass at these low heights (Thompson et al. 2017). Based on the above criteria, 5 CMEs were selected from the K-Cor catalogue that occurred between 2014 February and 2016 January.

5.2.3 The GCS fitting to STEREO and K-Cor data

The GCS model was developed to fit a synthetic flux-rope to a pair of coronagraph images taken from the two different vantage points offered by the positions of STEREO-A/B. A provision is also made for including observations from the LASCO coronagraphs as a third vantage point. To study how the CMEs evolve from inner corona, in this work, we first extended the model further to include observations of the IC from K-Cor of MLSO as a third vantage point (in the Sun-Earth line), as the FOV of K-Cor will largely aid in understanding the early evolution of CMEs. Since the header structure of K-Cor data is different than that of LASCO, the primary codes that generate the synthetic flux-rope, namely *rtscgcloud.pro* and *rtcloud.pro* needed to be modified. Hence a similar block of code (as was present for LASCO) was developed for the K-Cor observations by introducing relevant keywords for K-Cor data corresponding to the keywords for LASCO data to the above procedures. This was added with a condition that simultaneously, either K-Cor or LASCO observations are to be present along with the STEREO observations. Thanks to the overlapping FOVs, K-Cor observations were combined with COR-1, and LASCO with COR-2 observations, thus ensuring a three vantage point tracking throughout. The novelty of this work also lies in the fact that despite the unavailability of STEREO-B observations after 2016, we can still perform stereoscopy in the IC by combining data from COR-1A and K-Cor with the help of this extended GCS model. In the following steps we outline the procedure of fitting carried out in this work:

Step 1 – A pair of COR-1 images and a K-Cor image (taken at almost the same time) are selected where the CME front is well developed in all three images.

Step 2 – The fitting procedure is then followed as outlined in [Thernisien, Vourlidas, and Howard \(2009a\)](#); [Majumdar et al. \(2020b\)](#).

Step 2 – The above two steps are repeated for the successive images in which the CME front was well developed in both the K-Cor and COR-1 FOVs.

Step 3 – Since the time of appearance of CME in K-Cor FOV might be different than the same in COR-1 FOV, a K-Cor image is then selected for which the CME front is first observed. Since 3 vantage point observations are not available for this height, some of the model parameters are fixed, while the height, half-angle and aspect-ratio are re-adjusted as the model is fitted to the K-Cor images.

Step 4 – Finally, the model is fitted to LASCO and the pair of COR-2 images to capture the evolution in the outer corona. The uncertainty in fitting is determined in a similar way as mentioned in [Thernisien, Vourlidas, and Howard \(2009a\)](#); [Majumdar et al. \(2020b\)](#).

Examples of the GCS fitting to K-Cor and COR-1 images are shown in Figure 5.1 and a summary of the fitted parameters are given in Table 5.1. Panels (g) and (h) of Figure 5.1 further reflect the significance of this extended GCS model, for the study of 3D kinematics in inner corona, despite the unavailability of COR-1B data.

Date	Time (UT)	Long. (ϕ) (deg)	Lat. (θ) (deg)	T. angle (γ) (deg)	Height (h) (R_{\odot})	A. ratio (k)	H. angle (α) (deg)
2014-02-12	22:40:00	102	-10	-45	2.79	0.16	24
2014-06-14	19:45:00	84	-13	64	2.29	0.14	23
2014-06-26	22:15:00	290	29	-68	2.86	0.36	13
2014-04-29	20:45:00	142	-39	-81	2.29	0.16	13
2016-01-01	23:20:00	330	-22	83	2.47	0.22	22

TABLE 5.1: The GCS model parameters fitted to the CMEs are tabulated. The Time is the time of observation, ϕ , and θ are the longitude and latitude of the CME, the tilt-angle (γ) is the angle between the axis of symmetry of the CME and the solar equator, h is the height of the leading front, aspect-ratio (k) is the ratio of the minor to the major CME radius and α is the half-angle between the legs of the CME.

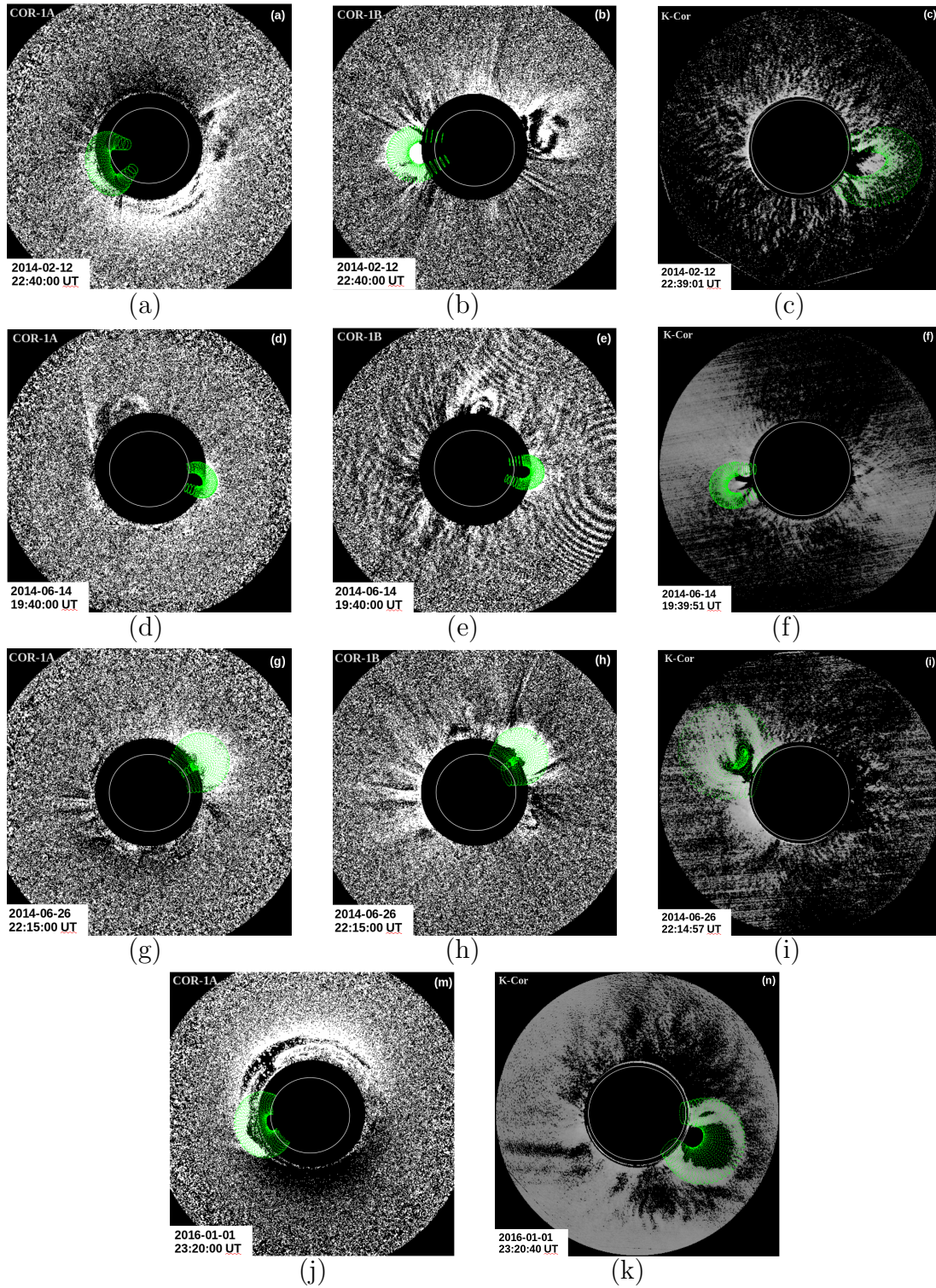


FIGURE 5.1: The fitting of the GCS flux-rope to K-Cor and the pair of COR-1 images for the 5 CMEs studied in this work.

5.3 Results

5.3.1 Improvement in the understanding of early CME kinematics

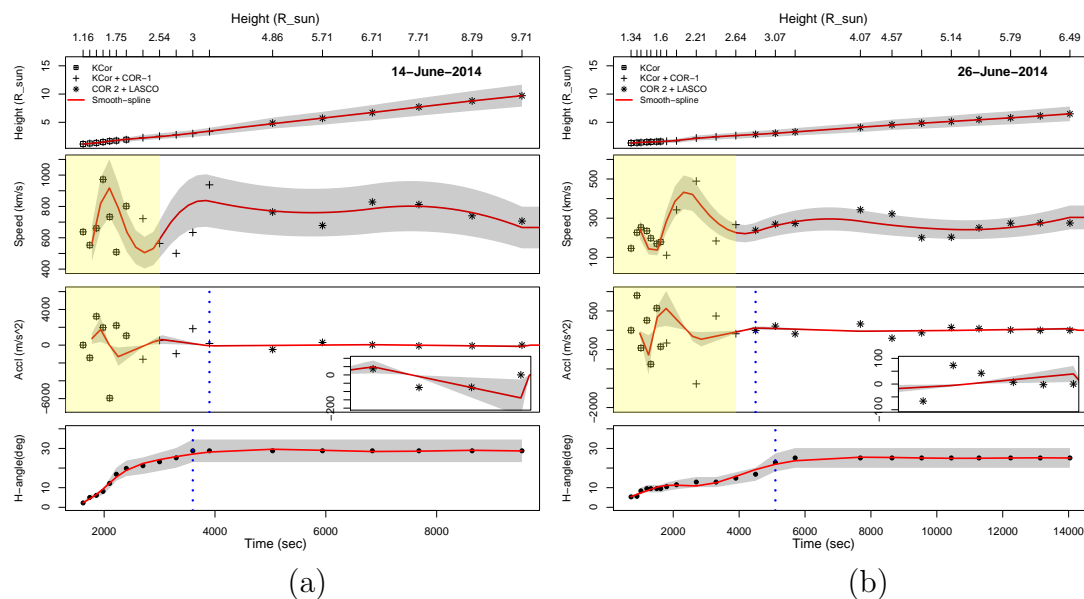


FIGURE 5.2: The complete 3D kinematic profiles of two out of five impulsive CMEs are shown as representative examples. The height–time data is fitted with a cubic smooth spline (shown in solid red line). The speed and acceleration plots are obtained by taking first and second order numerical derivatives of the height–time plot. The grey shaded region corresponds to the uncertainty in the fitted model parameters. The impulsive phase is highlighted in the second and third panels in yellow. An inset with a zoom into the residual acceleration phase is provided in the bottom right hand corner of the acceleration plots. Please note that the time axis of the zoomed insets is overlapped with the common time axis shown at the bottom. In the bottom, the evolution of the half–angle (α) parameter is plotted.

It should be noted here that although while selecting the events, no such pre-selection criteria was kept on the CMEs to be impulsive, yet it turned out that all the five CMEs studied, showed the impulsive phase. In Figure 5.2(a) and (b), we plot the 3D kinematic profiles of the CMEs that occurred on June 14, 2014, and June 26, 2014. On the top we plot the height–time data fitted with a cubic smooth spline (in red), followed by the speed and acceleration profiles (derived by

taking the first and second order numerical derivatives of the height-time data) in the second and third panels. The overall fitting procedure and the estimation of speed and acceleration is the same as reported in [Majumdar et al. \(2020b\)](#). It should be noted here that the average uncertainty in the fitting of the GCS model was found to be 20 percent, and we did not find any appreciable change in latitude/longitude of these events beyond their uncertainties. However, it is worthwhile to note that a change in latitude/longitude will influence the height measurements, and hence for events which show considerable deflections, these considerations should be taken into account in future for an even better estimate of the uncertainty region in the absolute lower heights in the height-time profiles. We also plot the variation of the half-angle parameter (α) in the bottom panel. In the third panel, an inset with a zoomed in plot of the residual acceleration phase is also provided in the right hand bottom corner. Please note that the time axis of the zoomed insets is overlapped with the common time axis shown at the bottom. We find that with the aid of the observations from K-Cor, it was possible to capture the initial impulsive acceleration phase of the CMEs uniquely in the WL data, thus escaping the need for combining EUV observations with WL observations for capturing the same, as was reported earlier in [Bein et al. \(2011a\)](#) (while the initial gradual rise phase seems to have been already got over by the time the CMEs reached the K-Cor FOV). It is worthwhile to point out that this was not possible in [Majumdar et al. \(2020b\)](#); [Cremades, Iglesias, and Merenda \(2020b\)](#), as for a number of events, the impulsive acceleration phase was already over by the time the CME entered the COR-1 FOV, leading to an underestimate of the true acceleration, magnitude and duration. Please note that in [Figure 5.2](#), we show the kinematic profiles as representative examples of the two of the five impulsive CMEs studied, so as to demonstrate the capturing of the impulsive phase by only using white light observations. Further, as K-Cor offers better cadence than COR-1 (in our case, we have used 2 minutes cadence data), it helps in better tracking of the CME in the lower heights. Nonetheless, it must be noted that during the tracking of CME in the K-Cor and COR-1 overlapping FOV, the fitted times will be limited

by the cadence of COR-1. In this regard, we would like to point out that although K-Cor data offers a better cadence of fifteen seconds, the CME front in them was fainter and tracking it was difficult. It should also be noted that, sometimes the leading edge in the K-Cor image gets diluted in the higher heights of its FOV. Now, although, this would introduce an uncertainty in the measured height, yet it's worth noting that the application of the GCS model leads to the tracking of a certain front of the CME (in this case the leading front) and not a certain point on the leading front. Thus, in such cases, the other view points from COR-1, where the CME leading front is better visible helps in tracking the CME through those heights, while we use K-Cor observations to track the CME in lower heights (as mentioned in Section 5.2.3), where the leading front is better visible. The blue vertical dotted lines in the acceleration and half-angle evolution plots denote the time (and height) at which the impulsive acceleration ceases and the half-angle becomes constant respectively. For the events studied, these heights happen to lie in the range of 2.5–3 R_{\odot} (consistent with Cremades, Iglesias, and Merenda 2020b; Majumdar et al. 2020b).

5.3.2 Insights on width expansion of CMEs

Use of three vantage point observations helped in better constraining the GCS parameters (nevertheless it should be noted that for the CME in 2016, only two vantage points were available, and for the heights below COR-1 FOV, only K-Cor observations are used). Multiple vantage point observations have shown that the width of a CME can be seen in two broad perspectives. CMEs tend to expand along the direction of their main axis giving their axial width, and in the direction perpendicular to it giving their lateral width (Cabello et al. 2016b) which corresponds to the face-on (FO) and edge-on (EO) CME widths as presented in Thernisien, Vourlidas, and Howard (2009a). Thus, instead of just studying the evolution of the half-angle parameter as a proxy of studying the width expansion,

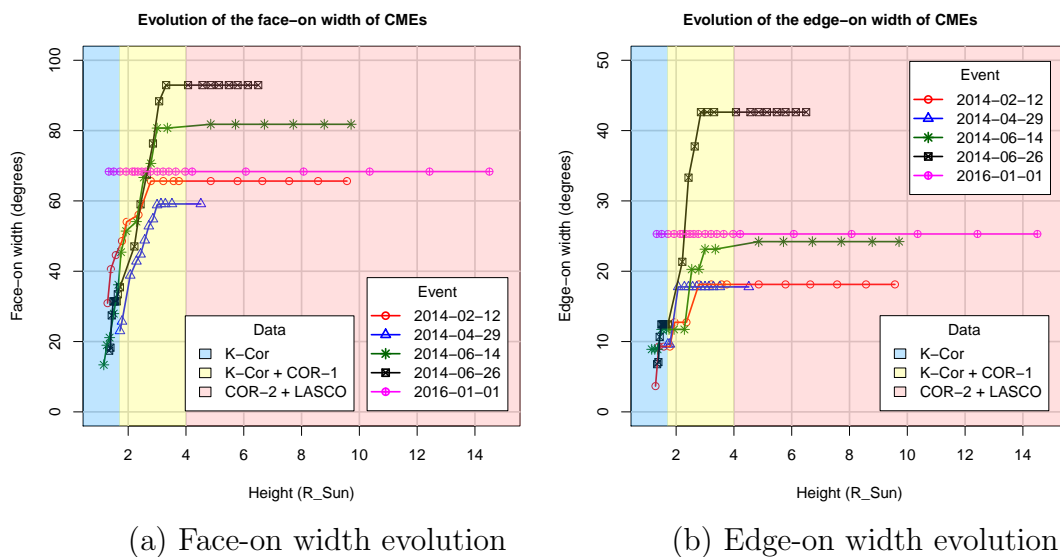


FIGURE 5.3: The evolution of the modelled (a) face-on and (b) edge-on width of CMEs in the inner corona. Different regions of the plot are highlighted according to the data used.

we use the half-angle (α) and the aspect-ratio (k) to calculate the FO and EO widths of the CMEs studied. This was possible once the GCS parameters for the CMEs were fixed by the three above-mentioned vantage points which were back-traced in the K-Cor FOV to heights of $\approx 1.1 R_{\odot}$. From Table 1 of [Thernisien \(2011b\)](#), the FO width (f_w) is related as,

$$f_w = 2(\alpha + \sin^{-1}k) \quad (5.1)$$

and the EO width (e_w) is related as,

$$e_w = 2 \sin^{-1}k. \quad (5.2)$$

In Figure 5.3(a) and (b) we plot the variation of the FO and EO widths of the CMEs with height. We find that initially, until $3 R_{\odot}$, both the FO and EO widths increase rapidly with height and then saturates, thus implying that in these lower heights, CMEs expand rapidly in both the axial and lateral directions. A similar behaviour was also reported by Cremades, Iglesias, and Merenda (2020b), but it should be noted that they combined EUV and WL observations to arrive at this conclusion, while our conclusions are based on using only WL data uniquely. In this context, it is worthwhile to note that despite fitting the GCS model to three vantage point observations, the estimation of half-angle and aspect-ratio can still have considerable uncertainties. One way to reduce such uncertainty is to use observations from instruments that are placed away from the ecliptic, as reported by Thernisien, Vourlidas, and Howard (2009a). So, in future, observations from the METIS (Fineschi et al. 2012) on-board the Solar Orbiter (Müller et al. 2013b) can be used to reach more precise estimation of these parameters. For the five CMEs, we found that the face-on width starts in the range of $10\text{-}30^{\circ}$ which expands and becomes constant at $60\text{-}90^{\circ}$. It should be noted that this was not possible in Majumdar et al. (2020b), since only two vantage point observations were used (which is also the case for the fifth event in Table 5.1 in this work), which often leads to a degeneracy in the α and γ parameters (as reported in Majumdar et al. (2020b); Thernisien, Vourlidas, and Howard (2009a)). Thus showing the importance of studying the true width of a CME, rather than the projected width, as the later is highly dependent on the observer's line of sight (LOS). It must be noted that many of the earlier studies have ignored LOS effects in the CME width, and hence statistical studies on the width distribution (such as Pant et al. 2021, and references therein) can suffer from these projection effects.

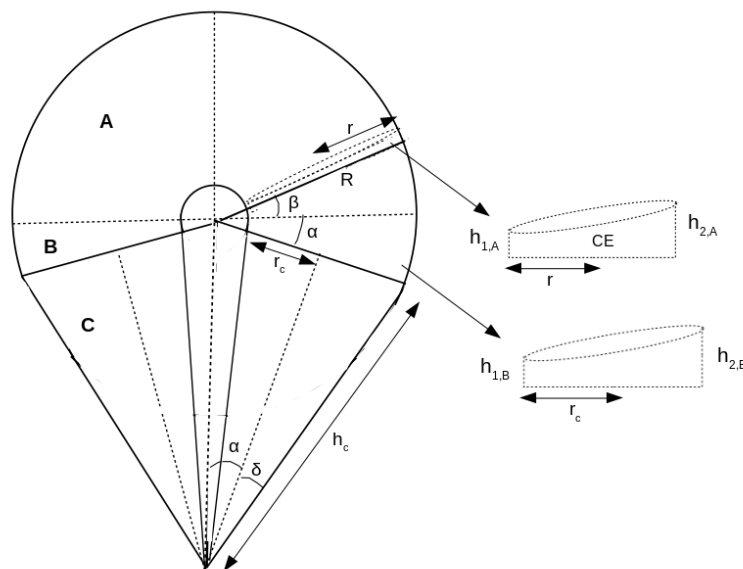


FIGURE 5.4: A schematic for the estimation of CME volume from the GCS reconstructed 3D flux-rope structure. The entire CME volume can be subdivided into three parts, A: the ellipsoidal front, B: the asymmetric middle disc and C: the conical legs. The figure is adapted from [Holzknecht et al. \(2018\)](#).

5.3.3 Evolution of modelled CME volume

As reported by [Holzknecht et al. \(2018\)](#), the volume of a CME can be estimated from the GCS model, and it can be considered to be comprised of three parts, an ellipsoidal leading front (A in Figure 5.4), a middle asymmetric disc (B in Figure 5.4) and the conical legs (C in Figure 5.4). It should be noted here that all mathematical expressions are based on the work of [Holzknecht et al. \(2018\)](#). In order to calculate the volume of part A (V_A), it is assumed that the ellipsoidal front is made of very thin asymmetric cylindrical elements (CE in Figure 5.4). Now, the entire volume of A is covered with the angle β (see Figure 5.4) ranging from 0° to 90° . So, we divide β into small fractions γ , and thus each CE consists of a constant γ ,

$$\gamma = \beta/n \quad (5.3)$$

where n is the number of thin CEs. It should be noted that each of these cylindrical elements (CEs) have two different heights $h_{1,A}$ and $h_{2,A}$ where the second height is greater than the first height (see Figure 5.4 right panel). These heights are as follows :

$$h_{2,A} = R \tan(\gamma) \quad (5.4)$$

and,

$$h_{1,A} = (R - 2r) \tan(\gamma) \quad (5.5)$$

Using these, the volume of each of these thin elements can be estimated as,

$$V_{CE} = \pi r^2 \left(\frac{h_{1,A} + h_{2,A}}{2} \right) = \pi r^2 (R - r) \tan(\gamma) \quad (5.6)$$

So, summing over all these elements, V_A is calculated as follows :

$$V_A = \sum_{\gamma} \pi r^2 (R - r) \tan(\gamma) \quad (5.7)$$

Similarly, volume of part B (V_B) is calculated for a cylinder with different heights $h_{1,B}$ and $h_{2,B}$. From Figure 5.4, let

$$r|_{\beta=0} = r_0 \quad (5.8)$$

and,

$$R|_{\beta=0} = R_0 \quad (5.9)$$

With these, we get the two heights of the cylinder as,

$$h_{2,B} = R_0 \sin(\alpha) \quad (5.10)$$

and,

$$h_{1,B} = (R_0 - 2r_0) \sin(\alpha) \quad (5.11)$$

which gives the volume as

$$V_B = \pi r_c^2 \left(\frac{h_{1,B} + h_{2,B}}{2} \right) = \pi r_c^2 (R_0 - r_0) \sin(\alpha) \quad (5.12)$$

where, r_c from Figure 5.4 and from [Thernisien \(2011b\)](#) is

$$r_c = h_c \sin(\delta) = kh_c \quad (5.13)$$

where h_c is the length of the conical legs. Finally, for the third part (C), which are the legs of the CME, it is simply the volume of the cone, which is the following:

$$V_C = \frac{1}{3} \pi r_c^2 h_c \quad (5.14)$$

where, h_c from [Thernisien, Vourlidas, and Howard \(2009a\)](#); [Thernisien \(2011b\)](#) is related to the GCS parameters as:

$$h_{\text{front}} = h_c \frac{1}{1-k} \frac{1 + \sin(\alpha)}{\cos(\alpha)} \quad (5.15)$$

Now, R and r are a function of the GCS model parameters k (aspect-ratio), h (height) and α (half-angle) and can be found from [Thernisien \(2011b\)](#). Since the model is axisymmetric, the total volume will thus be:

$$V_T = 2(V_A + V_B + V_C) \quad (5.16)$$

Thus using the above three GCS model parameters, the modelled volume of the CME can be studied. A study of the GCS volume evolution was reported earlier by [Holzknecht et al. \(2018\)](#), but they studied the volume evolution in the greater heights (15 - 215 R_\odot). [Temmer et al. \(2021\)](#) also used the GCS volume to study the CME density evolution with height in the outer corona (in the height range 15 - 30 R_\odot). But, in these studies, the crucial information of the volume evolution in the IC was missing. It should be noted that although CMEs are known to evolve self-similarly in the outer corona (see [Subramanian et al. 2014](#)), yet in the inner corona, their propagation is non self-similar (refer [Cremades, Iglesias, and Merenda 2020b](#); [Majumdar et al. 2020b](#)). Thus, an understanding of the evolution of modelled

CME volume in the IC demands our attention. In this regard, although [Temmer et al. \(2021\)](#) used the GCS volume to estimate the densities of the magnetic ejecta and the sheath regions, yet an understanding of the volume evolution of the CME leading front and the CME legs have somehow evaded our understanding. With the incorporation of K-Cor observations with COR-1 for GCS reconstruction, we now address these limitations in our understanding of CME volume evolution. Thus, we study the evolution of modelled volume of the CMEs in 3D in the inner and outer corona, separately for the different sections of the CME volume (A - the ellipsoidal front, B - the asymmetric disc and C - the conical legs as shown in [Figure 5.4](#)).

In [Figure 5.5](#), we plot the modelled total volume (V_T in black) evolution of the five CMEs with the distance from the Sun in (a), (b), (c), (d) and (e). We then fit a power law that reflects the dependence of CME volume on the distance from the Sun, as the CME propagates outwards. This is the first time that any power law relation is reported for the evolution of modelled CME volume with height. Also since we have the volume estimated separately for the ellipsoidal front, the middle asymmetric disc and the conical legs of the CME, we study the evolution of these volumes as well and fit a power law to them for a better understanding. For instance, it is in the IC where the CME starts forming, and thus studying the volume evolution of different parts of CMEs will enlighten us on the fact that whether CMEs retain their shape as they propagate from the IC to the outer corona. Further, a study of the associated power law profiles will help us understand the scale free behaviour of the volume expansion of CMEs with height. In other words, a single power law for all the different parts of the CME volume would imply a single unified mechanism that drives the volume expansion of CMEs, while different power laws would imply a differential volume expansion, and hence the possibility of different driving mechanisms. In addition to that, if the mechanism of acceleration and expansion of CME (that in turn affects the volume) is the same in inner and outer corona, then a single power law should be

followed by the volume evolution profile in the inner and outer corona. However, if the power laws are different in the inner and outer corona, then that would imply that probably the mechanism of increase in volume might be different in inner and outer corona (as an outcome of the Lorentz force in IC and pressure difference in outer corona). Thus all these possibilities motivated us to probe the evolution of modelled CME volume in the inner and outer corona.

Date	Volume Segment	Empirical Relation	R ² Values	P - Values
2014-02-12	Total (T)	$V_T = 10^{16} h_R^{3.89}$	0.96	1.5×10^{-11}
	A	$V_A = 10^{16} h_R^{3.92}$	0.96	2.0×10^{-11}
	B	$V_B = 10^{14} h_R^{3.91}$	0.96	4.7×10^{-11}
	C	$V_C = 10^{15} h_R^{3.62}$	0.97	2.9×10^{-12}
2014-06-14	Total (T)	$V_T = 10^{16} h_R^{4.35}$	0.96	8.3×10^{-13}
	A	$V_A = 10^{15} h_R^{4.49}$	0.92	5.1×10^{-9}
	B	$V_B = 10^{14} h_R^{4.82}$	0.91	4.1×10^{-9}
	C	$V_C = 10^{15} h_R^{3.12}$	0.99	2.2×10^{-16}
2014-06-26	Total (T)	$V_T = 10^{16} h_R^{3.98}$	0.95	2.3×10^{-15}
	A	$V_A = 10^{16} h_R^{4.19}$	0.93	1.9×10^{-13}
	B	$V_B = 10^{14} h_R^{4.65}$	0.96	2.7×10^{-14}
	C	$V_C = 10^{15} h_R^{3.60}$	0.96	2.2×10^{-16}
2014-04-29	Total (T)	$V_T = 10^{15} h_R^{5.72}$	0.95	1.2×10^{-8}
	A	$V_A = 10^{15} h_R^{6.87}$	0.93	1.0×10^{-7}
	B	$V_B = 10^{13} h_R^{6.92}$	0.94	7.3×10^{-8}
	C	$V_C = 10^{16} h_R^{3.29}$	0.93	1.2×10^{-7}
2016-01-01	Total (T)	$V_T = 10^{16} h_R^{3.99}$	0.96	2.8×10^{-15}
	A	$V_A = 10^{16} h_R^{4.19}$	0.95	9.3×10^{-14}
	B	$V_B = 10^{14} h_R^{4.65}$	0.99	2.2×10^{-16}
	C	$V_C = 10^{15} h_R^{3.60}$	0.99	2.2×10^{-16}

TABLE 5.2: The empirical relations for the volume evolution of CMEs with the corresponding R² values and P - values for the different sections of the CME.

The details of the fitted power laws are given in Table 5.2. In order to appreciate the fitted empirical relations, we provide the associated R² values that shows how well our model succeeds in determining the strength of the relationship between our model and the dependent variable on a scale of 0 - 1. We also provide the

associated p-value which shows the statistical significance of the fitted model. The average significance level was found to be 0.05 on average, and thus models with p-values lesser than 0.05 implies statistically significant result. We find that the power law index for the total volume ranges between 3.89 - 5.72, thus indicating that the volume of a CME keeps increasing with distance from the Sun within the investigated height. We further find that the volume of the leading ellipsoidal front (V_A) and that of the middle disc (V_B) varies with a higher power law index (ranging between 3.92 - 6.87 and 3.91 - 6.92 respectively) than that of the total volume, while the volume of the conical legs (V_C) varies with a much lower power law index (ranging between 3.12 - 3.62), thus indicating a differential volume evolution throughout a CME. This once again reflects the significance of studying both the FO and EO widths of a CME. It is important to note that the volume of the legs of the CME is largely influenced by the EO width of the CME, while the volume of the other two sections are influenced by both the FO and EO widths. However, it must also be kept in mind that the estimation of the volume of the legs by this method is possible only for CMEs with small aspect ratios (as is the case for majority of the events studied, please see Table 5.1), which will enable the identification of two separate legs distinctly (as seen in the K-Cor images in Figure 5.1). For future studies on CMEs with large aspect ratios, it should be kept in mind that there will be a substantial overlap of the legs and hence the estimation of the volume of the legs might be misleading in such cases.

From Figure 5.3, it can be seen that the EO widths are much lesser in magnitude as compared to the FO widths (which is an expected outcome of the geometry of the GCS model), and this is further reflected in the power laws as a slower increase of the volume of the legs of the CME as compared to the ellipsoidal front and middle disc. We also note that the power law for the total volume is substantially greater for the CME on 2014 June 14 and 2014 April 29, as compared to the other three cases. We found that these two CMEs were ejected from erupting quiescent prominences, while the other three events were ejected from active

regions. Recently, Pant et al. (2021) have reported a higher power law index for the width distribution of CMEs connected to quiescent erupting prominences than those connected to active regions. It seems the volume of a CME too shows a similar imprint of the source region, but our conclusion in this work is based on only five events and hence an extension of this study to a much larger sample set of events will help in better establishing our conclusions. In future these results will also provide better inputs to study the dynamics of mass accretion by the CMEs as they evolve in the lower heights.

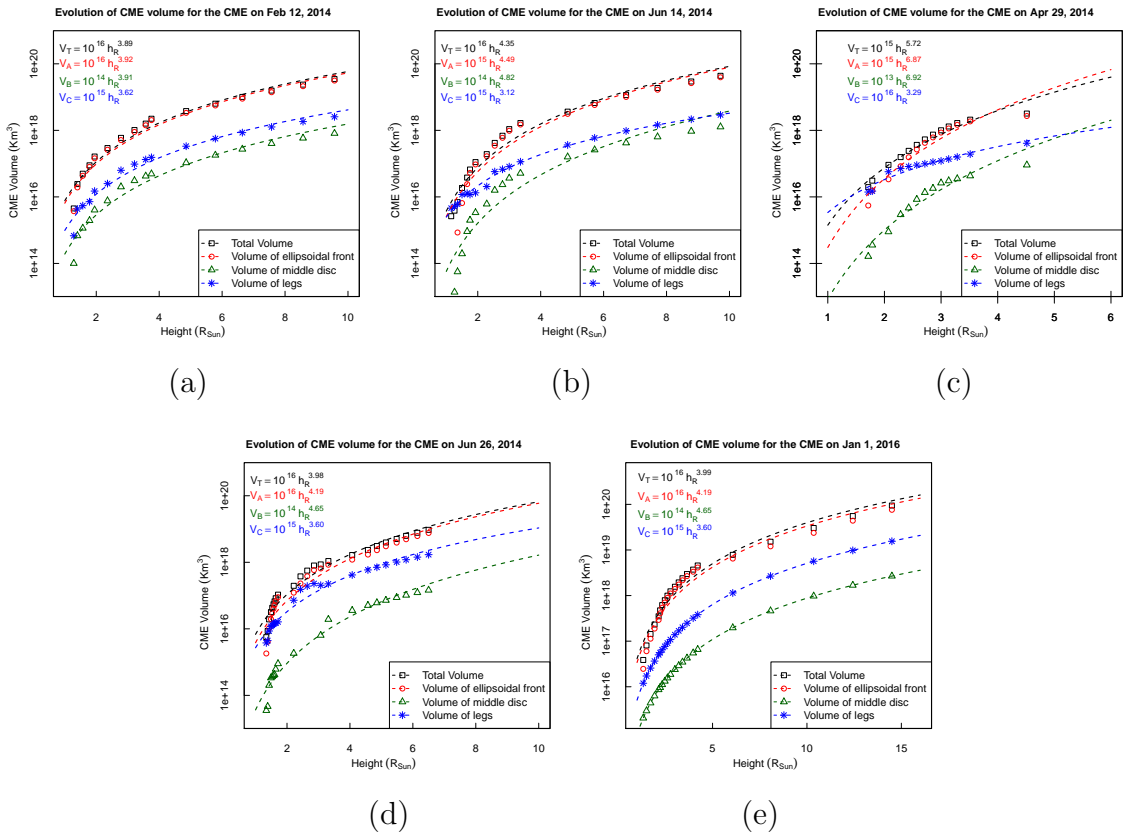


FIGURE 5.5: The evolution of the modelled CME volume and its different parts. The color coded plots denote evolution of different volume elements (the ellipsoidal front, the middle asymmetric disc and the conical legs) in the inner and outer corona.

Date	Region	Empirical Relation	R ² Values	P - Values
2014-02-12	$h_R < 4R_\odot$	$V = 10^{16} h_R^{4.93}$	0.95	1.5×10^{-6}
	$h_R > 4R_\odot$	$V = 10^{16} h_R^{3.28}$	0.99	2.3×10^{-7}
2014-06-14	$h_R < 4R_\odot$	$V = 10^{15} h_R^{6.15}$	0.98	1.5×10^{-10}
	$h_R > 4R_\odot$	$V = 10^{16} h_R^{3.54}$	0.99	2.5×10^{-8}
2014-06-26	$h_R < 4R_\odot$	$V = 10^{16} h_R^{5.08}$	0.91	2.4×10^{-8}
	$h_R > 4R_\odot$	$V = 10^{16} h_R^{3.82}$	0.99	3.1×10^{-9}
2014-04-29	$h_R < 4R_\odot$	$V = 10^{15} h_R^{5.72}$	0.95	1.2×10^{-8}
	$h_R > 4R_\odot$	–	–	–
2016-01-01	$h_R < 4R_\odot$	$V = 10^{16} h_R^{4.17}$	0.99	3.6×10^{-14}
	$h_R > 4R_\odot$	$V = 10^{17} h_R^{2.47}$	0.97	0.0002

TABLE 5.3: The empirical relations for the volume evolution of CMEs in the IC and outer corona with the corresponding R² values and P - values.

As discussed earlier, CMEs tend to evolve self-similarly in the outer corona, while the evolution in the IC is non self-similar. This change in behaviour of the CMEs provoked us further to study the total volume evolution of CMEs separately in the inner and outer corona. A close look at Figure 5.5 hints that the total volume of the CMEs shows different characteristics at different heights and that a single power law is not able to fit the volume evolution for the entire height range. So in Figure 5.6, we plot the evolution of the modelled total volume of the CMEs, and we fit two separate power law profiles for the evolution of volume below and beyond $4R_\odot$ (please see Table 5.3 for the details of fitting). It should be noted here that for the event on 2014 April 29, we could not track the CME much further in the COR-2 FOV, as the leading edge got depleted, and was difficult to track. Thus, it was not possible to probe the nature of variation of the modelled volume in the outer corona. We find that the volume evolution for all the events follow different power law profiles in the inner and outer corona. We find that the volume increases much more rapidly in the lower heights in the inner corona, as compared to the outer corona, and thus this clearly indicates towards the possibility of two different expansion mechanisms for CMEs in these two height regimes. The initial rapid expansion of volume can be attributed to the rapid angular width expansion in the IC as was recently reported by Cremades, Iglesias, and Merenda (2020b) and Majumdar et al. (2020b), while it seems the relatively slower volume

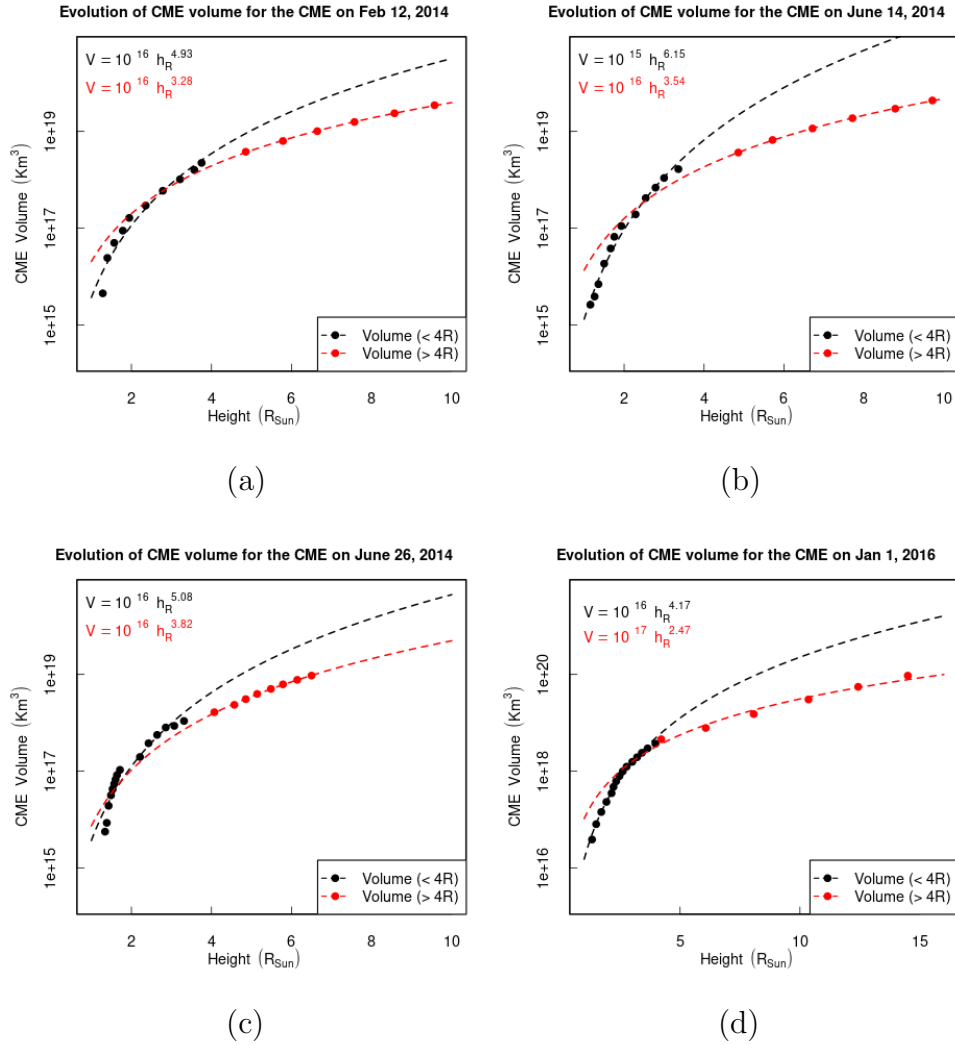


FIGURE 5.6: The evolution of the total modelled CME volume in the inner and outer corona. The data points and curve in black mark the volume in IC($< 4R_{\odot}$), while the ones in red are for those in the outer corona ($> 4R_{\odot}$).

expansion of CMEs in the outer corona might be a consequence of the total pressure difference in the inside and outside of the CME. These results thus strongly indicate how the kinematic properties of CMEs in the IC are strikingly different from the properties in the outer corona, lending support to the recent report by [Majumdar et al. \(2021a\)](#). It is also worthwhile to note the significance of the inclusion of K-Cor data along with the COR-1 data in order to arrive at these results. The measurements in the K-Cor FOV have facilitated in distinctly distinguishing the contrast in the evolution of modelled CME volume in the inner and outer corona.

5.4 Discussions and Conclusions

We first present the feasibility of implementing GCS on the K-Cor data-sets for the first time thereby providing additional vantage point for 3D reconstruction of CMEs in the inner corona. A proof of concept of this application is presented in Figure 5.1 by fitting the GCS model to the near-simultaneous images of K-Cor along with the observations from STEREO/SECCHI coronagraphs. The combined coronagraphic observations of K-Cor and STEREO/COR-1 in the IC and STEREO/COR-2 and SoHO/LASCO in the outer corona, allowed us to track and study the true evolution of CMEs in WL, covering a FOV starting from as low as $1.1 R_{\odot}$ which was never achieved earlier. This was possible once the GCS parameters for the CMEs were fixed by the three above-mentioned vantage points which were back-traced in the K-Cor FOV to heights of $\approx 1.1 R_{\odot}$. This facilitated in capturing the initial impulsive phase of the CMEs, where the kinematic parameters are known to change rapidly.

We were able to track the initial rapid expansion of CMEs in these lower heights, and thanks to three vantage point observations, we found that CMEs expand along both the axial and lateral directions rapidly in the initial part of the trajectory till a height of $3 R_{\odot}$, after which it saturates to a constant value. It should be noted here that for the CME in 2016 only two vantage points were available, while for the heights below the COR-1 FOV, only K-Cor observations were used. We noted that the CMEs can expand from $\sim 10^{\circ}$ to more than 90° in face-on width within inner corona. For the sample of CMEs we fitted, it could be identified that even though there was not much impulsiveness in the radial kinematics of the CMEs in the inner corona, we see a considerable expansion in their widths. An extension of this study on a larger data-set will provide better understanding of the Lorentz force in early kinematics of CMEs. In the future, an estimation of the true acceleration duration and magnitude can also be done at lower heights without any underestimate in the mentioned quantities, which was not possible in [Majumdar](#)

et al. (2020b); Cremades, Iglesias, and Merenda (2020b). It is worthwhile to note that we were able to do this using only WL data (within the limitations of the GCS model), hence ensuring that any ambiguity arising from tracking a CME in EUV and WL is further evaded. Thus, this work will largely help in improving on the shortcomings in previous studies on CME kinematics (Bein et al. 2011a; Subramanian et al. 2014; Cremades, Iglesias, and Merenda 2020b; Majumdar et al. 2020b). We further used the GCS model geometry to estimate the modelled total volume of the CME and also the modelled volumes of the ellipsoidal leading front, the asymmetric disc in middle and the conical legs separately. It should be noted that a correct estimation of the volumes of the different segments of the flux-rope requires the unambiguous identification of the inner edge of the flux-rope. But the identification of the inner edge of flux-rope is very difficult and tricky in the coronagraph images, and even if identified, it will suffer from high observer bias. However, provided the FOV of the coronagraph provides observation at the absolute lower heights to face-on CMEs (as is the case for K-Cor images in Figure 5.1), the inner edge of the flux-rope can be identified and gauged at the CME legs. Here, in this context, all CMEs analyzed in this work are assumed to be oriented face-on. We report for the first time, a power law variation of the modelled CME volume with distance from the Sun. We also found that the power law is higher for the ellipsoidal front and the disc than that for the conical legs, thus indicating that the volume expansion is dominated by the former two parts while the volume of the legs increases relatively slower, thus indicating that there is a differential volume expansion through a CME as it propagates from the inner to the outer corona. In this context, it must also be kept in mind that the estimation of the volume of the legs by this method is possible only for CMEs with small aspect ratios (as is in our case, please see Table 5.1), which will enable the identification of two separate legs distinctly (as seen in the K-Cor images in Figure 5.1). For future studies on CMEs with large aspect ratios, it should be kept in mind that there will be a substantial overlap of the legs and hence the estimation of the volume of the legs might be misleading in such cases. We also

studied the evolution of the modelled total volume of the CMEs in the inner and outer corona, and we found that CMEs tend to follow two distinctly different power law profiles below and beyond $4R_{\odot}$. This indicates at the possibility of two different expansion mechanisms of CMEs in the inner and outer corona. We believe these results need further attention in the future which will help us better understand the coupling of CME kinematics as they evolve from the inner to the outer corona. It is worthwhile to note that as a consequence of the constraints in the fitting procedure in the absolute lower heights (as outlined in Section 5.2.3), the height measurements will get influenced for CMEs which get deflected in the lower heights. Now, although the CMEs studied in this work did not show any appreciable deflection, yet in future such considerations should be kept in mind while studying CMEs that get deflected, as that will increase the uncertainty in the height measurements. In addition to that, this work ignores rotation of the CME in the lower heights as no such observable evidence was noted. Now despite the fact that no such observable signatures of deflections and rotations were noticed, it is worth noting that it is not that trivial to conclude on these properties, solely based on visual inspections. Hence, in future, possibly with the inclusion of above the ecliptic data from METIS on-board the Solar Orbiter, or observations from missions placed at the L5 point, we will be able to arrive at much stronger and better constrained conclusions. Thus in future for CMEs that exhibit rotation, a change in the tilt-angle parameter should also be considered while estimating the volume of the CME. Also, consideration of these processes (rotation and deflection) in future studies will also help in improving our understanding on the evolution of the volume of the front and legs of the CME.

In this context, it must also be noted here that these conclusions are specific to the geometry of the GCS model, which is an idealized geometrical figure that has its limitations and constrains (see [Thernisien, Vourlidas, and Howard 2009a](#)). Regarding the evolution of the legs, the identification of two separate legs of the CMEs require observation at the absolute lower heights. Thus the legs can be identified

in the K-Cor FOV, while its still not seen in the COR-1 FOV at the same time as shown in Figure 5.1, but it should also be noted that despite the promising FOV of K-Cor, yet the poor image quality due to challenges faced from being a ground based coronagraph makes it difficult to fit (refer the discussion in Section 5.2.2. In this regard, the upcoming ADITYA-L1 (Seetha and Megala 2017a) mission with the Visible Emission Line Coronagraph (VELC; Prasad et al. 2017b; Banerjee, Patel, and Pant 2017) (FOV : $1.05 - 3 R_{\odot}$) on-board and PROBA-3 (Renotte et al. 2014a) (FOV : $1.02 - 3 R_{\odot}$) with the giant ASPIICS (Lamy et al. 2017) will provide much better data and hence will help in arriving at much stronger conclusion on the evolution of CME legs. Having said that, it must also be noted that a true estimation of the volume of CME legs require the CME to be seen face-on, as a face-on view will help in identifying the inner edges of the CMEs and hence the volume of their legs. The studied CMEs in this work are all seen face-on in the K-Cor FOV (please see Figure 5.1). Thus, in future, for a larger statistical study, the appearance of the CME (being whether face-on or edge-on) should also be considered in the estimation of the volume of the CME legs. Apart from that, around one-third fraction of CMEs have been reported to have a flux-rope morphology (see Vourlidas et al. 2013), which happens to be the bedrock of the foundation of the GCS model, thus a study of these three separate sections of the flux-rope model of the CME will help us have a much better understanding on the validity of self-similar expansion, and thus provide more precise constraints to models that study flux-rope initiation and evolution

The cadence of K-Cor is better than that of COR-1, and this helped in tracking the CME more effectively in the lower heights, thus getting more number of data points in the impulsive phase. Since, the speed and acceleration of a CME are obtained by taking first and second order derivatives of the height-time data, it is essential to have as many number of data points as possible, especially in the initial impulsive phase, so that the derived quantities are better estimated (Byrne et al. 2012). In this regard, although K-Cor provides a cadence of fifteen seconds,

but the signal to noise in that data is not good enough for confident tracking of the CMEs in most of the cases, which made us use the two minute cadence data. Now although this is a substantial improvement on the cadence of COR-1, yet it barely needs explanation that data with even better cadence will further aid in our understanding of this initial rapid impulsive phase of CMEs. For this, again the data from upcoming space missions like ADITYA-L1 with the VELC, and PROBA-3 with the ASPIICS will help in overcoming this limitation by providing high cadence data with good resolution. The significance of this extension of the GCS model also lies in the fact that, despite the loss of STEREO-B (and hence COR-1B data) from 2016, this modified GCS model will still enable stereoscopy in the IC for the 3D study of early kinematics of CMEs in WL.

Chapter 6

Combining Radio Spectral and Imaging Observations in locating the source of Type-II burst

6.1 Introduction

CMEs are one of the most energetic explosions happening in the solar atmosphere, expelling large-scales of plasma and magnetic field, into the heliosphere with speeds ranging from a few tens to a few thousands of km s^{-1} (see [Webb and Howard \(2012a\)](#), for a review). CMEs are also one of the major drivers of space weather, that can drastically affect human technological systems ([Gosling et al. 1991](#); [Gosling 1993b](#)). Fast CMEs drive magneto-hydrodynamic shocks that accelerate energetic particles, a key player in space weather. In order to understand the shock-driving capability of CMEs, we need to investigate early CME kinematics

near the Sun. CMEs leave imprints in different wavelengths, so it is necessary to stitch multi-wavelength information for a better understanding of CME behaviour (Pick et al. 2006; Vršnak et al. 2006; Zucca et al. 2014; Kumari et al. 2017b).

CMEs show a wide range in their kinematic properties (Yashiro et al. 2004b, and references therein), with a three phase kinematic profile (Zhang et al. 2001b; Zhang et al. 2004; Webb and Howard 2012a). A major concern here is that for measurements done on the plane of the sky, the results may suffer from projection effects (Balmaceda et al. 2018c). In this regard, to reduce such projection effects, Thernisien, Vourlidas, and Howard (2009c) developed the GCS model that uses forward modelling to fit a flux-rope to CME images taken from multiple vantage points, to generate its 3D reconstruction. CMEs are also capable of driving shocks in the low corona and interplanetary (IP) medium (Hundhausen 1987), and the shock signatures can be tracked either directly from the white-light (WL) CME images (Sheeley, Hakala, and Wang 2000; Vourlidas et al. 2008) or from type II radio bursts (Gopalswamy 2006a). Gopalswamy et al. (2009b) reported on the relationship between type II bursts and CMEs showing their combined evolution from the corona into the IP medium. The authors reported that type II bursts provide the earliest signature of a shock that forms very close to the Sun's surface (Cane and Stone 1984; Cho et al. 2013; Gopalswamy et al. 2013; Kumari et al. 2017a).

Holman and Pesses (1983) suggested that the electrons which are responsible for the type II burst might get accelerated from the shock flanks, which implies that the height inferred from the type II burst location might be smaller than the height of the CME leading edge at that particular time. Also, since the rate of drift of the burst frequency is in turn controlled by the shock speed, and the density scale

height of the ambient corona (Gopalswamy et al. 2009b), it is important to understand which section of the shock surface hosts the type II burst source. In this regard, Jebaraj et al. (2020) used radio triangulation technique to probe the source of two type II bursts. Metric type II bursts are also often found to show splitting in their fundamental and harmonic bands. Smerd, Sheridan, and Stewart (1975) proposed an explanation to this band splitting in terms of the emission coming from the upstream and downstream shock regions, with the observational support to the theory reported by Vršnak et al. (2001). Band splitting in type II burst has proven to be useful to estimate the ambient coronal magnetic field in the inner corona (IC) (Smerd, Sheridan, and Stewart 1975; Cho et al. 2007). Direct estimate of the magnetic field in the IC from type II burst using an empirical electron density distribution was also reported by Kumari et al. (2019). Further, the coronal magnetic field strength beyond the IC can be estimated by the shock stand-off distance and the flux-rope radius of curvature as described by Gopalswamy and Yashiro (2011). Thus for a better understanding of the kinematics of CMEs and its interaction with the ambient medium we need to consider all aspects of the type II bursts and the associated CMEs.

We use type II - CME connection to understand several aspects of the evolution of CME, as it propagates into the heliosphere. We analyze the 26 January, 2014 CME at 08:36 UT by combining WL, radio, Extreme Ultra Violet (EUV), and X-ray data. We outline the data sources that we have used in Section 6.2, and provide a brief description and timeline of the event in Section 6.3, followed by our results in Section 6.4 and conclusions in Section 6.5.

6.2 Data Selection

We have used WL coronagraph data from the LASCO C2,C3 (Brueckner et al. (1995b)) onboard the SOHO, COR-1 and COR-2 coronagraphs of the SECCHI (Howard et al. 2008b) package on the STEREO (Kaiser et al. 2008b). We have used EUV data from different passbands of the AIA (Lemen et al. 2011) onboard SDO, Extreme Ultra Violet Imager (EUVI) onboard STEREO and EIT (Delaboudinière et al. 1995) onboard SOHO. X-ray flux from Geostationary Operational Environmental Satellite (GOES) (1-8 Å channel) provides the flare context. We have used radio data from the Gauribidanur Low-frequency Solar Spectrograph (GLOSS; Kishore et al. (2014)), the Gauribidanur RAdio heliograPH (GRAPH; (Ramesh et al. 1998)), Learmonth station of the Radio Solar Telescope Network (RSTN), Compound Astronomical Low frequency Low cost Instrument for Spectroscopy and Transportable Observatory (e-CALLISTO*; Monstein (2013)) at the Gauribidanur Radio Observatory[†] and the SWAVES instrument (Bougeret et al. 2008) onboard STEREO. Data from the Coordinated Data Analysis Workshop (CDAW) (Gopalswamy et al. 2009d) catalogue which lists the properties of CMEs detected manually in LASCO images onboard SOHO are also used[‡].

6.3 Event description and timeline

The CME on 26 January 2014 had a C1.5 class flare associated with it which was from an active region 11967 (NOAA) located at S16E106[§], which is 16° behind the east limb (see Figure 6.1). Since the flare is partly occulted, it is likely that the flare size is underestimated. The flare starts at \sim 8:24 UT, reaches its peak

*<http://www.e-callisto.org/>

†<https://www.iiap.res.in/centers/radio>

‡https://cdaw.gsfc.nasa.gov/CME_list/index.html

§https://www.solarmonitor.org/full_disk.php?date=20140128&type=shmi_mag1c®ion=&indexnum=1

at $\sim 8:36$ UT while ends at $\sim 9:48$ UT (see Figure 6.1, right panel). The CME is observed fully by LASCO (C2, C3) and SECCHI (COR-1, COR-2) on STEREO A and B. This CME is listed in the CDAW catalogue with a time of first appearance of 8:36:05 UT in the LASCO C2 FOV with an mean speed of 1088 km s^{-1} . The partial halo CME is propagating in the southeast direction with a central position angle (CPA) of 125° in the LASCO FOV. The CME decelerates in the LASCO C2 and COR-1, COR-2 FOV, indicating that the initial acceleration ended before the CME appeared in the FOV of COR-1 and LASCO C2. This is mainly due to a data gap in the COR-1 observation. The source region of the CME is also located and identified in the extreme ultraviolet images taken at 193 \AA by SDO/AIA. The source region as imaged by SDO/AIA at 193 \AA and the soft X-ray flare profile from GOES can be seen in Figure 6.1. During the CME eruption, STEREO A and B were located at W151 and E156, respectively. Therefore the CME is a limb event (W103) in STEREO-A FOV and a disk event (W50) in STEREO-B FOV implying that STEREO-A and LASCO measurements would not suffer much from projection effects.

The dynamic spectra of the type II radio burst recorded with GLOSS and from STEREO-B/WAVES, are shown in Figure 6.3. The type II burst shows a fundamental-harmonic structure in the metric and decameter-hectometric (DH) domains. The starting frequency is found to be ~ 90 MHz for the fundamental, at $\sim 8:34$ UT as seen in the Learmonth spectrograph[¶] belonging to the Radio Solar Telescope Network (RSTN). The burst then drifted towards the lower frequencies and continued to ~ 7.46 MHz in the DH domain at $\sim 8:52$ UT. The type II emission shows band-splitting. The continuation of the type II emission from metric to DH domain indicates the presence of a strong shock (Gopalswamy et al. 2005). It is

[¶]<https://www.sws.bom.gov.au/Category/WorldDataCentre/DataDisplayandDownload/Spectrograph/station/learmonth/images/14/20140126spectrograph.gif>

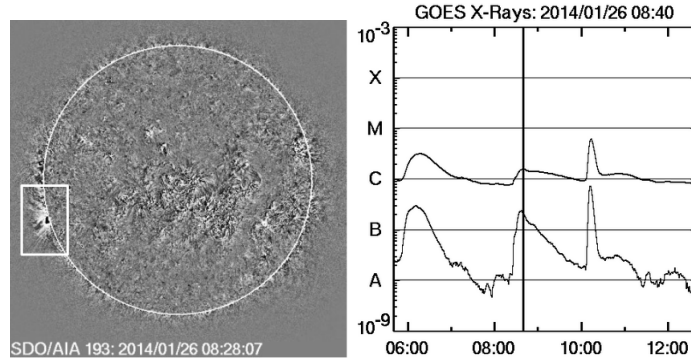


FIGURE 6.1: *Left:* The source region of the CME as observed in SDO/AIA 193 Å shown in the enclosed rectangle at the western limb. The image is made at 08:28:07 UT. The ‘white’ circle represents the photospheric Sun. *Right:* The GOES soft X-ray light curve of the associated C1.5 class flare on 26 January 2014. Note that the flare is occulted, so the actual soft X-ray intensity is expected to be higher than the one showed in the figure here.

important to note that the DH type II burst was observed only in STEREO^{||}, not in Wind/WAVES. Also it is best observed in STEREO-B because it observes more shock surface. STEREO-A sees only the harmonic. We also note the gap in the STEREO/COR-1 data which did not enable us to determine the CME kinematics at the onset of the type II burst accurately. We summarise the timeline of the event as observed by different instruments in Table 6.1.

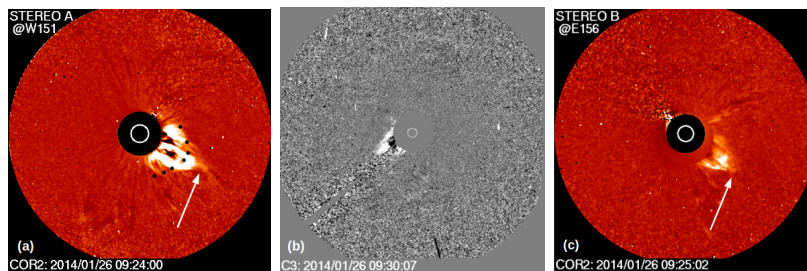


FIGURE 6.2: The CME on January 26, 2014 observed with (a) STEREO/COR-2A; (b) SOHO/LASCO-C3; and (c) STEREO/COR-2B. The diffused shock structure beyond the bright flux-rope can be seen in STEREO A and STEREO B views as marked with ‘white’ color arrow. The location of STEREO A and STEREO B were W151 and E156, respectively.

^{||}https://solar-radio.gsfc.nasa.gov/data/stereo/summary/2014/swaves_summary_20140126_c.png

Phenomenon	Data Source	Parameter	Observations
Type II burst	Gauribidanur spectrograph	Starting frequency (time)	180 MHz (8:28 UT)
Type II burst	Gauribidanur spectrograph	Ending frequency (time)	35 MHz (8:28 UT)
Type II burst	STEREO B/WAVES	Starting frequency (time)	16.46 MHz (8:40 UT)
Type II burst	STEREO B/WAVES	Ending frequency (time)	7.78 MHz (8:51 UT)
Flare	GOES X-Rays	Starting time	8:24 UT
Flare	GOES X-Rays	Peaking time	8:36 UT
Flare	GOES X-Rays	Ending time	9:48 UT
CME	LASCO C2	First appearance height (time)	2.27 R _⊙ (8:36 UT)
CME	LASCO C3	First appearance height (time)	6.01 R _⊙ (9:06 UT)
CME	STEREO A/COR 1	First appearance height (time)	3.14 R _⊙ (8:45 UT)
CME	STEREO A/COR 2	First appearance height (time)	4.84 R _⊙ (8:39 UT)
CME	STEREO B/COR 1	First appearance height (time)	2.93 R _⊙ (9:06 UT)
CME	STEREO B/COR 2	First appearance height (time)	3.14 R _⊙ (8:55 UT)

TABLE 6.1: Timeline of the January 26 2014 CME and the associated phenomena.

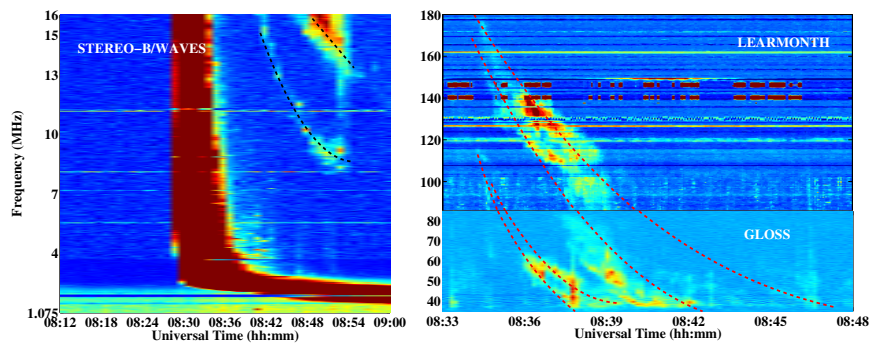


FIGURE 6.3: The figure shows the composite dynamic spectra of the metric type II burst recorded with the GLOSS (ground-based) and the DH continuation of the same as observed by STEREO B/WAVES. The start frequency of the Type II bursts is ~ 90 MHz as seen in Learmonth spectrograph. The type II burst shows fundamental harmonic structures in metric-DH wavelengths. The two bands are shown with ‘red’ lines.

6.4 Data Analysis and Results

6.4.1 CME Kinematics from white-light data

The CME as observed in STEREO/COR-2A, STEREO/COR-2B and SOHO/LASCO-C3 is shown in Figure 6.2. We track the CME shock front and the flux-rope structure in the COR-2A and COR-2B FOV (Figure 6.4(a) and (b), respectively). From linear fits to COR-2A (COR-2B) height-time measurements, we find the average shock speed to be 1392 km s^{-1} (1205 km s^{-1}) and that of the flux-rope to be 874 km s^{-1} (865 km s^{-1}). By making a linear fit to height-time data from the CDAW catalogue (Figure 6.4(c)) we find the average speed to be 1088 km s^{-1} , which is likely to be the shock speed as CDAW tracks the leading edge. Since STEREO-A and LASCO measurements have minimum projection effects (see section 6.1), with correction factors of 1.03 and 1.04 respectively, we find the true speeds in COR-2A to be 900 km s^{-1} (flux-rope) and 1434 km s^{-1} (shock), while the true speed in LASCO to be 1132 km s^{-1} . For STEREO-B it is a disk event, and hence the measurements will have large projection effects. With a correction

factor of 1.31, the estimated true speeds in COR-2B are 1133 km s^{-1} (flux-rope) and 1579 km s^{-1} (shock). A better way to remove projection effects, is to fit the GCS model to the pair of STEREO images to get their true evolution (Figure 6.5(a) and (b)). With the help of quadratic fits to height-time measurements in the CDAW catalogue, and from measurements from the GCS model, we find that the CME decelerated in the LASCO and COR-1, COR-2 FOV (Figure 6.5(c)). We further measured the leading edge of the CME at different Position Angles (PA) in the COR-2A FOV. In Figure 6.4(d) we plot the average speed of the leading edge versus PA. We find that the nose of the leading edge travelled with a much higher speed compared to the flanks, and that the extreme southern flank had higher speed than the extreme northern flank. The overall shape of this plot also reproduces the shape of the CME as observed in the coronagraph images (Figure 6.2(a) and (c)). Thus, we also see that tracking a single point to understand kinematics can be misleading.

6.4.2 Connecting Radio and White-Light Data

6.4.2.1 Shock Formation Height

It has been reported that Type-II bursts are often associated with CMEs that drive shock waves, and in such cases, the starting frequency of the Type-II burst can give an estimated shock formation height for the shock associated with the Type-II burst (Gopalswamy et al. 2013; Kumari et al. 2017a). From the radio dynamic spectrum from the Learmonth station of RSTN, we find the starting frequency is $\approx 115 \text{ MHz}$ at 8:34 UT for the fundamental. Gopalswamy et al. (2013) reported an empirical relation between the height of shock formation (r) and the start frequency of the Type-II burst [f_p] as follows,

$$f = 307.87r^{-3.78} - 0.14. \quad (6.1)$$

Using the starting frequency in the above relation, we get the height at which the signatures of shock wave (Type-II burst) were observed as $\approx 1.3 R_{\odot}$ from the Sun center, where R_{\odot} is the radius of the Sun. Since the above relation arises from a weak correlation between the two quantities, we also find the shock-formation height from the relation between the plasma frequency [f_p] and the plasma density [n_p], which is as follows,

$$f_p = 9 \times 10^{-3} \sqrt{n_p} \quad (6.2)$$

where f_p is in MHz, The n_p can be used from the coronal density model. In this work, we use the Newkirk coronal density model (Newkirk 1967). We plug in the starting frequency in Equation 6.2 to get an estimate of the density. With the estimated density, we use the Newkirk coronal density model to get the height of Type-II associated shock as $\approx 1.3R_{\odot}$, which matches well with what we got from equation 6.1.

From the height–time data obtained with LASCO-C2, the nose of the WL shock front appears in the FOV at $\approx 08:36$ UT at a height of $\approx 2.33 R_{\odot}$. Taking the instantaneous WL shock speed from the first two data points in C2 FOV, we calculate the height of the shock front at $\approx 8:34$ UT as $\approx 2.04 R_{\odot}$. This is higher than the height of the shock connected to the Type-II burst found from Equation 6.1. In such cases Gopalswamy et al. (2009b) suggested that the shock resulting in the Type-II burst might come from the electrons accelerated at CME flanks (which is at a lower height) and not from the nose. The radio-imaging observation was carried out with GRAPH at 80 MHz (see Figure 6.6a). The radio

image was made at $\approx 08:38 \pm 20$ sec UT, which corresponds to the harmonic band of the Type-II spectra. The radio contours are shown at 50 %, 72 %, 75 %, 87 %, and 99 % of the peak radio flux at 80 MHz. The contour intervals are at $\approx 6.6 \times 10^3$ Jy. The projected heliocentric distance for GRAPH is $\approx 1.06 R_{\odot}$. The active region was located at the back of the solar disk at $\approx 16^{\circ}$ from the east limb. The de-projected heliocentric distance was thus calculated to be at $\approx 1.1 R_{\odot}$ with a position angle of $\approx 157^{\circ}$, which is at the southern flank of the CME.

We confirm from the GRAPH image (Figure 6.6), that the burst source (produced by the shock wave) located at the southern CME flank produces the Type-II burst (please see Section 6.3 for a description of the imaging data), thus supporting our arguments which are i) The shock formation height inferred from Type-II burst start frequency gives a much lower height than the CME nose height at that time, thus arguing that the shock wave at the flanks of the CME might be the source of the Type-II burst; ii) This is because the flanks are at a lower height than the CME nose, and hence is expected to pass through denser region (as suggested by [Gopalswamy et al. \(2009b\)](#)). We also note that this was not possible in [Gopalswamy et al. \(2009b\)](#) to pinpoint which flank of the CME, the emission was coming from, as they did not have imaging observation of the Type-II burst. Additional support to this conclusion comes from the height–time variation of the north and south flanks of the CME in the COR-2A and LASCO-C2,-C3 FOV (Figure 6.6b and c). The average speeds of the north and south flanks were found to be around 579 Km s^{-1} and 754 Km s^{-1} respectively in the COR-2A FOV, and 619 km s^{-1} and 870 km s^{-1} in the LASCO FOV. This shows that the southern flank is at a higher speed, and thus is likely leading to the Type-II burst.

6.4.2.2 Metric Type-II Burst Continuing to DH Domain

As mentioned earlier in Section 6.3 and from Figure 6.3 we find that the brief DH Type-II burst is a part of the earlier metric Type-II. The DH Type-II burst was observed only in STEREO, not in *Wind*/WAVES, and that it is best observed in STEREO-B because it observes more shock surface. STEREO-A sees only the harmonic. This further supports the flank origin of the Type-II burst. On the other hand, we note that the shock is not fast enough to extend the Type-II emission to the kilometric domain, which happens for shocks at much higher speeds (Gopalswamy et al. 2005). It is quite surprising that the shock nose, where the speed is the highest, is radio quiet. One possibility is that the local Alfvén speed above the shock is close to the WL shock speed, rendering the Mach number to be too small (see, e.g., Gopalswamy et al. (2008)).

6.4.2.3 Alfvén Speed from Stand-off Distance of CME Driven Shock and Band-Split Measurement

Despite the ending of the Type-II burst at $\approx 08:52$ UT, we found the shock to be present in COR-2A images as the CME propagated further into the heliosphere. We follow Gopalswamy and Yashiro (2011) to get the Alfvén speed at the nose by the ending time of the burst. In the 09:24 UT COR-2A image, we measure the standoff distance $[\Delta R]$ as $\approx 0.99 R_{\odot}$ and a radius of curvature (R_c) of $\approx 1.34 R_{\odot}$ (at a height of $\approx 6 R_{\odot}$). Using these values in the Russell and Mulligan (2002) relation,

$$\frac{\Delta R}{R_c} = 0.81 \frac{(\gamma - 1)M^2 + 2}{(\gamma + 1)(M^2 - 1)}, \quad (6.3)$$

and the adiabatic index γ as 5/3 we get the Mach number $[M]$ as ≈ 1.31 . Using the local WL shock speed as 1250 km s⁻¹ in the relation,

$$V_A = \frac{V_{\text{shock}}}{M}, \quad (6.4)$$

we get an Alfvén speed of ≈ 954 km s⁻¹. This is higher than the typical Alfvén speed at these heights (Vršnak, Magdalenić, and Zlobec 2004), thus confirming weak shock conditions at the nose of the CME. We also use the band splitting of the Type-II burst to get the Alfvén speed. We follow a similar procedure to that reported by Vrřnak et al. (2001). We measure the width of the band splitting of the fundamental Type-II burst on the dynamic spectrum (Figure 6.3). The bandwidth is defined as

$$BW = (F_u - F_l)/F_l, \quad (6.5)$$

where F_u and F_l are respectively, the upper- and lower-band frequencies. The density jump $[X]$ across the shock front is related to the bandwidth as

$$X = (BW + 1)^2. \quad (6.6)$$

This density jump $[X]$ is further related to the Alfvénic Mach number $[M_A]$ through

$$M_A = \sqrt{X(X + 5)/2(4 - X)}. \quad (6.7)$$

Using the above relation, we get an average M_A of 1.45. From the heights inferred

from the lower band of the fundamental branch of the Type-II burst, we get an average shock speed associated with the Type-II burst as 1451 km s^{-1} , which from Equation 6.4 gives us an Alfvén speed of 1001 km s^{-1} . It is interesting that although the Alfvén speed is comparable at the CME nose at $6 R_{\odot}$ and from the band-split calculations, yet the Type-II burst is coming from the flank of the CME (Figure 6.6a).

6.4.2.4 The CME–Streamer Encounter

The sudden broadening in the DH Type-II burst seems to be due to the CME interaction with the streamer (as also reported earlier by Feng et al. (2012)) at the southern flank (see left panel of Figure 6.3). Movies of LASCO-C2 images show the CME hitting against the southern streamer at the time when the Type-II broadening was observed around 8:48 UT as shown in Figure 6.7, just before the Type-II burst ended. The region of interaction was also determined from LASCO movies, where it was seen that the left flank of the CME interacts with the streamer during its propagation. Since the spectral bump in the SWAVES dynamic spectra (Figure 6.3) occurred around the same time, the CME flank interacted with the streamer ($\approx 8:48 \text{ UT}$), we estimated the height at which the interaction takes place from LASCO images to be $\approx 2.58 R_{\odot}$, not too different from the expected height ($\approx 2.61 R_{\odot}$) from Equation (6.1). When the DH Type-II ended around 08:42 UT, the shock seems to have transited through the streamer. At 08:52 UT, when the Type-II ended, the nose was at a height of $5 R_{\odot}$, where the shock was not strong enough for producing a Type-II burst.

Type-II imaging observation confirmed that the source that produced the Type-II burst is located near the southern CME flank (Figure 6.6). Since the metric Type-II is getting continued into the DH Type-II burst, the emission continues at the southern flank as the shock moves out. The flank speeds are of $\approx 574 \text{ km s}^{-1}$

(north flank) and $\approx 754 \text{ km s}^{-1}$ (south flank) as derived by a linear fit to the distance-time plot of flanks shown in Figure 6.6. The speeds are not too different, yet only the southern flank has the source. At this time, the shock nose is at a higher speed on one hand, and on the other hand, the streamer present at the bottom (southern) might have aided the generation of the type-II emission. This is because the streamers are denser than the ambient corona and are known to be regions of low Alfvén speed compared to the normal corona. Also, the nose is at a height of $\approx 2 R_{\odot}$, where the Alfvén speed is near its peak value (Vršnak, Magdalenić, and Zlobec 2004), so the shock is relatively weaker at the nose to give rise to the Type-II burst. Thus the combination of WL and radio imaging along with radio dynamic spectrum provides conclusive evidence that the CME-streamer interaction is also additionally responsible for the generation of shock associated Type-II emission.

6.5 Summary and Conclusions

The primary finding of this article is that we were able to show that the Type-II burst during the 26 January 2014 CME originated from one of the flanks of the CME-driven shock. We combined EUV, radio, and WL data to understand the kinematic aspects associated with the CME including true speed, shock propagation speed, Alfvén speed and the association with Type-II bursts, that confirm this conclusion. We were also able to show that the nose region of the CME was radio quiet because of the high Alfvén speed, hence resulting in a Mach number very close to one there. We summarise in the following points, our main results from this work that supports our conclusion,

- We measured the average speeds of the shock front and flux-rope and found a substantial difference in their speeds. The stand-off distance of the shock

increases with height, consistent with the deceleration of the CME in the coronagraph FOV.

- The CME speeds measured at different position angles reveal that the nose was the fastest. However, the flanks are also fast enough to drive a shock and produce Type-II radio emission. Even though the northern and southern flanks had similar speeds, the southern flank interacted with a streamer, which may be the reason behind the (southern) flank origin of the Type-II burst. From LASCO-C2 data, the shock height was estimated to be at $\approx 2.04 R_{\odot}$, which was much higher than the shock-formation height inferred from Equation 6.1 ($\approx 1.3 R_{\odot}$), thus hinting at the possibility of the flanks being the source of the radio burst. A plot of the average flank speeds showed that the southern flank was relatively faster. Further, from the GRAPH contours, the southern flank was found to host the burst source. It is also worthwhile to note that the radio imaging observation of the Type-II burst enabled us in pinpointing the flank emission of the Type-II burst, which was not possible in [Gopalswamy et al. \(2009b\)](#).
- It was interesting that the shock nose, where the speed was highest, did not produce the Type-II emission. From the standoff-distance measurements at the CME nose, we found a higher Alfvén speed, confirming a weak shock there. Also, the presence and interaction of the streamer with the southern flank of the CME seems to have provided more favorable conditions for a strong shock at the flanks, thus validating our conclusions.

This work shows the importance of complementing spectral radio data with imaging data in locating the part of the CME driven shock responsible for accelerating electrons. An understanding of the location and origin of the shock waves that are associated with Type-II emission is a complex problem especially in the IC. Further, since shocks accelerate particles that affects space weather, it becomes

necessary to study and identify their origin, and this work particularly aims at improving our present understanding of the same. It should also be noted here that we obtained the shock formation height of $\approx 1.3 R_{\odot}$ using the radio data. This height is below the existing space-based WL coronagraphs used for analysis. It is worth mentioning that future space-based missions including *Aditya-L1* (Seetha and Megala 2017b; Raghavendra Prasad et al. 2017), PROBA-3 (Renotte et al. 2014b), and *Solar Orbiter* (Müller et al. 2013), are equipped with coronagraphs capable of observing the inner corona, a region with limited observations from existing space-based instruments. These instruments will be helpful in studies similar to this work to identify the WL counterparts of the radio imaging of the shock origin, thereby improving understanding of such phenomenon.

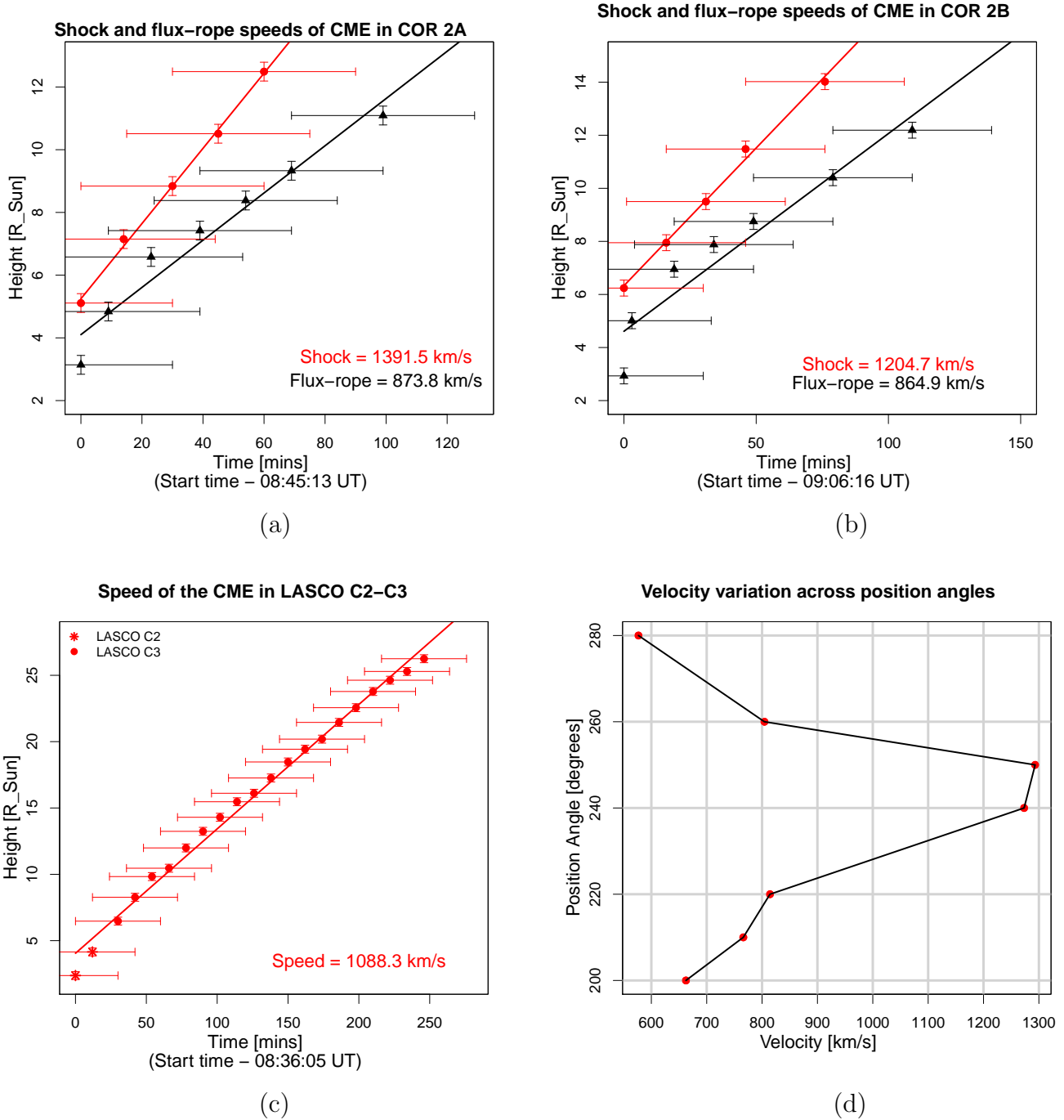
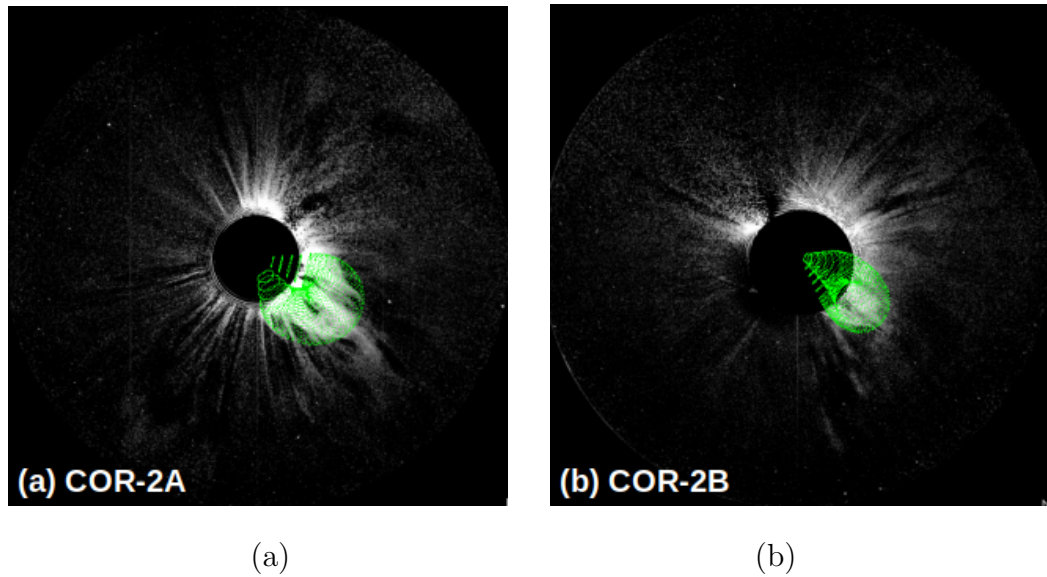
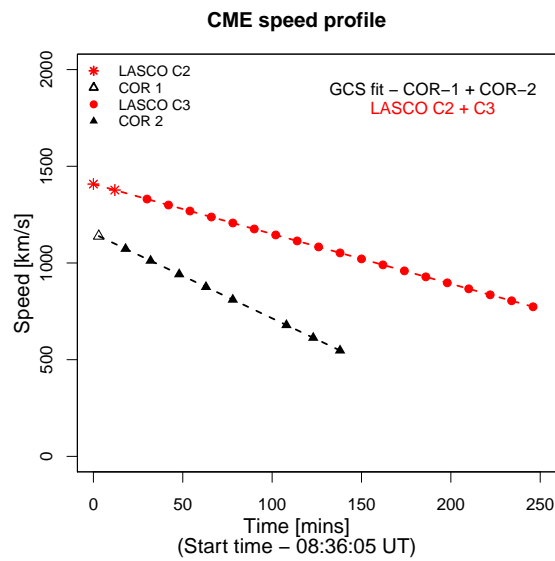


FIGURE 6.4: The height–time profile of CME shock and flux-rope as observed in (a) STEREO/COR-2A (measured at PA $\approx 242^\circ$); (b) STEREO/COR-2B (measured at PA $\approx 234^\circ$). In panel a and b, the red and blue points correspond to the shock front the flux-rope of the CME, respectively. The speed measured at the leading edge of the CME with the SOHO/LASCO data from CDAW catalogue (c). The CME leading edge speed variation with position angles is shown in panel d and the corresponding position angles are marked in Figure 6.2a



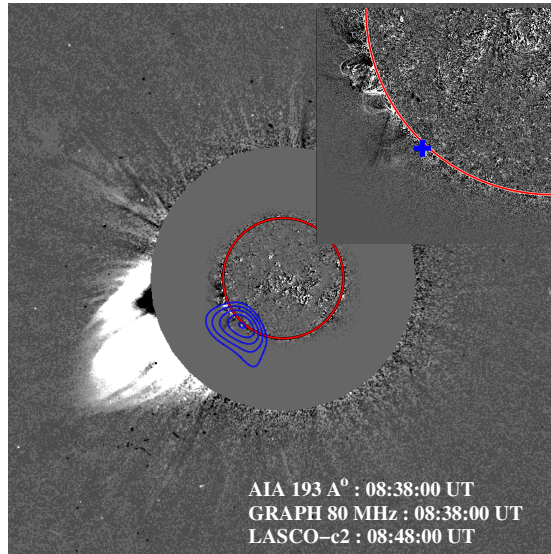
(a)

(b)

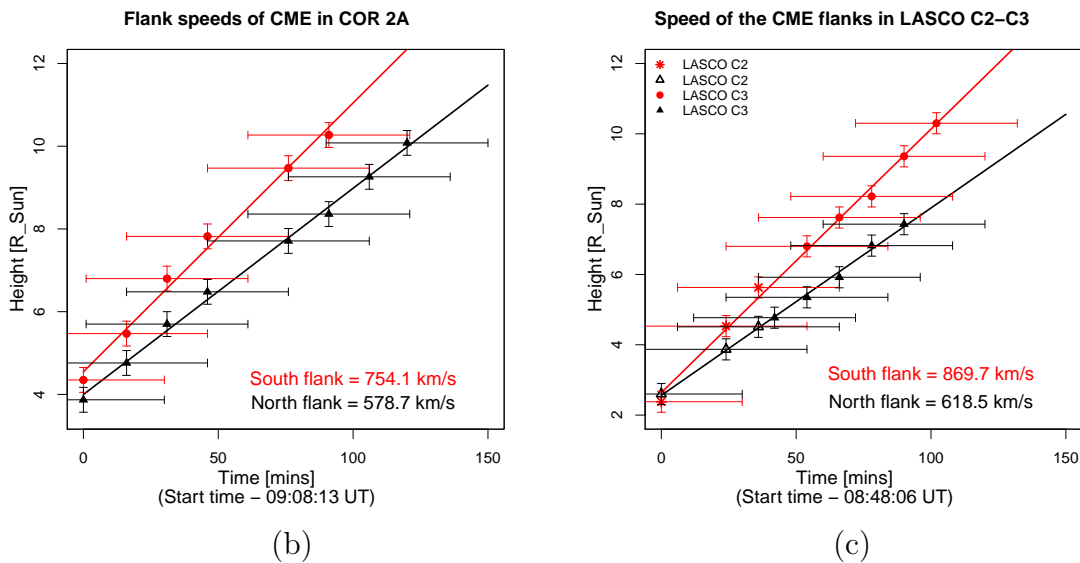


(c)

FIGURE 6.5: (a) The CME as observed in COR-2A; (b) COR-2B at 09:24 UT with the GCS model fit in green; (c) The variation of CME leading front speed with time in the LASCO C2 and C3 FOV and from the GCS model fit to the CME in the COR-1 and COR-2 A/B FOV. The CME is clearly decelerating in the coronagraphs FOV.



(a)



(b)

(c)

FIGURE 6.6: (a) The composite of the WL CME as seen in the SOHO/LASCO-C2 FOV with the 80 MHz contours obtained with GRAPH radio observations and the SDO/AIA-193 Å. The red circle marks the solar disk. The radio contours are shown at 50, 72, 75, 87, and 99% of the peak radio flux at 80 MHz. The contour intervals are at $\approx 6.6 \times 10^3$ Jy. The de-projected height of the radio contours are at $\approx 1.1R_{\odot}$ and the position angle is $\approx 157^{\circ}$. An inset with a zoom into the AIA image shows the spatial location of the associated flare (top right). The location of 80 MHz centroid is marked with blue color in the inset image; The North and South flank speeds of the CME from height-time measurements in (b) COR-2A FOV; and (c) in LASCO C2 and C3 FOV.

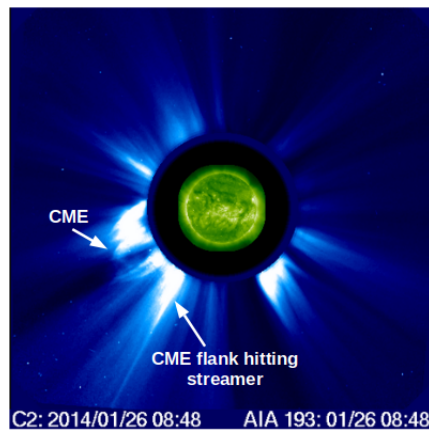


FIGURE 6.7: CME interacting with the streamer at the southern flank as depicted in the LASCO-C2 image at 08:48 UT. The LASCO image is superposed on with SDO/AIA 193 Å image.

Chapter 7

Study of velocity dispersion inside CMEs in inner corona

7.1 Introduction

CMEs are the major space weather drivers, which are capable of radically affecting the Sun-Earth connection and thus it is imperative to understand their kinematics (Gosling 1993a; Schwenn et al. 2005). The dynamics of a CME is an interplay between Lorentz force, gravitational force and viscous drag force, and it is the IC($< 3R_{Sun}$) which best manifests the role of Lorentz force in the same (Subramanian et al. 2014). But we are yet to have a clear understanding of the kinematics of CMEs in the IC(Majumdar et al. 2020b).

Kinematics of CMEs have been studied in the past both in EUV and white light(WL) (Zhang et al. 2001a; Vršnak, Magdalenić, and Zlobec 2004; Bein et al. 2011a; Cheng et al. 2020a). These authors have reported an initial impulsive acceleration of CMEs using EUV data and coronagraph data in the lower coronal

heights, showing little or no acceleration in the higher heights. It is understood now that around 75% of CMEs show a three part structure with a leading front, a dark cavity (the flux-rope) and the inner core (supposedly the prominence material). However, the individual behaviour of these three parts comprising a single entity (the CME), is poorly understood (Schmahl and Hildner 1977; Illing and Hundhausen 1985; Maričić et al. 2004). The morphological appearance of CMEs exhibiting three part structure are different as seen in WL and EUV (Song et al. 2019) and we propose to probe the individual kinematics of the three part structure of CMEs as observed in EUV and WL (in a well overlapping field of view), separately and compare their kinematic profiles, which may provide us with many interesting inferences on the evolution of their physical properties. Now, CMEs, as we understand, is not a rigid body but a plasma with embedded magnetic field (the flux-rope) and we would like to study the differences in velocity of propagation of the three parts moving from the inner core to the leading front, as the CMEs evolve from the inner corona (IC) to the Heliosphere. This difference in the velocity is termed as velocity dispersion in a CME (Webb and Jackson 1981; Simnett 2000). Also investigating the change in separation between the flux-rope and leading front, prominence and leading front with height will help us understand the association of this velocity dispersion with self similar expansion (i.e. the ratio of flux-rope minor radius to the major radius remaining constant with time, see Thernisien, Howard, and Vourlidas (2006b)) of CMEs in the inner corona. Since self-similar expansion (SSE) controls the kinematics of CMEs (Subramanian et al. 2014), a study of velocity dispersion and its effect on the SSE of CMEs in IC calls our attention for an effective utilization of upcoming coronagraph missions with capabilities of imaging the inner corona.

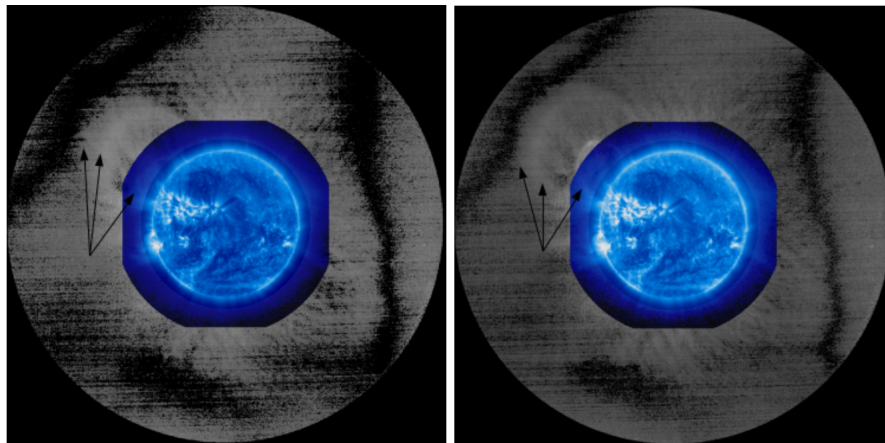


FIGURE 7.1: A three part structure CME as observed on 2015-07-02 at 17:44:12 (left) and 17:55:35 (right) UT by SWAP and K-COR. In the left panel it is seen that the filament is still in the SWAP field of view whereas, the leading front has travelled into K-COR. In the right panel, the leading front, flux-rope and filament can be identified with their separation increased than the first image.

7.2 Data sources

To study the dispersion in speed inside CMEs, we will use the data from SWAP on-board PROBA 2 and coronagraph K-COR at MLSO for addressing the above issue. SWAP has been observing the Sun's upper transition region and lower corona at 174 \AA with high cadence and wide field of view (upto $1.7 R_{sun}$). We will also compliment these data with the data from coronagraphs COR-1 (FOV of $1.5\text{--}4 R_{\odot}$), COR-2 (FOV of $2.5\text{--}15 R_{\odot}$) and Extreme UltraViolet Imager (EUVI) of the SECCHI package (Howard et al. 2002) on-board the twin STEREO spacecraft (STEREO; Kaiser et al. 2008a), the data from LASCO (Brueckner et al. 1995a) (FOV of $2.2\text{--}30 R_{\odot}$), and observations from different passbands of AIA on-board SDO (Lemen et al. 2011).

7.3 Working method

For this work, we plan to select CME events which shows the three part structure in the field-of-view of SWAP and K-COR (refer figure 7.1). Next using the images of SWAP we plan to track the CME (flux-rope and the prominence) in EUV, and then using the data from K-COR, we again track the CME (leading front and flux-rope) in WL. Figure 7.1 shows that though the CME structure seen in EUV is present in the SWAP field of view, it's leading front has already formed in the K-COR field of view. Also, in the right panel of Figure 7.1, the relative change in separation between the leading edge and prominence material can be seen to have increased, clearly showing presence of a velocity gradient from the prominence to the leading edge.

On tracking the flux-rope, it will provide us with information on the impulsive driving force (the Lorentz force), and on tracking the leading front, we will understand the dynamics of the plasma pile up. From the height-time data of the prominence, flux-rope and leading front, we will get their velocity and acceleration profiles and hence the presence of velocity dispersion inside a CME. A knowledge on this differential kinematic profiles will also establish the importance of modelling the prominence material (as a part of the three part structure CME) and not just the flux-rope or leading front for the existing CME models, placing us a cut above our present understanding of their kinematics in the inner corona. Again by tracking the change in separation between the three parts (as mentioned earlier) with height, we will get rich information on the effect of this velocity dispersion on SSE of CMEs in the IC (something on which we donot have a strong footing yet).

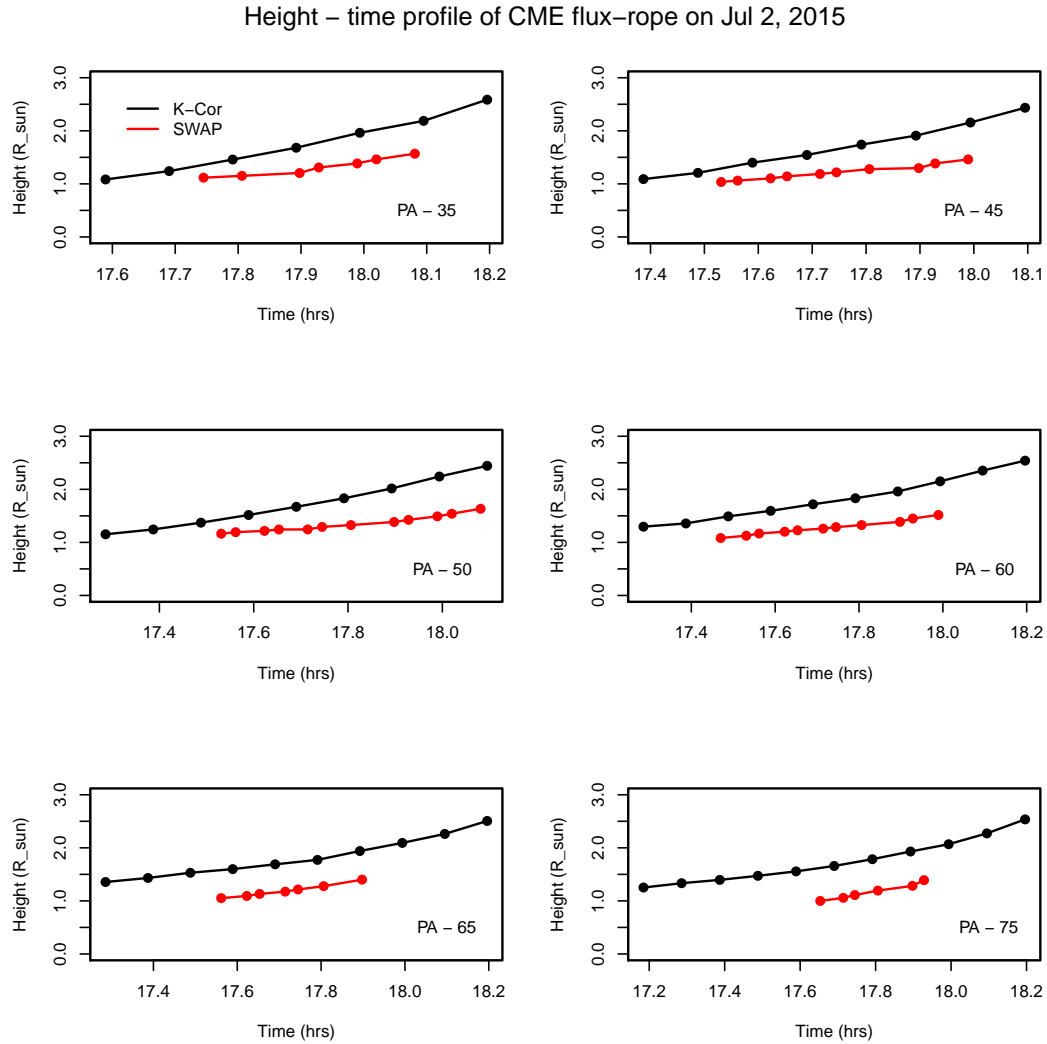


FIGURE 7.2: A height time profile of the CME flux-ropes and core in K-Cor and SWAP respectively, along different position angles is shown.

7.4 Results

In Figure 7.2, we see a height time plot of the CME flux-ropes and the core tracked in K-Cor and SWAP field of view. The different plots correspond to different position angles. We find that the separation between the core of the CME and the edge of the flux-ropes is increasing along all the position angles considered here. This clearly shows the difference in speeds of the two structures, and hence the presence of velocity dispersion.

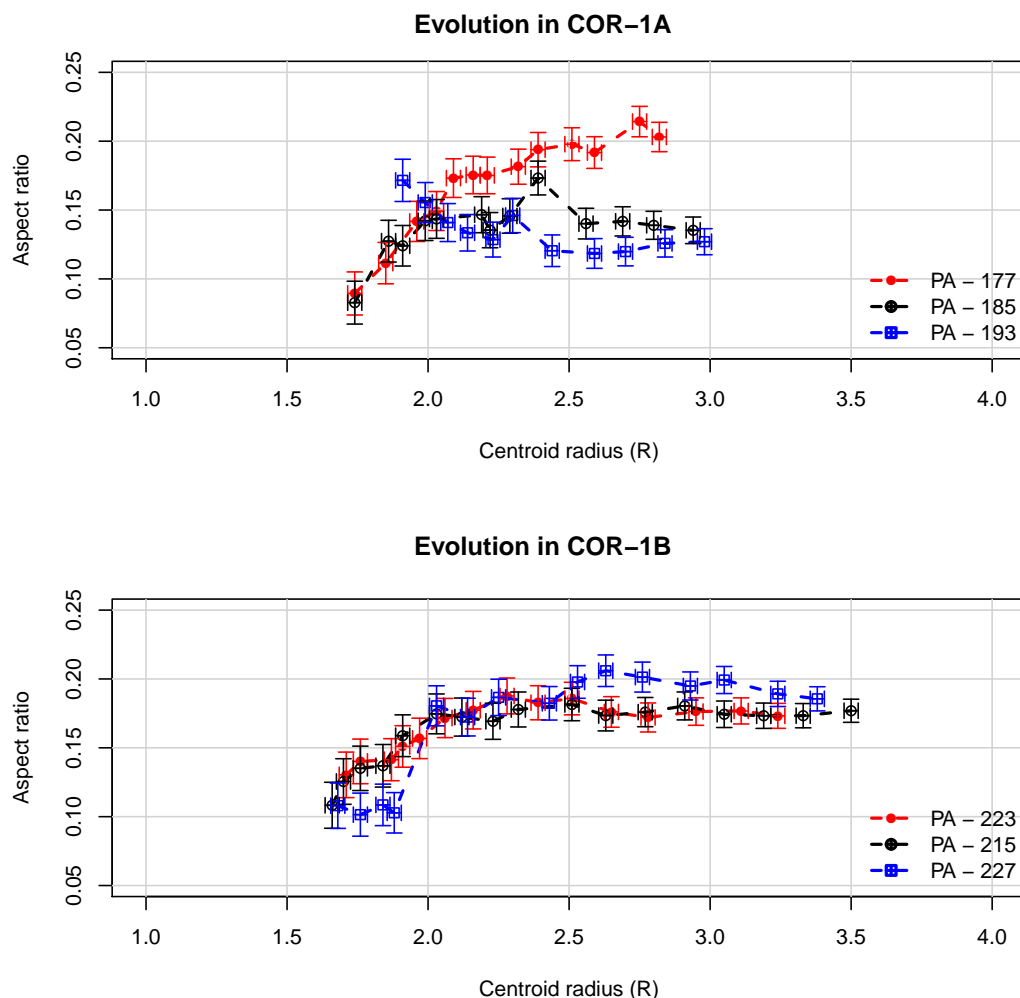


FIGURE 7.3: Evolution of the CME aspect ratio for the CME on 2012-03-12, as observed in the COR-1A and COR-1B field of view. The different color coded data points denoted different position angles of tracking.

In Figure 7.3, we plot a variation of the aspect ratio of the CME (the ratio of the flux-rope minor radius to the major radius) with the flux-rope centroid radius in COR-1A and COR-1B field of view. The different color coded data points denote tracking of the CME at different position angles. We find that the aspect ratio initially increases and then saturates after a certain height. This is the height at which self-similar expansion of the CME is expected to begin. What we notice is that the trend of the aspect ratio variation is different in different position angles. We see that along certain position angles, we find the aspect ratio is still showing

an increasing trend, while along one position angle, a decreasing trend is observed, which suggests that the rate of expansion of the minor radius is lesser than the rate of expansion of the major radius. We must note here, that these are measurements made on the plane of the sky, so a measurement of the same, using reconstruction techniques (for example, triangulation technique) will help in providing a better perspective.

7.5 Conclusion

Since this work is under progress, we are yet to arrive at results that will merit strong conclusions, but from the preliminary results, as shown in Figure 7.2 and Figure 7.3 it is clear that we have been successful in capturing the dispersion in radial velocity inside CMEs, that too in the inner corona, and the impact of it on the phenomena of self-similar expansion can also be noticed.

This study will throw light on the individual kinematic behaviours of the three part structure of CMEs and thus help us understand velocity dispersion inside them. This work will also help us to realize the significance of the assumption of SSE in CME kinematics in the IC in a much better way. Further, It will also provide rich inputs to the observation plans of upcoming missions like VELC on-board ADITYA L1 (Prasad et al. 2017b), which will be observing the IC in 3 visible and 1 IR channel and the giant ASPIICS on-board PROBA 3 (Renotte et al. 2014a) which will be observing the IC in 6 different passbands.

Chapter 8

Conclusion

This brings us to the final chapter of my thesis, where I would like to summarize the main conclusions from my thesis, thereby noting the relevance of these results to our current understanding of this research area, and to the present and upcoming solar missions that will be studying the solar corona. Finally, I would finish this chapter with the possible future prospects that one can carry forward from this thesis work.

The title of my thesis precisely hints at the two major areas where we are yet to reach a clear understanding regarding the behaviour of Coronal Mass Ejections, which are i) understanding of the early kinematics of CMEs in the inner corona (IC) region and ii) the coupling of this early kinematics in the lower heights to the kinematics happening at the higher heights, in the outer corona and the heliosphere. The different chapters of my thesis have thus, been devoted to works that have results dedicated to improve our understandings in the above two aspects. So, let me present here, in a nutshell, the main conclusions from each chapter of this thesis.

8.1 Chapter 3

This chapter aims at connecting the two major missing links in our understanding of CME kinematics, that are information in IC and discrepancies due to projection. This work studies the 3D kinematics of 59 CMEs in the inner and outer corona by implementing the GCS model (Thernisien, Vourlidas, and Howard 2009b) to the pair of simultaneous observations from COR-1 and COR-2 on-board STEREO-A and STEREO-B. The CMEs are further associated to the source regions they arise from, and this allowed me to connect the true kinematics of the CMEs to their source regions, thereby, studying the imprint of the source regions on the kinematics of CMEs, if any. The identified source regions are classified into three categories, (i) Active Regions, (ii) Prominence Eruptions and (iii) Active Prominences. One of the major results of this chapter is that it unifies the acceleration and width expansion of CMEs as a veritable manifestation of the same Lorentz force. From this unification, it was found that the height at which the impulsive acceleration of CMEs ceases, lies very close to the height at which the rapid width expansion stops, and further, it was found that statistically, these two heights lie mostly in the IC region, in a height range of 2.5-3 R_{\odot} . Thus, building on the premise that it is the same Lorentz force that is responsible for both expanding and accelerating a CME, this result provided the first observational evidence on the statistical height of imprint of Lorentz force on the kinematics of CMEs, by combining 3D acceleration and width expansion profiles in inner corona. This chapter then shows that the true acceleration duration and acceleration magnitudes are anti-correlated, and further, lends support towards the two dynamical classes of CMEs, (i) Impulsive and (ii) Gradual, thereby providing conclusive evidence that the former mainly arises from Active Regions while the later mostly comes from Prominence Eruptions. It shows that the CMEs from ARs are more energetic and hence shoots up to much higher speeds than those arising from PEs. A study of latitudinal deflections of these CMEs showed that the age-old way of studying latitude–position angle distributions to understand CME deflections

might be highly misleading, and only the true unprojected quantities should be used to come to a conclusion. This chapter also shows that the long tail in the distribution of peak speeds and accelerations gets contributed mostly from the CMEs connected to the active regions. Another important aspect of this chapter happens to be the insights obtained from a comparison of the average 3D speeds and the average projected speeds, the later taken from the CDAW catalogue. It seems that for such a comparison, it is very important to ensure the uniqueness of the CME feature that is being tracked in both the process. It further has also shown how misleading the 2D speeds can be for halo or partial-halo CMEs, and hence use of multiple vantage point observations in tracking the CMEs (if available), is encouraged.

8.2 Chapter 4

Having established the importance of studying the kinematics (especially the width and acceleration evolution) in inner corona, this chapter goes a step ahead and shows how the width distribution of slow and fast CMEs vary with the source regions they come from and how the kinematics in the IC gets coupled with the kinematics in the outer corona, the other aim of my thesis. This chapter shows several distinguishing properties that provides evidence in favour of the dynamical classification of CMEs into impulsive and gradual. Further, it shows that the ARs and PEs tend to have a say in classifying the CMEs into impulsive and gradual, and hence several influences and clear imprints of these source regions on the coupling of the kinematics is also presented. The major results of this chapter are i) The 3D peak acceleration is positively correlated with the peak speeds, but the correlation much stronger for the CMEs originating from APs. This behaviour is also seen in a correlation between the speed attained at peak acceleration versus the peak accelerations of the CMEs, thus hinting at the fact that APs should indeed be

considered as a different source region category and should not be included with either AR or PE. ii) An empirical relation is found between the mean speeds in IC and the overall linear speed. Such an empirical relation, besides being based on 3D quantities, will also help in the use of inner coronal observations in CME arrival time predictions, with a possibility of reducing considerably, the lead time of forecast. iii) An anti-correlation is obtained between the true average acceleration and the average speed in inner corona, which shows that the influence of drag force can start as early as in the inner corona. However, the correlation is much weaker for the CMEs arising from PEs, which hints at the possibility of a different CME-solar wind interaction for the CMEs coming from PEs. iv) This chapter also shows that CMEs from active and quiet regions of the Sun experience different acceleration phases, which gets reflected into their kinematics. v) The chapter also shows that a distribution of the heights at which a CME reaches peak acceleration peaks in the range of 2-3 R_{\odot} , which again largely overlaps with the results of Chapter 3. These results thus, lend support towards the possibility of two different ejection and propagation mechanisms for these two dynamical classes of CMEs.

8.3 Chapter 5

The results in the first two chapters have some inherent shortcomings and this chapter on one hand removes those shortcomings, at the same time brings newer insights on CME evolution in the inner corona. This chapter presents the first ever implementation of the GCS model to the ground based coronagraphic observations from K-Cor/MLSO. This enabled the use of combined ground and space-based stereoscopy of CMEs in inner corona. Another very significant aspect of this extended GCS model is that it would enable stereoscopy in the inner corona, even after the loss of STEREO-B in 2014. An application of this model to the

observations from COR-1 and COR-2 on-board STEREO-A/B along with K-Cor and SOHO/LASCO, have provided very significant insights into the understanding of CME kinematics. Firstly, this has enabled the capturing of the initial impulsive acceleration phase of the CMEs in 3D and that too, uniquely in white light (WL) observations, thus evading the inconsistencies that might arise from combining extreme ultraviolet and WL observations. Further, thanks to three vantage point fitting of the GCS model, the geometrical parameters could now be even better constrained, and a study of the face-on and edge-on widths of the CMEs was possible in inner and outer corona. Further, this chapter reports for the first time the evolution of the modelled true GCS volume of the CMEs in inner and outer corona. It shows that the different volumetric sections of the CMEs tend to follow different power laws in their volume evolution profile. It seems the leading elliptical front of the CME expands at a much faster rate than the CME legs, and hence hints at a differential volume expansion inside CMEs. Further, it also reports that the total CME volume follows a steeper power law profile in the inner corona, while a much flatter power law profile in the outer corona, thus clearly hinting towards the fact that possibly there being two different expansion mechanisms of CMEs at these two height regimes.

8.4 Chapter 6

This chapter shows the significance of radio observations in the understanding of certain aspects of CME kinematics. It studies a CME that occurred on 26 January 2014 that was found to be associated with a Type-II burst by using several space and ground based observations. The main aim of this work was to locate the source of the Type-II burst. From this chapter, it is shown that when the WL shock height is much higher than the shock height inferred from the type-II burst starting frequency, then the shock signatures might be coming from the CME

flanks instead of the leading CME nose. Finally, with the help of radio imaging observations, it was found that the source of the type-II burst was indeed located at the Southern flank of the CME. The chapter also points out a CME streamer interaction and how relevant it was in the type-II emission originating at the flanks. This chapter thus, shows the necessity of the use of radio spectral and imaging observations for pin pointing the section of the CME associated shock surface that accelerates the electrons that gives rise to the Type-II burst.

8.5 Chapter 7

It is understood now that around 75% of CMEs show a three part structure with a leading front, a dark cavity (the flux-rope) and the inner core (supposedly the prominence material). The morphological appearance of CMEs exhibiting three part structure are different as seen in WL and EUV and this chapter tries to probe the individual kinematics of the three part structure of CMEs as observed in EUV and WL (in a well overlapping FOV), separately and compare their kinematic profiles, which may provide many interesting inferences on the evolution of their physical properties. This work is under progress, and it is a part of my visit to the Royal Observatory of Belgium, as a part of the Guest Investigator program of the PROBA-2 mission. Now, CMEs, are not rigid bodies but a plasma with embedded magnetic field (the flux-rope) and this chapter aims to study the differences in velocity (called the velocity dispersion) of propagation of the three parts moving from the inner core to the leading front, as the CMEs evolve from the IC to the Heliosphere. This investigation will help in understanding the association of this velocity dispersion with self similar expansion and hence put better constraints on the validity of the later, in the context of inner coronal evolution of CMEs.

8.6 Novelty of the thesis

The works included in my thesis have pertained to different aspects of the kinematic behaviours of CMEs. The main novel aspects that my thesis contributes to our existing understanding of CMEs can be summed up as follows:

- First observational evidence (based on 3D acceleration and width evolution profiles) in support of the premise that the same Lorentz force is responsible for both accelerating and expanding a CME.
- First observational evidence on the statistical height of imprint of Lorentz force on CME kinematics by combining 3D acceleration and width expansion profiles.
- For the first time we report two different power laws for the width distribution of CMEs connected to different source regions (ARs and PEs).
- An empirical relation between the peak 3D speed and acceleration, showing that the two parameters are better coupled for CMEs originating from APs.
- An empirical relation relating the 3D inner coronal mean speed to the overall linear speed. Thus removing the dependency on outer coronal observations for arrival time predictions, a case for space missions which have dedicated inner coronal observations only.
- The drag forces can start acting even as early as in the IC region. At the same time, the influence of the drag force arising out of the CME-solar wind interaction is possibly different for CMEs originating from PEs.
- A similar height range ($2-3 R_{\odot}$) is presented where the CME tends to reach its peak acceleration. Thus providing another observational evidence in support of the fact that the Lorentz force is also responsible for propelling the CMEs in reaching their peak speeds.

- For the first time, the GCS model application has been extended to the use of ground based coronagraph K-Cor of MLSO : the Extended - GCS (EGCS) model.
- For the first time we were able to do 3 vantage point tracking of the CMEs in inner corona, uniquely in WL observations. This has allowed us to capture the complete impulsive acceleration phase of CMEs in WL, without needing the combination of extreme ultraviolet observations to do so.
- For the first time we have shown a power law variation of CME volume with height. We have shown that the total volume follows different power laws at different height regimes, which is below and beyond $4 R_{\odot}$.
- For the first time we have showed that the volume of different parts of the CME tend to follow different power laws, thus indicating towards a differential volume evolution inside CMEs.

8.7 Future Work

The conclusions on CME kinematics presented here in Chapters 3 and 4 are primarily based on 59 CME events. An extension of this work on an even larger sample set will help in arriving at stronger conclusions. The power laws on width distributions for different source region CMEs is based on projected width and hence a study on the distribution of the true width will be an important step forward. The conclusions presented in chapter 5 assumes that the CME flux-rope experiences no rotation. To have a better understanding on CME rotation, off the ecliptic observations will be crucial and hence in future extending the application of this EGCS model to the observations taken by the Solar Orbiter will be useful in understanding CME rotations. Also, the coronagraph VELC on-board the ADITYA L1 mission has very similar FOV as that of K-Cor, hence, in future,

an extension of the application of the EGCS model to the observations taken by VELC will be very crucial and useful. The empirical relation between the mean speed in IC and the overall linear speed that is expected to minimise the lead time of forecast in regard to CME arrival time predictions, need to be tested on real time data, as the result will be affected by the telemetry rate of the instrument as well.

We believe the results of this work will further help in planning observation campaigns for the existing and upcoming space missions which are/will be observing the inner corona, like the Solar Orbiter, PROBA-3/ASPIICS, ADITYA-L1/VELC. It will also provide rich inputs to the models that study CME ejection and evolution, thereby better constraining the model parameters.

Bibliography

- Aschwanden, M.J.: 2016, Global Energetics of Solar Flares. IV. Coronal Mass Ejection Energetics. *Astrophys. J.* **831**, 105. DOI. ADS.
- Aschwanden, M.J., Scholkmann, F., Béthune, W., Schmutz, W., Abramenko, V., Cheung, M.C.M., Müller, D., Benz, A., Chernov, G., Kritsuk, A.G., Scargle, J.D., Melatos, A., Wagoner, R.V., Trimble, V., Green, W.H.: 2018, Order out of Randomness: Self-Organization Processes in Astrophysics. *Space Sci. Rev.* **214**, 55. DOI. ADS.
- Bahcall, J.N.: 2001, High-energy physics: Neutrinos reveal split personalities. *Nature* **412**, 29. ADS.
- Bahcall, J.N., Huebner, W.F., Lubow, S.H., Parker, P.D., Ulrich, R.K.: 1982, Standard solar models and the uncertainties in predicted capture rates of solar neutrinos. *Rev. Mod. Phys.* **54**, 767. DOI. <https://link.aps.org/doi/10.1103/RevModPhys.54.767>.
- Bak, P., Tang, C., Wiesenfeld, K.: 1987, Self-organized criticality: An explanation of the 1/f noise. *Phys. Rev. Lett.* **59**, 381. DOI. <https://link.aps.org/doi/10.1103/PhysRevLett.59.381>.
- Balmaceda, L.A., Vourlidas, A., Stenborg, G., Dal Lago, A.: 2018a, How Reliable Are the Properties of Coronal Mass Ejections Measured from a Single Viewpoint? *Astrophys. J.* **863**, 57. DOI. ADS.
- Balmaceda, L.A., Vourlidas, A., Stenborg, G., Dal Lago, A.: 2018b, How Reliable Are the Properties of Coronal Mass Ejections Measured from a Single Viewpoint? *Astrophys. J.* **863**, 57. DOI. ADS.
- Balmaceda, L.A., Vourlidas, A., Stenborg, G., Dal Lago, A.: 2018c, How Reliable Are the Properties of Coronal Mass Ejections Measured from a Single Viewpoint? *Astrophys. J.* **863**, 57. DOI. ADS.
- Banerjee, D., Patel, R., Pant, V.: 2017, The inner coronagraph on board aditya-l1 and automatic detection of cmes. *Proceedings of the International Astronomical Union* **13**, 340–343. DOI.
- Bein, B.M., Berkebile-Stoiser, S., Veronig, A.M., Temmer, M., Muhr, N., Kienreich, I., Utz, D., Vršnak, B.: 2011a, Impulsive Acceleration of Coronal Mass Ejections. I. Statistics and Coronal Mass Ejection Source Region Characteristics. *Astrophys. J.* **738**, 191. DOI. ADS.
- Bein, B.M., Berkebile-Stoiser, S., Veronig, A.M., Temmer, M., Muhr, N., Kienreich, I., Utz, D., Vršnak, B.: 2011b, Impulsive Acceleration of Coronal Mass Ejections. I. Statistics and Coronal Mass Ejection Source Region Characteristics. *Astrophys. J.* **738**, 191. DOI. ADS.

- Bein, B.M., Berkebile-Stoiser, S., Veronig, A.M., Temmer, M., Vršnak, B.: 2012, Impulsive Acceleration of Coronal Mass Ejections. II. Relation to Soft X-Ray Flares and Filament Eruptions. *Astrophys. J.* **755**, 44. DOI. ADS.
- Bertaux, J.L., Pellinen, R., Chassefiere, E., Dimarellis, E., Goutail, F., Holzer, T.E., Kelha, V., Korpela, S., Kyrola, E., Lallement, R.: 1988, *SWAN: A study of solar wind anisotropies*, In ESA, The SOHO Mission. Scientific and Technical Aspects of the Instruments p 63-68 (SEE N90-13302 04-92). ADS.
- Bidhu, S., Iren, S., Benjamin, D.: 2017, Cme speed and angular width distributions during 23 and 24 solar cycle maximum.
- Biermann, L.: 1951, Kometenschweife und solare Korpuskularstrahlung. *Z. Astrophys.* **29**, 274. ADS.
- Billings, D.E.: 1966, *A guide to the solar corona*. ADS.
- Bosman, E., Bothmer, V., Nisticò, G., Vourlidis, A., Howard, R.A., Davies, J.A.: 2012, Three-Dimensional Properties of Coronal Mass Ejections from STEREO/SECCHI Observations. *Solar Phys.* **281**, 167. DOI. ADS.
- Bougeret, J.L., Goetz, K., Kaiser, M.L., Bale, S.D., Kellogg, P.J., Maksimovic, M., Monge, N., Monson, S.J., Astier, P.L., Davy, S., Dekkali, M., Hinze, J.J., Manning, R.E., Aguilar-Rodriguez, E., Bonnin, X., Briand, C., Cairns, I.H., Cattell, C.A., Cecconi, B., Eastwood, J., Ergun, R.E., Fainberg, J., Hoang, S., Huttunen, K.E.J., Krucker, S., Lecacheux, A., MacDowall, R.J., Macher, W., Mangeney, A., Meetre, C.A., Moussas, X., Nguyen, Q.N., Oswald, T.H., Pulupa, M., Reiner, M.J., Robinson, P.A., Rucker, H., Salem, C., Santolik, O., Silvis, J.M., Ullrich, R., Zarka, P., Zouganelis, I.: 2008, S/WAVES: The Radio and Plasma Wave Investigation on the STEREO Mission. *Space Sci. Rev.* **136**, 487. DOI. ADS.
- Boursier, Y., Lamy, P., Llebaria, A., Goudail, F., Robelus, S.: 2009, The ARTEMIS Catalog of LASCO Coronal Mass Ejections. Automatic Recognition of Transient Events and Marseille Inventory from Synoptic maps. *Solar Phys.* **257**, 125. DOI. ADS.
- Brueckner, G.E., Howard, R.A., Koomen, M.J., Korendyke, C.M., Michels, D.J., Moses, J.D., Socker, D.G., Dere, K.P., Lamy, P.L., Llebaria, A., Bout, M.V., Schwenn, R., Simnett, G.M., Bedford, D.K., Eyles, C.J.: 1995a, The Large Angle Spectroscopic Coronagraph (LASCO). *Solar Phys.* **162**, 357. DOI. ADS.
- Brueckner, G.E., Howard, R.A., Koomen, M.J., Korendyke, C.M., Michels, D.J., Moses, J.D., Socker, D.G., Dere, K.P., Lamy, P.L., Llebaria, A., Bout, M.V., Schwenn, R., Simnett, G.M., Bedford, D.K., Eyles, C.J.: 1995b, The Large Angle Spectroscopic Coronagraph (LASCO). *Solar Phys.* **162**, 357. DOI. ADS.
- Burkepile, J.T., Hundhausen, A.J., Stanger, A.L., St. Cyr, O.C., Seiden, J.A.: 2004, Role of projection effects on solar coronal mass ejection properties: 1. A study of CMEs associated with limb activity. *Journal of Geophysical Research (Space Physics)* **109**, A03103. DOI. ADS.
- Byrne, J.P., Morgan, H., Habbal, S.R., Gallagher, P.T.: 2012, AUTOMATIC DETECTION AND TRACKING OF CORONAL MASS EJECTIONS. II. MULTISCALE FILTERING OF CORONAGRAPH IMAGES. *The Astrophysical Journal* **752**, 145. DOI. <https://doi.org/10.1088%2F0004-637x%2F752%2F2%2F145>.

- Byrne, J.P., Morgan, H., Habbal, S.R., Gallagher, P.T.: 2012, Automatic Detection and Tracking of Coronal Mass Ejections. II. Multiscale Filtering of Coronagraph Images. *Astrophys. J.* **752**, 145. DOI. ADS.
- Cabello, I., Cremades, H., Balmaceda, L., Dohmen, I.: 2016a, First Simultaneous Views of the Axial and Lateral Perspectives of a Coronal Mass Ejection. *Solar Phys.* **291**, 1799. DOI. ADS.
- Cabello, I., Cremades, H., Balmaceda, L., Dohmen, I.: 2016b, First Simultaneous Views of the Axial and Lateral Perspectives of a Coronal Mass Ejection. *Solar Phys.* **291**, 1799. DOI. ADS.
- Cane, H.V., Stone, R.G.: 1984, Type II solar radio bursts, interplanetary shocks, and energetic particle events. *Astrophys. J.* **282**, 339. DOI. ADS.
- Cane, H.V., Richardson, I.G., St. Cyr, O.C.: 2000, Coronal mass ejections, interplanetary ejecta and geomagnetic storms. *Geophys. Res. Lett.* **27**, 3591. DOI. ADS.
- Canfield, R.C., Hudson, H.S., McKenzie, D.E.: 1999, Sigmoidal morphology and eruptive solar activity. *Geophys. Res. Lett.* **26**, 627. DOI. ADS.
- Carley, E.P., Vilmer, N., Vourlidis, A.: 2020, Radio observations of coronal mass ejection initiation and development in the low solar corona. *Frontiers in Astronomy and Space Sciences* **7**, 79. DOI. ADS.
- Chen, A.Q., Chen, P.F., Fang, C.: 2006, On the CME velocity distribution. *Astron. Astrophys.* **456**, 1153. DOI. ADS.
- Cheng, X., Zhang, J., Kliem, B., Török, T., Xing, C., Zhou, Z.J., Inhester, B., Ding, M.D.: 2020a, Initiation and Early Kinematic Evolution of Solar Eruptions. *Astrophys. J.* **894**, 85. DOI. ADS.
- Cheng, X., Zhang, J., Kliem, B., Török, T., Xing, C., Zhou, Z.J., Inhester, B., Ding, M.D.: 2020b, Initiation and Early Kinematic Evolution of Solar Eruptions. *Astrophys. J.* **894**, 85. DOI. ADS.
- Cho, K.-S., Lee, J., Gary, D.E., Moon, Y.-J., Park, Y.D.: 2007, Magnetic Field Strength in the Solar Corona from Type II Band Splitting. *Astrophys. J.* **665**, 799. DOI. ADS.
- Cho, K.-S., Gopalswamy, N., Kwon, R.-Y., Kim, R.-S., Yashiro, S.: 2013, A High-frequency Type II Solar Radio Burst Associated with the 2011 February 13 Coronal Mass Ejection. *Astrophys. J.* **765**, 148. DOI. ADS.
- Clauset, A., Rohilla Shalizi, C., Newman, M.E.J.: 2007, Power-law distributions in empirical data. *ArXiv e-prints*. ADS.
- Colaninno, R.C.: 2012, Investigation of the Forces that Govern the Three-Dimensional Propagation and Expansion of Coronal Mass Ejections from Sun to Earth. PhD thesis, George Mason University, Virginia. ADS.
- Cremades, H., Bothmer, V.: 2004, On the three-dimensional configuration of coronal mass ejections. *Astron. Astrophys.* **422**, 307. DOI. ADS.
- Cremades, H., Iglesias, F.A., Merenda, L.A.: 2020a, Asymmetric expansion of coronal mass ejections in the low corona. *Astron. Astrophys.* **635**, A100. DOI. ADS.

- Cremades, H., Iglesias, F.A., Merenda, L.A.: 2020b, Asymmetric expansion of coronal mass ejections in the low corona. *Astron. Astrophys.* **635**, A100. DOI. ADS.
- de Wijn, A.G., Burkepile, J.T., Tomczyk, S., Nelson, P.G., Huang, P., Gallagher, D.: 2012, Stray light and polarimetry considerations for the COSMO K-Coronagraph. In: Stepp, L.M., Gilmozzi, R., Hall, H.J. (eds.) *Ground-based and Airborne Telescopes IV, Society of Photo-Optical Instrumentation Engineers (SPIE) Conference Series* **8444**, 84443N. DOI. ADS.
- Delaboudinière, J.-P., Artzner, G.E., Brunaud, J., Gabriel, A.H., Hochedez, J.F., Millier, F., Song, X.Y., Au, B., Dere, K.P., Howard, R.A., Kreplin, R., Michels, D.J., Moses, J.D., Defise, J.M., Jamar, C., Rochus, P., Chauvineau, J.P., Marioge, J.P., Catura, R.C., Lemen, J.R., Shing, L., Stern, R.A., Gurman, J.B., Neupert, W.M., Maucherat, A., Clette, F., Cugnon, P., van Dessel, E.L.: 1995, EIT: Extreme-Ultraviolet Imaging Telescope for the SOHO Mission. *Solar Phys.* **162**, 291. DOI. ADS.
- Dere, K.P., Brueckner, G.E., Howard, R.A., Koomen, M.J., Korendyke, C.M., Kreplin, R.W., Michels, D.J., Moses, J.D., Moulton, N.E., Socker, D.G., St. Cyr, O.C., Delaboudinière, J.P., Artzner, G.E., Brunaud, J., Gabriel, A.H., Hochedez, J.F., Millier, F., Song, X.Y., Chauvineau, J.P., Marioge, J.P., Defise, J.M., Jamar, C., Rochus, P., Catura, R.C., Lemen, J.R., Gurman, J.B., Neupert, W., Clette, F., Cugnon, P., van Dessel, E.L., Lamy, P.L., Llebaria, A., Schwenn, R., Simnett, G.M.: 1997, EIT and LASCO Observations of the Initiation of a Coronal Mass Ejection. *Solar Phys.* **175**, 601. DOI. ADS.
- D'Huys, E., Seaton, D.B., Poedts, S., Berghmans, D.: 2014, Observational Characteristics of Coronal Mass Ejections without Low-coronal Signatures. *Astrophys. J.* **795**, 49. DOI. ADS.
- D'Huys, E., Berghmans, D., Seaton, D.B., Poedts, S.: 2016, The Effect of Limited Sample Sizes on the Accuracy of the Estimated Scaling Parameter for Power-Law-Distributed Solar Data. *Solar Phys.* **291**, 1561. DOI. ADS.
- Domingo, V., Fleck, B., Poland, A.I.: 1995, The SOHO Mission: an Overview. *Solar Phys.* **162**, 1. DOI. ADS.
- Dominique, M., Hochedez, J.-F., Schmutz, W., Dammasch, I.E., Shapiro, A.I., Kretschmar, M., Zhukov, A.N., Gillotay, D., Stockman, Y., BenMoussa, A.: 2013, The LYRA Instrument Onboard PROBA2: Description and In-Flight Performance. *Solar Phys.* **286**, 21. DOI. ADS.
- Feng, S.W., Chen, Y., Kong, X.L., Li, G., Song, H.Q., Feng, X.S., Liu, Y.: 2012, Radio Signatures of Coronal-mass-ejection-Streamer Interaction and Source Diagnostics of Type II Radio Burst. *Astrophys. J.* **753**, 21. DOI. ADS.
- Fineschi, S., Antonucci, E., Naletto, G., Romoli, M., Spadaro, D., Nicolini, G., Abbo, L., Andretta, V., Bemporad, A., Berlicki, A., Capobianco, G., Crescenzo, G., Da Deppo, V., Focardi, M., Landini, F., Massone, G., Malvezzi, M.A., Moses, J.D., Nicolosi, P., Pancrazzi, M., Pelizzo, M.-G., Poletto, L., Schühle, U.H., Solanki, S.K., Telloni, D., Teriaca, L., Uslenghi, M.: 2012, METIS: a novel coronagraph design for the Solar Orbiter mission. In: Takahashi, T., Murray, S.S., den Herder, J.-W.A. (eds.) *Space Telescopes and Instrumentation 2012: Ultraviolet to Gamma Ray, Society of Photo-Optical Instrumentation Engineers (SPIE) Conference Series* **8443**, 84433H. DOI. ADS.

- Foukal, P.V.: 2004, *Solar Astrophysics, 2nd, Revised Edition*. [ADS](#).
- Fröhlich, C., Romero, J., Roth, H., Wehrli, C., Andersen, B.N., Appourchaux, T., Domingo, V., Telljohann, U., Berthomieu, G., Delache, P., Provost, J., Toutain, T., Crommelynck, D.A., Chevalier, A., Fichot, A., Däppen, W., Gough, D., Hoeksema, T., Jiménez, A., Gómez, M.F., Herreros, J.M., Roca Cortés, T., Jones, A.R., Pap, J.M., Willson, R.C.: 1995, VIRGO: Experiment for Helioseismology and Solar Irradiance Monitoring. *Solar Phys.* **162**, 101. [DOI](#). [ADS](#).
- Gabriel, A.H., GOLF Team: 1991, Global oscillations at low frequency from the SOHO mission (GOLF). *Advances in Space Research* **11**, 103. [DOI](#). [ADS](#).
- Gallagher, P.T., Lawrence, G.R., Dennis, B.R.: 2003, Rapid Acceleration of a Coronal Mass Ejection in the Low Corona and Implications for Propagation. *Astrophys. J. Lett.* **588**, L53. [DOI](#). [ADS](#).
- Galvin, A.B., Kistler, L.M., Popecki, M.A., Farrugia, C.J., Simunac, K.D.C., Ellis, L., Möbius, E., Lee, M.A., Boehm, M., Carroll, J., Crawshaw, A., Conti, M., Demaine, P., Ellis, S., Gaidos, J.A., Googins, J., Granoff, M., Gustafson, A., Heirtzler, D., King, B., Knauss, U., Levasseur, J., Longworth, S., Singer, K., Turco, S., Vachon, P., Vosbury, M., Widholm, M., Blush, L.M., Karrer, R., Bochsler, P., Daoudi, H., Etter, A., Fischer, J., Jost, J., Opitz, A., Sigrist, M., Wurzl, P., Klecker, B., Ertl, M., Seidenschwang, E., Wimmer-Schweingruber, R.F., Koeten, M., Thompson, B., Steinfeld, D.: 2008, The Plasma and Suprathermal Ion Composition (PLASTIC) Investigation on the STEREO Observatories. *Space Sci. Rev.* **136**, 437. [DOI](#). [ADS](#).
- Gilbert, H.R., Holzer, T.E., Burkepile, J.T., Hundhausen, A.J.: 2000, Active and eruptive prominences and their relationship to coronal mass ejections. *The Astrophysical Journal* **537**, 503. [DOI](#). <https://doi.org/10.1086%2F309030>.
- Gopalswamy, N.: 2004, A Global Picture of CMEs in the Inner Heliosphere. In: Poletto, G., Suess, S.T. (eds.) *The Sun and the Heliosphere as an Integrated System, Astrophysics and Space Science Library* **317**, 201. [DOI](#). [ADS](#).
- Gopalswamy, N.: 2006a, Coronal Mass Ejections and Type II Radio Bursts. *Geophys. Mono. Ser.165, Am. Geophys. Un., Washington DC, 207*. [DOI](#). [ADS](#).
- Gopalswamy, N.: 2006b, Coronal Mass Ejections of Solar Cycle 23. *Journal of Astrophysics and Astronomy* **27**, 243. [DOI](#). [ADS](#).
- Gopalswamy, N.: 2017, Extreme Solar Eruptions and their Space Weather Consequences. *arXiv e-prints*, arXiv:1709.03165. [ADS](#).
- Gopalswamy, N., Yashiro, S.: 2011, The Strength and Radial Profile of the Coronal Magnetic Field from the Standoff Distance of a Coronal Mass Ejection-driven Shock. *Astrophys. J. Lett.* **736**, L17. [DOI](#). [ADS](#).
- Gopalswamy, N., Lara, A., Lepping, R.P., Kaiser, M.L., Berdichevsky, D., St. Cyr, O.C.: 2000a, Interplanetary acceleration of coronal mass ejections. *Geophys. Res. Lett.* **27**, 145. [DOI](#). [ADS](#).
- Gopalswamy, N., Lara, A., Lepping, R.P., Kaiser, M.L., Berdichevsky, D., St. Cyr, O.C.: 2000b, Interplanetary acceleration of coronal mass ejections. *Geophys. Res. Lett.* **27**, 145. [DOI](#). [ADS](#).

- Gopalswamy, N., Shimojo, M., Lu, W., Yashiro, S., Shibasaki, K., Howard, R.A.: 2003, Prominence eruptions and coronal mass ejection: A statistical study using microwave observations. *The Astrophysical Journal* **586**, 562. DOI. <https://doi.org/10.1086%2F367614>.
- Gopalswamy, N., Aguilar-Rodriguez, E., Yashiro, S., Nunes, S., Kaiser, M.L., Howard, R.A.: 2005, Type II radio bursts and energetic solar eruptions. *Geophys. Res. (Space Phys)* **110**, A12S07. DOI. ADS.
- Gopalswamy, N., Yashiro, S., Xie, H., Akiyama, S., Aguilar-Rodriguez, E., Kaiser, M.L., Howard, R.A., Bougeret, J.-L.: 2008, Radio-Quiet Fast and Wide Coronal Mass Ejections. *Astrophys. J.* **674**, 560. DOI. ADS.
- Gopalswamy, N., Mäkelä, P., Xie, H., Akiyama, S., Yashiro, S.: 2009a, CME interactions with coronal holes and their interplanetary consequences. *Journal of Geophysical Research (Space Physics)* **114**, A00A22. DOI. ADS.
- Gopalswamy, N., Thompson, W.T., Davila, J.M., Kaiser, M.L., Yashiro, S., Mäkelä, P., Michalek, G., Bougeret, J.-L., Howard, R.A.: 2009b, Relation Between Type II Bursts and CMEs Inferred from STEREO Observations. *Solar Phys.* **259**, 227. DOI. ADS.
- Gopalswamy, N., Dal Lago, A., Yashiro, S., Akiyama, S.: 2009c, The Expansion and Radial Speeds of Coronal Mass Ejections. *Central European Astrophysical Bulletin* **33**, 115. ADS.
- Gopalswamy, N., Yashiro, S., Michalek, G., Stenborg, G., Vourlidas, A., Freeland, S., Howard, R.: 2009d, The SOHO/LASCO CME Catalog. *Earth Moon and Planets* **104**, 295. DOI. ADS.
- Gopalswamy, N., Yashiro, S., Michalek, G., Stenborg, G., Vourlidas, A., Freeland, S., Howard, R.: 2009e, The SOHO/LASCO CME Catalog. *Earth Moon and Planets* **104**, 295. DOI. ADS.
- Gopalswamy, N., Akiyama, S., Yashiro, S., Mäkelä, P.: 2010, Coronal Mass Ejections from Sunspot and Non-Sunspot Regions. *Astrophysics and Space Science Proceedings* **19**, 289. DOI. ADS.
- Gopalswamy, N., Xie, H., Mäkelä, P., Akiyama, S., Yashiro, S., Kaiser, M.L., Howard, R.A., Bougeret, J.-L.: 2010, INTERPLANETARY SHOCKS LACKING TYPE II RADIO BURSTS. *The Astrophysical Journal* **710**, 1111. DOI. <https://doi.org/10.1088%2F0004-637x%2F710%2F2%2F1111>.
- Gopalswamy, N., Thompson, W.T., Davila, J.M., Kaiser, M.L., Yashiro, S., Mäkelä, P., Michalek, G., Bougeret, J.-L., Howard, R.A.: 2012, Erratum: Relation Between Type II Bursts and CMEs Inferred from STEREO Observations. *Solar Phys.* **277**, 459. DOI. ADS.
- Gopalswamy, N., Xie, H., Mäkelä, P., Yashiro, S., Akiyama, S., Uddin, W., Srivastava, A.K., Joshi, N.C., Chandra, R., Manoharan, P.K., Mahalakshmi, K., Dwivedi, V.C., Jain, R., Awasthi, A.K., Nitta, N.V., Aschwanden, M.J., Choudhary, D.P.: 2013, Height of shock formation in the solar corona inferred from observations of type II radio bursts and coronal mass ejections. *Advances in Space Research* **51**, 1981. DOI. ADS.
- Gopalswamy, N., Akiyama, S., Yashiro, S., Xie, H., Mäkelä, P., Michalek, G.: 2014, Anomalous expansion of coronal mass ejections during solar cycle 24 and its space weather implications. *Geophys. Res. Lett.* **41**, 2673. DOI. ADS.

- Gosling, J.T.: 1993a, The solar flare myth. *J. Geophys. Res.* **98**, 18937. DOI. ADS.
- Gosling, J.T.: 1993b, The solar flare myth. *J. Geophys. Res.* **98**, 18937. DOI. ADS.
- Gosling, J.T., Hildner, E., MacQueen, R.M., Munro, R.H., Poland, A.I., Ross, C.L.: 1975, Direct Observations of a Flare Related Coronal and Solar Wind Disturbance. *Solar Phys.* **40**, 439. DOI. ADS.
- Gosling, J.T., McComas, D.J., Phillips, J.L., Bame, S.J.: 1991, Geomagnetic activity associated with earth passage of interplanetary shock disturbances and coronal mass ejections. *J. Geophys. Res.* **96**, 7831. DOI. ADS.
- Grotian, W.: 1939, Zur Frage der Deutung der Linien im Spektrum der Sonnenkorona. *Naturwissenschaften* **27**, 214. DOI. ADS.
- Gui, B., Shen, C., Wang, Y., Ye, P., Liu, J., Wang, S., Zhao, X.: 2011, Quantitative Analysis of CME Deflections in the Corona. *Solar Phys.* **271**, 111. DOI. ADS.
- Halain, J.-P., Berghmans, D., Seaton, D.B., Nicula, B., De Groof, A., Mierla, M., Mazzoli, A., Defise, J.-M., Rochus, P.: 2013, The SWAP EUV Imaging Telescope. Part II: In-flight Performance and Calibration. *Solar Phys.* **286**, 67. DOI. ADS.
- Hansen, R.T., Garcia, C.J., Groganard, R.J.-M., Sheridan, K.V.: 1971, A coronal disturbance observed simultaneously with a white-light corona-meter and the 80 MHz Culgoora radioheliograph. *Proceedings of the Astronomical Society of Australia* **2**, 57. ADS.
- Hess, P., Zhang, J.: 2014, Stereoscopic Study of the Kinematic Evolution of a Coronal Mass Ejection and Its Driven Shock from the Sun to the Earth and the Prediction of Their Arrival Times. *Astrophys. J.* **792**, 49. DOI. ADS.
- Holman, G.D., Pesses, M.E.: 1983, Solar type II radio emission and the shock drift acceleration of electrons. *Astrophys. J.* **267**, 837. DOI. ADS.
- Holzknicht, L., Temmer, M., Dumbović, M., Wellenzohn, S., Krikova, K., Heinemann, S.G., Rodari, M., Vršnak, B., Veronig, A.M.: 2018, CME volume calculation from 3D GCS reconstruction. *Central European Astrophysical Bulletin* **42**, 3. ADS.
- Hovestadt, D., Bochsler, P., Grünwaldt, H., Gliem, F., Hilchenbach, M., Ipavich, F.M., Judge, D.L., Axford, W.I., Balsiger, H., Bürgi, A., Coplan, M., Galvin, A.B., Geiss, J., Gloeckler, G., Hsieh, K.C., Kallenbach, R., Klecker, B., Lee, M.A., Livi, S., Managadze, G.G., Marsch, E., Möbius, E., Neugebauer, M., Reiche, K.-U., Scholer, M., Verigin, M.I., Wilken, D., Wurz, P.: 1995, The Charge, Element, and Isotope Analysis System CELIAS on SOHO. In: Benz, A.O., Krüger, A. (eds.) *Coronal Magnetic Energy Releases* **444**, 271. DOI. ADS.
- Howard, R.A., Michels, D.J., Sheeley, J. N. R., Koomen, M.J.: 1982, The observation of a coronal transient directed at Earth. *Astrophys. J. Lett.* **263**, L101. DOI. ADS.
- Howard, R.A., Moses, J.D., Vourlidas, A., Newmark, J.S., Socker, D.G., Plunkett, S.P., Korendyke, C.M., Cook, J.W., Hurley, A., Davila, J.M., Thompson, W.T., St Cyr, O.C., Mentzell, E., Mehalick, K., Lemen, J.R., Wuelser, J.P., Duncan, D.W., Tarbell, T.D., Wolfson, C.J., Moore, A., Harrison, R.A., Waltham, N.R., Lang, J., Davis, C.J., Eyles, C.J., Mapson-Menard, H., Simnett, G.M., Halain,

- J.P., Defise, J.M., Mazy, E., Rochus, P., Mercier, R., Ravet, M.F., Delmotte, F., Auchere, F., Delaboudiniere, J.P., Bothmer, V., Deutsch, W., Wang, D., Rich, N., Cooper, S., Stephens, V., Maahs, G., Baugh, R., McMullin, D., Carter, T.: 2008a, Sun Earth Connection Coronal and Heliospheric Investigation (SECCHI). *Space Sci. Rev.* **136**, 67. DOI. ADS.
- Howard, R.A., Moses, J.D., Vourlidas, A., Newmark, J.S., Socker, D.G., Plunkett, S.P., Korendyke, C.M., Cook, J.W., Hurley, A., Davila, J.M., Thompson, W.T., St Cyr, O.C., Mentzell, E., Mehalick, K., Lemen, J.R., Wuelser, J.P., Duncan, D.W., Tarbell, T.D., Wolfson, C.J., Moore, A., Harrison, R.A., Waltham, N.R., Lang, J., Davis, C.J., Eyles, C.J., Mapson-Menard, H., Simnett, G.M., Halain, J.P., Defise, J.M., Mazy, E., Rochus, P., Mercier, R., Ravet, M.F., Delmotte, F., Auchere, F., Delaboudinière, J.P., Bothmer, V., Deutsch, W., Wang, D., Rich, N., Cooper, S., Stephens, V., Maahs, G., Baugh, R., McMullin, D., Carter, T.: 2008b, Sun Earth Connection Coronal and Heliospheric Investigation (SECCHI). *Space Sci. Rev.* **136**, 67. DOI. ADS.
- Howard, R., Moses, J.D., Socker, D., Dere, K.P., Cook, J.W.: 2002, Sun earth connection coronal and heliospheric investigation (secchi). *Advances in Space Research* **29**, 2017. DOI.
- Howard, T.: 2011, *Coronal Mass Ejections: An Introduction* **376**. DOI. ADS.
- Hundhausen, A.J.: 1987, The Origin and Propagation of Coronal Mass Ejections (R). In: Pizzo, V.J., Holzer, T., Sime, D.G. (eds.) *Sixth International Solar Wind Conference* **2**, 181. ADS.
- Hundhausen, A.J., Sawyer, C.B., House, L., Illing, R.M.E., Wagner, W.J.: 1984a, Coronal mass ejections observed during the solar maximum mission: Latitude distribution and rate of occurrence. *J. Geophys. Res.* **89**, 2639. DOI. ADS.
- Hundhausen, A.J., Sawyer, C.B., House, L., Illing, R.M.E., Wagner, W.J.: 1984b, Coronal mass ejections observed during the solar maximum mission: Latitude distribution and rate of occurrence. *J. Geophys. Res.* **89**, 2639. DOI. ADS.
- Hutton, J., Morgan, H.: 2017a, Automated detection of coronal mass ejections in three-dimensions using multi-viewpoint observations. *Astron. Astrophys.* **599**, A68. DOI. ADS.
- Hutton, J., Morgan, H.: 2017b, Automated detection of coronal mass ejections in three-dimensions using multi-viewpoint observations. *Astron. Astrophys.* **599**, A68. DOI. ADS.
- Illing, R.M.E., Hundhausen, A.J.: 1985, Observation of a coronal transient from 1.2 to 6 solar radii. *J. Geophys. Res.* **90**, 275. DOI. ADS.
- Illing, R.M.E., Hundhausen, A.J.: 1986, Disruption of a coronal streamer by an eruptive prominence and coronal mass ejection. *J. Geophys. Res.* **91**, 10951. DOI. ADS.
- Isenberg, P.A., Forbes, T.G.: 2007, A three-dimensional line-tied magnetic field model for solar eruptions. *The Astrophysical Journal* **670**, 1453. DOI. <https://doi.org/10.1086%2F522025>.
- Jebaraj, I.C., Magdalenić, J., Podladchikova, T., Scolini, C., Pomoell, J., Veronig, A.M., Dissauer, K., Krupar, V., Kilpua, E.K.J., Poedts, S.: 2020, Using radio triangulation to understand the origin of two subsequent type II radio bursts. *Astron. Astrophys.* **639**, A56. DOI. ADS.

- Joshi, A.D., Srivastava, N.: 2011a, Acceleration of Coronal Mass Ejections from Three-dimensional Reconstruction of STEREO Images. *Astrophys. J.* **739**, 8. DOI. ADS.
- Joshi, A.D., Srivastava, N.: 2011b, Acceleration of Coronal Mass Ejections from Three-dimensional Reconstruction of STEREO Images. *Astrophys. J.* **739**, 8. DOI. ADS.
- Kahler, S.: 1977, The morphological and statistical properties of solar X-ray events with long decay times. *Astrophys. J.* **214**, 891. DOI. ADS.
- Kahler, S.W., Akiyama, S., Gopalswamy, N.: 2012, DEFLECTIONS OF FAST CORONAL MASS EJECTIONS AND THE PROPERTIES OF ASSOCIATED SOLAR ENERGETIC PARTICLE EVENTS. *The Astrophysical Journal* **754**, 100. DOI. <https://doi.org/10.1088%2F0004-637x%2F754%2F2%2F100>.
- Kaiser, M.L., Kucera, T.A., Davila, J.M., St. Cyr, O.C., Guhathakurta, M., Christian, E.: 2008a, The STEREO Mission: An Introduction. *Space Sci. Rev.* **136**, 5. DOI. ADS.
- Kaiser, M.L., Kucera, T.A., Davila, J.M., St. Cyr, O.C., Guhathakurta, M., Christian, E.: 2008b, The STEREO Mission: An Introduction. *Space Sci. Rev.* **136**, 5. DOI. ADS.
- Kay, C., Opher, M., Evans, R.M.: 2013, Forecasting a Coronal Mass Ejection's Altered Trajectory: ForeCAT. *Astrophys. J.* **775**, 5. DOI. ADS.
- Kay, C., Opher, M., Evans, R.M.: 2015, GLOBAL TRENDS OF CME DEFLECTIONS BASED ON CME AND SOLAR PARAMETERS. *The Astrophysical Journal* **805**, 168. DOI. <https://doi.org/10.1088%2F0004-637x%2F805%2F2%2F168>.
- Kishore, P., Kathiravan, C., Ramesh, R., Rajalingam, M., Barve, I.V.: 2014, Gauribidanur Low-Frequency Solar Spectrograph. *Solar Phys.* **289**, 3995. DOI. ADS.
- Kliem, B., Lin, J., Forbes, T.G., Priest, E.R., Török, T.: 2014, CATASTROPHE VERSUS INSTABILITY FOR THE ERUPTION OF a TOROIDAL SOLAR MAGNETIC FLUX ROPE. *The Astrophysical Journal* **789**, 46. DOI. <https://doi.org/10.1088%2F0004-637x%2F789%2F1%2F46>.
- Krieger, A.S., Timothy, A.F., Roelof, E.C.: 1973, A Coronal Hole and Its Identification as the Source of a High Velocity Solar Wind Stream. *Solar Phys.* **29**, 505. DOI. ADS.
- Kumari, A., Ramesh, R., Kathiravan, C., Gopalswamy, N.: 2017a, New Evidence for a Coronal Mass Ejection-driven High Frequency Type II Burst near the Sun. *Astrophys. J.* **843**, 10. DOI. ADS.
- Kumari, A., Ramesh, R., Kathiravan, C., Wang, T.J.: 2017b, Strength of the Solar Coronal Magnetic Field - A Comparison of Independent Estimates Using Contemporaneous Radio and White-Light Observations. *Solar Phys.* **292**, 161. DOI. ADS.
- Kumari, A., Ramesh, R., Kathiravan, C., Wang, T.J., Gopalswamy, N.: 2019, Direct estimates of the solar coronal magnetic field using contemporaneous extreme-ultraviolet, radio, and white-light observations. *Astrophys. J.* **881**, 24. DOI.

- Lamy, P.L., Vivès, S., Curdt, W., Damé, L., Davila, J., Defise, J.-M., Fineschi, S., Heinzl, P., Howard, R., Kuzin, S., Schmutz, W., Tsinganos, K., Zhukov, A.: 2017, ASPICS: a giant, white light and emission line coronagraph for the ESA proba-3 formation flight mission. In: *Society of Photo-Optical Instrumentation Engineers (SPIE) Conference Series, Society of Photo-Optical Instrumentation Engineers (SPIE) Conference Series* **10565**, 105650T. DOI. ADS.
- Lang, K.R.: 1995, Sun, Earth and Sky. *Earth Moon and Planets* **70**, 1. DOI. ADS.
- Leibacher, J.W., Noyes, R.W., Toomre, J., Ulrich, R.K.: 1985, Helioseismology. *Scientific American* **253**, 48. DOI. ADS.
- Lemen, J., Title, A., Boerner, P., Chou, C., Drake, J., Duncan, D., Edwards, C., Friedlaender, F., Heyman, G., Hurlburt, N., Katz, N., Kushner, G., Levay, M., Lindgren, R., Mathur, D., McFeaters, E., Mitchell, S., Rehse, R., Waltham, N.: 2011, The atmospheric imaging assembly (aia) on the solar dynamics observatory (sdo). *Solar Physics* **275**, 17. DOI.
- Lodders, K.: 2003, Solar System Abundances and Condensation Temperatures of the Elements. *Astrophys. J.* **591**, 1220. DOI. ADS.
- Lugaz, N., Farrugia, C.J., Davies, J.A., Möstl, C., Davis, C.J., Roussev, I.I., Temmer, M.: 2012, THE DEFLECTION OF THE TWO INTERACTING CORONAL MASS EJECTIONS OF 2010 MAY 23-24 AS REVEALED BY COMBINED IN SITU MEASUREMENTS AND HELIOSPHERIC IMAGING. *The Astrophysical Journal* **759**, 68. DOI. <https://doi.org/10.1088%2F0004-637x%2F759%2F1%2F68>.
- Lugaz, N., Farrugia, C.J., Winslow, R.M., Small, C.R., Manion, T., Savani, N.P.: 2017, Importance of CME radial expansion on the ability of slow CMEs to drive shocks. *The Astrophysical Journal* **848**, 75. DOI. <https://doi.org/10.3847%2F1538-4357%2Faa8ef9>.
- Luhmann, J.G., Curtis, D.W., Schroeder, P., McCauley, J., Lin, R.P., Larson, D.E., Bale, S.D., Sauvaud, J.-A., Aoustin, C., Mewaldt, R.A., Cummings, A.C., Stone, E.C., Davis, A.J., Cook, W.R., Kecman, B., Wiedenbeck, M.E., von Roseninge, T., Acuna, M.H., Reichenthal, L.S., Shuman, S., Wortman, K.A., Reames, D.V., Mueller-Mellin, R., Kunow, H., Mason, G.M., Walpole, P., Korth, A., Sanderson, T.R., Russell, C.T., Gosling, J.T.: 2008, STEREO IMPACT Investigation Goals, Measurements, and Data Products Overview. *Space Sci. Rev.* **136**, 117. DOI. ADS.
- MacQueen, R.M., Fisher, R.R.: 1983, The Kinematics of Solar Inner Coronal Transients. *Solar Phys.* **89**, 89. DOI. ADS.
- MacQueen, R.M., Csoeke-Poeckh, A., Hildner, E., House, L., Reynolds, R., Stanger, A., Tepoel, H., Wagner, W.: 1980a, The High Altitude Observatory coronagraph/polarimeter on the Solar Maximum Mission. *Solar Phys.* **65**, 91. DOI. ADS.
- MacQueen, R.M., Csoeke-Poeckh, A., Hildner, E., House, L., Reynolds, R., Stanger, A., Tepoel, H., Wagner, W.: 1980b, The High Altitude Observatory Coronagraph/Polarimeter on the Solar Maximum Mission. *Solar Phys.* **65**, 91. DOI. ADS.
- Majumdar, S., Pant, V., Patel, R., Banerjee, D.: 2020a, Connecting 3D Evolution of Coronal Mass Ejections to Their Source Regions. *Astrophys. J.* **899**, 6. DOI. ADS.

- Majumdar, S., Pant, V., Patel, R., Banerjee, D.: 2020b, Connecting 3D Evolution of Coronal Mass Ejections to Their Source Regions. *Astrophys. J.* **899**, 6. DOI. ADS.
- Majumdar, S., Patel, R., Pant, V., Banerjee, D.: 2021a, An Insight into the Coupling of CME Kinematics in Inner and Outer Corona and the Imprint of Source Regions. *Astrophys. J.* **919**, 115. DOI. ADS.
- Majumdar, S., Paavan Tadepalli, S., Sankar Maity, S., Deshpande, K., Kumari, A., Patel, R., Gopalswamy, N.: 2021b, Imaging and Spectral Observations of a Type-II Radio Burst Revealing the Section of the CME-Driven Shock that Accelerates Electrons. *arXiv e-prints*, arXiv:2103.09536. ADS.
- Maričić, D., Vršnak, B., Stanger, A.L., Veronig, A.: 2004, Coronal Mass Ejection of 15 May 2001: I. Evolution of Morphological Features of the Eruption. *Solar Phys.* **225**, 337. DOI. ADS.
- Meng, W.-J., Le, G.-M., Lin, Z.-X., Zhang, Y., Yang, X.-X.: 2014, Distribution of CMEs with Different Angular Widths and Comparison with the Phase of Sunspot Number in the 23rd Solar Cycle. *Chinese Astronomy and Astrophysics* **38**, 85. DOI. ADS.
- Mierla, M., Davila, J., Thompson, W., Inhester, B., Srivastava, N., Kramar, M., St. Cyr, O.C., Stenborg, G., Howard, R.A.: 2008a, A Quick Method for Estimating the Propagation Direction of Coronal Mass Ejections Using STEREO-COR1 Images. *Solar Phys.* **252**, 385. DOI. ADS.
- Mierla, M., Davila, J., Thompson, W., Inhester, B., Srivastava, N., Kramar, M., St. Cyr, O.C., Stenborg, G., Howard, R.A.: 2008b, A Quick Method for Estimating the Propagation Direction of Coronal Mass Ejections Using STEREO-COR1 Images. *Solar Phys.* **252**, 385. DOI. ADS.
- Mierla, M., Inhester, B., Marqué, C., Rodriguez, L., Gissot, S., Zhukov, A.N., Berghmans, D., Davila, J.: 2009, On 3D Reconstruction of Coronal Mass Ejections: I. Method Description and Application to SECCHI-COR Data. *Solar Phys.* **259**, 123. DOI. ADS.
- Mierla, M., Inhester, B., Antunes, A., Boursier, Y., Byrne, J.P., Colaninno, R., Davila, J., de Koning, C.A., Gallagher, P.T., Gissot, S., Howard, R.A., Howard, T.A., Kramar, M., Lamy, P., Liewer, P.C., Maloney, S., Marqué, C., McAteer, R.T.J., Moran, T., Rodriguez, L., Srivastava, N., St. Cyr, O.C., Stenborg, G., Temmer, M., Thernisien, A., Vourlidas, A., West, M.J., Wood, B.E., Zhukov, A.N.: 2010, On the 3-D reconstruction of Coronal Mass Ejections using coronagraph data. *Annales Geophysicae* **28**, 203. DOI. ADS.
- Mierla, M., Inhester, B., Rodriguez, L., Gissot, S., Zhukov, A., Srivastava, N.: 2011, On 3D reconstruction of coronal mass ejections: II. Longitudinal and latitudinal width analysis of 31 August 2007 event. *Journal of Atmospheric and Solar-Terrestrial Physics* **73**, 1166. DOI. ADS.
- Mierla, M., Seaton, D.B., Berghmans, D., Chifu, I., De Groof, A., Inhester, B., Rodriguez, L., Stenborg, G., Zhukov, A.N.: 2013, Study of a Prominence Eruption using PROBA2/SWAP and STEREO/EUVI Data. *Solar Phys.* **286**, 241. DOI. ADS.
- Mitalas, R., Sills, K.R.: 1992, On the Photon Diffusion Time Scale for the Sun. *Astrophys. J.* **401**, 759. DOI. ADS.

- Monstein, C.: 2013, CALLISTO and the e-CALLISTO network. In: *EGU Gen Assemb Conf Abs.* [ADS](#).
- Moon, Y.-J., Choe, G.S., Wang, H., Park, Y.D., Gopalswamy, N., Yang, G., Yashiro, S.: 2002, A Statistical Study of Two Classes of Coronal Mass Ejections. *Astrophys. J.* **581**, 694. [DOI](#). [ADS](#).
- Moore, R.L., Sterling, A.C., Suess, S.T.: 2007, The width of a solar coronal mass ejection and the source of the driving magnetic explosion: A test of the standard scenario for CME production. *The Astrophysical Journal* **668**, 1221. [DOI](#). <https://doi.org/10.1086%2F521215>.
- Moran, T.G., Davila, J.M., Thompson, W.T.: 2010, Three-Dimensional Polarimetric Coronal Mass Ejection Localization Tested Through Triangulation. *Astrophys. J.* **712**, 453. [DOI](#). [ADS](#).
- Morgan, H., Byrne, J.P., Habbal, S.R.: 2012, AUTOMATICALLY DETECTING AND TRACKING CORONAL MASS EJECTIONS. i. SEPARATION OF DYNAMIC AND QUIESCENT COMPONENTS IN CORONAGRAPH IMAGES. *The Astrophysical Journal* **752**, 144. [DOI](#). <https://doi.org/10.1088%2F0004-637x%2F752%2F2%2F144>.
- Morgan, H., Byrne, J.P., Habbal, S.R.: 2012, Automatically Detecting and Tracking Coronal Mass Ejections. I. Separation of Dynamic and Quiescent Components in Coronagraph Images. *Astrophys. J.* **752**, 144. [DOI](#). [ADS](#).
- Morgan, H., Habbal, S.R., Woo, R.: 2006, The Depiction of Coronal Structure in White-Light Images. *Solar Phys.* **236**, 263. [DOI](#). [ADS](#).
- Muller, D., Fleck, B., Dimitoglou, G., Caplins, B.W., Amadigwe, D.E., García Ortiz, J.P., Wamsler, B., Alexanderian, A., Hughitt, V.K., Ireland, J.: 2009, JHelioviewer: Visualizing Large Sets of Solar Images Using JPEG 2000. *Computing in Science and Engineering* **11**, 38. [DOI](#). [ADS](#).
- Müller, D., Marsden, R.G., St. Cyr, O.C., Gilbert, H.R., The Solar Orbiter Team: 2013, Solar orbiter. *Solar Phys.* **285**, 25. [DOI](#).
- Müller, D., Marsden, R.G., St. Cyr, O.C., Gilbert, H.R.: 2013a, Solar Orbiter . Exploring the Sun-Heliosphere Connection. *Solar Phys.* **285**, 25. [DOI](#). [ADS](#).
- Müller, D., Marsden, R.G., St. Cyr, O.C., Gilbert, H.R.: 2013b, Solar Orbiter . Exploring the Sun-Heliosphere Connection. *Solar Phys.* **285**, 25. [DOI](#). [ADS](#).
- Müller, D., Nicula, B., Felix, S., Verstringe, F., Bourgoignie, B., Csillaghy, A., Berghmans, D., Jiggins, P., García-Ortiz, J.P., Ireland, J., Zahniy, S., Fleck, B.: 2017, JHelioviewer. Time-dependent 3D visualisation of solar and heliospheric data. *Astron. Astrophys.* **606**, A10. [DOI](#). [ADS](#).
- Müller-Mellin, R., Kunow, H., Fleißner, V., Pehlke, E., Rode, E., Röschmann, N., Scharmberg, C., Sierks, H., Rusznyak, P., McKenna-Lawlor, S., Elenndt, I., Sequeiros, J., Meziat, D., Sanchez, S., Medina, J., Del Peral, L., Witte, M., Marsden, R., Henrion, J.: 1995, COSTEP - Comprehensive Suprathermal and Energetic Particle Analyser. *Solar Phys.* **162**, 483. [DOI](#). [ADS](#).
- Murray, S.A., Guerra, J.A., Zucca, P., Park, S.-H., Carley, E.P., Gallagher, P.T., Vilmer, N., Bothmer, V.: 2018, Connecting Coronal Mass Ejections to Their Solar Active Region Sources: Combining Results from the HELCATS and FLARE-CAST Projects. *Solar Phys.* **293**, 60. [DOI](#). [ADS](#).

- Newkirk, J. Gordon: 1967, Structure of the Solar Corona. *Annu. Rev. Astron. Astrophys* **5**, 213. DOI. ADS.
- Noci, G., Kohl, J.L., Huber, M.C.E., Antonucci, E., Fineschi, S., Gardner, L.D., Naletto, G., Nicolosi, P., Raymond, J.C., Romoli, M., Spadaro, D., Strachan, L., Tondello, G., van Ballegooijen, A.: 1995, The Ultraviolet Coronagraph Spectrometer. In: Benz, A.O., Krüger, A. (eds.) *Coronal Magnetic Energy Releases* **444**, 261. DOI. ADS.
- O’Kane, J., Green, L., Long, D.M., Reid, H.: 2019, Stealth Coronal Mass Ejections from Active Regions. *Astrophys. J.* **882**, 85. DOI. ADS.
- Olmedo, O., Zhang, J., Wechsler, H., Poland, A., Borne, K.: 2008, Automatic Detection and Tracking of Coronal Mass Ejections in Coronagraph Time Series. *Solar Phys.* **248**, 485. DOI. ADS.
- Pant, V., Willems, S., Rodriguez, L., Mierla, M., Banerjee, D., Davies, J.A.: 2016, Automated Detection of Coronal Mass Ejections in STEREO Heliospheric Imager Data. *Astrophys. J.* **833**, 80. DOI. ADS.
- Pant, V., Majumdar, S., Patel, R., Chauhan, A., Banerjee, D., Gopalswamy, N.: 2021, Investigating width distribution of slow and fast cmes in solar cycles 23 and 24. *Frontiers in Astronomy and Space Sciences* **8**, 73. DOI. <https://www.frontiersin.org/article/10.3389/fspas.2021.634358>.
- Parker, E.N.: 1958, Dynamics of the Interplanetary Gas and Magnetic Fields. *Astrophys. J.* **128**, 664. DOI. ADS.
- Patchett, B.E., Harrison, R.A., Sawyer, E.C., Aschenbach, B., Culhane, J.L., Doschek, G.A., Gabriel, A.H., Huber, M.C.E., Jordan, C., Kjeldseth-Moe, O.: 1988, *CDS: The Coronal Diagnostic Spectrometer*, In ESA, The SOHO Mission. Scientific and Technical Aspects of the Instruments p 39-42 (SEE N90-13302 04-92). ADS.
- Patel, R., Pant, V., Iyer, P., Banerjee, D., Mierla, M., West, M.J.: 2021a, Automated Detection of Accelerating Solar Eruptions Using Parabolic Hough Transform. *Solar Phys.* **296**, 31. DOI. ADS.
- Patel, R., Pant, V., Iyer, P., Banerjee, D., Mierla, M., West, M.J.: 2021b, Automated Detection of Accelerating Solar Eruptions Using Parabolic Hough Transform. *Solar Phys.* **296**, 31. DOI. ADS.
- Patsourakos, S., Vourlidas, A., Kliem, B.: 2010, Toward understanding the early stages of an impulsively accelerated coronal mass ejection. SECCHI observations. *Astron. Astrophys.* **522**, A100. DOI. ADS.
- Pesnell, W.D., Thompson, B.J., Chamberlin, P.C.: 2012, The Solar Dynamics Observatory (SDO). *Solar Phys.* **275**, 3. DOI. ADS.
- Pick, M., Forbes, T.G., Mann, G., Cane, H.V., Chen, J., Ciaravella, A., Cremades, H., Howard, R.A., Hudson, H.S., Klassen, A., Klein, K.L., Lee, M.A., Linker, J.A., Maia, D., Mikic, Z., Raymond, J.C., Reiner, M.J., Simnett, G.M., Srivastava, N., Tripathi, D., Vainio, R., Vourlidas, A., Zhang, J., Zurbuchen, T.H., Sheeley, N.R., Marqué, C.: 2006, Multi-Wavelength Observations of CMEs and Associated Phenomena. Report of Working Group F. *Space Sci. Rev.* **123**, 341. DOI. ADS.

- Pierantoni, G., Carley, E.P., Byrne, J.P., Perez-Suarez, D., Gallagher, P.T.: 2014, a Workflow-Oriented Approach to Propagation Models in Heliophysics. *Computer Science* **3**, 271. DOI. ADS.
- Podolska, K., Hruska, F., Truhlik, V.: 2016, A measurement of the TPMU - PROBA II Microsatellite Instrument and its comparison with the SWARM Langmuir Probes results. In: *EGU General Assembly Conference Abstracts, EGU General Assembly Conference Abstracts, EPSC2016*. ADS.
- Prasad, B., Banerjee, D., Singh, J., Subramanya, N., Kumar, A., Kamath, P., Kathiravan, s., Venkata, S., Rajkumar, N., Natarajan, V., Juneja, M., Somu, P., Pant, V., Shaji, N., Sankarsubramanian, K., Patra, A., Venkateswaran, R., Adoni, A., Narendra, S., Jaiswal, B.: 2017a, Visible emission line coronagraph on aditya-11. *Current Science* **113**, 613. DOI.
- Prasad, B., Banerjee, D., Singh, J., Subramanya, N., Kumar, A., Kamath, P., Kathiravan, s., Venkata, S., Rajkumar, N., Natarajan, V., Juneja, M., Somu, P., Pant, V., Shaji, N., Sankarsubramanian, K., Patra, A., Venkateswaran, R., Adoni, A., Narendra, S., Jaiswal, B.: 2017b, Visible emission line coronagraph on aditya-11. *Current Science* **113**, 613. DOI.
- R Core Team: 2018, *R: A language and environment for statistical computing*. R Foundation for Statistical Computing, Vienna, Austria. R Foundation for Statistical Computing. <https://www.R-project.org/>.
- Raghavendra Prasad, B., Banerjee, D., Singh, J., Nagabhushana, S., Kumar, A., Kamath, P.U., Kathiravan, S., Venkata, S., Rajkumar, N., Natarajan, V., Juneja, M., Somu, P., Pant, V., Shaji, N., Sankarsubramanian, K., Patra, A., Venkateswaran, R., Adoni, A.A., Narendra, S., Haridas, T.R., Mathew, S.K., Krishna, R.M., Amareswari, K., Jaiswal, B.: 2017, Visible Emission Line Coronagraph on Aditya-L1. *Current Science* **113**, 613. DOI.
- Ramesh, R., Subramanian, K.R., Sundararajan, M.S., Sastry, C.V.: 1998, The Gauribidanur Radioheliograph. *Solar Phys.* **181**, 439. DOI. ADS.
- Renotte, E., Baston, E.C., Bemporad, A.r., Capobianco, G., Cernica, I., Darakchiev, R., Denis, F., Desselle, R., De Vos, L., Fineschi, S., Focardi, M., Górski, T., Graczyk, R., Halain, J.-P., Hermans, A., Jackson, C., Kintziger, C., Kosiec, J., Kranitis, N., Landini, F., Lédl, V., Massone, G., Mazzoli, A., Melich, R., Mollet, D., Mosdorf, M., Nicolini, G., Nicula, B., Orleański, P., Palau, M.-C., Pancrazzi, M., Paschalis, A., Peresty, R., Plessieria, J.-Y., Rataj, M., Romoli, M., Thizy, C., Thomé, M., Tsinganos, K., Wodnicki, R., Walczak, T., Zhukov, A.: 2014a, ASPIICS: an externally occulted coronagraph for PROBA-3: Design evolution. In: *Proc. Spie., Society of Photo-Optical Instrumentation Engineers (SPIE) Conference Series* **9143**, 91432M. DOI. ADS.
- Renotte, E., Baston, E.C., Bemporad, A., Capobianco, G., Cernica, I., Darakchiev, R., Denis, F., Desselle, R., De Vos, L., Fineschi, S., Focardi, M., Górski, T., Graczyk, R., Halain, J.-P., Hermans, A., Jackson, C., Kintziger, C., Kosiec, J., Kranitis, N., Landini, F., Lédl, V., Massone, G., Mazzoli, A., Melich, R., Mollet, D., Mosdorf, M., Nicolini, G., Nicula, B., Orleański, P., Palau, M.-C., Pancrazzi, M., Paschalis, A., Peresty, R., Plessieria, J.-Y., Rataj, M., Romoli, M., Thizy, C., Thomé, M., Tsinganos, K., Wodnicki, R., Walczak, T., Zhukov, A.: 2014b, ASPIICS: an externally occulted coronagraph for PROBA-3: Design evolution. In: Oschmann, J. Jacobus M., Clampin, M., Fazio, G.G., MacEwen, H.A. (eds.) *Space Telescopes and Instrumentation 2014: Optical, Infrared, and Millimeter Wave, Pro. SPIE* **9143**, 91432M. DOI. ADS.

- Richardson, J.D., Kasper, J.C., Wang, C., Belcher, J.W., Lazarus, A.J.: 2008, Cool heliosheath plasma and deceleration of the upstream solar wind at the termination shock. *Nature* **454**, 63. DOI. ADS.
- Riley, P., Mays, M.L., Andries, J., Amerstorfer, T., Biesecker, D., Delouille, V., Dumbović, M., Feng, X., Henley, E., Linker, J.A., Möstl, C., Nuñez, M., Pizzo, V., Temmer, M., Tobiska, W.K., Verbeke, C., West, M.J., Zhao, X.: 2018, Forecasting the Arrival Time of Coronal Mass Ejections: Analysis of the CCMC CME Scoreboard. *Space Weather* **16**, 1245. DOI. ADS.
- Robbrecht, E., Berghmans, D.: 2004, Automated recognition of coronal mass ejections (CMEs) in near-real-time data. *Astron. Astrophys.* **425**, 1097. DOI. ADS.
- Robbrecht, E., Berghmans, D., Van der Linden, R.A.M.: 2009, Automated LASCO CME Catalog for Solar Cycle 23: Are CMEs Scale Invariant? *Astrophys. J.* **691**, 1222. DOI. ADS.
- Ross, J.E., Aller, L.H.: 1976, The Chemical Composition of the Sun. *Science* **191**, 1223. DOI. ADS.
- Russell, C.T., Mulligan, T.: 2002, On the magnetosheath thicknesses of interplanetary coronal mass ejections. *Planet Space Sci* **50**, 527 . DOI.
- Sachdeva, N., Subramanian, P., Colaninno, R., Vourlidis, A.: 2015, CME PROPAGATION: WHERE DOES AERODYNAMIC DRAG “TAKE OVER”? *The Astrophysical Journal* **809**, 158. DOI. <https://doi.org/10.1088%2F0004-637x%2F809%2F2%2F158>.
- Sachdeva, N., Subramanian, P., Vourlidis, A., Bothmer, V.: 2017, CME Dynamics Using STEREO and LASCO Observations: The Relative Importance of Lorentz Forces and Solar Wind Drag. *Solar Phys.* **292**, 118. DOI. ADS.
- Santandrea, S., Gantois, K., Strauch, K., Teston, F., Tilmans, E., Baijot, C., Gerrits, D., De Groof, A., Schwehm, G., Zender, J.: 2013, PROBA2: Mission and Spacecraft Overview. *Solar Phys.* **286**, 5. DOI. ADS.
- Sarkar, R., Srivastava, N., Mierla, M., West, M.J., D’Huys, E.: 2019, Evolution of the Coronal Cavity From the Quiescent to Eruptive Phase Associated with Coronal Mass Ejection. *Astrophys. J.* **875**, 101. DOI. ADS.
- Scherrer, P.H., Bogart, R.S., Bush, R.I., Hoeksema, J.T., Kosovichev, A.G., Schou, J., Rosenberg, W., Springer, L., Tarbell, T.D., Title, A., Wolfson, C.J., Zayer, I., MDI Engineering Team: 1995, The Solar Oscillations Investigation - Michelson Doppler Imager. *Solar Phys.* **162**, 129. DOI. ADS.
- Scherrer, P.H., Schou, J., Bush, R.I., Kosovichev, A.G., Bogart, R.S., Hoeksema, J.T., Liu, Y., Duvall, T.L., Zhao, J., Title, A.M., Schrijver, C.J., Tarbell, T.D., Tomczyk, S.: 2012, The Helioseismic and Magnetic Imager (HMI) Investigation for the Solar Dynamics Observatory (SDO). *Solar Phys.* **275**, 207. DOI. ADS.
- Schmahl, E., Hildner, E.: 1977, Coronal mass-ejections-kinematics of the 19 December 1973 event. *Solar Phys.* **55**, 473. DOI. ADS.
- Schwenn, R.: 2006, Space Weather: The Solar Perspective. *Living Reviews in Solar Physics* **3**, 2. DOI. ADS.
- Schwenn, R., Marsch, E.: 1990, *Physics of the Inner Heliosphere I. Large-Scale Phenomena*. DOI. ADS.

- Schwenn, R., dal Lago, A., Huttunen, E., Gonzalez, W.D.: 2005, The association of coronal mass ejections with their effects near the Earth. *Annales Geophysicae* **23**, 1033. DOI. ADS.
- Seaton, D.B., Mierla, M., Berghmans, D., Zhukov, A.N., Dolla, L.: 2011, SWAP-SECCHI Observations of a Mass-loading Type Solar Eruption. *Astrophys. J. Lett.* **727**, L10. DOI. ADS.
- Seaton, D.B., Berghmans, D., Nicula, B., Halain, J.-P., De Groof, A., Thibert, T., Bloomfield, D.S., Raftery, C.L., Gallagher, P.T., Auchère, F., Defise, J.-M., D’Huys, E., Lecat, J.-H., Mazy, E., Rochus, P., Rossi, L., Schühle, U., Slemzin, V., Yalim, M.S., Zender, J.: 2013, The SWAP EUV Imaging Telescope Part I: Instrument Overview and Pre-Flight Testing. *Solar Phys.* **286**, 43. DOI. ADS.
- Seetha, S., Megala, S.: 2017a, Aditya-l1 mission. *Current Science* **113**, 610. DOI.
- Seetha, S., Megala, S.: 2017b, Aditya-L1 mission. *Cur. Science* **113**, 610. DOI.
- Sheeley, J. N. R., Michels, D.J., Howard, R.A., Koomen, M.J.: 1980, Initial observations with the SOLWIND coronagraph. *Astrophys. J. Lett.* **237**, L99. DOI. ADS.
- Sheeley, N.R., Hakala, W.N., Wang, Y.-M.: 2000, Detection of coronal mass ejection associated shock waves in the outer corona. *J. Geophys. Res.* **105**, 5081. DOI. ADS.
- Sheeley, N.R., Walters, J.H., Wang, Y.-M., Howard, R.A.: 1999, Continuous tracking of coronal outflows: Two kinds of coronal mass ejections. *J. Geophys. Res.* **104**, 24739. DOI. ADS.
- Shen, C., Wang, Y., Pan, Z., Zhang, M., Ye, P., Wang, S.: 2013a, Full halo coronal mass ejections: Do we need to correct the projection effect in terms of velocity? In: *AGU Fall Meeting Abstracts 2013*, SH31B. ADS.
- Shen, C., Wang, Y., Pan, Z., Zhang, M., Ye, P., Wang, S.: 2013b, Full halo coronal mass ejections: Do we need to correct the projection effect in terms of velocity? *Journal of Geophysical Research (Space Physics)* **118**, 6858. DOI. ADS.
- Simnett, G.M.: 2000, The relationship between prominence eruptions and coronal mass ejections. *Journal of Atmospheric and Solar-Terrestrial Physics* **62**, 1479. DOI. ADS.
- Smerd, S.F., Sheridan, K.V., Stewart, R.T.: 1975, Split-Band Structure in Type II Radio Bursts from the Sun. *Astrophys. Letters* **16**, 23. ADS.
- Song, H.Q., Zhang, J., Li, L.P., Liu, Y.D., Zhu, B., Wang, B., Zheng, R.S., Chen, Y.: 2019, The Structure of Solar Coronal Mass Ejections in the Extreme-ultraviolet Passbands. *Astrophys. J.* **887**, 124. DOI. ADS.
- Spiegel, E.A., Zahn, J.-P.: 1992, The solar tachocline. *Astron. Astrophys.* **265**, 106. ADS.
- St. Cyr, O.C., Burkepile, J.T., Hundhausen, A.J., Lecinski, A.R.: 1999a, A comparison of ground-based and spacecraft observations of coronal mass ejections from 1980-1989. *J. Geophys. Res.* **104**, 12493. DOI. ADS.
- St. Cyr, O.C., Burkepile, J.T., Hundhausen, A.J., Lecinski, A.R.: 1999b, A comparison of ground-based and spacecraft observations of coronal mass ejections from 1980-1989. *J. Geophys. Res.* **104**, 12493. DOI. ADS.

- St. Cyr, O.C., Plunkett, S.P., Michels, D.J., Paswaters, S.E., Koomen, M.J., Simnett, G.M., Thompson, B.J., Gurman, J.B., Schwenn, R., Webb, D.F., Hildner, E., Lamy, P.L.: 2000, Properties of coronal mass ejections: SOHO LASCO observations from January 1996 to June 1998. *J. Geophys. Res.* **105**, 18169. DOI. ADS.
- Subramanian, P., Dere, K.P.: 2001, Source regions of coronal mass ejections. *The Astrophysical Journal* **561**, 372. DOI. <https://doi.org/10.1086%2F323213>.
- Subramanian, P., Dere, K.P.: 2001, Source Regions of Coronal Mass Ejections. *Astrophys. J.* **561**, 372. DOI. ADS.
- Subramanian, P., Arunbabu, K.P., Vourlidas, A., Mauriya, A.: 2014, SELF-SIMILAR EXPANSION OF SOLAR CORONAL MASS EJECTIONS: IMPLICATIONS FOR LORENTZ SELF-FORCE DRIVING. *The Astrophysical Journal* **790**, 125. DOI. <https://doi.org/10.1088%2F0004-637x%2F790%2F2%2F125>.
- Suryanarayana, G.S.: 2019a, Correlations between the CME acceleration, other CME parameters and flare energy. *Journal of Atmospheric and Solar-Terrestrial Physics* **185**, 1. DOI. ADS.
- Suryanarayana, G.S.: 2019b, Correlations between the CME acceleration, other CME parameters and flare energy. *Journal of Atmospheric and Solar-Terrestrial Physics* **185**, 1. DOI. ADS.
- Temmer, M.: 2016, Kinematical properties of coronal mass ejections. *Astronomische Nachrichten* **337**, 1010. DOI. ADS.
- Temmer, M., Veronig, A.M., Vršnak, B., Rybák, J., Gömöry, P., Stoiser, S., Maričić, D.: 2008, Acceleration in fast halo CMEs and synchronized flare HXR bursts. *The Astrophysical Journal* **673**, L95. DOI. <https://doi.org/10.1086%2F527414>.
- Temmer, M., Veronig, A.M., Kontar, E.P., Krucker, S., Vršnak, B.: 2010, COMBINEDSTEREO/RHESSISTUDY OF CORONAL MASS EJECTION ACCELERATION AND PARTICLE ACCELERATION IN SOLAR FLARES. *The Astrophysical Journal* **712**, 1410. DOI. <https://doi.org/10.1088%2F0004-637x%2F712%2F2%2F1410>.
- Temmer, M., Holzknicht, L., Dumbović, M., Vršnak, B., Sachdeva, N., Heinemann, S.G., Dissauer, K., Scolini, C., Asvestari, E., Veronig, A.M., Hofmeister, S.J.: 2021, Deriving CME Density From Remote Sensing Data and Comparison to In Situ Measurements. *Journal of Geophysical Research (Space Physics)* **126**, e28380. DOI. ADS.
- Thernisien, A.: 2011a, Implementation of the Graduated Cylindrical Shell Model for the Three-dimensional Reconstruction of Coronal Mass Ejections. *Astrophys. J. Suppl.* **194**, 33. DOI. ADS.
- Thernisien, A.: 2011b, Implementation of the Graduated Cylindrical Shell Model for the Three-dimensional Reconstruction of Coronal Mass Ejections. *Astrophys. J. Suppl.* **194**, 33. DOI. ADS.
- Thernisien, A., Vourlidas, A., Howard, R.A.: 2009a, Forward Modeling of Coronal Mass Ejections Using STEREO/SECCHI Data. *Solar Phys.* **256**, 111. DOI. ADS.

- Thernisien, A., Vourlidas, A., Howard, R.A.: 2009b, Forward Modeling of Coronal Mass Ejections Using STEREO/SECCHI Data. *Solar Phys.* **256**, 111. DOI. ADS.
- Thernisien, A., Vourlidas, A., Howard, R.A.: 2009c, Forward Modeling of Coronal Mass Ejections Using STEREO/SECCHI Data. *Solar Phys.* **256**, 111. DOI. ADS.
- Thernisien, A.F.R., Howard, R.A., Vourlidas, A.: 2006a, Modeling of Flux Rope Coronal Mass Ejections. *Astrophys. J.* **652**, 763. DOI. ADS.
- Thernisien, A.F.R., Howard, R.A., Vourlidas, A.: 2006b, Modeling of Flux Rope Coronal Mass Ejections. *Astrophys. J.* **652**, 763. DOI. ADS.
- Thompson, W.T., St. Cyr, O.C., Burkepile, J.T., Posner, A.: 2017, Automatic Near-Real-Time Detection of CMEs in Mauna Loa K-Cor Coronagraph Images. *Space Weather* **15**, 1288. DOI. ADS.
- Torsti, J., Valtonen, E., Lumme, M., Peltonen, P., Eronen, T., Louhola, M., Riihonen, E., Schultz, G., Teittinen, M., Ahola, K., Holmlund, C., Kelhä, V., Leppälä, K., Ruuska, P., Strömmer, E.: 1995, Energetic Particle Experiment ERNE. *Solar Phys.* **162**, 505. DOI. ADS.
- Tousey, R.: 1973, The solar corona. In: *Space Research Conference* **2**, 713. ADS.
- Tripathi, D., Bothmer, V., Cremades, H.: 2004, The basic characteristics of EUV post-eruptive arcades and their role as tracers of coronal mass ejection source regions. *Astron. Astrophys.* **422**, 337. DOI. ADS.
- Uchida, Y.: 1962, On the Exciters of Type II and Type III Solar Radio Bursts. *Journal of the Physical Society of Japan Supplement* **17**, 234. ADS.
- Vernazza, J.E., Avrett, E.H., Loeser, R.: 1981, Structure of the solar chromosphere. III. Models of the EUV brightness components of the quiet sun. *Astrophys. J. Suppl.* **45**, 635. DOI. ADS.
- Vourlidas, A., Howard, R.A.: 2006, The Proper Treatment of Coronal Mass Ejection Brightness: A New Methodology and Implications for Observations. *Astrophys. J.* **642**, 1216. DOI. ADS.
- Vourlidas, A., Wu, S., Wang, A.H., Subramanian, P., Howard, R.: 2008, Direct detection of a coronal mass ejection-associated shock in large angle and spectrometric coronagraph experiment white-light images. *The Astrophysical Journal* **598**, 1392. DOI.
- Vourlidas, A., Howard, R.A., Esfandiari, E., Patsourakos, S., Yashiro, S., Michalek, G.: 2010, Comprehensive Analysis of Coronal Mass Ejection Mass and Energy Properties Over a Full Solar Cycle. *Astrophys. J.* **722**, 1522. DOI. ADS.
- Vourlidas, A., Lynch, B.J., Howard, R.A., Li, Y.: 2013, How Many CMEs Have Flux Ropes? Deciphering the Signatures of Shocks, Flux Ropes, and Prominences in Coronagraph Observations of CMEs. *Solar Phys.* **284**, 179. DOI. ADS.
- Vourlidas, A., Balmaceda, L.A., Stenborg, G., Lago, A.D.: 2017, Multi-viewpoint coronal mass ejection catalog based on STEREOCOR2 observations. *The Astrophysical Journal* **838**, 141. DOI. <https://doi.org/10.3847/2F1538-4357/2Faa67f0>.

- Vršnak, B., Magdalenić, J., Zlobec, P.: 2004, Band-splitting of coronal and interplanetary type II bursts. III. Physical conditions in the upper corona and interplanetary space. *Astron. Astrophys.* **413**, 753. DOI. ADS.
- Vršnak, B., Sudar, D., Ruždjak, D.: 2005, The CME-flare relationship: Are there really two types of CMEs? *Astron. Astrophys.* **435**, 1149. DOI. ADS.
- Vršnak, B., Aurass, H., Magdalenić, J., Gopalswamy, N.: 2001, Band-splitting of coronal and interplanetary type II bursts. I. Basic properties. *Astron. Astrophys.* **377**, 321. DOI. ADS.
- Vršnak, B., Ruždjak, D., Sudar, D., Gopalswamy, N.: 2004, Kinematics of coronal mass ejections between 2 and 30 solar radii. What can be learned about forces governing the eruption? *Astron. Astrophys.* **423**, 717. DOI. ADS.
- Vršnak, B., Warmuth, A., Temmer, M., Veronig, A., Magdalenić, J., Hillaris, A., Karlický, M.: 2006, Multi-wavelength study of coronal waves associated with the CME-flare event of 3 November 2003. *Astron. Astrophys.* **448**, 739. DOI. ADS.
- Vršnak, B., Maričić, D., Stanger, A.L., Veronig, A.M., Temmer, M., Roša, D.: 2007a, Acceleration Phase of Coronal Mass Ejections: I. Temporal and Spatial Scales. *Solar Phys.* **241**, 85. DOI. ADS.
- Vršnak, B., Maričić, D., Stanger, A.L., Veronig, A.M., Temmer, M., Roša, D.: 2007b, Acceleration Phase of Coronal Mass Ejections: I. Temporal and Spatial Scales. *Solar Phys.* **241**, 85. DOI. ADS.
- Wang, J., Hoeksema, J.T., Liu, S.: 2019, On Deflection of Solar Coronal Mass Ejections by the Ambient Coronal Magnetic Field Configuration. *arXiv e-prints*, arXiv:1909.06410. ADS.
- Wang, Y.-M., Colaninno, R.: 2014, Is Solar Cycle 24 Producing More Coronal Mass Ejections Than Cycle 23? *Astrophys. J. Lett.* **784**, L27. DOI. ADS.
- Webb, D., Howard, T.: 2012a, Coronal mass ejections: Observations. *Living Reviews in Solar Physics* **9**. DOI.
- Webb, D., Howard, T.: 2012b, Coronal mass ejections: Observations. *Living Reviews in Solar Physics* **9**. DOI.
- Webb, D.F., Jackson, B.V.: 1981, Kinematical Analysis of Flare Spray Ejecta Observed in the Corona. *Solar Phys.* **73**, 341. DOI. ADS.
- Wilhelm, K., Curdt, W., Marsch, E., Schühle, U., Lemaire, P., Gabriel, A., Vial, J.-C., Grewing, M., Huber, M.C.E., Jordan, S.D., Poland, A.I., Thomas, R.J., Kühne, M., Timothy, J.G., Hassler, D.M., Siegmund, O.H.W.: 1995, SUMER - Solar Ultraviolet Measurements of Emitted Radiation. *Solar Phys.* **162**, 189. DOI. ADS.
- Wood, B.E., Karovska, M., Chen, J., Brueckner, G.E., Cook, J.W., Howard, R.A.: 1999, Comparison of Two Coronal Mass Ejections Observed by EIT and LASCO with a Model of an Erupting Magnetic Flux Rope. *Astrophys. J.* **512**, 484. DOI. ADS.

- Woods, T.N., Eparvier, F.G., Hock, R., Jones, A.R., Woodraska, D., Judge, D., Didkovsky, L., Lean, J., Mariska, J., Warren, H., McMullin, D., Chamberlin, P., Berthiaume, G., Bailey, S., Fuller-Rowell, T., Sojka, J., Tobiska, W.K., Viereck, R.: 2012, Extreme Ultraviolet Variability Experiment (EVE) on the Solar Dynamics Observatory (SDO): Overview of Science Objectives, Instrument Design, Data Products, and Model Developments. *Solar Phys.* **275**, 115. DOI. ADS.
- Yashiro, S., Michalek, G., Gopalswamy, N.: 2008, A comparison of coronal mass ejections identified by manual and automatic methods. *Annales Geophysicae* **26**, 3103. DOI. ADS.
- Yashiro, S., Gopalswamy, N., Michalek, G., Howard, R.A.: 2003, Properties of narrow coronal mass ejections observed with LASCO. *Advances in Space Research* **32**, 2631. DOI. ADS.
- Yashiro, S., Gopalswamy, N., Michalek, G., St. Cyr, O.C., Plunkett, S.P., Rich, N.B., Howard, R.A.: 2004a, A catalog of white light coronal mass ejections observed by the SOHO spacecraft. *Journal of Geophysical Research (Space Physics)* **109**, A07105. DOI. ADS.
- Yashiro, S., Gopalswamy, N., Michalek, G., St. Cyr, O.C., Plunkett, S.P., Rich, N.B., Howard, R.A.: 2004b, A catalog of white light coronal mass ejections observed by the SOHO spacecraft. *Journal of Geophysical Research (Space Physics)* **109**, A07105. DOI. ADS.
- Yashiro, S., Akiyama, S., Gopalswamy, N., Howard, R.A.: 2006, Different Power-Law Indices in the Frequency Distributions of Flares with and without Coronal Mass Ejections. *Astrophys. J. Lett.* **650**, L143. DOI. ADS.
- Ying, B., Bemporad, A., Feng, L., Lu, L., Gan, W., Li, H.: 2020, Extensive Study of a Coronal Mass Ejection with UV and White-light Coronagraphs: The Need for Multiwavelength Observations. *Astrophys. J.* **899**, 12. DOI. ADS.
- Zhang, J., Dere, K.P.: 2006, A statistical study of main and residual accelerations of coronal mass ejections. *The Astrophysical Journal* **649**, 1100. DOI. <https://doi.org/10.1086%2F506903>.
- Zhang, J., Dere, K.P., Howard, R.A., Kundu, M.R., White, S.M.: 2001a, On the Temporal Relationship between Coronal Mass Ejections and Flares. *Astrophys. J.* **559**, 452. DOI. ADS.
- Zhang, J., Dere, K.P., Howard, R.A., Kundu, M.R., White, S.M.: 2001b, On the Temporal Relationship between Coronal Mass Ejections and Flares. *Astrophys. J.* **559**, 452. DOI. ADS.
- Zhang, J., Dere, K.P., Howard, R.A., Vourlidas, A.: 2004, A study of the kinematic evolution of coronal mass ejections. *The Astrophysical Journal* **604**, 420. DOI. <https://doi.org/10.1086%2F381725>.
- Zhao, X., Dryer, M.: 2014, Current status of CME/shock arrival time prediction. *Space Weather* **12**, 448. DOI. ADS.
- Zhao, X.H., Feng, X.S., Xiang, C.Q., Liu, Y., Li, Z., Zhang, Y., Wu, S.T.: 2010, Multi-spacecraft Observations of the 2008 January 2 CME in the Inner Heliosphere. *Astrophys. J.* **714**, 1133. DOI. ADS.

- Zhao, X.H., Feng, X.S., Feng, H.Q., Li, Z.: 2017, Correlation between Angular Widths of CMEs and Characteristics of Their Source Regions. *Astrophys. J.* **849**, 79. DOI. ADS.
- Zucca, P., Pick, M., Démoulin, P., Kerdraon, A., Lecacheux, A., Gallagher, P.T.: 2014, Understanding Coronal Mass Ejections and Associated Shocks in the Solar Corona by Merging Multiwavelength Observations. *Astrophys. J.* **795**, 68. DOI. ADS.
- Zuccarello, F.P., Seaton, D.B., Mierla, M., Poedts, S., Rachmeler, L.A., Romano, P., Zuccarello, F.: 2014, Observational Evidence of Torus Instability as Trigger Mechanism for Coronal Mass Ejections: The 2011 August 4 Filament Eruption. *Astrophys. J.* **785**, 88. DOI. ADS.